Optimization and Fracture Mechanics Analysis of the Set-in Nozzle of a PWR Reactor Pressure Vessel

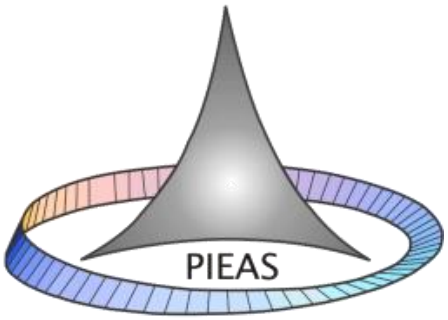

Usman Tariq Murtaza

2016

Department of Mechanical Engineering
Pakistan Institute of Engineering and Applied Sciences
Nilore, Islamabad, Pakistan

This page intentionally left blank.

Pakistan Institute of Engineering and Applied Sc
Nilore, Islamabad, 45650 Pakistan

Thesis Examiners

Student's Name: Usman Tariq Murtaza	**Department:** DME (PIEAS)
Registration Number: 04-7-1-001-2012	**Date of Registration:** 28-11-2011
Thesis Title: Optimization and Facture Mechanics Analysis of the Set-in Nozzle of a PWR Reactor Pressure Vessel	

Foreign Reviewers (Names and Affiliations)
1. Dr.-Ing. Sümer Şahin, Faculty of Engineering, ATILIM University, Turkey
2. Dr. Martin Tango, School of Engineering, Acadia University, Canada.
3. Dr. Tahir Abbas, Managing Director, CINAR Ltd., U.K.

Thesis Defense Examiners (Names and Affiliations)
1. Dr. Akhlaq Ahmed, DCE, PINSTECH, NILORE, Islamabad
2. Dr. Muhammad Mujahid, Professor, SCME, NUST,H-12, Islamabad
3. Dr. Sikandar M. Mirza, CS, DPAM, PIEAS, Islamabad

Head of the Department (Name) **:** Engr. Dr. Rizwan Alim Mufti Signatures/Date _____

Thesis Submission Approval

This is to certify that the work contained in this thesis entitled **Optimization and Fracture Mechanics Analysis of the Set-in Nozzle of a PWR Reactor Pressure Vessel**, was carried out by **Usman Tariq Murtaza**, and in my opinion, it is fully adequate, in scope and quality, for the degree of **Ph.D.** Furthermore, it is hereby approved for submission for review and thesis defense.

Supervisor: _____
Name: **Prof. Dr. M. Javed Hyder**
Date: 19 February, 2016
Place: PIEAS, Islamabad.

Head, Department of Mechanical Engineering: _____
Name: **Dr. Rizwan Alim Mufti**
Date: 19 February, 2016
Place: PIEAS, Islamabad.

Optimization and Fracture Mechanics Analysis of the Set-in Nozzle of a PWR Reactor Pressure Vessel

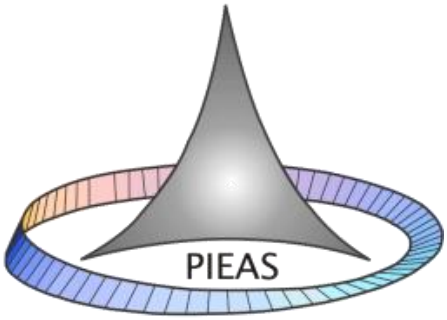

Usman Tariq Murtaza

Submitted in partial fulfillment of the requirements
for the degree of Ph.D.
February, 2016

Department of Mechanical Engineering
Pakistan Institute of Engineering and Applied Sciences
Nilore, Islamabad, Pakistan

Dedications

Dedicated to my country

“The Islamic Republic of Pakistan”

Declaration of Originality

I hereby declare that the work contained in this thesis and the intellectual content of this thesis are the product of my own work. This thesis has not been previously published in any form nor does it contain any verbatim of the published resources which could be treated as infringement of the international copyright law. I also declare that I do understand the terms ‘copyright’ and ‘plagiarism,’ and that in case of any copyright violation or plagiarism found in this work, I will be held fully responsible of the consequences of any such violation.

_____

(**Usman Tariq Murtaza**)
19 February, 2016
PIEAS, Islamabad.

Copyrights Statement

Acknowledgement

All praises to almighty ALLAH, the creator of the universe, for blessing us with knowledge and endowing the status of super creature. I am always grateful to almighty ALLAH, the most benevolent and merciful, who blessed me throughout my life despite my limitations, and gave me the ability to undertake such a challenging task and proceed towards completion. This is a mercy from my Lord. My succor is only with ALLAH. In Him I have put my trust, and to Him do I always turn.

I extend my sincerest thanks to my supervisor, **Prof. Dr. M. Javed Hyder** for his generous guidance and moral support during my Ph.D. I appreciate his endless patience, positive attitude, ability to provide assistance and especially his willingness to put his students before his work. His valuable suggestions and persuasive criticism has led me to complete my goal successfully. I am also indebted to **Dr. Rizwan Alim Mufti**, **Dr. Ajmal Shah** and all other faculty members of the department for their corporation and encouragement to attain my goal.

I gratefully acknowledge **Pakistan Institute of Engineering and Applied Sciences** (PIEAS) for the financial support provided through IT and Telecom Endowment fund (IT&TEF). In this context, I want to acknowledge **Mr. Naeem Ahmed** as the director of IT&TEF, PIEAS. It was his gratifying attitude that set me free from my financial worries throughout Ph.D. He really deserves special thanks for his generous support.

_____

(**Usman Tariq Murtaza**)
PIEAS, Islamabad.

Table of Contents

List of Figures

List of Tables

Abstract

This thesis mainly focuses on optimization and fracture mechanics analysis of a set-in nozzle using a finite element based (FEM) based computational software, the 'ANSYS Workbench'. The analyzed set-in nozzle belongs to a typical reactor pressure vessel (RPV) of a 300 MW pressurized water reactor, which is made of a nuclear grade steel designated as *'SA-508 Gr.3 Cl.1'*.

In the first part of the thesis, that is called the optimization of the set-in nozzle, an optimized design of the nozzle is proposed. It has been demonstrated that the maximum stress intensity along the optimized nozzle including the highest stress concentration point does not predict yielding according to Tresca yield theory and is therefore a safe design of the nozzle. It has also been shown using the 'design-by-analysis' approach that the safety margin of the optimized nozzle is equal to at least 2.0 according to the criterion given in ASME code [1].

In the second part of the thesis, that is called the fracture mechanics analysis of the set-in nozzle, it is investigated that if during operation corner crack initiates at highest stress concentration point (nozzle-cylinder intersection) of the nozzle, then what is the critical crack depth up to which the RPV can be operated safely. For the purpose, initially, a 'pallet body approach' for the assessment of three-dimensional corner cracks was proposed in this study. The approach is capable of efficiently computing stress intensity factors (SIFs) along the crack front. Using the approach a wide range of corner surface crack was analyzed in order to investigate the critical crack depth. The cracks were observed under normal operating conditions, small-break loss of coolant accident (SB-LOCA) conditions, and Rancho-Seco transient (RST) conditions of the plant. The SIFs of the wide range corner cracks under these plant's conditions have also been presented in a suitable graphical format, which provides a useful tool for the fracture mechanics analysis of the set-in nozzle. As a conclusion, it has been demonstrated that the corner crack having dimensions '$a = 0.05t$' is the critical crack for the optimized nozzle, where *'a'* is the depth of the crack and *'t'* is the thickness of the vessel's wall at nozzle-cylinder intersection.

Finally, in the fracture mechanics analysis, the effects of operational thermal stresses on the SIFs of the corner cracks under normal operating conditions were also investigated. A coupled field structural-thermal analysis under combined pressure plus thermal loadings was performed to simulate such effects. It has been demonstrated that the operational thermal stresses actually reduce the SIFs of the corner cracks, and therefore do not threaten the integrity of the RPV.

List of Publications

Journal Publications

- Usman Tariq Murtaza and M. Javed Hyder, "The Effects of Thermal Stresses on the Elliptical Surface Cracks in PWR Reactor Pressure Vessel," Theoretical and Applied Fracture Mechanics, vol. 75C, pp. 124–136, 2015.

- Usman Tariq Murtaza and M. Javed Hyder, "Optimization of the Size and Shape of the Set-in Nozzle for a PWR Reactor Pressure Vessel," Nuclear Engineering and Design, vol. 284C, pp. 219-227, 2015.

Conference Publications

- Usman Tariq Murtaza and M. Javed Hyder, "Methodology to Analyze 3D Curved Surface Cracks Using Hybrid Finite Elements," in Proceedings of the 2014 International Young Engineers Convention, Lahore, 2014, pp. 158-165.

- Usman Tariq Murtaza and M. Javed Hyder, "Design by Analysis versus Design by Formula of a PWR Reactor Pressure Vessel," in Proceedings of the 2015 International MultiConference of Engineers and Computer Scientists, Hong Kong, 2015, pp. 942-946.

- Usman Tariq Murtaza and M. Javed Hyder, "An Approach for the Simulations of the Fatigue Crack Growth," Accepted for Publication in Proceedings of the World Congress on Engineering, London, 2016.

List of Abbreviations

PWR	Pressurized water reactor
RPV	Reactor pressure vessel
ASME	American Society of Mechanical Engineering
DBA	Design by analysis
DBF	Design by formula
LOCA	Loss of coolant accident
SB-LOCA	Short break loss of coolant accident
RST	Rancho-Seco transient
ECCS	Emergency core cooling system
ICS	Integrated control system
EOL	End of life
RVI	Reactor vessel insulation
ERVC	External reactor vessel cooling
HSCP	Highest stress concentration point
GPD	Gross plastic deformation
TES	Twice elastic slope
SESC-FP	Semi elliptical surface crack in finite plate
SESC-TP	Semi elliptical surface crack in thick pipe
SIF	Stress intensity factor
LEFM	Linear elastic fracture mechanics
EPFM	Elastic plastic fracture mechanics
FF	Fluence factor
CF	Chemistry factor
S.I	Stress intensity according to Tresca yield criterion

List of Symbols

R	Inner radius of the set-in nozzle
θ	Taper angle at the nozzle-cylinder intersection
X	Span where taper of the nozzle starts from
a	Minor axis of surface crack
c	Major axis of surface crack
ϕ	Angle of the crack tip with major axis of the crack
t	Thickness of the RPV wall at the set-in nozzle intersection
t_{ins}	Thickness of the reactor vessel insulation
t_{air}	Thickness of the annular chamber of air between RPV and RVI
Q	Flaw shape parameter
E_{neu}	Neutron energy
f	Neutron fluence
E	Young's modulus of material
S_{m}	Design stress intensity of the material
K_{IC}	Fracture toughness of a material
K_{IN}^{p}	LEFM based SIF under only pressure (primary) loadings at normal operating temperature
K_{IN}^{ps}	LEFM based SIF under both pressure (primary) & thermal (secondary) loadings in normal operating conditions
K_{JN}^{p}	EPFM based SIF under only pressure (primary) loadings at normal operating temperature
K_{JN}^{ps}	EPFM based SIF under both pressure (primary) & thermal (secondary) loadings in normal operating conditions
K_{IS}^{ps}	LEFM based SIF under both pressure (primary) & thermal (secondary) loadings in SB-LOCA accidental conditions
K_{JS}^{ps}	EPFM based SIF under both pressure (primary) & thermal (secondary) loadings in SB-LOCA accidental conditions
K_{IR}^{ps}	LEFM based SIF under both pressure (primary) & thermal (secondary) loadings in RST accidental conditions

K_{JR}^{ps}	EPFM based SIF under both pressure (primary) & thermal (secondary) loadings in RST accidental conditions
ν	Poisson's ratio of material
α	Angle between set-in nozzle and set-out nozzle
β	Angle of load-deflection curve with the ordinate
γ	Angle of collapse limit line with the ordinate
σ_h	Hoop stress
σ_r	Radial stress
σ_{ys}	Initial yield strength of the material
σ_{ult}	Ultimate strength of the material
σ_f	Flow strength of the material

1 Introduction

Pakistan is currently facing the most severe energy crises of its history. Economical installations of nuclear power reactors and their safe operations have become mandatory to cope with the energy crises and the field has become an important research area for Pakistani students and researchers. Currently, in the world, there are mainly two types of nuclear power reactors. These are 'thermal reactors' and 'fast reactors'. This thesis focuses on the reactor pressure vessel (RPV) of a pressurized water reactor (PWR) which is one of the most widely used nuclear thermal power reactors [2].

1.1 Research Motivation

The design of pressurized water reactor on indigenous basis has already been started in our country. The designing of various components of the reactor including the RPV is still under progress and does require certain specialties in different fields of engineering. In this context, optimization and fracture mechanics analysis of different parts of the RPV are highly demanding, in our country, in order to control the economy and safety of the nuclear power plants. This thesis will introduce knowledge and numerical techniques to perform optimization and fracture mechanics analysis of the set-in nozzle of the reactor pressure vessel.

1.2 Goal of the Thesis

There are two ultimate goals of this thesis.

1. To learn mechanical engineering design of the pressurized components used in nuclear industry under the rules specified in Section III of American Society of Mechanical Engineering (ASME) Code.
2. To learn fracture mechanics analysis or structural integrity analysis of the pressurized engineering components used in nuclear industry under the rules specified in Section XI of the ASME code.

An initial study in the direction of these goals has been performed, in this thesis, considering a typical reactor pressure vessel of a 300 MW pressurized water reactor.

1.3 Objectives of the Thesis

This research work was divided into four interlinked phases. Each phase has an objective as given below.

Objective 1. In the first phase of the research, the objective was to investigate the safe design of the set-in nozzle for the RPV. For the purpose, starting from the typical design of the set-in nozzle, an optimization was performed by modifying three design variables which control the size and shape of the nozzle. These variables are, inner radius of the nozzle, taper angle at the nozzle-cylinder intersection, and the span of the nozzle. The effects of these variables were combinedly investigated on the behaviour of the stress intensity (Tresca yield theory) and the mass of the nozzle. The stress intensity and the mass of the nozzle are called the state variables. It is observed that the two state variables conflict one another that means if one increases, the other decreases. Definitely, the increase in the mass of the nozzle reduces the value of the stress intensity along the nozzle and hence increases the factor of safety along the nozzle. But it should be noted that large safety factors lead to increasing the material thickness, while the safety is not necessarily increased; recall that the fracture toughness decreases with increasing thickness [3, 4], and stress corrosion cracking at components operating in corrosive environments is expected to be higher in thicker parts [5]. Therefore, in this study, the set-in nozzle has been optimized in a way that it satisfies the conservative Tresca yield criterion as well as the limitation of constant mass of the nozzle. In other words, the optimization is performed such that the nozzle has to fulfil two criterions (Tresca and constant mass) instead of the single failure criterion. After optimization process, the optimized nozzle was also verified by 'design-by-analysis (DBA)' approach as described in ASME code [1]. The DBA concludes that the optimized design of the nozzle is a safe design with minimum safety margin of 2.0.

Objective 2. It is widely accepted that surface cracks normally initiate at the stress concentration points of nozzles. In order to assess the safety of our optimized set-in nozzle in the presence of corner cracks, a crack analysis technique was inevitably required. Hence, in the second phase of the research work, the objective

was to develop a crack analysis approach which has been developed successfully. The approach was named 'pallet body approach' for crack assessment. The approach is capable of inserting 3D surface crack at nozzle-cylinder intersection of the vessel and generating high quality mesh in the cracked region. The approach is capable of efficiently computing stress intensity factors (SIFs) along the crack front which have been compared with the results of the Newman and Raju analysis [6] and the ASME code [7]. In addition, the SIFs produced by the approach can be used for the investigation of the loading and unloading beach marks, and corresponding life of a component during the process of crack growth. The approach has also been validated by comparing these parameters with the experimental work of Reytier [8].

Objective 3. The fracture mechanics analysis of the optimized set-in nozzle was the third objective of this research work. For the purpose, a wide range of corner surface cracks was postulated at the nozzle-cylinder intersection of the RPV. The cracks were observed under normal operating, small break loss of coolant accident (SB-LOCA) and Rancho-Seco transient (RST) conditions of the plant. In this phase, for the determination of the critical crack depth, the stress intensity factors (SIFs) of all the cracks were compared with the fracture toughness value of the vessel's steel (*SA-508 Gr.3 Cl.1*). The effects of material embrittlement due to nuclear environment have also been incorporated in the fracture toughness of the material.

Objective 4. In the fourth phase of the thesis, the effects of the operational thermal stresses on the SIFs of the corner cracks were investigated.

1.4 Structure of the Thesis

This thesis has been organized into nine chapters as given below in Table 1.1.

Table 1.1 Thesis Structure.

Chapter No.	Chapter Title
1	Introduction
2	Pressurized Water Reactor
3	Literature Survey
4	Problem Description
5	Optimization
6	Pallet Body Approach
7	Fracture Mechanics Analysis of the Set-in Nozzle
8	The Effects of Operational Thermal Stresses on SIFs
9	Conclusion and Future Work

2 Pressurized Water Reactor

This chapter contains a brief introduction of the pressurized water reactor (PWR) and its three accidental conditions, which have been used in this thesis.

2.1 Pressurized Water Reactor

The pressurized water reactor comes under the classification of light water cooled, light water moderated thermal nuclear power reactor. Figure 2-1 shows functional diagram of a typical PWR nuclear power plant. The plant principally contains three loops: primary, secondary and tertiary loops. The primary loop usually has four important components. These are:

1. Reactor pressure vessel (RPV)
2. Reactor coolant system pump (RCS Pump)
3. Pressurizer
4. Steam generator

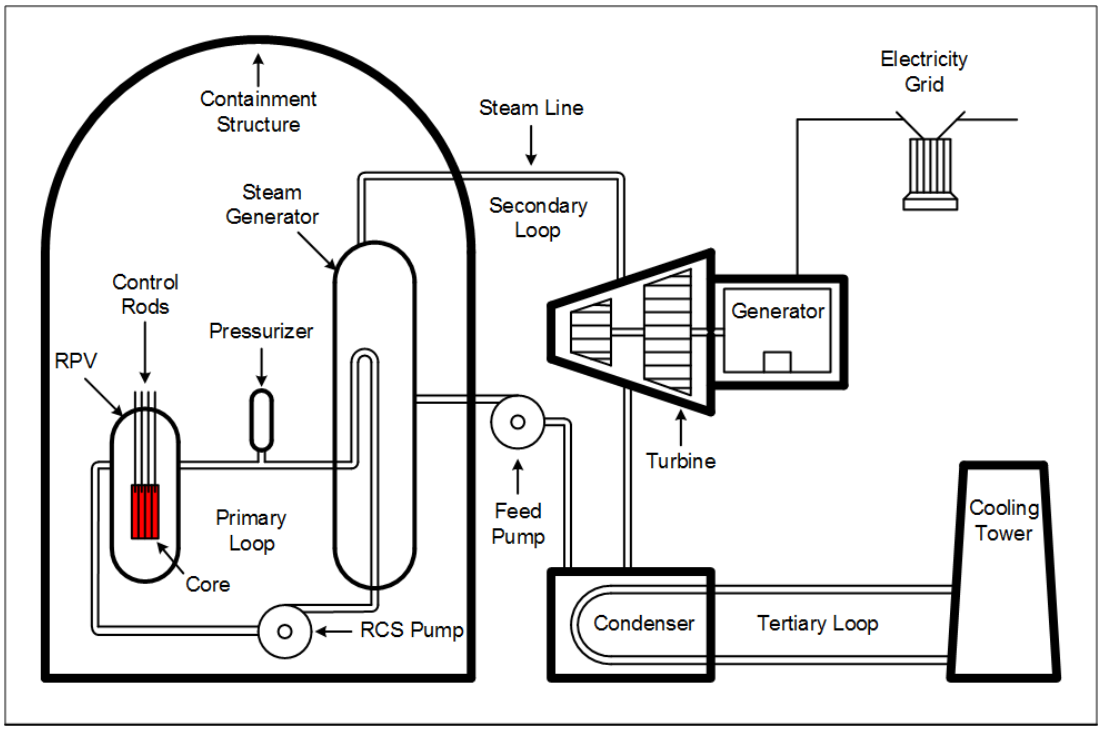

Figure 2-1 Functional diagram of a PWR nuclear power plant [9].

The components in the primary loop are normally called 'Class 1 components' according to the definition of ASME code [1]. The reactor pressure vessel contains the reactor's core in which fission chain reaction takes place. The chain reaction is controlled by a series of control rods, usually made of cadmium, that are inserted into the reactor core. The control rods absorb neutron to cut down on the number of neutrons that are available for the fission process. When the fission reaction takes place in an atom of uranium, energy approximately at the rate of 200 *MeV* per nucleus is produced. This energy appears in the form of kinetic energy of the fission fragments. These fast moving fragments besides colliding with one another also collide with the uranium atoms. In this way, their kinetic energy is transformed into heat energy. This heat energy is transported from the core to the steam generator by the use of reactor's coolant (light water) which flows in the primary loop of the plant. This heat is then used to produce steam (in the steam generator) which in turn rotates the turbine to produce electricity. For simplicity, Figure 2-1 only shows one primary loop and one secondary loop of the plant. In actual practice, several loops are normally attached to reactor pressure vessels in order to increase the power output of the plant. The primary core cooling system and its piping and components are enclosed in a specially designed structure called 'containment building'.

The name 'pressurized water reactor' is derived from the fact that reactor coolant in the primary loop is kept under high pressure in order to avoid boiling of the coolant (water). The average operational pressure and temperature of the reactor's coolant are approximately 15.2 *MPa* and $300\ ^{\circ}C$ respectively while boiling point of the coolant is about $345\ ^{\circ}C$ at 15.2 *MPa*. By maintaining such a high pressure in the primary loop, it is possible to prevent the coolant from boiling and to avoid formation of steam inside the reactor pressure vessel (RPV). In this way, higher heat content can be retained in the coolant. Since the design of the set-in nozzle of the reactor pressure vessel is the focus of this thesis, so a brief discussion about the vessel will be useful.

2.2 Reactor Pressure Vessel

The reactor pressure vessel, which contains most of the pressurized coolant, is the central and the most important component of the PWR. It also contains the reactor core (see Figure 2-1) with hundreds of fuel assemblies and control rods regulating the fission process. Figure 2-2 shows a simplified sketch of flow path of the reactor's

coolant through the RPV. The coolant enters the vessel through the set-in nozzle and flows through the core where it absorbs heat. After receiving the heat, the coolant leaves the vessel through the set-out nozzle. The cylindrical shell containing set-in and set-out nozzles is called 'nozzle-belt' of the RPV. These nozzles are essentially required for transportation of heat energy from the core to the secondary loop (steam generator) of the reactor. The presence of such nozzles generates geometric discontinuities in the vessel and therefore may threatens the integrity of the vessel. Around the geometric discontinuities or the nozzles, effects of stress concentrations and higher stress gradients are normally observed along the axial, circumferential as well as through-the-thickness directions [10, 11]. It is a well-known fact that the magnitude of stresses in the vicinity of the nozzles highly depends on the size and shape of the nozzles [12]. Therefore, the dimensions of a nozzle should be optimized in order to reduce the values of stresses as much as possible.

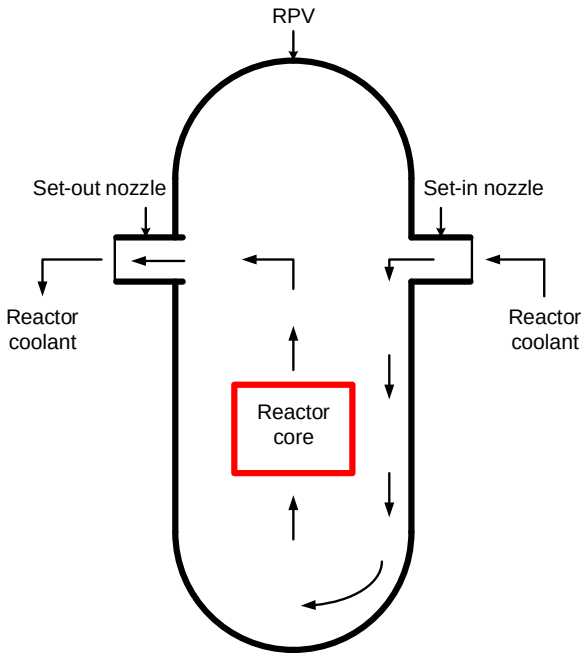

Figure 2-2 Flow path of reactor's coolant.

The reactor pressure vessels, during their service, have to operate under normal operating and accidental conditions of the plant. The normal operating conditions are the ones, which design engineers normally set for components before their operations. The safety analysis under such conditions can be performed before a component put into service due to the availability of these conditions at any time. However, the accidental conditions, which are actually the unanticipated events, cannot be

forecasted exactly. Hence, the safety analysis of engineering components under accidental conditions can never be performed before the occurrences of such events. However, in order to ensure the safety of a component before its installations, it is highly recommended [13] to perform safety analysis under the most severe accidental conditions which that kind of component have ever encountered in its history. In this research work, following accidental conditions of the pressurized water reactor (PWR) were used.

2.3 Accidental Conditions of the PWR

In this study, the safety analysis or the fracture mechanics analysis of the optimized set-in nozzle was performed under normal operating conditions and two types of accidental conditions of the plant. The accidental conditions considered for the fracture analysis include loss of coolant accident (LOCA) and Rancho Seco transient (RST) conditions. However, in order to understand the operational thermal stresses considered in Ch. 8, a brief introduction of the core melting accident will be useful which has also been added below.

2.3.1 Loss of Coolant Accident

The loss of coolant accident (LOCA) is one of the most severe accidents which had ever occurred in the history of PWRs. The accidental conditions in which the reactor's coolant from the primary loop of the reactor losses in excess of normal make-up of the system is called LOCA conditions. It mainly occurs due to a pipe breakage in the primary loop of the reactor. The LOCA is one of the most severe accidental conditions of the pressurized water reactor. To cope with the LOCA situations, emergency core cooling system (ECCS) of the reactor becomes activated which cools the reactor core and provides additional shutdown capability. The ECCS normally injects cold water into the RPV through the set-in nozzle, whenever an accident initiation signal is received. This sudden cooling causes huge thermal (secondary) stresses, in addition to pressure (primary) stresses, in reactor pressure vessel. Such an accident is called pressurized thermal shock (PTS) according to the 10 CFR 50.61 definition [14].

The fracture mechanics analysis under PTS is indispensable because such events result in much higher stresses in RPV as compared to normal operating

conditions. Such PTS may threaten the integrity of the vessel because relatively smaller cracks may become critical under these events. During LOCA, the most critical PTS transient is expected to occur at the set-in nozzle since the cold water is injected into the RPV through this nozzle.

2.3.2 Rancho-Seco Transient

The Rancho-Seco nuclear power plant is a single unit, two-loop (Babcock and Wilcox) pressurized water reactor situated in USA. On December 26, 1985 [15], power to the integrated control system (ICS) of the Rancho-Seco's reactor was lost during the operation. ICS demand signals automatically went to mid-scale, closing the main feed water valves to 50 percent and opening the atmospheric dump valves, turbine bypass valves, and one set of auxiliary feed water valves to 50 percent. The high pressure of the reactor coolant system, in turn, tripped off the reactor. It took the operators 26 minutes to restore power to the ICS (by flipping a switch from "off" to "on"). During the event, a severe PTS was observed because the temperature of the coolant of the reactor was dropped quickly while the internal pressure of the vessel was remained at higher level. Rancho-Seco transient (RST), as nuclear engineers call this event, is one of the most severe accidental conditions of the PWRs.

2.3.3 Core Melting Accident

A core melting accident in PWRs is an accidental condition in which heat generated by the core of the reactor exceeds the heat removed by the cooling systems to the point where at least one nuclear fuel element crosses its melting point. In such accidental conditions the fuel rods in the core, melt down and become a molten core which is also called corium. One of the solutions to handle the corium is that the corium is allowed to flow to the lower head of the RPV where it is retained finally. The lower head of the RPV containing corium is continuously cooled by providing external reactor vessel cooling (ERVC). For the ERVC a water flow passage outside the RPV is essentially required. The effects of providing such external passage on the RPV and its different design aspects have been the area of active research since the happening of this incident at Three Mile Island unit 2 [16-18].

3 Literature Survey

This chapter contains a brief overview of research related to optimization, crack analysis, and fracture mechanics analysis of different structures, which laid down the basis of this thesis. The contribution of this research work has also been added as the last section of this chapter.

3.1 Optimization of Engineering Components using FEA

Since 2000, finite element analysis (FEA) has been included as a standard practice in most of mechanical engineering design codes. The FEA offers a great deal of promise over other approaches mainly experimental, in the sense of low cost, high speed, complete information, and ability to simulate realistic and ideal conditions. Starting research on optimization of an opening in a pressure vessel using FEA, Prof. Hyder (supervisor of this thesis) has been extending his work, by supervising a number of theses on the topic, during the last decade [19-24].

In 2007, Hyder and Asif [11] presented that size and location of an opening has important effects and irregular behaviour on Von-Mises stress in pressure vessels. In their optimization methodology, the effects of three parameters were studied independently in order to find out optimum location and size of the opening. These parameters were diameter of the opening, internal diameter of the cylinder in which opening was made, and location of the opening from cylinder top. In the methodology, firstly, the effects of changing the cylinder diameter on the Von-Mises stress were investigated and it was observed that as the internal diameter increases the stress value also increases. Secondly, the effects of increasing the diameter of the opening were investigated and it was found that the stress value initially decreases and then become constant with opening size. Lastly, the effects of changing the location of the opening were investigated and it was found that the optimum location is at 1/8 of cylinder height.

In 2010, Hassan and Hyder [19] showed that highest values of stresses in an RPV occurs due to the combined pressure plus thermal loadings. Further, effects of

weight of the RPV is negligible when compared to pressure and thermal loadings. In addition, the maximum stress intensity (Tresca yield criterion) occurs at the nozzle-cylinder intersection of the RPV.

In 2011, Javaid and Hyder [20] while investigating the effects of constraints on the nozzle in a pressure vessel, explored that supports of the nozzles should allow free displacements which occur during the operation of the vessel. In 2011, Gul and Hyder [21], while optimizing the thickness and shape of a pressure vessel head, revealed that the strength of the head depends on curvature and thickness of the head. It was observed that magnitude of the Von-Mises stress decreases with the increase in radius of curvature of the head. It was concluded that elliptical head is the optimum shape considering manufacturing cost and magnitude of Von-Mises stresses.

In 2012, Khan and Hyder [22] reported that considerable material can be saved by designing a pressure vessel using finite element based design-by-analysis rules. It was also observed that diameter of the nozzle plays an important role in controlling the magnitude of stresses at the nozzle-cylinder intersection. In 2014, Haseeb and Hyder [24] while evaluating the strength of the set-in nozzle of an RPV, concluded from the CFD analysis that the effects of the back pressure of reactor's coolant at the nozzle are negligible.

3.2 Fracture Mechanics Analysis

It is widely accepted that material flaws, pre-cracks and fatigue cracks initiated at stress concentration points normally lead to catastrophic failure of engineering structures. Therefore, fracture mechanical assessment of crack-like defects is of great importance. In the past 50 years, fracture mechanics has been developed into an independent interdisciplinary field, which resides between engineering mechanics, materials science, and solid-state physics. Fracture mechanics defines load parameters and criteria in order to assess crack behaviour in materials and components under static, dynamic, or cyclic loading [25].

Inspired by the work of Irwin [26], many researchers have performed analysis of surface cracks in different geometries and loading conditions during the last five decades. Some of the early studies used techniques such as alternating method [27-29], boundary element method [30-32], virtual crack extension method [33-35], the

line spring model [36-38] and the weight function approach [39]. After availability of computers and finite element methods, relatively higher attention has been given to the analysis of surface cracks using finite element analysis (FEA).

3.2.1 Analysis of Surface Cracks using FEA

In the beginning of crack analysis using FEA, Newman and Raju [6, 40-42] conducted a comprehensive analysis of 3D semi-elliptical surface cracks in simple geometries such as finite plates and cylindrical shells. In 1979, they presented SIFs for shallow and deep semi-elliptical surface cracks in finite plate (SESC-FP) for both tension and anti-plane bending loadings. In their studies, SIFs along the whole crack fronts were presented in a suitable format of empirical relationships. The effects of the width of plate on the SIFs were also investigated [6]. In addition, they also presented SIFs for a wide range of internal surface cracks in simple pressurized cylinders [42]. Their research work was considered as definitive by the engineering community and is still being most widely used for comparison and validation purposes.

In 2002, Ayhan and Nied [43] employed the concept of enriched finite elements around a crack front for the analysis of cracks. It was demonstrated that the enriched finite elements around the crack tip could effectively be used for the evaluation of SIFs of 3D cracks. Edge cracked bar and semi-circular surface crack in a semi-infinite solid were used for the demonstration of enriched elements. In 2004, working on SESC-FP specimen, Ayhan [44] evaluated mixed mode SIFs for inclined and deflected surface cracks using the concept of enriched finite elements. It was shown with confidence that using the technique, SIFs can be computed in a very convenient and direct method, without a need for post-processing the finite element solutions. Using the technique, the problem of inclined penny-shaped embedded crack in a cylindrical body was also solved. In 2007, Ayhan further extended the work and provided the mixed mode SIFs for inclined and deflected corner cracks in finite plate [45].

In 2005, Diamantoudis and Labeas [46], using global-local finite element technique in FEA, evaluated SIFs of semi-elliptical surface cracks postulated at the stress concentration areas of an industrial pressure vessel. They demonstrated that fracture model using sub-modelling technique is computationally more efficient when

compared with full fracture model of the pressure vessel. They indicated that the approach could be extended to the solutions of the problem of cracks' interaction.

In 2007, Shahani and Habibi [47], using FEA and sub-modelling methodology, evaluated SIFs of the circumferential semi-elliptical surface cracks in a cylinder under combined loading. The authors successfully used isoparametric 20 node elements and singular form of these elements around the crack front. They proved a non-symmetric distribution of SIFs along the crack front under the application of tension, bending moment and torsion.

In 2008, Bremberg and Dhondt [48, 49], presented a novel approach for inserting crack using FEM. In the approach, final fracture model was developed using hexahedral elements around the crack front and the tetrahedral elements in the domain of remaining structure. The tetrahedral elements were used to take the benefit of flexible meshing capabilities in the complex geometries while the hexahedral elements, around the crack front, were used to capture accurate crack parameters. The fracture model of the through-the-thickness crack specimen was developed for the presentation of the approach.

In 2008, Guerrero et al. [50], while working on fracture analysis of an industrial pressure vessel, presented that the design rules based on FEA allow removing the unnecessary conservatism of design codes. They analyzed pressure vessel made of high strength steel assuming the existence of the worst case crack allowed by the European standards in order to demonstrate the safe use of these steels. The authors demonstrated that the presence of cracks on pressure vessels made of high strength P500 steel do not endanger the safety of the vessel. Hence, the application of high strength steel is fully safe even under the worst allowed conditions resulting in significant reductions of wall thickness, weights and costs [51].

In 2011, Nart and Ayhan [52], proposed an approach for surface crack insertion and mesh generation around the crack tip using tetrahedron elements. The authors used Tri-angle and Tetgen softwares for tetrahedron mesh generation in the cracked region. They used an un-cracked finite element model of a plate, and modified its mesh using the chunk mesh concept in the area of the crack. Using the approach, they successfully developed a fracture model of the SESC-FP specimen and validated the approach with the Newman and Raju analysis [6]. They concluded from

the study that the fracture model with full tetrahedral elements is a valid model and yields accurate fracture solutions.

In 2014, Uslu et al. [53], while working on the SESC-FP specimen, presented SIFs along the crack front under thermal or displacement controlled loads. The approach of enriched finite elements was used in their work. It was demonstrated that the cracks under thermal loading produces lower SIFs when compared to the cracks under equivalent mechanical loading.

3.2.2 Simulations of Fatigue Crack Growth

The phenomena of fatigue under cycling loading is one of the major crack growth mechanisms [54]. Numerical modelling of a crack growth has been an active area of research during the last two decades. In this context, in 1998, Dhondt [55] successfully simulated planner crack growth in mode-I conditions using FEA. In 1999, Lin and Smith [56, 57], while working on SESC-FP specimen, developed a multi degree of freedom finite element based numerical approach for the prediction of fatigue crack growth. The authors claimed that with the developed technique, a step-by-step crack growth can be predicted. They explored that SIFs are sensitive to the shapes of the cracks. They concluded that semi-elliptical profile is always maintained during crack growth for tension as well as bending loadings.

In 2000, Carter et al. [58], developed FRANC3D code using FEA which is capable of simulating crack growth in different conditions. In 2001, Hou et al. [59], developed ZENCRACK code using FEA. Using this code, it is possible to introduce single or multiple cracks into an already structured mesh, and to compute the fracture parameters along the crack fronts. Such fracture parameters may be used for the prediction of the crack growth. In 2003, Schöllmann et al. [60], also developed a crack growth software named ‘ADAPCRACK3D’ which can be used for the prediction of fatigue crack growth under complex loading conditions. The modified crack closure methods were utilized in the software along with FEM.

In 2011, Ayhan [61] proposed a methodology for fatigue crack simulations using enriched finite elements around the crack front. The author simulated the fatigue crack growth in SESC-FP specimen under bending loading. He demonstrated that the presented methodology could be used with confidence in terms of both

evolving crack front shapes and the crack growth life. In 2014, Uslu et al. [62], showed that crack growth lives are higher under thermal or displacement loading when compared to the equivalent mechanical or stress loading.

3.2.3 Fracture Mechanics Analysis of RPVs

Fracture mechanics analyses or safety analyses of RPVs under various loading conditions have been an area of active research for the last few decades. In this context, Bangash [2] in 1984, performed a finite element based analysis and design of Sizewell-B RPV of a pressurized water reactor under normal and unanticipated events of the plant. The author pinpointed some vulnerable areas of the RPV after computing factors of safety in such areas. He employed 20 nodes isoparametric finite elements model for the stress analysis of the RPV. He demonstrated that the most important areas of the RPV from the fracture assessment point of view are inlet and outlet nozzles, top and bottom head, and the beltline region of the vessel. He plotted hoop stress distributions under pressure loading of 17.24 *MPa* for different regions of the RPV and corroborated the results for inlet and outlet nozzles. In his fracture analysis, the unflawed vessel was first treated and then the cracked vessel including flaws at various incremental loads was analyzed.

In 1999, Siegele et al. [63], performed fracture mechanics analysis of the RPV nozzle under loss of coolant accident (LOCA). In the study, they argued that the nozzle regions face higher stresses and lower temperature in the event of the LOCA, and is therefore vulnerable and may threaten the integrity of the RPV. Hence, the safety assessment of the nozzle must be performed. After postulating the circular cracks at nozzle-cylinder intersection, they computed SIFs as functions of crack tip temperatures. In their study, the analytical approaches used for solutions of surface cracks in cylindrical portions were extended for the solutions of corner cracks at the nozzle-cylinder intersection. In the same year, Kim and Jin [17], performed structural integrity analysis of an RPV under the external reactor vessel cooling condition. The integrity analysis of the lower head of the RPV was performed during the transient state of reactor vessel cooling.

In 2000, He and Isozaki [64], performed fracture mechanics analysis of the beltline region of the RPV of a Chinese pressurized water reactor. The authors conducted the fracture analysis under small-break loss of coolant accident, large-

break loss of coolant accident and Rancho-Seco transients. They employed ADINA code for development of crack mesh and for the fracture analysis. They investigated that which type of flaw and transient condition is most detrimental for the beltline region of the RPV. They also demonstrated that large-break loss of coolant accident is less severe pressurized thermal shock when compared to small-break loss of coolant accident and Rancho-Seco transients. The authors assessed the fracture integrity of the RPV by comparing the stress intensity factors of different cracks with the fracture toughness of the material.

In 2001, Colak and Ozdere [65] performed a comparative study of a four loop reactor pressure vessel's integrity under different LOCA conditions. Deterministic and probabilistic approaches were employed for the analysis of beltline region under pressurized thermal shocks due to LOCA conditions. Computer code VISA-II was utilized for the calculations of vessel's failure probabilities. Among the analyzed cases, a medium break loss of coolant accident induced by a 50-cm^2 break in the hot leg yields the higher vessel rupture probability. In 2003, Colak and Ozdere [66] also conducted the integrity analyzes of reactor pressure vessels of eastern and western pressurized water reactors.

In 2014, Chen et al. [67], performed fracture mechanics analysis of the beltline region of a reactor pressure vessel under the event of pressurized thermal shock. The authors stated that analysis under such unanticipated events is the key element of the integrity evaluation. They further argued that the guidance of ASME code for integrity evaluation has been prepared under conservative assumptions. They computed SIFs of five semi-elliptical surface cracks postulated in the beltline region of RPV in order to investigate the most detrimental crack. The finite element based commercial software the ABAQUS was used for the fracture analysis. They accomplished the fracture evaluation by comparing the SIFs of the cracks with the fracture toughness of the used material. They concluded that while analyzing the surface cracks in the RPV, both the deepest and surface (edge) point of the crack should be considered because the safety margin at the deepest point is not always smaller than that of the surface point.

Based on the literature review, a few research challenges (need of the research) were observed which have been described in the following section.

3.3 Research Contribution of the Thesis

In the light of the above-mentioned studies, research work on 'optimization and fracture mechanics analysis of the set-in nozzle of an RPV of a 300 MW pressurized water reactor' was conducted in this thesis. Moreover, the developed knowledge and techniques can be applied confidently to all other vulnerable parts of the vessel, which finally completes optimization and fracture mechanics analysis of the whole RPV.

In the domain of optimization, it was observed that the adopted methodologies in the literature (as described in Section 3.1) investigate the effects of optimization parameters independently and do not explore the correlated effects of the parameters. In order to cope with the situation, an optimization methodology has been presented in this study, which is capable of investigating the correlated effects of optimization parameters. In the methodology, all the design parameters (variables) selected for optimization of the set-in nozzle together form a design point. Using various design points covering the limits of the design variables, response surfaces of the state variables are generated. The maximum stress intensity and the mass of the nozzle were selected as the 'state variables' in this study. The response surfaces of the state variables are searched for the optimum design, which fulfills the optimization criterion set for this study (see Section 1.3, objective 1). For optimization, a full 3D hexahedral finite element (FE) model of the RPV was developed (using slicing and dicing technique) for the accurate computations of the stress state especially around the set-in nozzle. The adopted optimization methodology and the meshing technique to develop FE model of the vessel have been published [12] in an internationally reputed journal titled 'Nuclear Engineering and Design'. The procedure to evaluate load bearing capability of the RPV on the basis of 'design-by-analysis' was also established which has been presented in an internationally recognized conference named International Multi-Conference of Engineers and Computer Scientists [68]. The details of the optimization methodology, the meshing technique, and the design-by-analysis approach will be covered in Ch. 5 of this thesis.

Moving ahead in the research work, for analyzing a cracked RPV, a crack analysis approach capable of inserting 3D surface crack and generating mesh in the cracked region was also developed. The approach was named the 'pallet body approach'. The approach can be used for the computation of stress intensity factors

along the cracks front. The approach has been validated by comparing the results with standard studies available in the literature [6-8] . The 'pallet body approach' has been published [69] in an internationally reputed journal titled 'Theoretical and Applied Fracture Mechanics'. The details of the approach will be covered in Ch. 6 of this thesis. The motivation behind the development of the 'pallet body approach' was the observation that most of crack analysis studies in the literature (as mentioned in Section 3.2.1) use the approaches that are limited to elliptical or regular shape of cracks. However, in real engineering structures, we may encounter cracks or inherent material flaws having irregular crack fronts such as undulated cracks. The undulated crack may has a wave-like crack front as shown in Figure 3-1 [70].

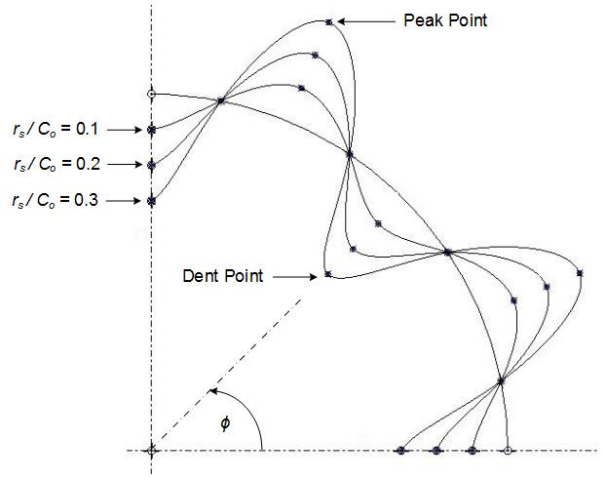

Figure 3-1 Shape of undulated crack front [70].

The undulated crack fronts shown in Figure 3-1 was defined by a cosine function based on circular path as given in Eq. (3-1). The variation *(d_c)* from the circular path of radius *'C_o'* can be represented mathematically by:

$$d_c = -r_s \cos(4V\phi) \tag{3-1}$$

Where;

V = Frequency of cosine function.

ϕ = Crack face angle (radians).

r_s = Amplitude of the cosine curve.

The developed 'pallet body approach' is capable of analyzing edge, embedded and corner cracks having straight, elliptical, circular, inclined and undulated crack fronts.

The elliptical and circular corner cracks have been analyzed thoroughly using the developed ‘pallet body approach’ in this thesis. The modeling of undulated crack front using the ‘pallet body approach’ has been presented in International Young Engineers Convention [70]. However, inclined corner cracks and undulated corner cracks at the nozzle-cylinder intersection of the RPV will be analyzed using the ‘pallet body approach’ during the extension of this thesis (see Section 9.3).

Finally, in the fracture mechanics analysis of RPVs as stated in Section 3.2.3, it was observed that SIFs covering a wide range of corner cracks at the nozzle-cylinder intersection are missing in the contemporary literature. Hence, in this research work, SIFs for a wide range of corner cracks (starting from minute crack) have been presented in a suitable graphical format under normal as well as the accidental conditions of the plant. The details of the fracture mechanics analysis of the optimized set-in nozzle will be covered in Ch. 7 and 8 of this thesis.

4 Problem Description

In this thesis, optimization and fracture mechanics analysis of a set-in nozzle of a reactor pressure vessel has been performed. The engineering drawing of the reactor pressure vessel is shown in Figure 4-1. The Figure 4-1 (a) shows the cut-section view through the set-in and the set-out nozzles of the vessel. The Figure 4-1 (b) shows the top view of the vessel. It is a typical double loop cylindrical RPV of a 300 MW pressurized water reactor [12, 23]. It has two inlet (set-in) and two outlet (set-out) nozzles. The angle between the inlet and outlet nozzles is equal to 60° and it is denoted by *'α'* as shown in Figure 4-1 (b). The vessel has a geometrical symmetry, and the plane of symmetry is shown in Figure 4-1 (b). The vessel is supported by providing the support pads under the inlet and outlet nozzles as shown in the Figure 4-1 (b). The Figure 4-1 (b) also shows tangential and radial directions of the vessel.

The inlet nozzles usually used in such RPVs are set-in nozzles, which have flange set into the vessel wall [71]. The Figure 4-2 (a) presents the typical design of the set-in nozzle while Figure 4-2 (b) shows the design parameters of the nozzle namely the inner radius of the nozzle *(R)*, the taper angle at the nozzle-cylinder intersection (θ), and the span where taper of the nozzle starts from (X). The numerical values of the design parameters of the typical set-in nozzle are given in the Figure 4-2 (a) which are *R* = 375 *mm*, $\theta = 3.5^{\circ}$, and *X* = 900 *mm*. This design of the typical set-in nozzle will be used as input design for optimization process. The thickness of the vessel's wall at the nozzle-cylinder intersection is denoted by parameter *'t'* which has the value *'t* = 400 *mm'* as shown in the Figure 4-2 (a). The Figure 4-2 (b) shows the support pads, vertical direction of the RPV, axial direction of the set-in nozzle, and path for temperature profiles which will be used in Ch. 7.

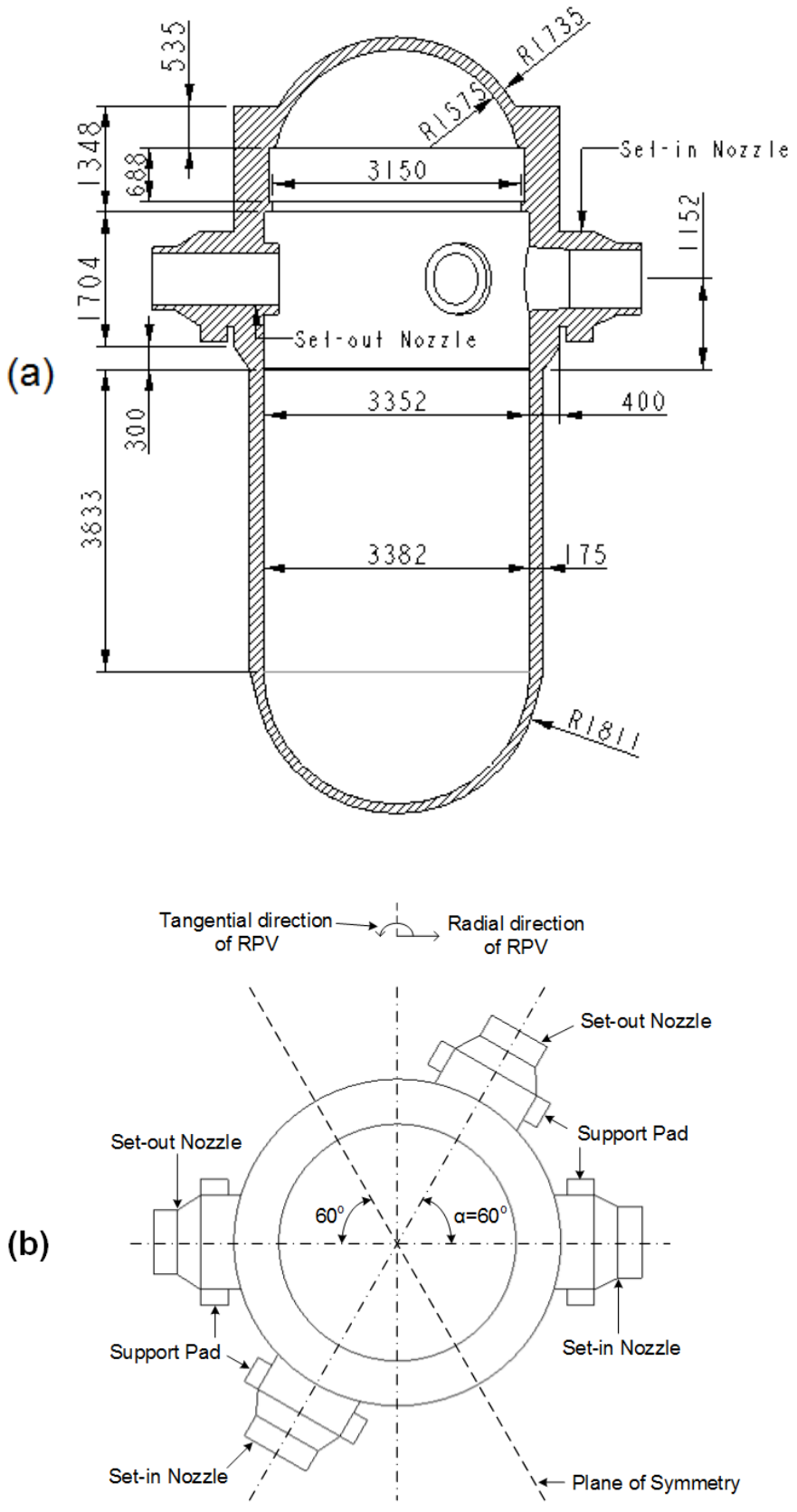

Figure 4-1 Engineering drawing of the typical RPV (a) Cut-section view through the nozzles, dimensions in *mm* (b) Top view.

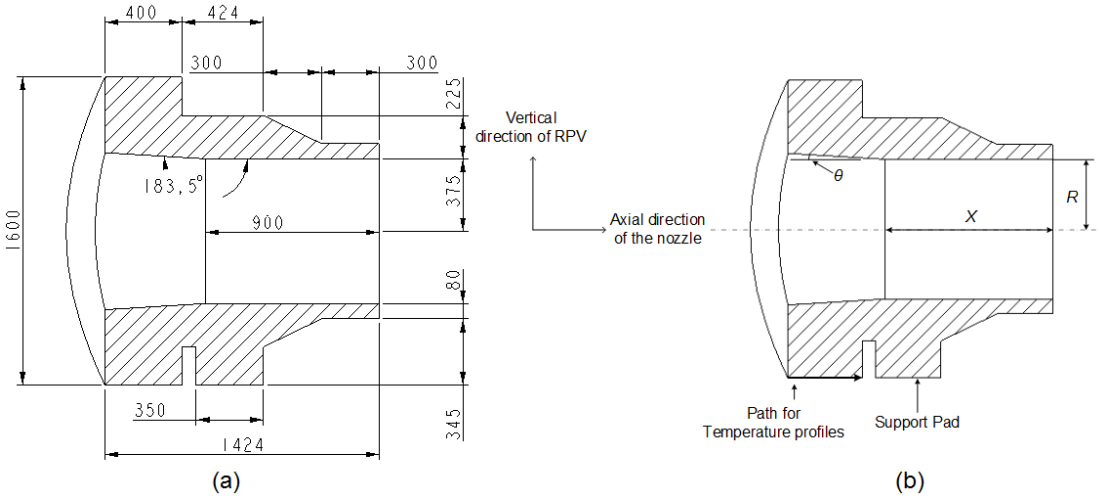

Figure 4-2 (a) Typical set-in nozzle, dimensions in *mm* (b) Description of the nozzle.

4.1 Material of the RPV

A nuclear grade steel, designated in ASME code as *'SA-508 Gr.3 Cl.1'* was selected as the material for the RPV [72]. The material has nominal composition (3/4*Ni*-1/2*Mo*-*Cr*-*V*). The mechanical and thermal characteristics of the material are listed in Table 4.1, while the density of the material is 7750 kg/m^3 [72]. The true stress-strain characteristics of the material *(SA-508 Gr.3 Cl.1)* at room and at high temperatures are shown graphically in the Figure 4-3 [64].

Table 4.1 Mechanical and thermal characteristics of *'SA-508 Gr.3 Cl.1'* steel [72].

Temperature ***(°C)***	**Young's modulus** ***(GPa)***	**Poisson's ratio**	**Yield Strength** ***(MPa)***	**Conductivity** $(W.(m.^oC)^{-1})$	**Specific heat** $(J / kg.^oC)$	**Mean coefficient of thermal expansion** $(1 / ^oC)$
50	191	0.3	345	38.3	465.81	1.18E-05
100	187	0.3	323	38.8	489.03	1.21E-05
150	184	0.3	314	38.8	508.39	1.24E-05
200	181	0.3	305	38.6	527.74	1.27E-05
250	178	0.3	299	38.1	545.81	1.30E-05
275	176	0.3	296	37.8	556.78	1.33E-05
288	175	0.3	294	37.6	562.26	1.35E-05
300	174	0.3	292	37.5	567.74	1.36E-05
350	171	0.3	285	36.8	588.39	1.36E-05

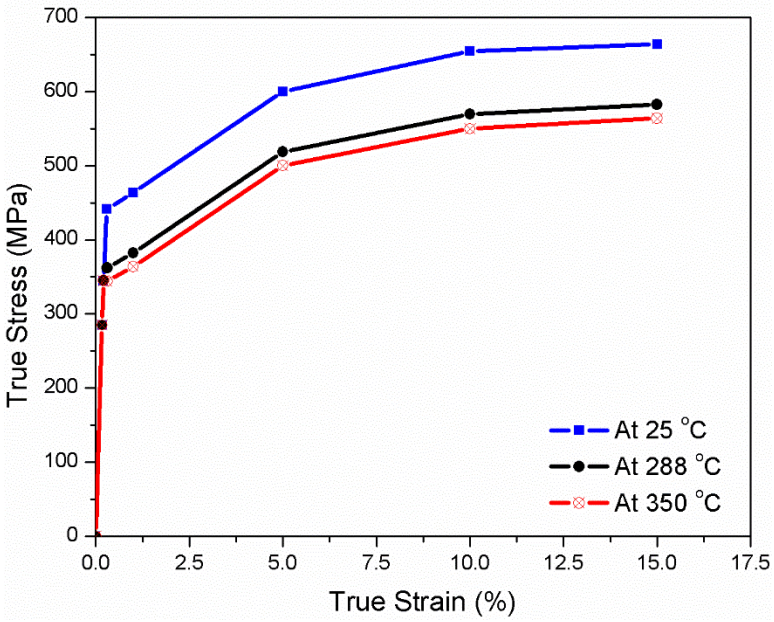

Figure 4-3 True stress-strain characteristics of the *'SA-508 Gr.3 Cl.1'* steel [64].

4.1.1 The Embrittlement of the RPV's Material

It is a well-known fact that the nuclear environment, which is the environment of the RPV, causes embrittlement (loss of ductility) of the material. The fission chain reactions of U-235, in the core of the vessel, emit high-energy neutrons that affect the internal surface of the vessel. These neutrons (during collisions with the material) alter the behaviour of the material on the micro and nano-structural level and hence, modify the mechanical properties of the material. One of these modifications is the embrittlement of the material. In fact, the embrittlement shifts the fracture toughness (K_{IC}) curve of the material to the higher temperatures resulting brittle behaviour of the material at relatively higher temperatures.

In practice, neutrons having kinetic energy higher than *'1 MeV'* constitute the fluence that is considered to be capable of triggering damage mechanisms (embrittlement) in steels; these neutrons are referred to as fast neutrons. Typical design end-of-life (EOL) neutron fluence ($E_{neu} > 1$ *MeV*) for PWRs is in the order of 10^{19} n/cm^2. According to '10 CFR 50.61' guide [14], fracture mechanics analysis of nuclear components should be performed considering the EOL neutron fluence, before the reactor is put into service. The US regulatory guide 'US R.G. 1.99' [73] contains an approach to calculate the fracture toughness of the material which

incorporates the EOL neutron fluence. This regulatory approach has been used here in order to compute the fracture toughness value of *'SA-508 Gr.3 Cl.1'* steel.

4.1.2 The Fracture Toughness of the RPV's Material

It is widely accepted that the average number of neutrons produced per fission reaction is about two and a half. The majority of these neutrons are prompt neutrons emitted at the time of fission. A small fraction is of delayed neutrons, which typically appear from seconds to minutes later. The number of neutrons from fission depends upon both the identity of the fissionable nuclide and the energy of the incident neutron. The energy distribution or spectrum for neutrons emitted by fission is relatively independent of the energy of the neutron causing the fission. For many practical purposes, the empirical expression given in Eq.(4-1) provides an adequate approximation to the neutron spectrum during the fission of uranium-235 which happens in the core of the RPV [74].

$$n(E_{neu}) = 0.453e^{-1.036E_{neu}}.\sinh(2.29E_{neu})^{0.5} \quad (4\text{-}1)$$

Where E_{neu} is the energy of the neutron given in *MeV*.

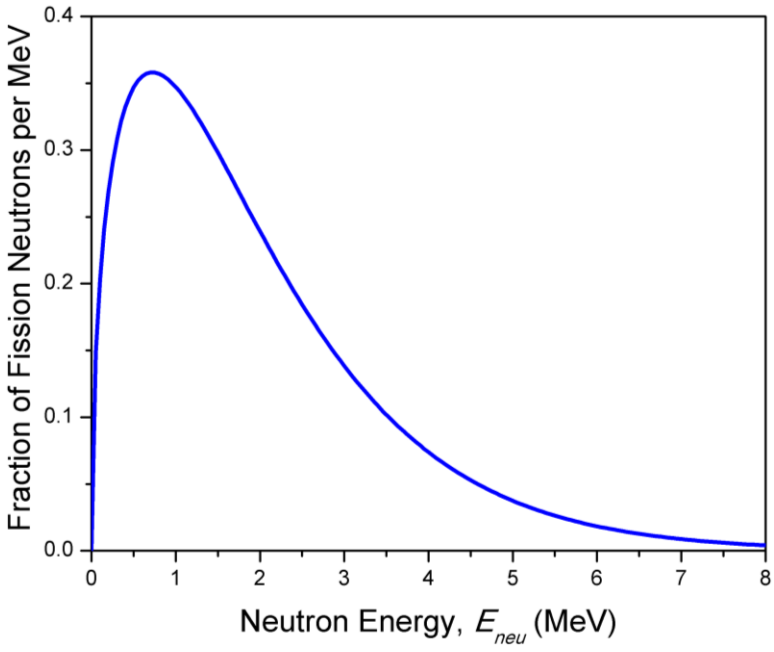

Figure 4-4 Fission neutron energy spectrum for thermal fission U-235.

The neutron energy distribution (spectrum) has been plotted in Figure 4-4, which indicates that the fission neutrons produced in a nuclear reactor have an energy

ranging from 0.1 *MeV* to approximately 8 *MeV*, and therefore they are high-energy neutrons. The peak of the curve corresponds to the most probable fission neutron energy that is 0.7 *MeV*. However, the average energy of the fission neutrons are 2 *MeV*.

As already mentioned that the fast fission neutrons with energy more than 1 *MeV* (E_{neu} > 1 *MeV*) form a fluence that is capable of damaging the microstructure of the steel. Generally, the neutron fluence results an increase in strength and a decrease in fracture toughness of the material. An analytical expression given in ASME code [75] has been used for determination of lower bound fracture toughness of '*SA-508 Gr.3 Cl.1*' steel under the effects of neutrons (neutron fluence). The analytical expression is called ASME reference critical stress intensity factor curve and is given by Eq. (4-2) [75].

$$K_{IC} = 36.5 + 22.783 \exp[0.036(T - RT_{NDT})] \tag{4-2}$$

Where;

K_{IC} = Fracture toughness of the material, in $MPa\sqrt{m}$.

T = Temperature, in $^{\circ}C$.

RT_{NDT} = Nil-ductility transition reference temperature for irradiated material.

The irradiated material means that the material has been served under nuclear environment, which contains neutrons having energy more than 1 MeV. The 'RT_{NDT}' can be evaluated using the Eq. (4-3) as given in US regulatory guide 'US R.G. 1.99' [73].

$$RT_{NDT} = \text{ initial } RT_{NDT} + \Delta RT_{NDT} + \text{ margin} \tag{4-3}$$

Where,

initial RT_{NDT} = Initial reference nil-ductility temperature of fresh material.

ΔRT_{NDT} = Increase in temperature as a result of irradiation.

margin = Account for uncertainties in the parameters.

The 'ΔRT_{NDT}' can be evaluated using the Eq. (4-4) as given in the US regulatory guide 'US R.G. 1.99' [73].

$$\Delta RT_{NDT} = (\mathrm{CF}) f^{(0.28-0.1\log f)} = (\mathrm{CF}) \times (\mathrm{FF}) \tag{4-4}$$

Where,

f = Neutron fluence in units of 10^{19} neutrons/cm^2 (E_{neu} > 1 MeV).

FF = Fluence factor.

CF = Chemistry factor based on the copper and nickel content.

In this study, a typical end-of-life fluence equal to 4×10^{19} neutrons/cm^2 has been taken at the set-in nozzle of the RPV. The initial reference nil-ductility temperature was measured by drop weight and Charpy impact test of the material *'SA-508 Gr.3 Cl.1'* which is equal to $-20\ ^{\circ}\mathrm{C}$ and hence '$\text{initial } RT_{NDT} = -20\ ^{\circ}\mathrm{C}$' [64]. Using the regulatory approach described above, the nil-ductility transition temperature for irradiated *'SA-508 Gr.3 Cl.1'* steel has been calculated which is 'RT_{NDT} = 79.6 ºC'. Using this value, the Eq. (4-2) becomes.

$$K_{IC} = 36.5 + 22.783\exp[0.036(T - 79.6)] \tag{4-5}$$

The ASME code, IWB-3613 [13] recommends that a safety factor of $\sqrt{2}$ should be applied on fracture toughness value for the determination of critical crack dimensions at nozzle-cylinder intersection of the vessel. Using the factor of safety Eq. (4-5) is converted to Eq. (4-6).

$$K_{IC} = 25.81 + 16.11\exp[0.036(T - 79.6)] \tag{4-6}$$

The Eq. (4-6) gives lower bound fracture toughness value for '*SA-508 Gr.3 Cl.1*' steel. Using this exponential curve the fracture toughness increases without bound and this curve does not predict the upper bound fracture toughness. In ASME fitness-for-service standard [76, 77], a cut-off to the exponential curve at $K_{IC} = 220\ MPa\sqrt{m}$ is recommended for '*SA-508 Gr.3 Cl.1*' steel. Applying factor of safety equal to $\sqrt{2}$, the upper bound fracture toughness becomes $K_{IC} = 155.6\ MPa\sqrt{m}$. The fracture toughness curve drawn using Eq. (4-6) and upper bound fracture toughness value is shown in Figure 4-5.

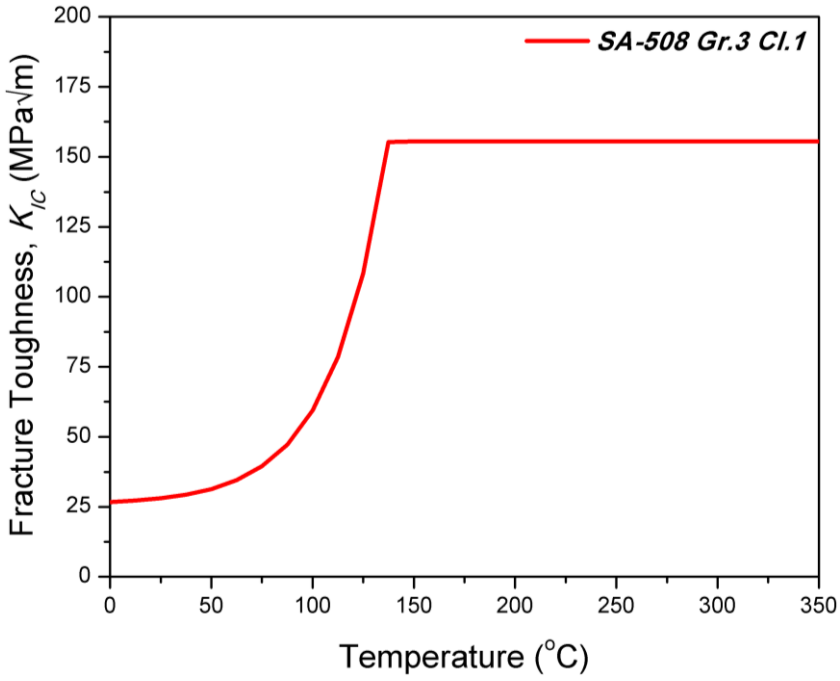

Figure 4-5 Fracture toughness curve of irradiated *'SA-508 Gr.3 Cl.1'*.

This fracture toughness curve will be used as the limiting criteria for the determination of critical crack size under different operating conditions of the reactor.

4.2 Limitations of the Thesis

The following limitations may be taken into account whenever to refer this thesis.

1. The effects of radiation on the fracture toughness of the '*SA-508 Gr.3 Cl.1*' steel was determined using regulatory approaches as described in US regulatory guide 'US R.G. 1.99' and ASME code [73, 75]. However, it should be noted that microstructural evolution of the metal lattice under radiation is not captured computationally.
2. The effects of stainless steel cladding inside the RPV has been ignored throughout the thesis.
3. The upper head of the RPV is normally a flanged hemi-spherical head. In this thesis as the set-in nozzle is under design considerations, therefore the effects of flange of the upper head are neglected.

4.3 Boundary Conditions

The following boundary conditions (B.Cs) have been applied for the optimization and fracture mechanics analysis of the set-in nozzle.

1. Taking the advantage of the geometric and loading symmetry, as shown in Figure 4-1 (b), only half of the RPV was modeled for the analysis. The half of the vessel contains one set-in nozzle and one set-out nozzle.
2. The mass of the full RPV, with the material *'SA-508 Gr.3 Cl.1'* is 239.70 *tonne*. The effects of the weight of the vessel have also been considered in the analyses.
3. The support pads are free to move in the tangential and radial directions of the RPV (see Figure 4-1 (b)) while they are fixed in the vertical direction of the vessel (see Figure 4-2). In ANSYS Workbench, frictionless support feature was applied on the lower faces of the vessel's support pads. It prevents the supports from moving in the vertical direction of the vessel and allows their movement in the radial and tangential directions of the vessel.
4. Along with the support pads, in order to properly support the heavy vessel, the skirt type support is also recommended at the lower hemisphere of the RPV [78]. The lower hemisphere of the vessel was fixed in the analyses in order to incorporate the effects of skirt support. The assumption is valid in our case because the skirt support has negligible effects on the nozzle, which is very faraway from the lower head of the vessel.
5. The internal pressure equals to 17.16 *MPa* (P_{int} = *17.16 MPa)* was applied to the RPV. This is the design pressure [64] of the RPV.
6. The behaviour of the material at *'T* = $350\ ^{o}C$ *'* was used for the optimization of the nozzle. This is the design temperature of the RPV [64].
7. The internal pressure and the temperature for the fracture mechanics analysis of the optimized nozzle under accidental conditions were taken from SB-LOCA and RST conditions defined in Section 4.5.
8. The bending loads caused by the support pads on the nozzles have been taken into account.
9. The effects of axial loads on the nozzles have also been considered. The effects are negligible [24] because the support pads are free to move in the axial direction of the nozzle.

4.4 Optimization of the Set-in Nozzle

First of all, starting from a typical set-in nozzle as shown in Figure 4-2 (a), the size and shape of the nozzle was optimized in this research work. The optimization was performed by changing three design variables, which control the size and shape of the set-in nozzle. These design variables are:

1. The inner radius of the nozzle (R).
2. The taper angle at the nozzle-cylinder intersection (θ).
3. The span where taper of the nozzle starts from (X).

The design variables of the set-in nozzle are shown in Figure 4-2 (b). The limits imposed on the design variables for the optimization process are listed in Table 4.2. The mass of the typical set-in nozzle with the material *'SA-508 Gr.3 Cl.1'* is equal to 8767.1 *kg*.

Table 4.2 The limits of the design variables.

Design Variable	Lower Bound Value	Typical Design Value	Upper Bound Value
R	350 *mm*	375 *mm*	400 *mm*
X	600 *mm*	900 *mm*	1200 *mm*
θ	1^o	3.5^o	6^o

For the optimization of the nozzle, 3D finite element analysis was performed using the Tresca yield theory. It is also called maximum shear stress theory. The Figure 4-6 gives the comparison of the Von-Mises yield theory with the Tresca yield theory for a biaxial stress state [10]. Where σ_A, σ_B, S_{yt}, and S_{yc} are the symbols as given in ref. [10]. It is evident from Figure 4-6 that Tresca theory always gives results on the conservative side, because its graph is inside the Von-Mises ellipse. It is due to the reason that the tresca yield theory has also been used for the design of nuclear class 1 components in ASME code, NB-3212 [1]. As per ASME code [1, 4], the stress intensity (*S.I*) according to Tresca yield criterion can be defined by Eq. (4-7).

$$S.I = \sigma_h - \sigma_r \tag{4-7}$$

Where 'σ_h' and 'σ_r' are the values of two principal stresses called hoop stress and radial stress in RPV, respectively.

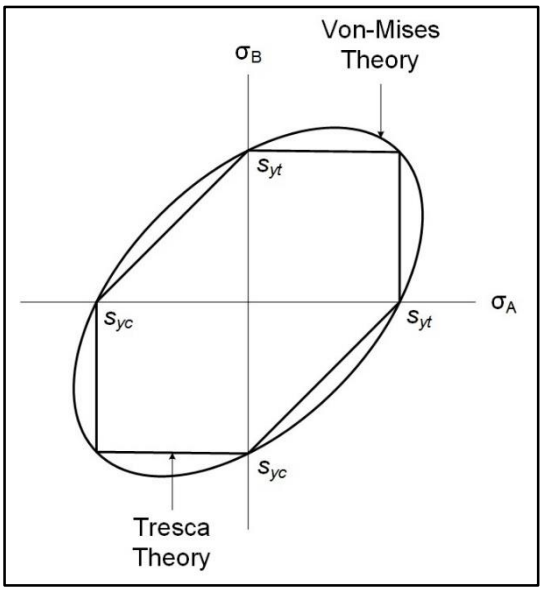

Figure 4-6 Comparison of the Von-Mises and the Tresca theories [10].

In the optimization process, the target was to minimize the value of maximum stress intensity along the set-in nozzle below the yield strength of the vessel's steel in order to ensure no yielding state of the nozzle. The design optimization was achieved with the limitation that the mass of the nozzle remains constant as already discussed in Section 1.3 (objective 1). The stress intensity according to Tresca yield theory and the mass of the nozzle are called state variables of the nozzle in this study.

4.5 Fracture Mechanics Analysis of the Optimized Set-in Nozzle

The fracture mechanics analysis of a component can generally be performed by postulating an initial crack of a defined size, which represents a crack size that is observed during non-destructive testing or which can be expected during the lifetime of the component [51]. For the fracture mechanics analysis of the optimized set-in nozzle, the integrity confirmation at the nozzle-cylinder intersection is compulsory since this is the highest stress concentration point (HSCP) of the nozzle and corner cracks normally initiate at this point during the operation of the plant. Therefore, a wide range of corner cracks was postulated at the nozzle-cylinder intersection of the RPV. The finite element modelling of the cracked vessel was done using the 'pallet body approach' of crack analysis which is developed during the course of this study. Both the linear elastic fracture mechanics (LEFM) based stress intensity factors (K_I)

and the elasto-plastic fracture mechanics (EPFM) based stress intensity factors (K_J) for all the cracks have been computed. The SIFs were computed under normal operating conditions, small-break loss of coolant accidental (SB-LOCA) conditions, and Rancho-Seco transient (RST) conditions of the plant. The pressurized thermal shock (PTS) occurred under SB-LOCA and RST conditions are as given below.

4.5.1 PTS under Small Break Loss of Coolant Accident

The temperature and pressure of the reactor's coolant under the SB-LOCA are shown in the Figure 4-7 [64]. The Figure 4-7 shows that at full power operation of the reactor, the SB-LOCA event continues for 5000 *sec*. The temperature starts to decrease with cold emergency core cooling water injection. System pressure decreases rapidly because the coolant flow rate through the pipe breakage is greater than the charging and emergency core cooling flow rate.

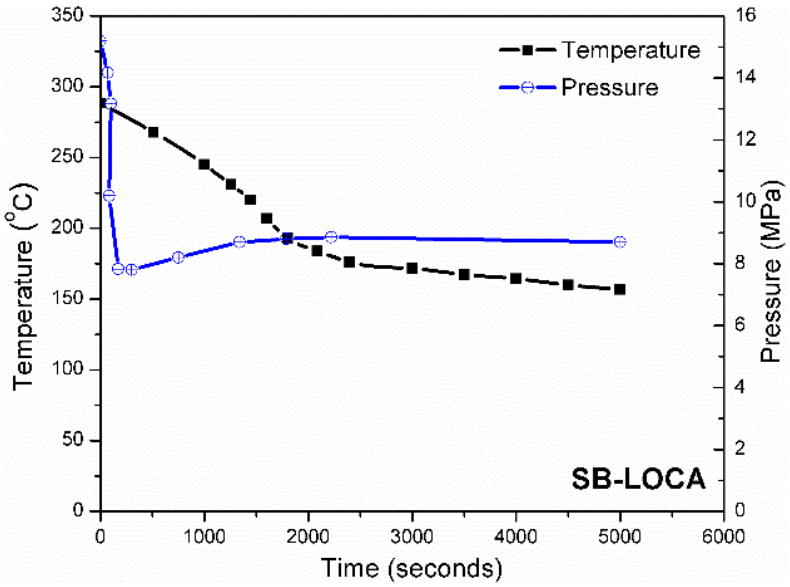

Figure 4-7 Temperature and pressure of the coolant under SB-LOCA [64].

4.5.2 PTS under Rancho-Seco Transient

The PTS transient generated under the RST was also considered for fracture mechanics analysis in this study. The temperature and pressure of the reactor's coolant under RST conditions are shown in the Figure 4-8 [64]. The Figure 4-8 shows that the RST event continues for 6000 *sec*.

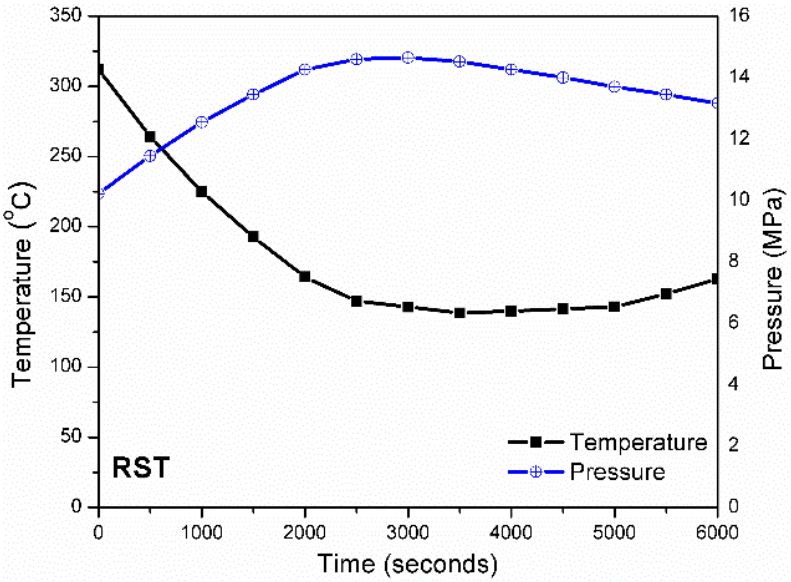

Figure 4-8 Temperature and pressure of the coolant under RST [64].

After evaluating, the SIFs of the wide range of corner surface cracks under above mentioned loading conditions, the critical crack size was investigated finally which does not threatens the integrity of the RPV. It was achieved by comparing the computed stress intensity factors of the corner cracks with the fracture toughness value of the vessel's material (*SA-508 Gr.3 Cl.1*) as shown in Figure 4-5.

4.6 The Effects of Operational Thermal Stresses on SIFs

The effects of operational thermal stresses on the SIFs of the corner cracks were also investigated during the course of this study. In order to understand the considered operational thermal stresses the following discussion will be useful.

As already mentioned in Section 2.1 that the RPV contains pressurized reactor's coolant (water) which has a temperature about 300 °C. The hot RPV normally hangs in the reactor's cavity, which can be thought as a well of concrete as shown in Figure 4-9. In this scenario, the heat continuously transfer from the hot vessel to surrounding concrete structures. In order to prevent the loss of heat to the concrete structures, a thermal insulation called reactor vessel insulation (RVI) is normally used which encloses the hot RPV. The prevention of the heat loss is the primary concern of the RVI, but it can be useful for ERVC under core melting accidental conditions (see Section 2.3.3) if a gap (water flow passage) is maintained between RPV and RVI. This gap actually forms an annular chamber between RPV

and RVI. In core melting accidental conditions, the cooling water can be flooded through this annular chamber which directly cools the RPV. The water flow path for ERVC is schematically shown in Figure 4-9.

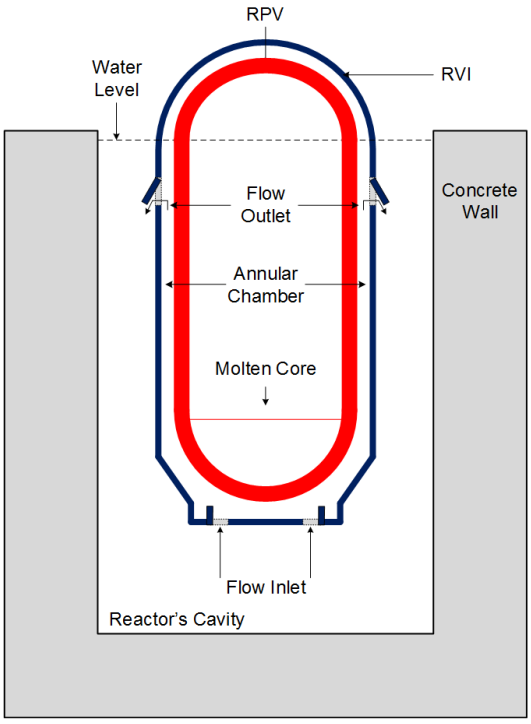

Figure 4-9 Water flow path under external reactor vessel cooling.

The annular chamber for ERVC is very useful in core melting accidental conditions but in normal operating conditions, the annular chamber is filled with air forming an annular chamber of air (air shield) as shown in Figure 4-10.

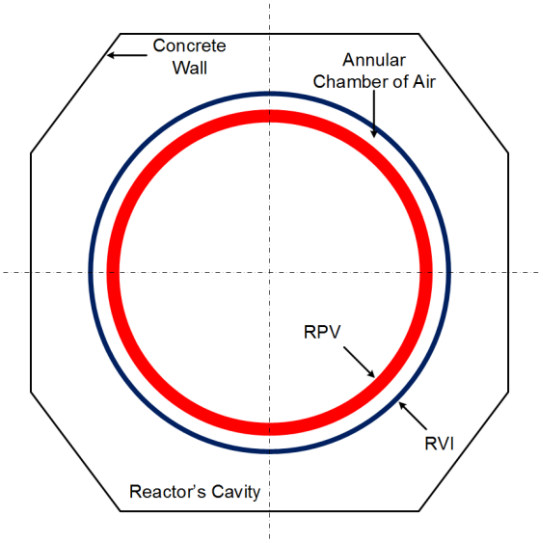

Figure 4-10 Annular chamber of air under normal operating conditions.

In this setting, both the air shield and the reactor vessel insulation (RVI) create resistance to the heat transfer from the hot vessel to its surrounding structures. Under normal operating conditions, the reactor's cavity cooling system uses flowing air to cool down the environment of the cavity. The reactor's cavity cooling system reduces the temperature of the RVI up to $25\ ^{\circ}\mathrm{C}$. Because of the heat transfer from RPV to the surroundings, a temperature gradient exists in the wall of the RPV, which finally generates thermal stresses in the vessel's wall. The effects of such operational thermal stresses on the SIFs of the corner cracks postulated at the nozzle-cylinder intersection of the RPV were investigated in this study. Such an analysis requires a coupled field structural-thermal analysis considering both the pressure plus thermal stresses.

4.6.1 The Operational Thermal Stresses

As already discussed, the reactor's coolant after releasing heat in the steam generator enters into the RPV through the set-in nozzle. The temperature of the coolant is approximately $288\ ^{\circ}C$ when it enters into the RPV. On the other hand, the temperature of the reactor's cavity is normally maintained at $25\ ^{\circ}C$ with the help of reactor cavity cooling system. For the simplicity, temperatures at the inner surface of the RPV and at the outer surface of the RVI are taken as $288\ ^{\circ}C$ and $25\ ^{\circ}C$, respectively.

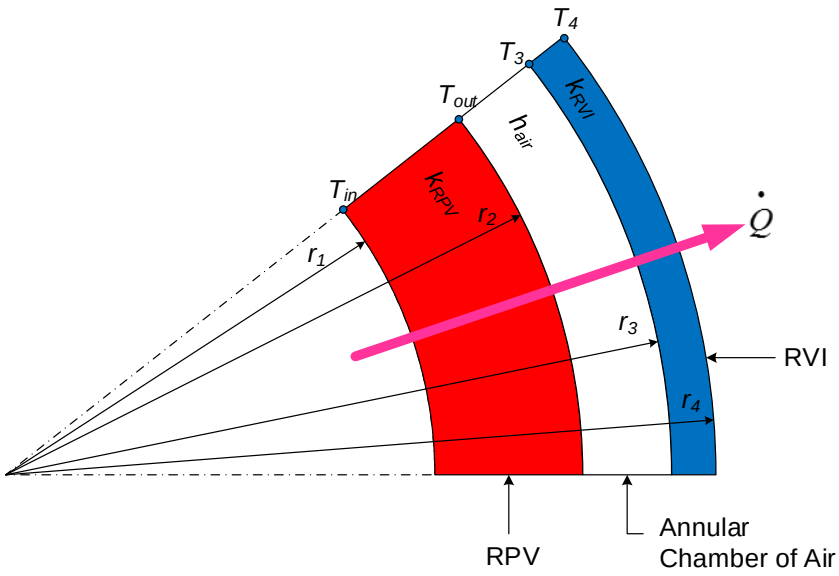

Figure 4-11 The heat transfer from the nozzle-belt to the surroundings.

The heat transfer from the RPV, through the air shield, to the surrounding structures can be modeled as a steady state and one-dimensional heat transfer case. The schematic representation of the concept of heat transfer through a section of the nozzle-belt is shown in the Figure 4-11. The material of the RPV is *'SA-508 Gr.3 Cl.1'* while the material of the RVI is selected as *'SA-240'* steel [17]. The thickness of the RPV at the nozzle beltline is *'t* = 400 *mm'* while the thickness of the reactor vessel insulation, *'t_{ins}* = 75 *mm'*. The thickness of the annular chamber of air between the reactor pressure vessel and the reactor vessel insulation is *'t_{air} = 150 mm'* [17].

The problem can be solved just like a steady state heat transfer through multilayered cylindrical shells. This problem involves conduction through the RPV and RVI and convection at the outer surface of the vessel and at the inner surface of the insulation. The steady state heat transfer rate through the system can be expressed in an equation form as:

$$\dot{Q} = \frac{T_{in} - T_4}{R_{total}} \tag{4-8}$$

Where 'R_{total}' is the total thermal resistance, which can be expressed as:

$$R_{total} = R_{RPV} + R_{conv,1} + R_{conv,2} + R_{RVI} \tag{4-9}$$

and,

T_{in} = Temperature of the inner surface of RPV.

T_4 = Temperature of the outer surface of RVI.

R_{RPV} = Thermal resistance of RPV.

$R_{conv,1}$ = Thermal resistance at the outer surface of RPV.

$R_{conv,2}$ = Thermal resistance at the inner surface of RVI.

R_{RVI} = Thermal resistance of the RVI.

By substituting the values, Eq. (4-9) can be represented as:

$$R_{total} = \frac{\ln(r_2 / r_1)}{2\pi L_n k_{RPV}} + \frac{1}{h_{air}.2\pi r_2 L_n} + \frac{1}{h_{air}.2\pi r_3 L_n} + \frac{\ln(r_4 / r_3)}{2\pi L_n k_{RVI}} \tag{4-10}$$

where;

h_{air} = Convective heat transfer coefficient of air.

k_{RPV} = Thermal conductivity of reactor pressure vessel.

k_{RVI} = Thermal conductivity of reactor vessel insulation.

r_1, r_2, r_3 and r_4 = radius as shown in Figure 4-11.

L_n = Length of the section of the nozzle-belt.

Table 4.3 The values of the variables used in heat transfer calculation.

Variable	Value	Variable	Value
T_{in}	$288\ ^{\circ}C$	r_4	2301 *mm*
T_4	$25\ ^{\circ}C$	k_{RPV}	$38.70\ W/m.^{\circ}C$
r_1	1676 *mm*	k_{RVI}	$14.80\ W/m.^{\circ}C$
r_2	2076 *mm*	h_{air}	$10.45\ W/m.^{\circ}C$
r_3	2226 *mm*	L_n	1000 *mm*

Using the Eq. (4-8) and the values given in Table 4.3 the rate of heat transfer has been calculated as '$\dot{Q} = 17061.78\ W$'. Once '$\dot{Q}$' is known, the temperature at the outer surface of the RPV can be calculated using the relationship given in Eq. (4-11).

$$\dot{Q} = \frac{T_{in} - T_{out}}{R_{RPV}} \tag{4-11}$$

Where T_{out} = Temperature at the outer surface of RPV. The temperature of the outer surface of RPV has been found as $T_{out} = 272.98\ ^{\circ}C$. The temperature difference between the inner and outer surface of the RPV at the nozzle-belt region is approximately $\Delta T = 15.02\ ^{\circ}C$. This temperature difference will be used in order to find out the temperature gradient along the wall of the vessel. Finally, the thermal stresses in the wall generated due to the temperature gradient have been computed through finite element analysis which will be presented in Ch. 8. The effects of such operational thermal stresses have been investigated on SIFs of the corner cracks postulated at the nozzle-cylinder intersection of the RPV.

5 Optimization

In this chapter, starting from a typical design of the set-in nozzle, an optimized design of the nozzle has been proposed. As already described in Section 4.1 that the nozzle is made of nuclear grade steel designated as *'SA-508 Gr.3 Cl.1'*. It has been assumed in this chapter, that the set-in nozzle is completely crack free and the material of the nozzle is completely homogenous. The motivation behind the optimization is that the design of the typical set-in nozzle produces stresses along the nozzle that predict yielding (according to Tresca yiled theory) especially at the nozzle-cylinder intersection. The aim of the optimization is to investigate an optimized design of the nozzle, which does not predict yielding at any point of the nozzle provided that the mass of nozzle is also kept constant as the typical nozzle. Hence, the optimization has been performed such that the nozzle has to fulfil two criterions (Tresca and constant mass) instead of the single failure criterion.

Once the design of the nozzle was finalized according to above-mentioned criterion, the load bearing capacity of the 'RPV with optimized nozzle' has also been determined using the design-by-analysis (DBA) approach [1]. The DBA approach as described in ASME code [1], requires an elastic plastic stress analysis of the vessel which has also been performed.

For the optimization and the design by analysis, a full high quality hexahedral finite element (FE) model of the RPV was developed initially. Such an FE model is inevitably required for accurate 3D stress state especially along the nozzle. The details of the FE model are given below.

5.1 The Finite Element Model of the RPV

The 'ANSYS Workbench' software was utilized for modelling, meshing, and finite element analysis required for the optimization and the design-by-analysis of the RPV. The 'ANSYS DesignModeler' is a module for CAD modeling while 'ANSYS Mechanical' module is used to generate mesh and perform finite element analysis. Traditionally, a hexahedral mesh is computationally more efficient and preferable

than the tetrahedral mesh. For creating hexahedral mesh in a body, sweep mesh is one of the methods which may be utilized. By definition, a body can be swept into hexahedral mesh if it contains at least a pair of topologically similar faces. Topologically similar faces can simply be defined as two faces having equal number of vertices and essentially connected by a smooth path. Such faces are called the source and target faces in the sweep mesh method. The 'Mechanical' module normally mesh the source face with quadrilateral elements and then copy that mesh onto the target face, resulting a hexahedral mesh in the body.

For creating an all-hexahedral finite element model of the RPV, sweep mesh method was utilized. The vessel as one part structure does not fulfill the topological requirements for sweeping and is therefore not amenable to hexahedral mesh. In order to make the vessel amenable for sweep mesh, slicing and dicing technique, was utilized for the creation of the geometry. Using the technique the unsweepable vessel was decomposed into several sweepable bodies. Each sweepable body, having topologically consistent source and target faces, is shown with a different color in Figure 5-1 (a). The sweepable multibody RPV was then glued together to make a single part. The gluing is also compulsory to ensure consistent nodes at the connecting faces of the sweepable bodies.

In 'ANSYS Mechanical' module, the sweep method is the default meshing approach if the structure's topology is recognized as sweepable. Once the prepared model of the RPV was transferred to the 'ANSYS Mechanical', the free mesher of the module could generate an efficient hexahedral mesh as shown in Figure 5-1 (b). The FE model of the vessel has a skewness equal to 0.872. The skewness, a measure of mesh quality, ranges from 0 to 1, the smaller the better; and FE model having skewness less than 0.95 is acceptable for finite element analysis [79]. As the developed FE model has the skewness value less than 0.95, it is therefore an acceptable model for the analysis. The FE model shown in Figure 5-1 (b) contains a total of 41988 finite elements and 203848 nodes. The element type used for the stress analysis is Solid-186, which is a higher order 3-D, 20 node brick element with mid-side nodes and curved edges.

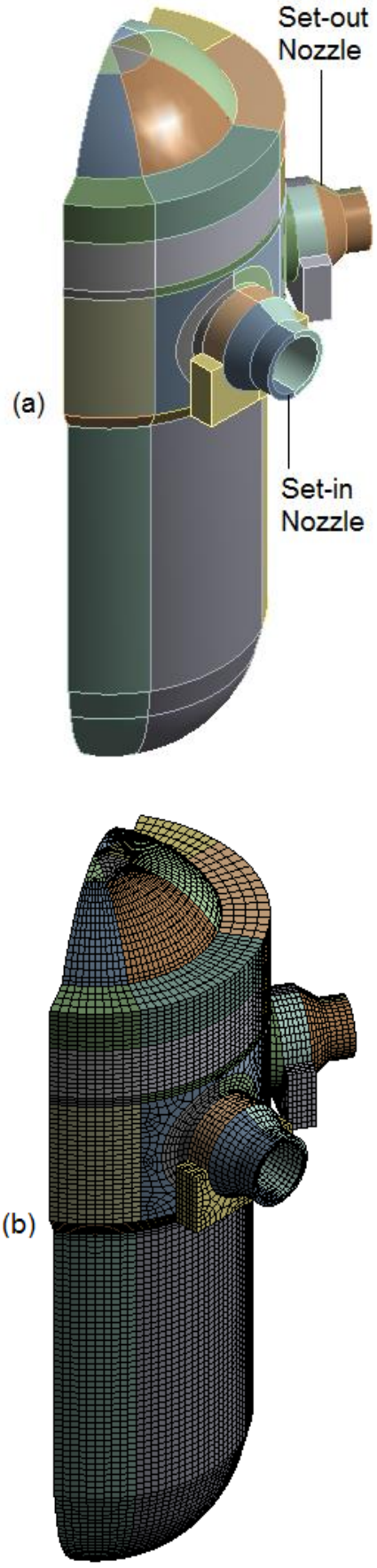

Figure 5-1 (a) Sweepable bodies in the RPV (b) Full FE model of the RPV.

5.2 Stress Analysis of the Typical Set-in Nozzle

As already discussed in Section 4.4 that the three design variables control the size and shape of the set-in nozzle: the inner radius of the nozzle *(R)*, the taper angle at the nozzle-cylinder intersection *(θ)* and the span where the taper of the nozzle starts from *(X)*. The values of these design variables in case of the typical set-in nozzle are 'R = 375 *mm*', 'θ = 3.5º' and 'X = 900 *mm*' as shown in Figure 4-2. The mass of this typical set-in nozzle (see Figure 4-2 (a)) with the material *'SA-508 Gr.3 Cl.1'* is 8767.1 *kg*.

In order to compute the hoop stress (σ_h) and stress intensity *(S.I)* along the typical set-in nozzle, stress analysis was performed using the FE model of the vessel shown in Figure 5-1 (b). The internal pressure of the vessel was kept equal to design pressure which is 17.16 *MPa* and the temperature of the vessel was kept equal to design temperature which is $350\ ^{o}C$ (see Section 0). The hoop stress and stress intensity distributions along the whole typical set-in nozzle are shown in Figure 5-2 and Figure 5-3, respectively. It is obvious from the results that the nozzle-cylinder intersection has the maximum values of hoop stresses and stress intensity compared to all other locations of the nozzle. The maximum values of the hoop stress and stress intensity are equal to 278.39 *MPa* and 296.06 *MPa*, respectively. Hence, nozzle-cylinder intersection is the highest stress concentration point (HSCP) of the set-in nozzle.

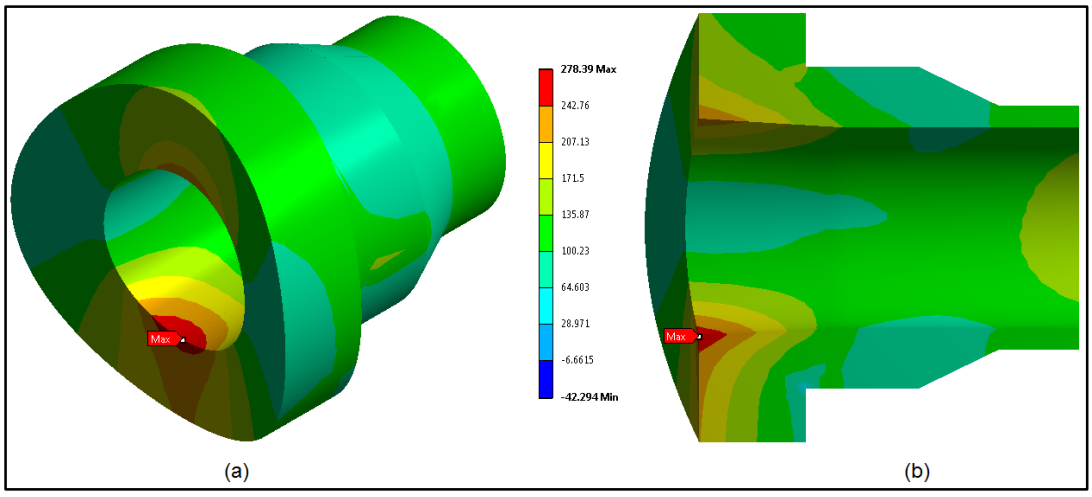

Figure 5-2 The hoop stress distributions in the typical set-in nozzle, values in *MPa* (a) Isometric view (b) Cut section view.

It is also evident from the distributions of the stress intensity (see Figure 5-3) that according to Tresca yield theory (see Eq. (4-7)) yielding will occur at the nozzle-cylinder intersection of the vessel. It is because that the stress intensity value at this location exceeds yield strength of the material, which is equal to 285 *MPa* at the design temperature ($350\ ^{o}C$) of the vessel (see Table 4.1). Hence, a design of the nozzle which does not produce any yielding along the nozzle is required which will be investigated through the optimization in Section 5.4.

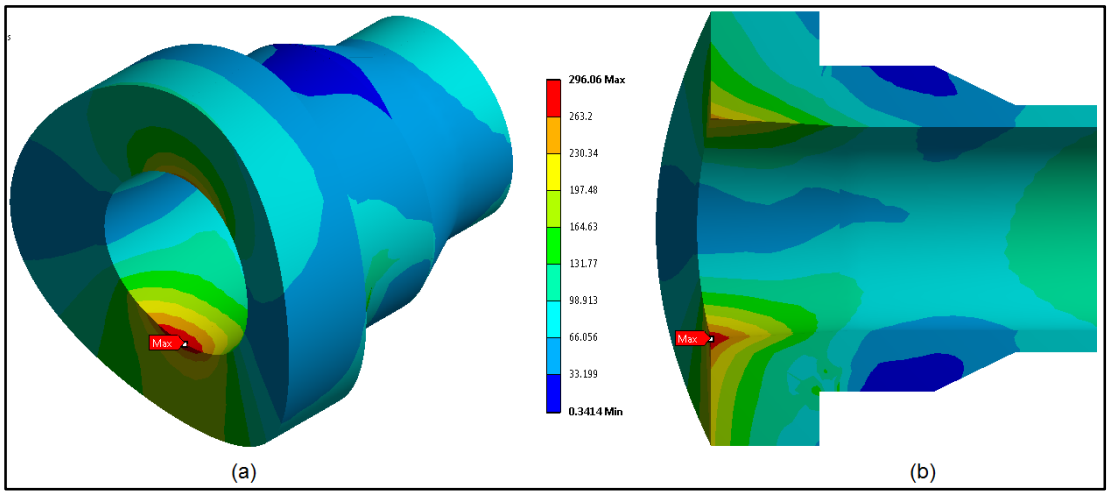

Figure 5-3 The stress intensity distributions in the typical set-in nozzle, values in *MPa* (a) Isometric view (b) Cut section view.

5.3 Mesh Independent Study of the FE Model of the RPV

In order to show that hexahedral FE model of the RPV (generated in Section 5.1) yields converging and mesh independent results, a basic mesh independent study was also performed. In this regard, a plot of the maximum stress intensity versus number of nodes has been shown in Figure 5-4. By increasing the number of nodes, an increasing trend in the maximum stress intensity is seen. It is evident from the curve that stress intensity at the value of 296.06 *MPa* becomes converged when the number of nodes reaches around 203848. That is why, the FE model of the RPV having 203848 nodes was selected for the stress analysis and the optimization of the nozzle.

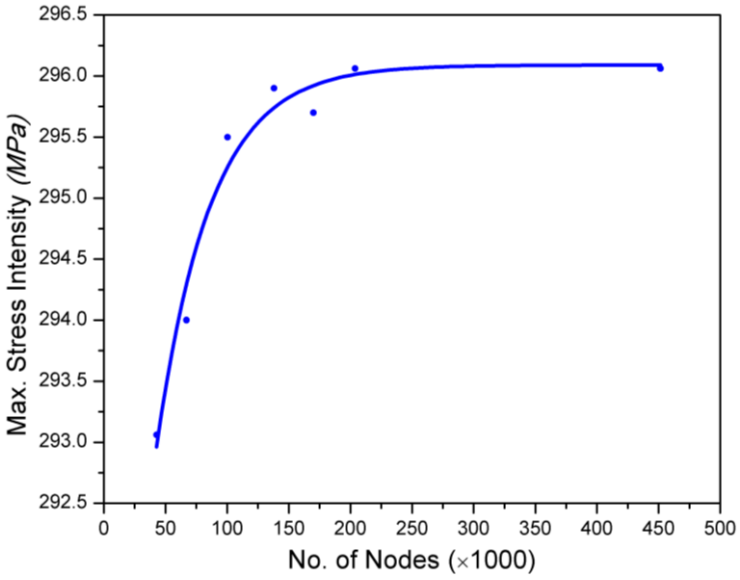

Figure 5-4 Mesh independent study.

5.4 Optimization of the Set-in Nozzle

The optimization of the set-in nozzle has been performed using a method called design of experiments [79] in the 'ANSYS Workbench'. The adopted methodology is capable of investigating the correlated effects of the design variables on the state variables (see Section 4.4) of the nozzle.

5.4.1 Design of Experiments

In order to search an optimum design of the nozzle that ensures 'maximum S.I' at the nozzle-cylinder intersection below the yield strength (285 *MPa*) of the material subject to the constant nozzle's mass, simulations with several combinations of design variables were performed. For the simulations, the lower and upper bound limits applied on the design variables are listed in Table 4.2. The combinations of design variables (design points) were chosen according to central composite design method [79]. Fifteen design points and their corresponding values of maximum stress intensity and mass of the nozzle are given in Table 5.1.

5.4.2 Response Surfaces

As already mentioned, the *'mass of the nozzle'* and *'maximum stress intensity'* have been nominated as the state variables in this optimization process. All the design points and corresponding response values of the state variables are used to best-fit mathematical functions (typically 2nd order polynomials). These functions are called

response surfaces. Using the design points listed in Table 5.1, the response surfaces of the *'maximum stress intensity'* and the *'mass of the* nozzle' have been constructed and are presented in Figure 5-5 and Figure 5-6, respectively.

Table 5.1 Design points along with max. *S.I* and mass of the nozzle.

Design Points	*R* *(mm)*	*X* *(mm)*	*θ* *(Degrees)*	*S.I* at nozzle-cylinder intersection *(MPa)*	Mass of the nozzle *(kg)*
1(typical)	375	900	3.5	296.3	8767.1
2	350	1200	1.0	284.3	9315.4
3	350	1200	6.0	278.2	9269.5
4	400	600	1.0	308.9	8397.4
5	400	600	6.0	318.8	7718.1
6	400	1200	1.0	305.7	8510.4
7	400	1200	6.0	298.0	8455.3
8	375	900	1.0	297.1	8891.5
9	375	900	6.0	296.3	8635.3
10	375	600	3.5	301.8	8519.1
11	375	1200	3.5	292.1	8904.8
12	350	900	3.5	286.4	9165.1
13	400	900	3.5	307.4	8335.6
14	350	600	1.0	287.6	9217.4
15	350	600	6.0	296.1	8626.0

The response surfaces were constructed by fixing the value of the taper angle *(θ)* and by changing the span *(X)* and the radius *(R)* of the set-in nozzle. The Figure 5-5 (a), (b), (c), (d), (e) and (f) show the response surfaces of the *'maximum stress intensity'* at the nozzle-cylinder intersection when the nozzle has taper angle *(θ)* equal to 1°, 2°, 3°, 4°, 5° and 6°, respectively. Whereas Figure 5-6 (a), (b), (c), (d), (e) and (f) show the response surfaces of the *'mass of the nozzle'* when the nozzle has taper angle *(θ)* equal to 1°, 2°, 3°, 4°, 5° and 6°, respectively.

In order to search the constructed response surfaces for the optimized point which fulfills our set criterion having two objectives (maximum stress intensity below 285 *MPa* and the constant mass around 8767.1 *kg*), genetic algorithm (GA) based multi-objective optimization was performed. GA is a robust optimization algorithm and a wide class of problems can be solved using this algorithm. It is one of the global optimization techniques and does ensure the convergence to the global optimum [12, 80]. The optimization using multi-objective genetic algorithm (MOGA) can be performed using ANSYS workbench [81].

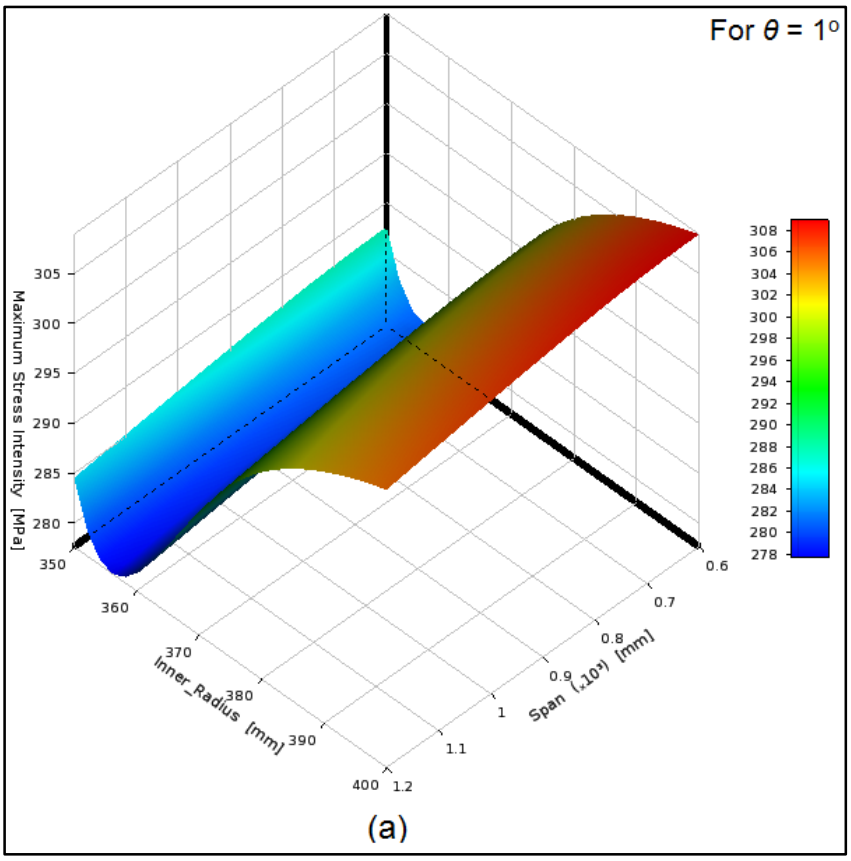

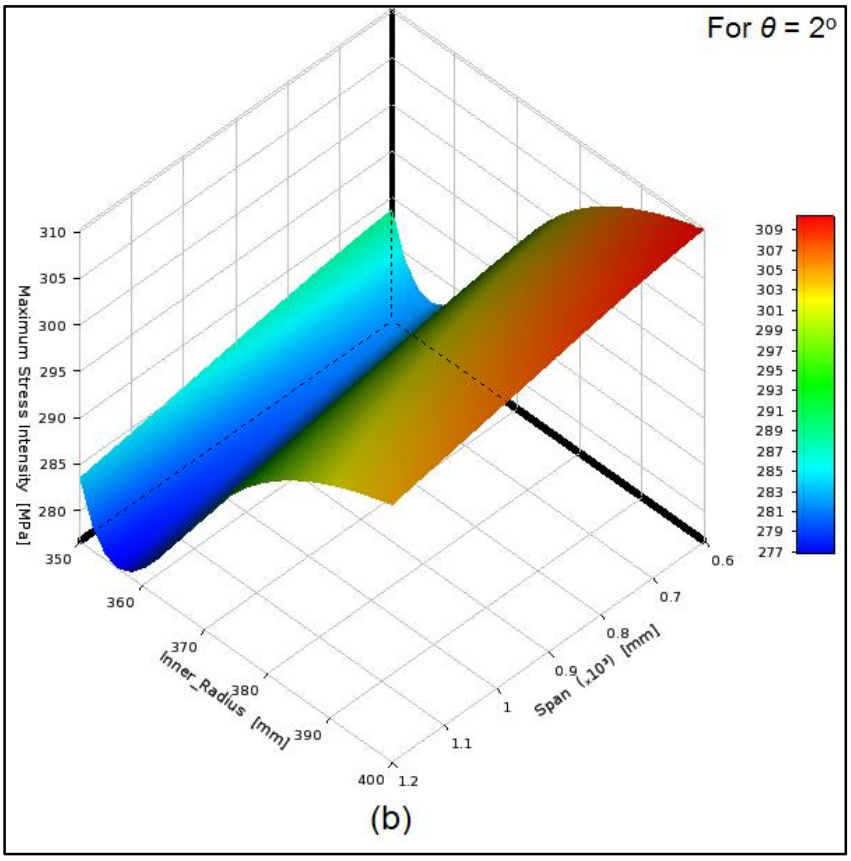

Figure 5-5 Response surfaces of the max. stress intensity …

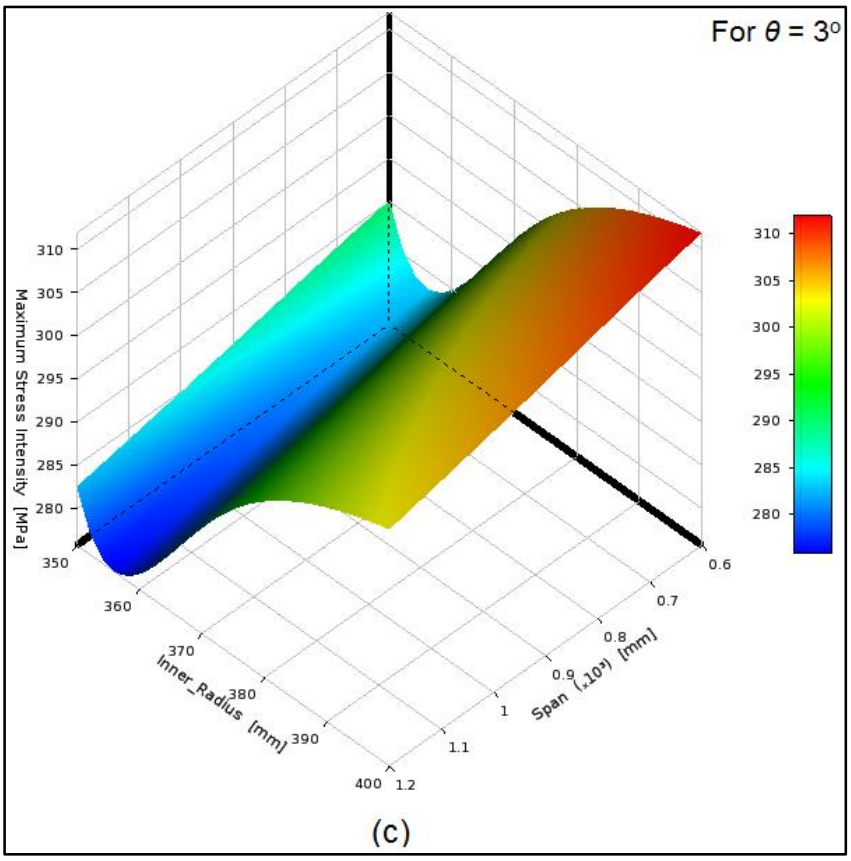

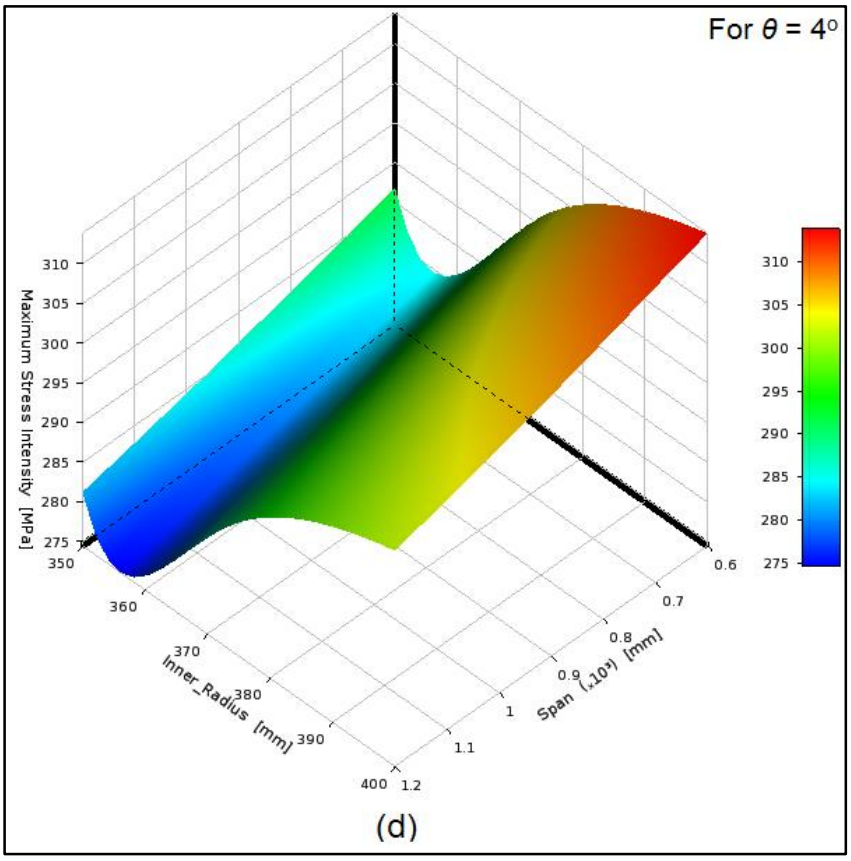

Figure 5-5 Response surfaces of the max. stress intensity …

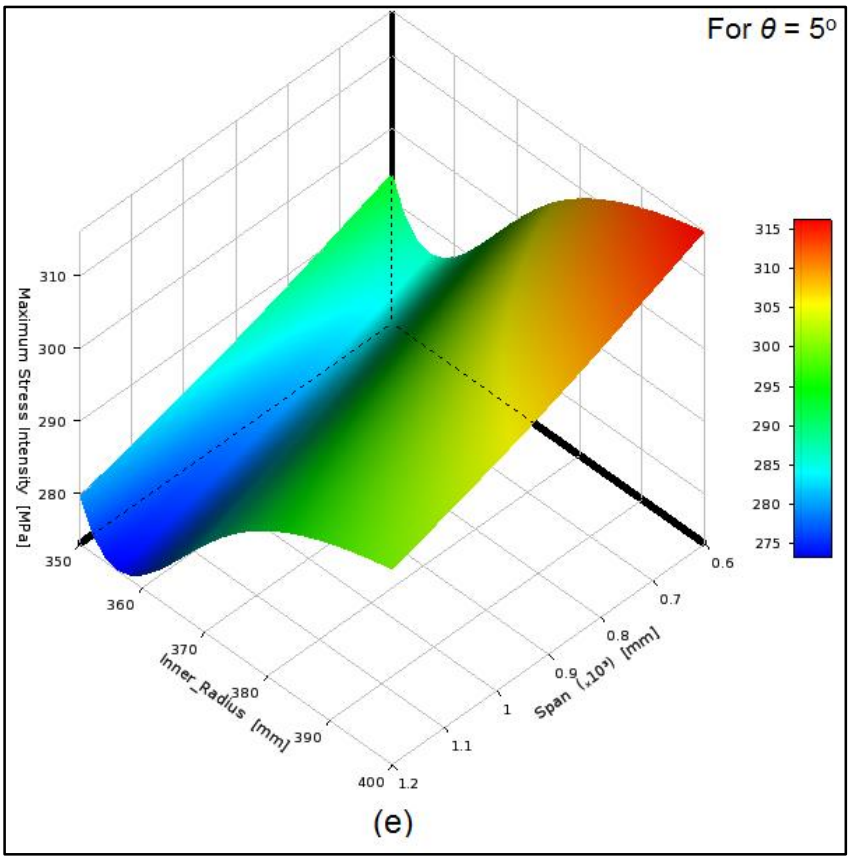

(e)

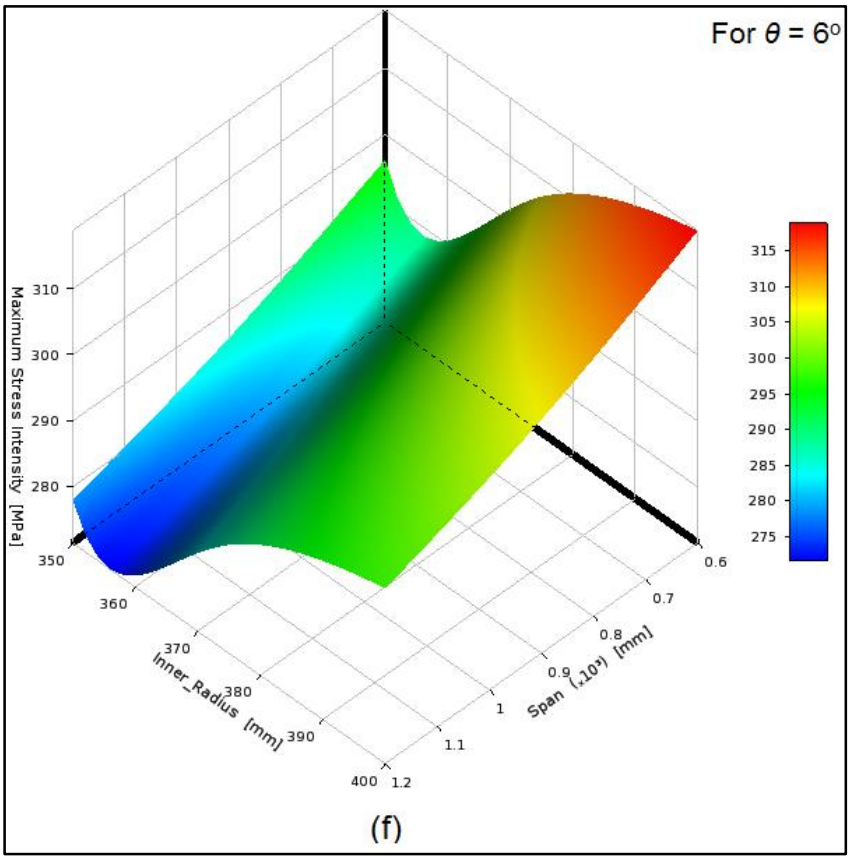

(f)

Figure 5-5 Response surfaces of the max. stress intensity.

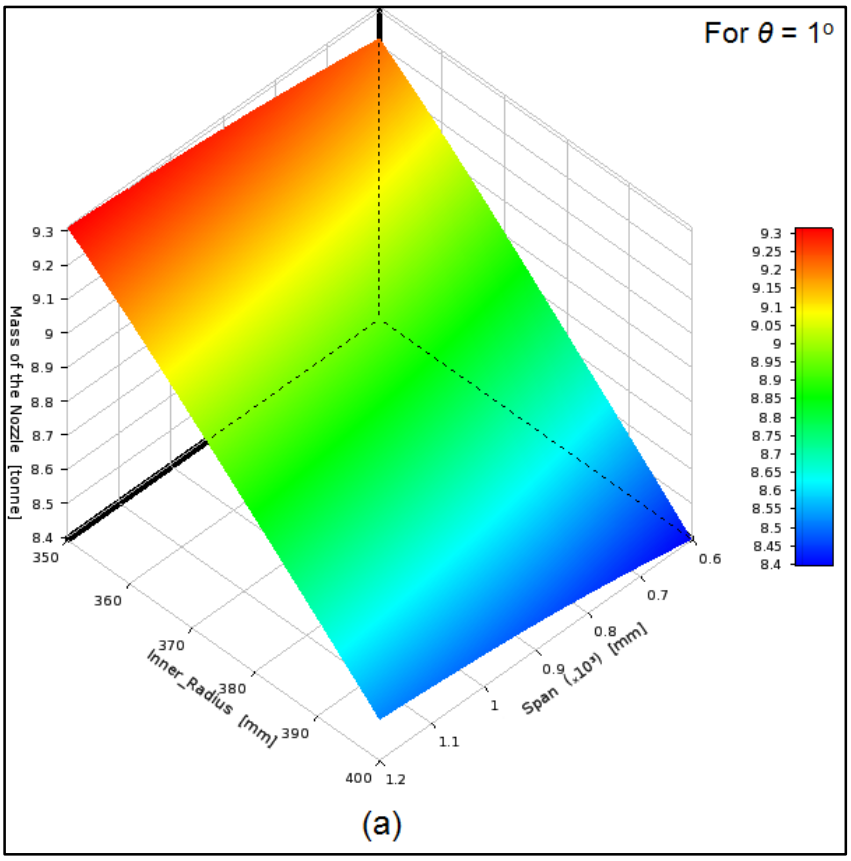

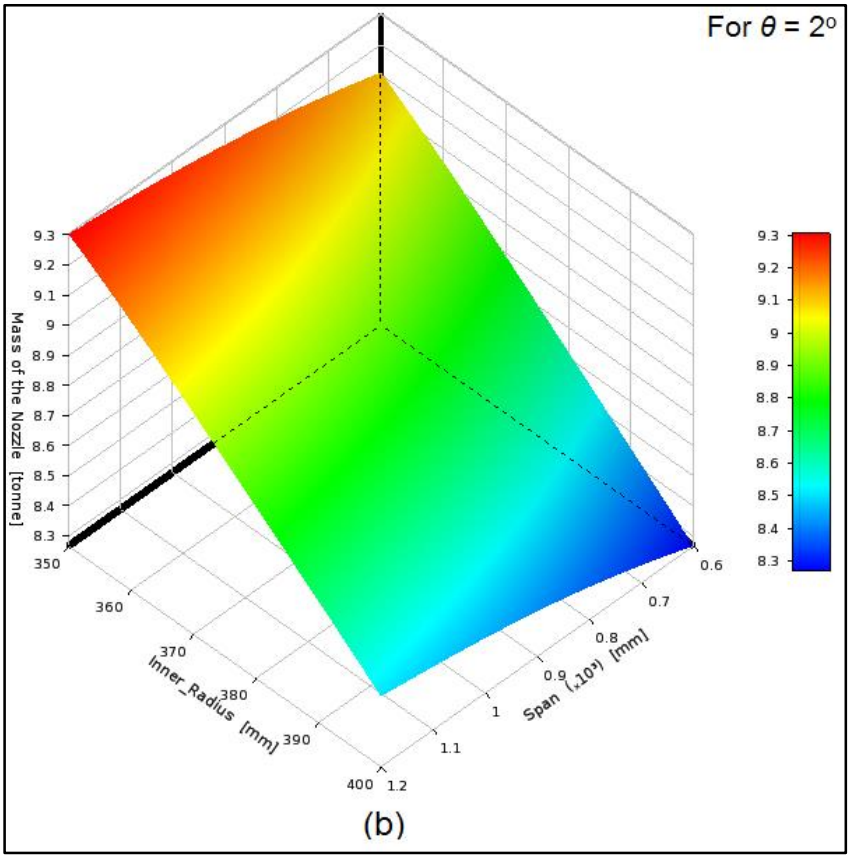

Figure 5-6 Response surfaces of the mass of the nozzle …

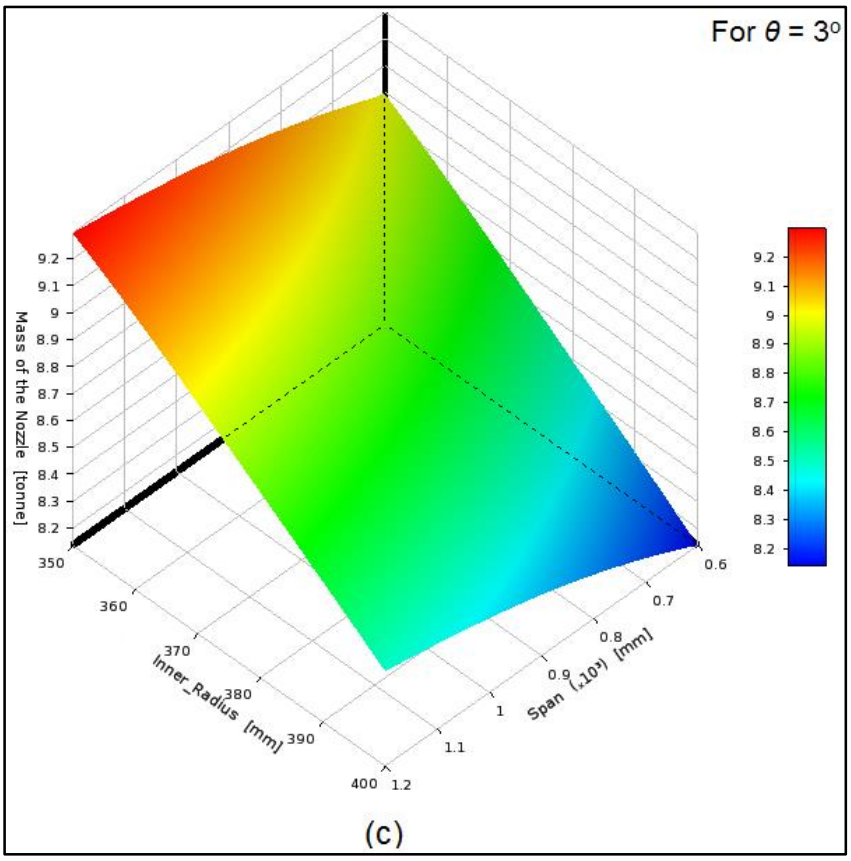

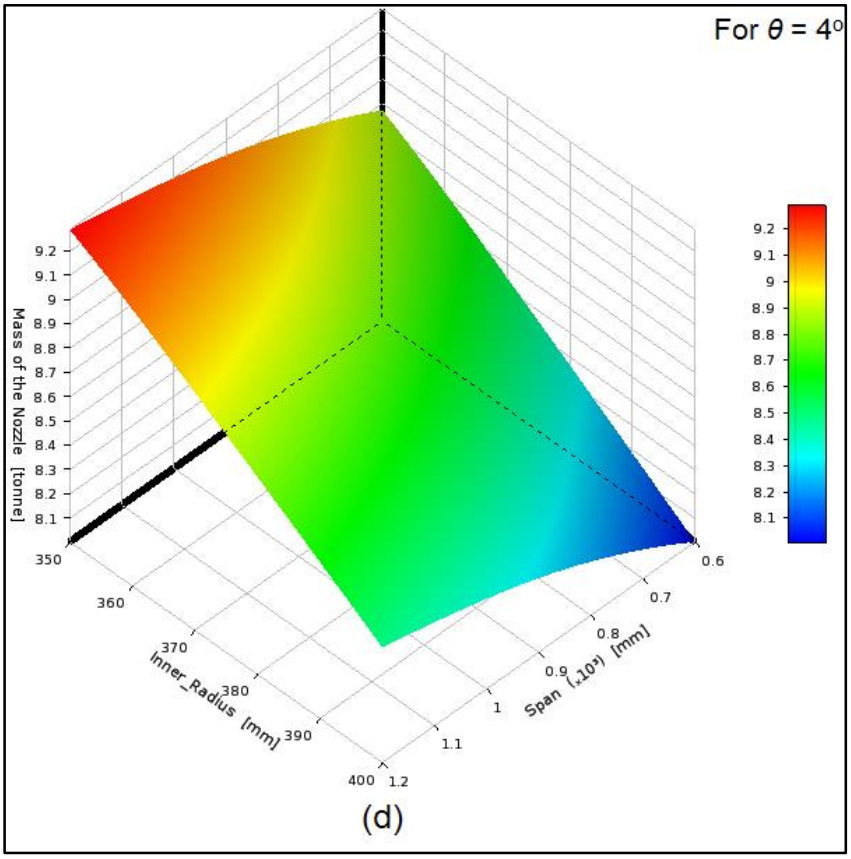

Figure 5-6 Response surfaces of the mass of the nozzle …

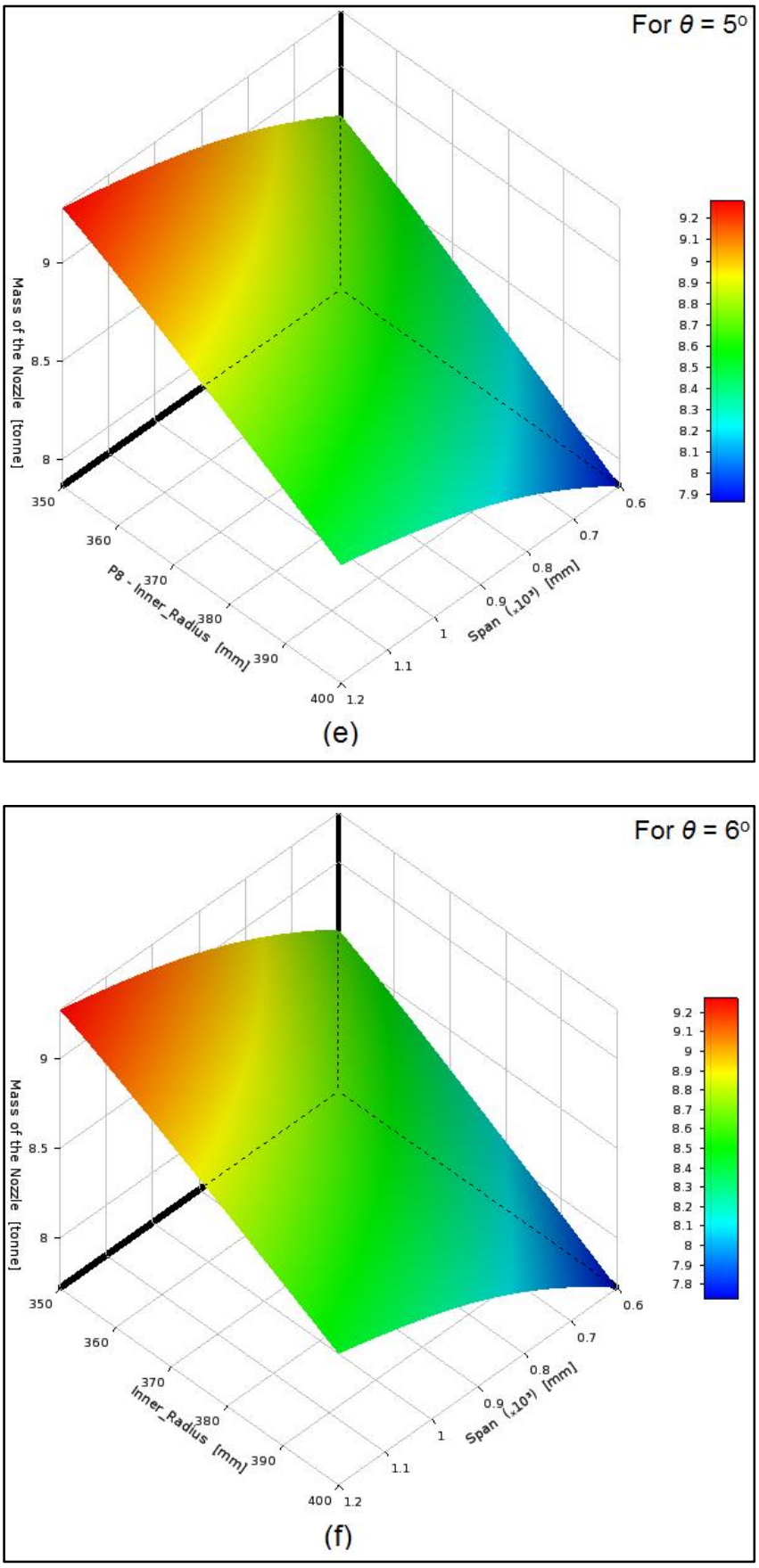

Figure 5-6 Response surfaces of the mass of the nozzle.

MOGA is based on the controlled elitism concepts and supports multiple objectives and constraints and aims at finding the global optimum. Generally, it works with the coding of the parameter set, not the parameters themselves. In the process, the values of the design variables *R, X,* and θ will be replaced into their binary equivalents. The MOGA searches for a population of points, not a single point. It converts the 0's and 1's of the binary equivalent into bits then mutates and crossovers the bits to produce children who then become parents. There is a strategy involved in MOGA that only the fittest can survive and form new generation [80].

The simulations, using MOGA, in ANSYS workbench require the pre-defined values of the parameters: population size, crossover probability, mutation probability, and number of generations. The population size must be greater than or equal to the number of design variables (*R, X, θ)*. The minimum recommended number is 10 times the number of design variables; the larger the population size is, the better are the chances of finding the design space that contains the best solution [81]. The population size of 100 samples was used in this study.

The crossover combines two chromosomes (parents) to produce a new chromosome (children). The idea behind crossover is that the new chromosome may be better than both of the parents if it takes the best characteristics from each of the parents. The value of the crossover probability must be within 0 and 1. A smaller value indicates a more stable population and a faster (but less accurate) solution; the parents are copied directly to the new population if the value is 0. A high probability of crossover (> 0.9) is recommended [81]; therefore, a crossover probability equal to 0.98 was used in this study.

Mutation alters one or more gene values in a chromosome from its initial state. This can result in entirely new gene values being added to the gene pool. With these new gene values, the GA may be able to arrive at a better solution than was previously possible. Mutation is an important part of the genetic search, as it helps to prevent the population from stagnating at any local optima. The value of the mutation probability must be between 0 and 1. A larger value indicates a more random algorithm; the algorithm becomes the pure random search if the value is 1. A low probability of mutation (< 0.2) is recommended [81]; therefore, a mutation probability equal to 0.01 was used in this study.

The number of generations is the maximum number of iterations which algorithm executes. If the number of iterations reaches the maximum number of iterations before the optimization attains convergence, iterations will stop. The maximum number of generations equal to 20 was used in this study.

Using MOGA, the constructed response surfaces were searched for the optimized point. The investigated optimized design of the set-in nozzle has the dimensions 'R = 358.13 *mm*', 'X = 776.42 *mm*', and 'θ = 6.0º'. It is evident from Figure 5-5 (f) and Figure 5-6 (f) that taper angle equal to 6º with 'R = 358.13 *mm*', and 'X = 776.42 *mm*' fulfills both the requirements of our set criterion for the optimization. The response surfaces predicts the *'maximum S.I* = 283.14 *MPa'* (see Figure 5-5 (f)) with the mass of the optimized nozzle equal to 8763.3 *kg* (see Figure 5-6 (f)). While comparing the mass of the typical set in nozzle (8767.1 *kg)* with the mass of the optimized set-in nozzle (8763.3 *kg),* it can be concluded that the mass remains almost constant. The engineering drawing of the proposed optimized set-in nozzle is shown in Figure 5-7. This design of the set-in nozzle will be used for fracture mechanics analysis in Ch. 7 and Ch. 8 of this thesis.

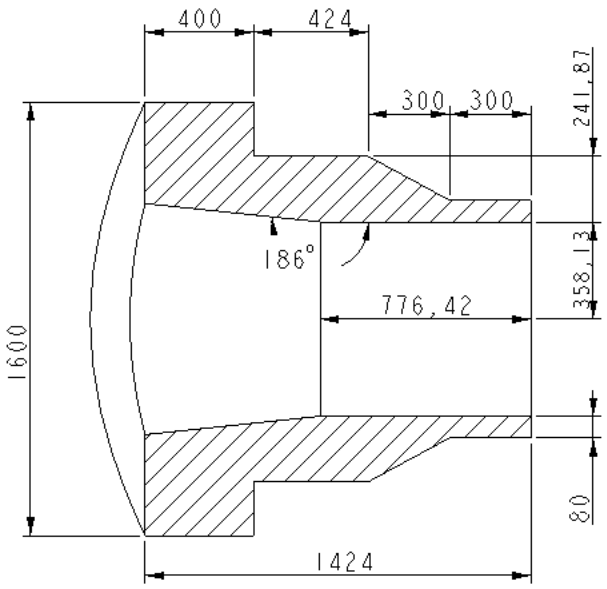

Figure 5-7 The optimized design of the set-in nozzle, dimensions in *mm*.

5.5 Stress Analysis of the Optimized Nozzle

The distributions of hoop stress and stress intensity along the optimized set-in nozzle have been shown in Figure 5-8 and Figure 5-9 respectively.

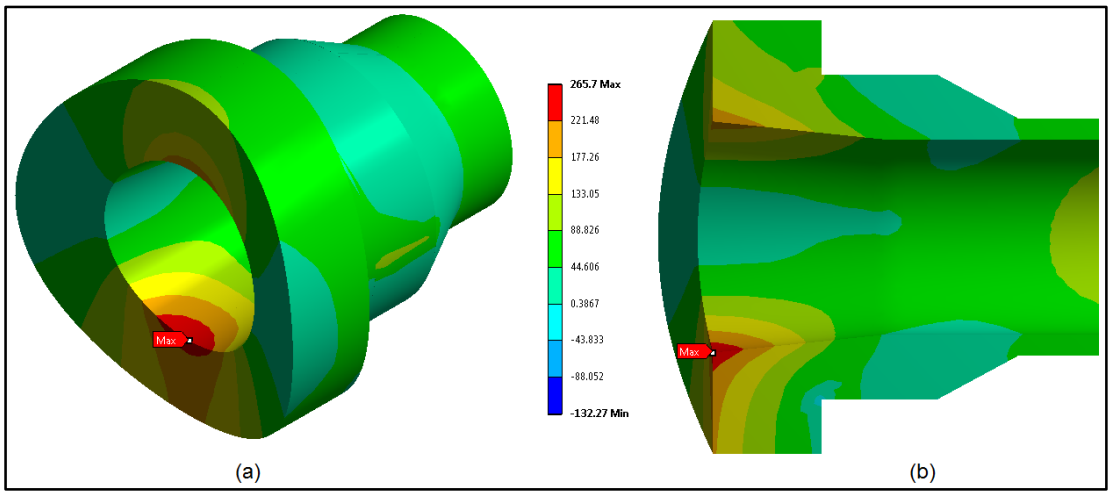

Figure 5-8 The hoop stress distributions in the optimized set-in nozzle, values in *MPa* (a) Isometric view (b) Cut section view.

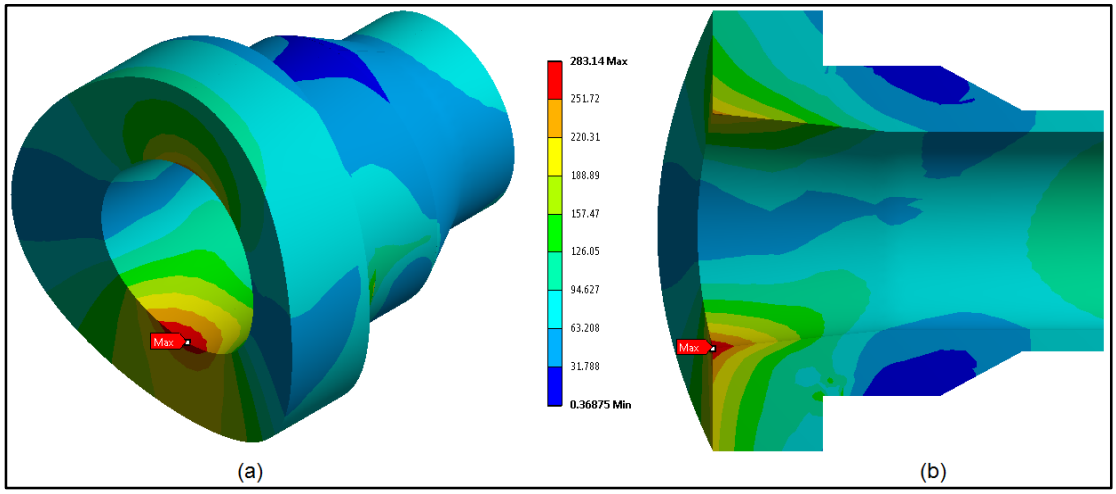

Figure 5-9 The stress intensity distributions in the optimized set-in nozzle, values in *MPa* (a) Isometric view (b) Cut section view.

It is evident from Figure 5-8 and Figure 5-9 that in case of optimized set-in nozzle, values of the hoop stress and the *'maximum S.I'* are equal to 265.7 *MPa* and 283.14 *MPa*, respectively. It is clear from the Figure 5-9 that yielding will not occur at any point of the nozzle. It is because the maximum stress intensity along the nozzle is below the yield strength (285 *MPa*) of the material.

The design of the optimized set-in nozzle (see Figure 5-7) was investigated using the linear elastic material model of the RPV's steel (*SA-508 Gr.3 Cl.1*) at $350\ ^{\circ}C$ (see Table 4.1). However, in order to ensure the safety of the vessel, a more physical elastic plastic failure analysis of the 'RPV with optimized set-in nozzle' has

also been performed and the results are presented in Section 5.6. This analysis is called 'design-by-analysis (DBA)' according to the ASME code [1, 68].

5.6 Design-by-Analysis of the Optimized Set-in Nozzle

The maximum limit load capability of the RPV with the optimized set-in nozzle was also determined using the rules of DBA approach. The approach as described in ASME code, article NB-3200 (Section III) [1] uses elastic-plastic stress analysis of the vessel. The elastic plastic characteristics of the vessel's steel (*SA-508 Gr.3 Cl.1*) at $350\ ^{\circ}\mathrm{C}$, as shown in Figure 4-3, were used for this analysis. The approach mainly consists of two application rules, which have been used as given below.

5.6.1 Application Rule 1

In application rule 1, the elastic plastic stress analysis including strain hardening and large deformation effects is required for determining the plastic analysis collapse load. The plastic analysis collapse load is the load, which produces gross plastic deformation (GPD) which finally gives the allowable load for the component. According to ASME code, article NB-3228 [1], the allowable load is defined as "…the specified loading should not exceed two-thirds of the plastic analysis collapse load…". Thus the allowable load is

$$P_a = \frac{2}{3} P_p \tag{5-1}$$

where 'P_p' is the plastic collapse load.

The plastic analysis collapse load of the vessel can be determined using the twice-elastic-slope (TES) criterion as specified in ASME code, Mandatory Appendix II-1430 [1]. The TES criterion is based on the load-displacement response of the vessel which is obtained by elastic plastic analysis [82]. The elastic plastic finite element analysis of the vessel was conducted using the incremental iterative approach. For the purpose, the internal pressure of the vessel was increased in steps of $1\ MPa$ .The corresponding radial displacement of the vessel for each incremental step was noted down. A graph has been plotted by taking incremental internal pressure as the ordinate and the corresponding radial displacement of the vessel as the abscissa of the graph. The graph of the load versus the radial displacement has been shown in the Figure 5-10.

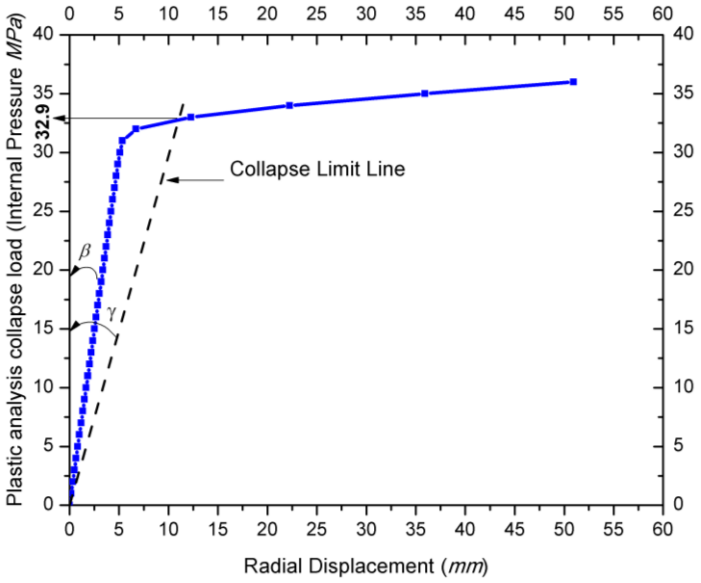

Figure 5-10 The internal pressure versus radial displacement of the RPV.

Using the TES criterion [1], the plastic analysis collapse load can be determined from the load-displacement graph. The TES states that the plastic collapse load (P_p) can be determined from the intersection of the load-displacement curve and the collapse limit line [83, 84] as shown in Figure 5-10. The 'collapse limit line' can be drawn through the origin such that it makes an angle '$\gamma = \tan^{-1}(2\tan\beta)$' with the ordinate, where 'β' is the angle which linear part of the load-displacement curve makes with the ordinate as shown in Figure 5-10.

Hence, the plastic analysis collapse load according to TES is 32.9 *MPa*, as shown in Figure 5-10. Putting the value of plastic collapse load (P_p) in the Eq. (5-1), the maximum allowable pressure of the vessel is $P_a = (2/3)\times 33 = 21.9\ MPa$. It should be noted that in Eq. (5-1), a safety factor equal to 1.5 has been applied. Hence, the allowable pressure of the 'RPV with the optimized nozzle' is 21.9 *MPa* with the safety factor of 1.5.

5.6.2 Application Rule 2

In application rule 2, ASME code, article NB-3228.5 [1] requires that 'the range of primary plus secondary membrane plus bending stress intensity should be $\leq 3S_m$'.

$$(|\sigma_{\max} - \sigma_{\min}|) \leq 3S_m \qquad (5\text{-}2)$$

Where, 'S_m' is the design stress intensity value of the vessel's material (SA-*508 Gr.3 Cl.1)* which is equal to '184 *MPa*' as given in Tables 2A of ASME code [72]. The 'σ_{max}' and 'σ_{min}' are the largest and smallest principal stresses, respectively. The left hand side of the Eq. (5-2) is equivalent to the value of stress intensity according to the Tresca yield criterion [4]. Hence, according to Eq. (5-2), the maximum stress intensity along the optimized set-in nozzle should be less than 552 *MPa*.

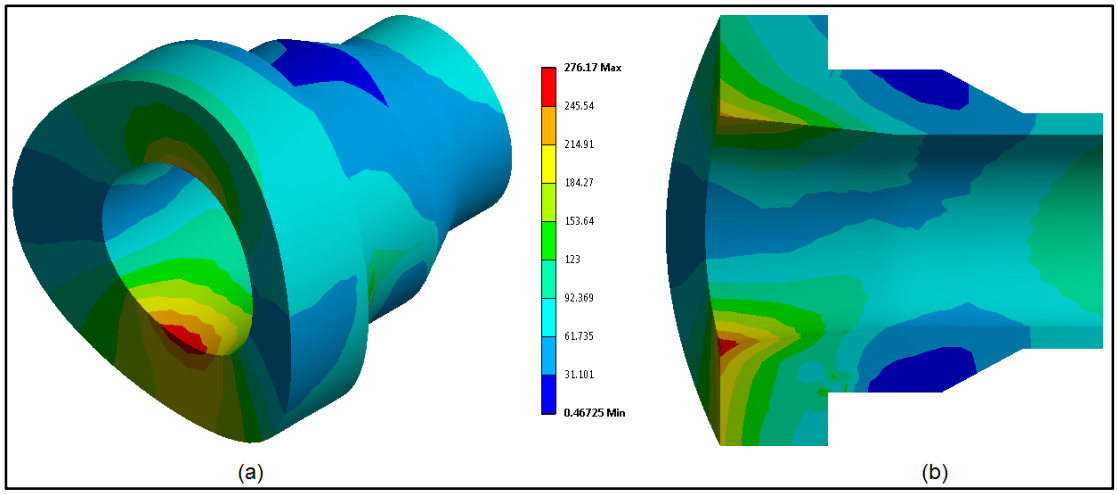

Figure 5-11 Elastic plastic distributions of stress intensity *(MPa)*.

The elastic plastic stress analysis of the 'RPV with optimized nozzle' has been performed at the design pressure (17.16 *MPa*) of the vessel. The results or the stress intensity distributions along the optimized set-in nozzle are shown in Figure 5-11. It is evident from the results that the maximum stress intensity is equal to 276.17 *MPa*, and it is at the nozzle-cylinder intersection of the vessel. This maximum stress intensity is clearly below the '$3S_m$', and the minimum margin of safety (according to Eq. (5-2)) is equal to $552/276.17 = 2$. Hence, it can be concluded from the DBA analysis that the 'RPV with the optimized set-in nozzle' is a safe design and the margin of safety at the design pressure is equal to 2.

Hence, it can be concluded for the computations in this chapter, that the proposed optimized design of the nozzle can be used with confidence for the RPV of a 300 MW pressurized water reactor.

5.7 Summary of the Chapter

This chapter proposes an optimized set-in nozzle for the reactor pressure vessel of a 300 MW pressurized water reactor. The chapter can be summarized as below.

1. The optimized design of the nozzle has the dimensions 'R = 358.13 *mm*', 'X = 776.42 *mm*', and '$\theta = 6^{o}$' (see Figure 5-7); where *'R'* is the inner radius of the nozzle, *'θ'* is the taper angle at the nozzle-cylinder intersection and *'X'* is the span of the nozzle.
2. The proposed design of the nozzle does not threaten yielding, at design pressure and temperature, along any point of the nozzle even according to very conservative Tresca yield criterion [4].
3. The maximum allowable pressure of the 'RPV with optimized nozzle' is 21.9 *MPa*.
4. The margin of safety of the nozzle is equal to '2' as per the design by analysis criterion of ASME code [1].

6 Pallet Body Approach

In this chapter, an approach to analyze 3D surface cracks was developed using ANSYS Workbench. The approach is capable of inserting the crack in an engineering structure and generating mesh in the cracked region of the structure. The approach has been named the 'pallet body approach'. The approach is capable of computing stress intensity factors (SIFs) along the whole crack front. The approach has been validated by comparing the results with the Newman and Raju analysis [6], ASME code [7], and the experimental work of Reytier [8]. The comparison shows a good agreement. The details of the approach has been given below.

6.1 The Pallet Body Fracture Model

The preparation of the fracture model using the pallet body approach mainly consists of six steps, which have been described below.

6.1.1 Step No. 1: Formation of Un-cracked Structure

In this step, the computer model of an un-cracked structure is made. The structure selected for this demonstration is a finite plate of steel. Figure 6-1 (a) shows a semi elliptical surface crack in finite plate (SESC-FP) and is called a SESC-FP specimen. The SESC-FP specimen and the crack have the dimensions '$2b$ = 1000 *mm*', '$2h$ = 2000 *mm*', 't_p = 500 *mm*', 'a/c = 0.30', and 'a/t_p = 0.05', where the parameters a, c, b, t_p, h, T_F and ϕ are as shown in Figure 6-1 (a) and (b). The computer model of the finite plate was done in 'ANSYS DesignModeler' and it is shown in Figure 6-2.

6.1.2 Step No. 2: Formation of Crack's Profile Body

In this step, modeling of the crack's profile body as per dimensions of the crack is performed. In the body, the triangular crack faces are required to be coincident at the crack front. The elliptical crack's profile body for SESC-FP specimen is shown in Figure 6-3. The thickness of the body was taken equal to '1 *mm*'.

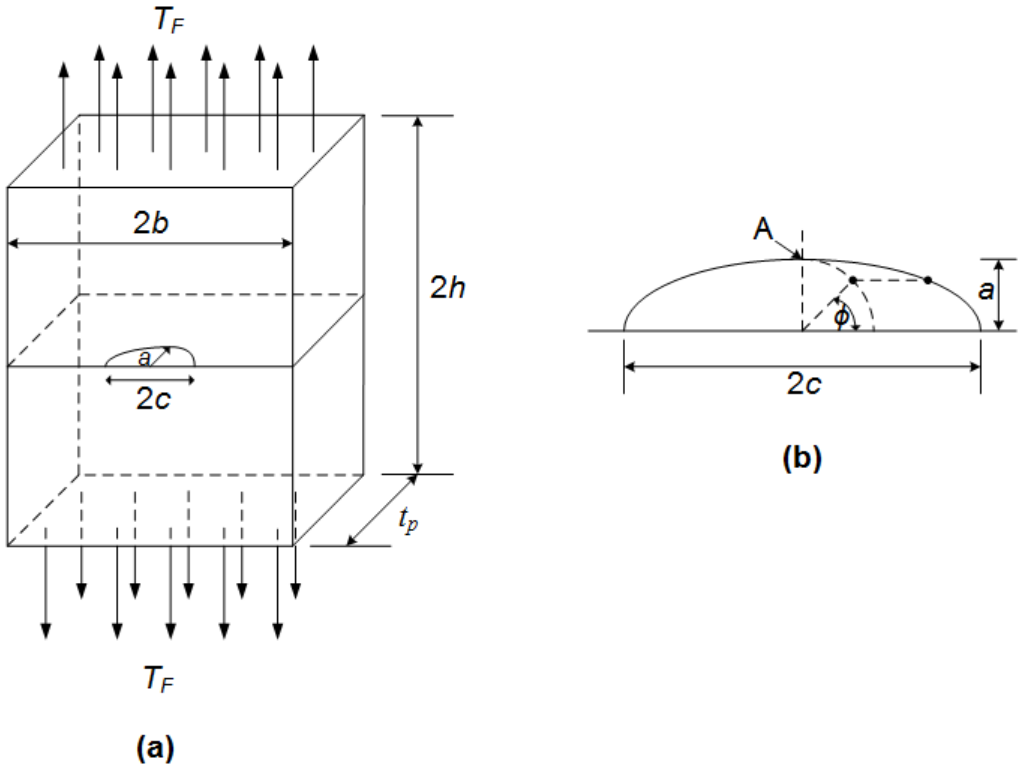

Figure 6-1 (a) SESC-FP specimen (b) Crack tip position parameters.

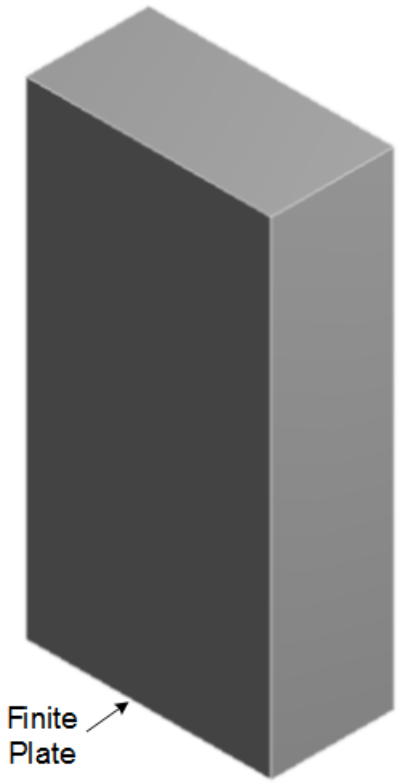

Figure 6-2 Step No. 1: Formation of un-cracked structure.

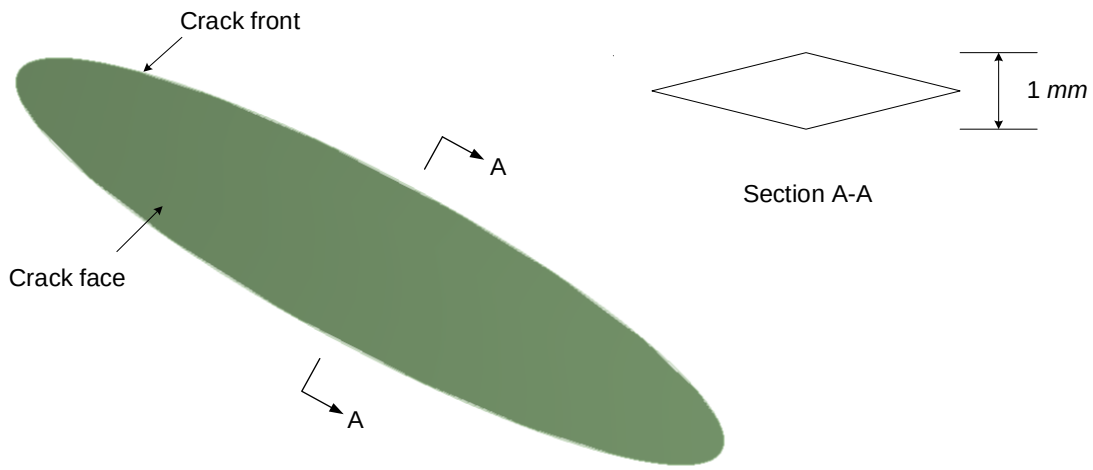

Figure 6-3 Step No. 2: Formation of crack's profile body.

6.1.3 Step No. 3: Crack Insertion in the Structure

In this step, insertion of the surface crack in the structure is made. In order to model the surface crack in finite plate, the crack's profile body was subtracted from the un-cracked finite plate. As a result, the finite plate having semi-elliptical surface crack was created which is shown in Figure 6-4.

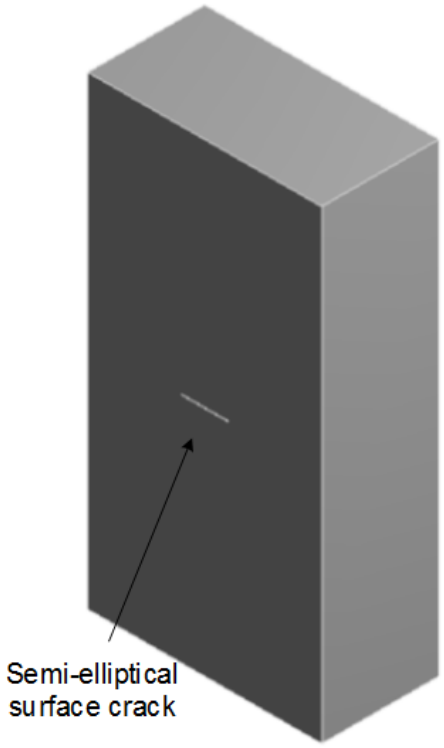

Figure 6-4 Step No. 3: Crack insertion in the structure.

6.1.4 Step No. 4: Formation of the Pallet Bodies

In this step, pallet shape bodies are generated around the crack front as shown Figure 6-5. For the formation of the pallet bodies, a tube-like volume (hereinafter called 'the tube') was swept around the crack front initially. The radius of the tube is dependent on the curvature of the crack front. The tube radius is not fixed and changes as the *'a/c'* ratio of the elliptical crack changes. The skewness (see Section 5.1) of the FE mesh around the crack front is dependent on the radius of the tube. The radius of the tube equal to 5 *mm* was taken for this fracture model which resulted a mesh of skewness equals to 0.50 around the crack front. After the successful modeling of the tube around the crack front, it was further sliced into small pallet shape bodies (hereinafter called 'the pallets'). It is due to the use of these pallets that the approach has been named the 'pallet body approach'. The pallets were generated in such a way that the ends of the pallets were perpendicular to the crack front. The local coordinate system of the pallets is shown in Figure 6-5. The divisions of the crack front and hence the number of pallets may vary in the range of zero to infinity. In this model, the crack front has been divided into 120 small segments and therefore 120 pallets have been generated around the crack front. Increasing the number of pallets will decrease the skewness value and hence will improve the mesh quality. At the end of this step, the sliced pallets were glued together.

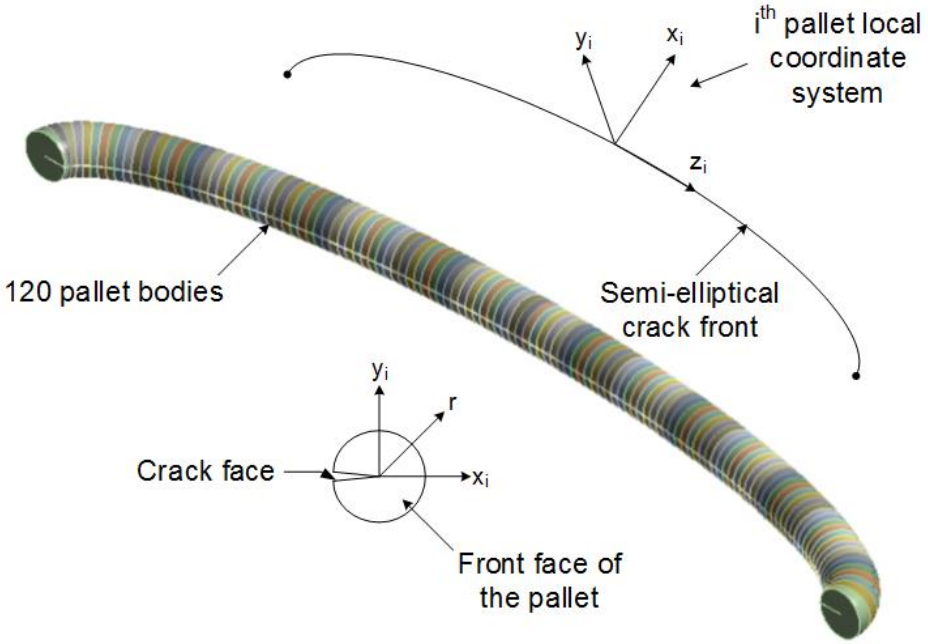

Figure 6-5 Step No. 4: Formation of the pallet bodies.

6.1.5 Step No. 5: Hexa-hedralizing the Pallets

In this step, hexa-hedralizing of the pallets is performed. For the purpose, the sweepable pallets were filled with sweep mesh using purely quadratic hexahedral or brick Solid-186 (20 node) elements. The brick elements are ordered in layers around the crack front. The skewness of the FE mesh around the crack front is also dependent upon the number of layers. In this fracture model, six layers of equal height were generated in each pallet body as shown in Figure 6-6. The first layer, around the crack front, is meshed using hexahedral wedge-shaped (20-node collapsed quarter point) singular elements which exhibit $1/\sqrt{r}$ behaviour where '*r*' is the distance from the crack front as shown in Figure 6-5. The singular elements are essentially required as the stress and strain fields around the crack front generally have high gradients. The stresses and strains are singular at the crack front that are varying as $1/\sqrt{r}$. To capture such singularities in stresses and strains, singular elements around the crack front are inevitably required.

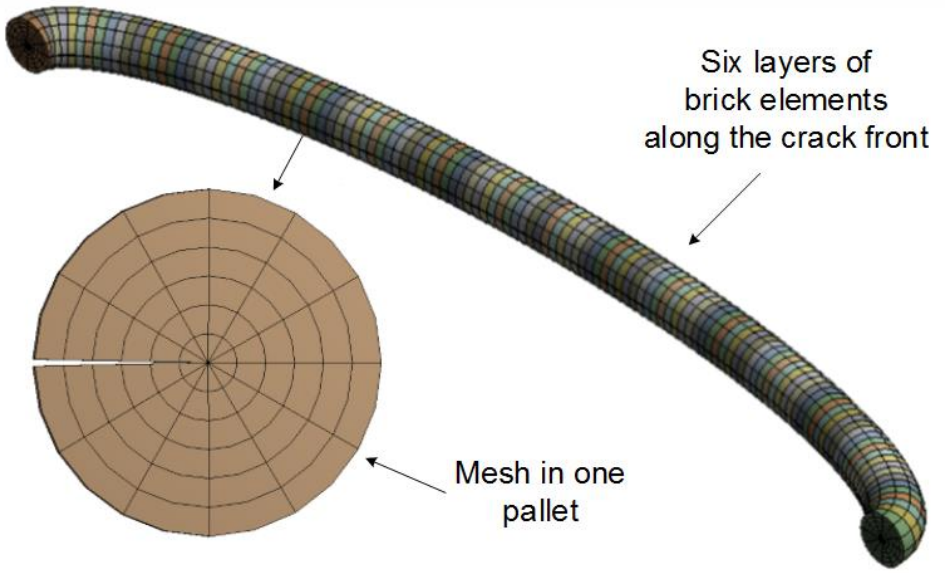

Figure 6-6 Step No. 5: Hexa-hedralizing the pallets.

6.1.6 Step No. 6: Tetra-hedralizing the Remaining Structure

In this step, the remaining volume except the tube containing pallets is meshed using quadratic tetrahedral Solid-187 (10 node) elements as shown in Figure 6-7. Free mesher of the 'ANSYS Mechanical' module will create the tetrahedral mesh in the remaining structure.

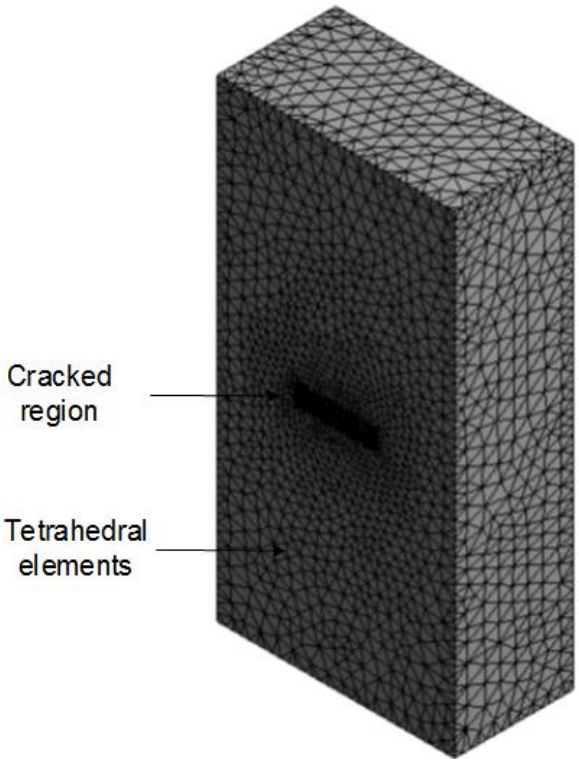

Figure 6-7 Step No. 6: Tetra-hedralizing the remaining structure.

Once the layers of higher order brick elements are generated around the crack front, these layers can be used as the volumes for J-integral evaluation which is carried out by the fracture tool in 'ANSYS Mechanical'. The J-Integral evaluation is based on the domain integral method as developed by Shih et al. [85]. The domain integration formulation applies volume integration for 3-D problems to calculate J-Integral. Finally, stress intensity factor along the crack front can be evaluated using the expression given in Eq. (6-1) [25, 54].

$$K = \sqrt{\frac{J.E}{(1-\nu^2)}} \tag{6-1}$$

Where;

K = stress intensity factor.

J = Value of J-integral around the crack front.

E = Young's modulus of the material.

ν = Poisson's ratio of the material.

The fracture model developed using the 'pallet body approach' has been given the name as the 'pallet body fracture model'.

6.2 Verification of the Pallet Body Approach

In order to validate the 'pallet body approach', the pallet body fracture models of the following two specimens were developed.

1. Semi-elliptical surface crack in finite plate (SESC-FP) specimen.
2. Semi-elliptical surface crack in thick pipe (SESC-TP) specimen.

The SIFs along the crack front in SESC-FP specimen are available in the literature and the work of Newman and Raju [6] has been considered as the definite in this regard. However, the SIFs along the crack front in SESC-TP specimen are available in ASME code [7]. M. Reytier [8] has performed an experimental work, in order to capture the crack growth beach marks and the corresponding life of the SESC-FP specimen under bending load.

The results of these three studies have been used in order to compare the 'pallet body approach' for fracture analysis. The comparison with Newman and Raju analysis and with the ASME code have been shown in Section 6.2.1 and Section 6.2.3. Moreover, the mesh independent study of the 'pallet body approach' is given in Section 6.2.2. The comparison with the work of Reytier [8] has been given in Section 6.2.4.

6.2.1 The Comparison with Newman and Raju Analysis

The semi-elliptical surface crack in finite plate (SESC-FP) specimen has been shown in Figure 6-1. The empirical relationship for the evaluation of SIFs in SESC-FP specimen, proposed by Newman and Raju [6], is given in Eq. (6-2).

$$K_I = \left(S_t + HS_b\right)\sqrt{\pi \frac{a}{Q} F\left(\frac{a}{t_p}, \frac{a}{c}, \frac{c}{b}, \phi\right)} \tag{6-2}$$

Where;

Q = Flaw shape parameter and it is equal to $Q \cong 1 + 4.593(a/c)^{1.65}$.

S_t = Remote uniform-tensile stress in SESC-FP specimen.

S_b = Remote bending stress on the outer fiber of the SESC-FP specimen.

H and F = Variables as provided by Newman and Raju in the ref. [6].

The remaining parameters in Eq. (6-2), have been described in Section 6.1. For the SESC-FP specimen, structural steel having Young's modulus '$E = 200\ GPa$' and Poisson's ratio '$\nu = 0.3$' was selected while the tensile force equal to '$T_F = 100\ MN$' was applied on the top and bottom faces of the specimen (see Figure 6-1 (a)). The 'pallet body fracture model' of the SESC-FP specimen prepared for the fracture analysis has been shown in Figure 6-7. The details of the FE mesh of the SESC-FP specimen are given in Table 6.1.

Table 6.1 Details of FE mesh of SESC-FP specimen.

Region	Element Type	No. of elements	No. of nodes	No. of layers	No. of pallets
Tube like volume around the crack front	Solid-186	8640	37189	06	120
Full model including tube like volume	Solid-186 and Solid-187	32249	70690	06	120

The SIF solutions of SESC-FP specimen computed using 'pallet body fracture model' and using Newman and Raju [6] analysis are shown in Figure 6-8 for comparison of the two approaches.

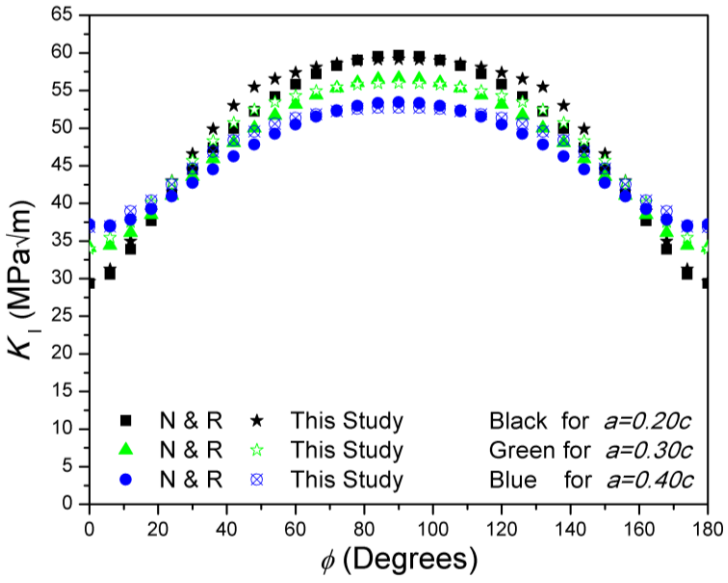

Figure 6-8 The 'pallet body approach' versus Newman and Raju [6] analysis.

The comparison has been done along the whole crack front of the semi-elliptical surface crack. The comparison between the two methods showed a good agreement and the difference between the results was maximum of 5% along the whole crack

front. It is evident from Figure 6-8 that the developed 'pallet body fracture model' also produce accurate SIFs at the edges of the crack that is at $\phi = 0^{\circ}$ or 180°. The accurate SIFs at the edges are due to the development of small pallets around the whole crack front including crack edges as shown in Figure 6-5.

6.2.2 Mesh Independent Study of SESC-FP Specimen's Fracture Model

The basic mesh independent study of the 'pallet body fracture model' of SESC-FP specimen has been presented in this section. The Figure 6-9 shows the graph of the number of nodes of the fracture model versus the SIF at the deepest point at $\phi = 90^{\circ}$ of the crack (see Figure 6-1 (b)). It is evident from the exponentially growing graph that the 'pallet body fracture model' produces mesh independent results and the SIF at 65,000 nodes is almost constant. It is due to the fact that the fracture model of SESC-FP specimen having 70690 nodes (see Table 6.1) were selected for the computations of SIFs in this study.

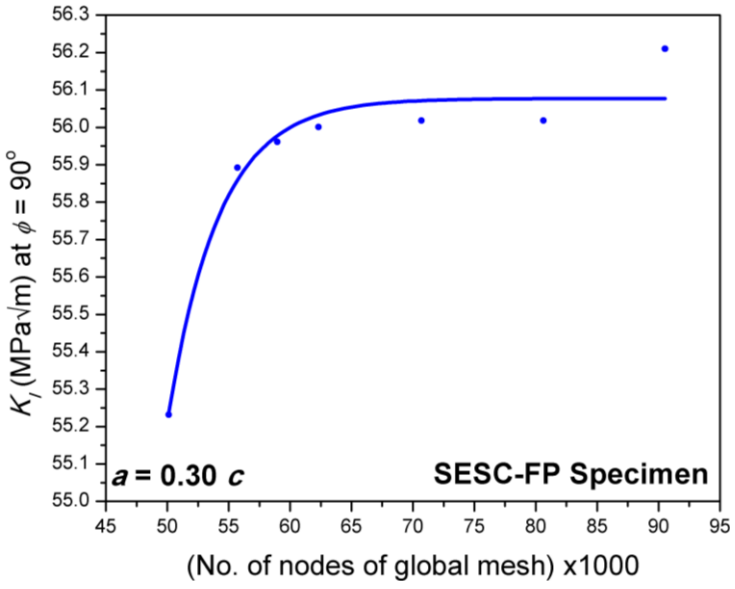

Figure 6-9 Mesh independent study of SESC-FP specimen's fracture model.

6.2.3 The Comparison with ASME Code

The semi-elliptical surface crack in thick pipe (SESC-TP) specimen is shown in Figure 6-10. It is an internally pressurized thick pipe having semi-elliptical surface crack in the radial-longitudinal plane of the pipe. The SIF at the deepest point *'A'* (See Figure 6-10 (b)) of the crack is available in Article A-3000, Section XI of the ASME

code [7]. According to ASME code, the SIF at the deepest point of the crack front can be calculated using the cubic polynomial stress relation given in Eq. (6-3).

$$K_I = \left[\left(A_o + A_p\right)G_o + A_1G_1 + A_2G_2 + A_3G_3\right]\sqrt{\frac{\pi a}{Q}} \tag{6-3}$$

Where; A_p = internal pressure if the pressure acts on the crack surface, A_i (i = 0-3) are the stress coefficients obtained from through-the-thickness stress distribution, G_i (i = 0-3) are geometrical correction factors as provided in ASME code [7].

The SESC-TP specimen given in Figure 6-10 (a), has the dimensions 'L = 4000 *mm*', 'R_i = 1000 *mm*', 't_c = 500 *mm*', 'a/c = 0.20', 'a/t_c = 0.05', 'P_{int} = 50 *MPa*'. For SESC-TP specimen, structural steel having Young's modulus 'E = 200 *GPa* and Poisson's ratio '$\nu = 0.3$' was selected. The 'pallet body fracture model' of the SESC-TP specimen prepared for the fracture analysis is shown in Figure 6-11. The details of the FE mesh of SESC-TP specimen are given in Table 6.2.

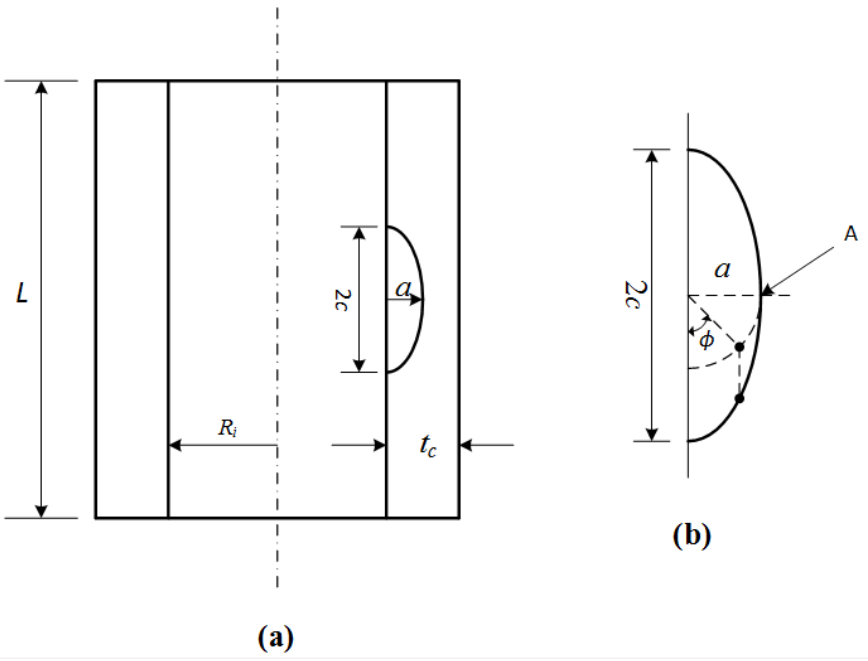

Figure 6-10 (a) Semi-elliptical surface crack in thick pipe (b) Crack tip position parameters.

The comparison of the 'pallet body fracture model' with the method described in ASME code was done by considering only the maximum SIF value at the deepest point *'A'* of the surface crack, since ASME code presents SIF solution only at the deepest point of the surface crack in thick pipe. The SIF solutions of SESC-TP

specimen computed using 'pallet body fracture model' and using ASME code are shown in Figure 6-12 for comparison of the two approaches. The comparison between the two approaches showed a good agreement, not exceeding a difference of 4%.

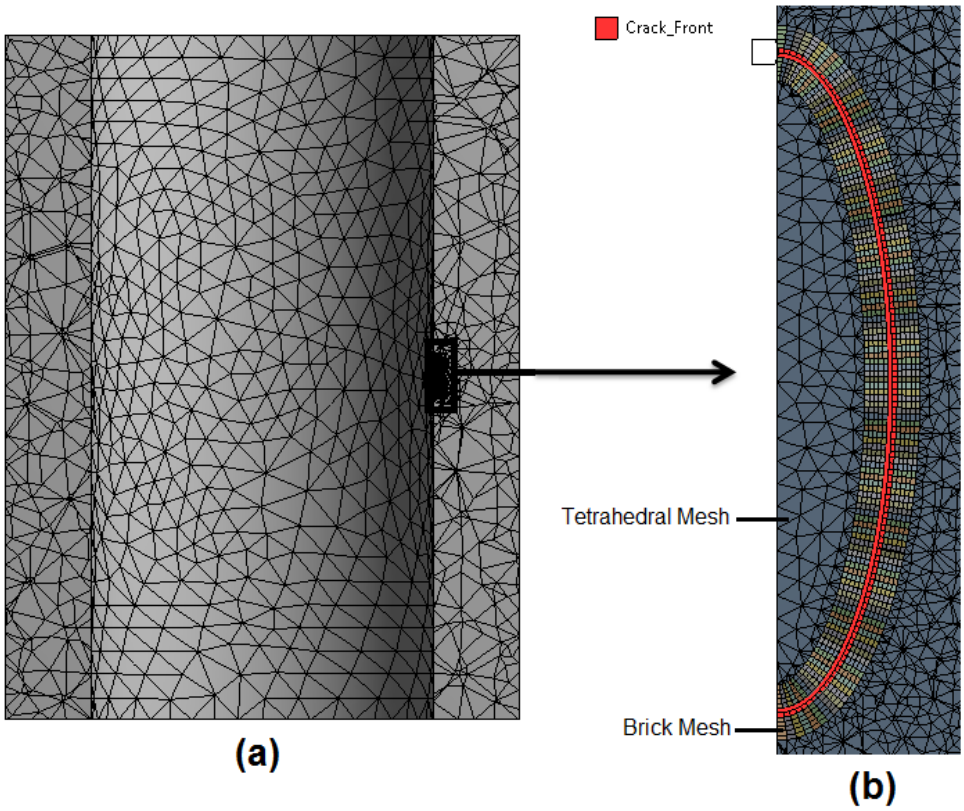

Figure 6-11 FE mesh of semi-elliptical surface crack in thick pipe (b) Close-up view of the cracked region.

Table 6.2 Details of FE mesh of SESC-TP specimen.

Region	Element Type	No. of elements	No. of nodes	No. of layers	No. of pallets
Tube like volume around the crack front	Solid-186	8640	37189	06	120
Full model including tube like volume	Solid-186 and Solid-187	32555	74509	06	120

The good agreement of the results with the standard studies gave confidence to use the developed 'pallet body approach' for complex cases such as elliptical corner surface cracks at nozzle-cylinder intersection of the RPV.

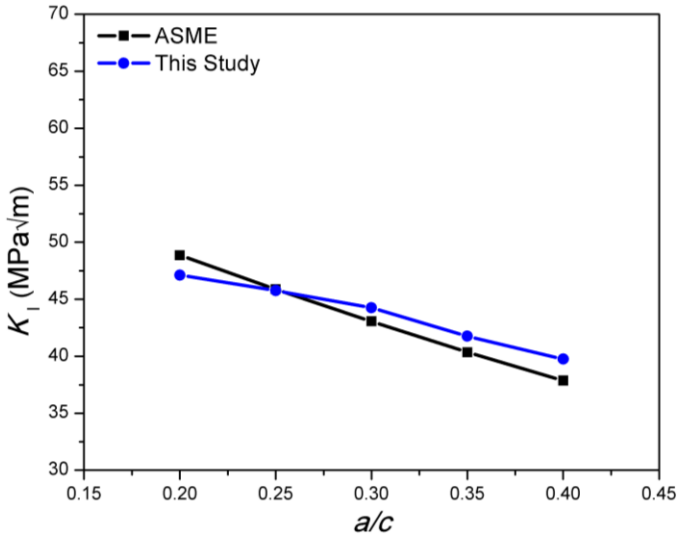

Figure 6-12 Comparison of 'pallet body approach' with the ASME code.

6.2.4 The Comparison with the Work of Reytier

Experimental Set-up by Reytier

The beach mark is one of the macroscopically visible signatures, which can be observed during the crack growth process. The Reytier [8] has captured, experimentally, the loading and unloading beach marks (hereinafter called 'the profiles') during the fatigue crack growth in SESC-FP specimen subjected to cyclic bending loadings. The schematic view of the SESC-FP specimen used in the work is shown in the Figure 6-13.

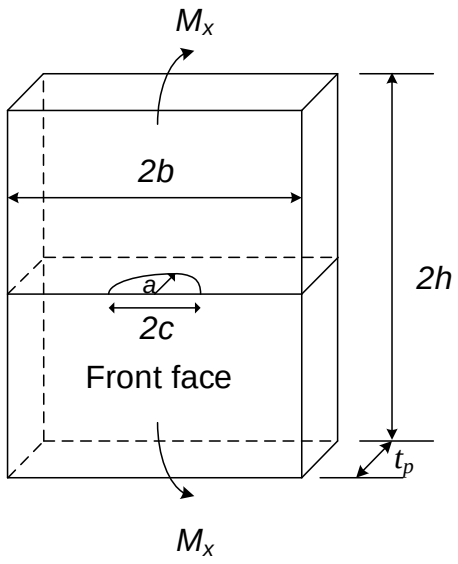

Figure 6-13 SESC-FP specimen under bending cyclic loadings.

The specimen is made of the 'martensitic *P91* steel*'*. The dimensions of the specimen are '$2b$ = 350 *mm*', '$2h$ = 590 *mm*', and 't_p = 30 *mm*'. The value of the moment 'M_x = 14.450 *KN*' was applied on the upper and lower faces of the specimen as shown in Figure 6-13. The applied moment generates tangential bending stresses $'\Delta\sigma_b = 284.6 \text{ MPa}'$ and $'\Delta\sigma_b = -284.6 \text{ MPa}'$ in the front face and the bottom face (opposite of front) of the specimen, respectively.

The Reytier has followed the crack growth starting from a pre-crack with dimensions $a_1 = 6.9\ mm,\ c_1 = 124\ mm$ in the specimen. The *'a_1'* and *'c_1'* are the initial minor and major axis of the surface crack. In his experiment, the Reytier [8] has used the Paris Law [78] given in Eq. (6-4), as a crack growth model.

$$\frac{da}{dN} = C(\Delta K)^n \tag{6-4}$$

Where;

ΔK = Range of SIF in $MPa\sqrt{m}$.

da/dN = Crack growth rate in *mm/cycles*.

C = Material intercept constant relating crack growth rate to stress-intensity range and crack size.

n = Material constant equal to the slope of the 'log *da/dN*' versus 'log *ΔK'* curve.

The 'martensitic P*91* steel' has crack growth related properties $C = 7.1\times10^{-7}$, n =1.85 and mechanical properties $E = 160\ GPa,\ \nu = 0.3$ [8]. Using these material properties, the Paris law given in Eq. (6-4) can be re-written in the form of Eq. (6-5).

$$\frac{da}{dN} = 7.1\times10^{-7}\left(\Delta K\right)^{1.85} \tag{6-5}$$

The Reytier has captured the crack growth surface and the corresponding life to approach the final crack in his experiment as shown in Figure 6-14 and Figure 6-15, respectively.

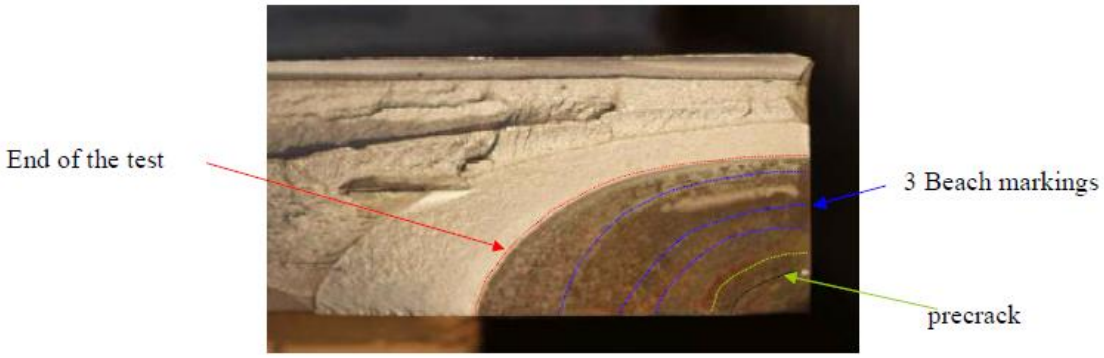

Figure 6-14 Fracture surface captured by Reytier [8].

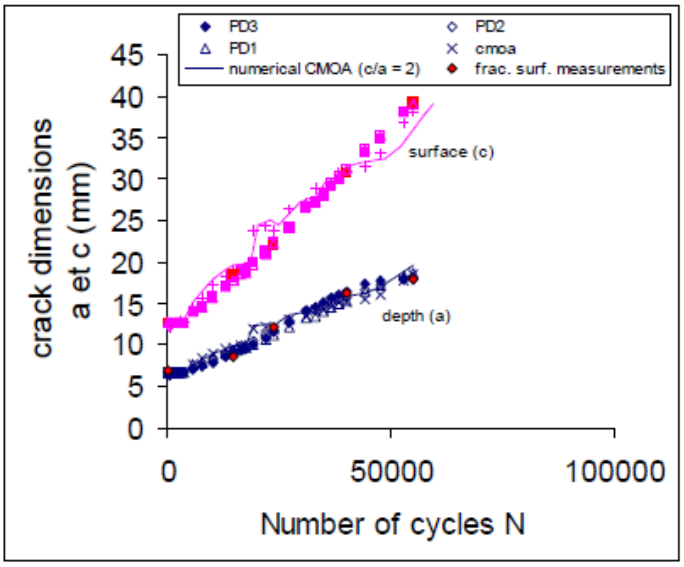

Figure 6-15 Life in fatigue cycles for crack growth estimated by Reytier [8].

The Computational Crack Growth's Model

In this study, the crack growth profiles and the corresponding life have been captured using the stress intensity factors (SIFs) computed by the 'pallet body approach' proposed in the Section 6.1 above. The same (as set by Reytier) SESC-FP specimen and the loading conditions were used for the comparison. The similar type of finite element fracture model, of the specimen, as shown in the Section 6.1 was used for this analysis. In the 'pallet body fracture model' of SESC-FP specimen, the crack front was decomposed into 120 small pallets (see Figure 6-5). Each pallet has a nodal point at the start and at the end of the pallet and hence 121 nodal points were arranged along the complete crack front.

For starting the computations the pre-crack ($a_1 = 6.9\ mm,\ c_1 = 124\ mm$) in the finite plate was modeled initially. The SIF at all the 121 nodal points of the crack front were computed using the pallet body approach. The nodal point, which has the maximum SIF, has been named as the 'leading node'. If the advancement of the leading node is assumed then the corresponding advancement of all other nodes along the crack front (profile) can be determined using the model [61, 62] given in Eq. (6-6).

$$\Delta a_i^j = \Delta a_{\max}^j \left(\frac{\Delta K_i^j}{\Delta K_{\max}^j} \right)^n \tag{6-6}$$

Where;

Δa_i^j = Advancement of *'i_{th}'* node on the a *'j_{th}'* crack profile.

$\Delta a_{\max}^j$ = Advancement of the 'leading node' on a *'j_{th}'* crack profile.

ΔK_i^j = Range of SIF at *'i_{th}'* node on *'j_{th}'* crack profile.

$\Delta K_{\max}^j$ = Range of SIF at the 'leading node' on the *'j_{th}'* crack profile.

Once the advancements of all the nodal points along the crack front are computed, then the new crack front (crack profiles) can be plotted from the data. As already mentioned that the advancement of the 'leading node (*Δa_{max}*)' is the input information for each iteration. The smaller the value one assigns to *'Δa_{max}'*, the better results can be achieved at the cost of increase in number of iterations. The values of *'Δa_{max}'* used for this analysis are given in Table 6.3. Computations of the all crack profiles up to the final crack front completes one iteration of the crack growth. More iterations are recommended in order to check the convergence of the captured crack profiles especially where experimental data is not available.

Table 6.3 Advancement of the Leading Node.

Crack Profiles	Formula	Δa_{max}
1st to 10th	a_1 / 10	0.7 *mm*
11th to 15th	a_{10} / 10	1.0 *mm*
16th to 19th	a_{15} / 10	1.3 *mm*
20th to 26th	a_{19} / 10	1.5 *mm*

Using the Eq. (6-6) and the data given in Table 6.3, the 26 crack profiles were computed during the crack growth. The dimensions of all the 26 cracks profiles are given in Table 6.4. The crack profiles are also shown graphically in Figure 6-16.

The SIFs along the whole crack fronts of all the 26 crack profiles have also been given in Figure 6-17. It is clear from the patterns of SIFs that during the crack growth process, the SIF at edge ($\phi = 0^\circ$ or 180°) of the crack increases while it decreases at the depth ($\phi = 90^\circ$) of the crack. This means that the crack grows faster in the direction of major axis than the minor axis.

Table 6.4 Dimensions of the crack profiles during crack growth.

Profile No.	**1**	**2**	**3**	**4**	**5**	**6**	**7**	**8**	**9**
a (mm)	6.900	7.322	7.719	8.094	8.451	8.792	9.119	9.434	9.736
c (mm)	12.400	12.886	13.372	13.858	14.344	14.83	15.316	15.802	16.288
Profile No.	**10**	**11**	**12**	**13**	**14**	**15**	**16**	**17**	**18**
a (mm)	10.100	10.659	11.184	11.678	12.151	12.606	13.252	13.85	14.407
c (mm)	16.895	17.868	18.844	19.82	20.793	21.764	23.222	24.682	26.145
Profile No.	**19**	**20**	**21**	**22**	**23**	**24**	**25**	**26**	
a (mm)	14.929	15.584	16.187	16.753	17.28	17.772	18.233	18.666	
c (mm)	27.609	29.564	31.522	33.479	35.439	37.399	39.366	41.334	

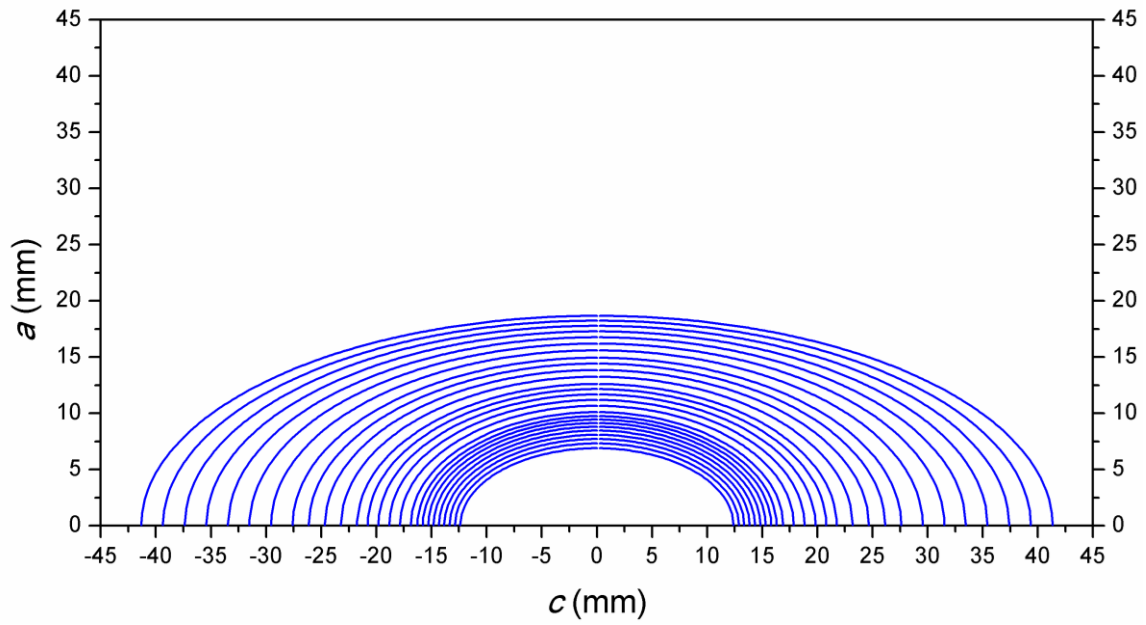

Figure 6-16 Crack profiles predicted during crack growth simulations.

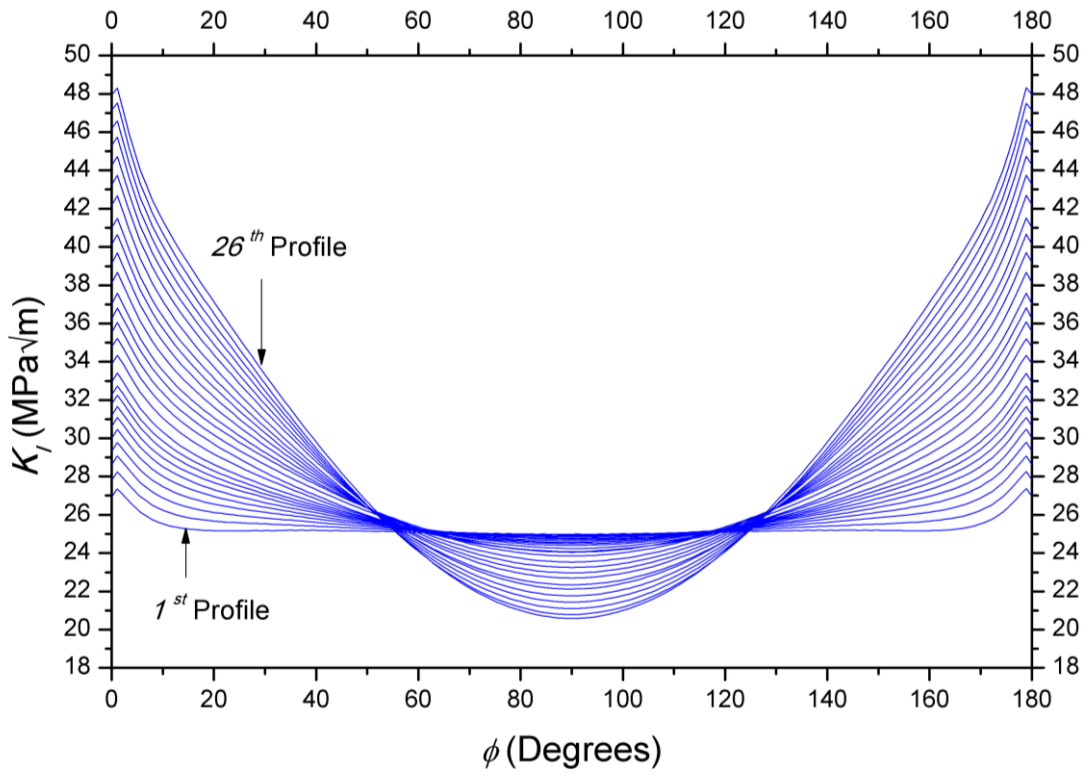

Figure 6-17 SIFs along all the 26 crack profiles.

The computationally captured crack profiles have been compared with the experimentally observed crack growth profiles by Reytier [8]. For the comparison, the computationally captured crack profiles have been placed beside the experimentally captured crack profiles in Figure 6-18. The comparison showed a very good agreement between the profiles captured by two methods.

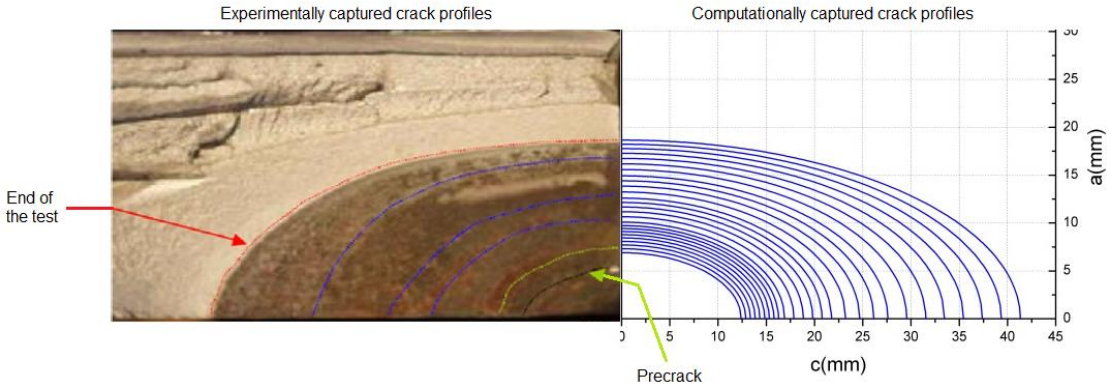

Figure 6-18 Comparison of the beach marks.

The Computational Crack's Life Predictions Model

The Paris Law given in Eq. (6-4), can be converted into a form suitable for calculating the crack growth cycles between the two consecutive crack profiles: the *'j_{th}'* and the *'$(j+1)_{th}$'*. By the integration of the Eq. (6-4), the number of loading and unloading cycles in between the two consecutive crack profiles can be rearranged as [61]:

$$\Delta N_j^{j+1} = \int_j^{j+1} \frac{da}{C\Delta K^n} = \frac{1}{C}\int_j^{j+1} \Delta K^{-n}.da \tag{6-7}$$

Assuming a linear function for the range of stress intensity factor $'\Delta K = A + B.a'$, the Eq. (6-7) can be re-written as:

$$\Delta N_j^{j+1} = \frac{1}{C}\int_j^{j+1} (A+B.a)^{-n}.da = \frac{1}{C}.\frac{(A+B.a)^{1-n}}{(1-n).B}\Bigg\|_j^{j+1} \tag{6-8}$$

Hence,

$$\Delta N_j^{j+1} = \left\{\frac{\left(A+B.a_{j+1}\right)^{(1-n)}}{C.B.(1-n)}\right\} - \left\{\frac{\left(A+B.a_j\right)^{(1-n)}}{C.B.(1-n)}\right\} \tag{6-9}$$

where *'A'* and *'B'* are constants which can be determined by solving the following linear system of equations.

$$\begin{aligned} \Delta K_i^{j+1} &= A + B.a_{j+1} \\ \Delta K_i^{j} &= A + B.a_j \end{aligned} \tag{6-10}$$

Where;

'a_j' and *'a_{j+1}'* are the minor axis or depth of *'j_{th}'* and *'$(j+1)_{th}$'* crack fronts

ΔK_i^j = Range of SIF at *'i_{th}'* node on *'j_{th}'* crack profile.

ΔK_i^{j+1} = range of SIF at *'i_{th}'* node on *'$(j+1)_{th}$'* crack profile.

The Eq. (6-9) will give the life between the two consecutive crack profiles. The incremental life till the 26th crack's profile (see Table 6.4) was computed and then summed together to get the accumulated fatigue life of the component. For the comparison with the work of the Reytier [8], the accumulated fatigue loading cycles versus crack dimensions have also been plotted graphically as shown in as shown in

Figure 6-19. It is evident from the comparison that the anticipated fatigue life is in admirable agreement with the experimental data.

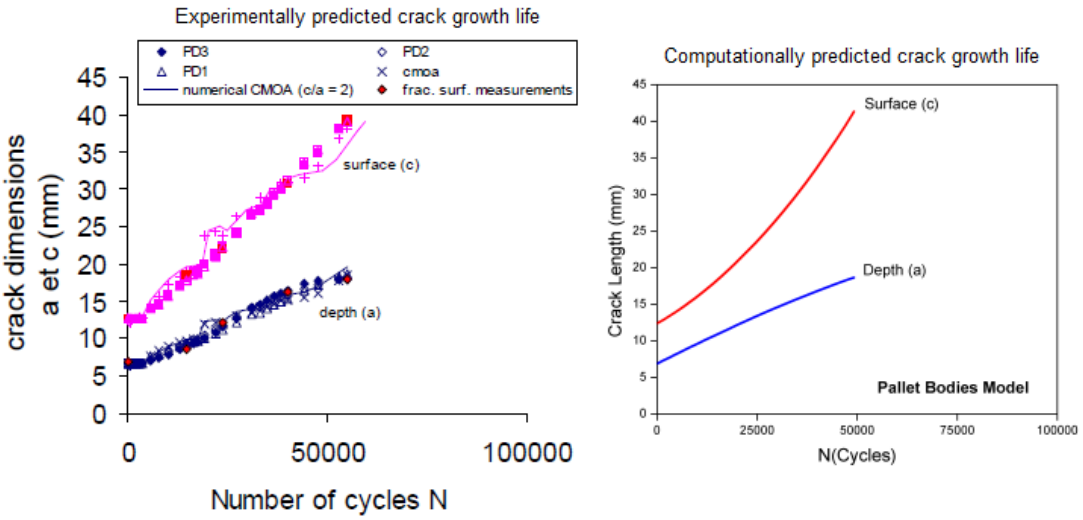

Figure 6-19 Comparison of the crack dimensions during growth.

Hence, the stress intensity factors computed using the pallet body approach are the accurate and can be used with confidence for the prediction of crack's profiles and the corresponding life of the component during the growth of the crack.

6.3 Fatigue Crack Growth in the RPV

The computations of the crack's profiles and the corresponding fatigue life of the component presented in Section 6.2.4, was performed in order to validate the 'pallet body approach' for crack assessment. However, the procedure presented can be used for the fatigue crack growth of the corner cracks at the nozzle-cylinder intersection of the reactor pressure vessel (see Ch. 5). The life estimation of the RPV in the presence of the manufacturing defect, which is one of the future works of this thesis (see Section 9.3), can be performed using the pallet body approach and the fatigue crack growth model for RPV's steel (*SA-508 Gr.3 Cl.1*). The fatigue crack growth model of the vessel's exposed to the pressurized water reactor's environment at $288\ ^{\circ}C$ is available in the ASME code [86]. The model is reproduced here in Eq. (6-11), for the reference.

$$\frac{da}{dN} = C_{\circ}(\Delta K)^{n} \tag{6-11}$$

Where;

$$C_{\circ} = 2.13\times10^{-6} S$$

$$n = 1.95$$

and '*S'* is the scaling constant and is given by

S = 1.0 for $0 \le R \le 0.25$

= (3.75 R + 0.06) for $0.25 < R < 0.65$

= 2.5 for $0.65 \le R \le 1.0$

and *'R'* is the stress ratio which is given by

$$R = \frac{K_{\min}}{K_{\max}}$$

6.4 Summary of the Chapter

This chapter proposes a 'pallet body approach' for three dimensional crack's assessment in ANSYS Workbench. The approach is capable of computing stress intensity factors of the crack. The approach has been validated by comparing the SIFs in different styles with the work of Newman and Raju [6], the ASME code [7], and the Reytier [8]. The comparison showed admirable agreement with the studies. The difference of the approach with the Newman and Raju and the ASME code is within 5% and 4%, respectively. It has also been demonstrated that the pallet body fracture model can be used for the computations of the crack profiles and the corresponding life of the component during the process of fatigue crack growth.

7 Fracture Mechanics Analysis of the Set-in Nozzle

In this chapter, fracture mechanics analysis of the optimized set-in nozzle has been performed under normal operating conditions, SB-LOCA conditions, and RST conditions of the plant. The basic assumption behind this chapter is that the optimized nozzle-cylinder intersection of the vessel contains a corner crack. The crack may be a manufacturing defect or it may appear, during the operation of the vessel, at the highest stress concentration point of the nozzle. The motivation behind this analysis is that whether such cracks can be tolerated or not; and if they can be tolerated then what is the dimension of the critical crack depth under the various loading conditions.

For the purpose, a wide range of corner surface cracks of various dimensions was postulated at the nozzle-cylinder intersection of the vessel. The limits of the cracks were '$0.01 < a/t < 0.25$' and '$0.33 < a/c < 1.0$', where *'a'* and *'c'* represent minor and major axis of the crack respectively; and '*t'* is the thickness of the vessel wall at the nozzle-cylinder intersection. The value of *'t = 400 mm'* as shown in Figure 4-2. The stress intensity factors (SIFs) of all the corner cracks have been computed numerically using the 'pallet body fracture model' of the RPV under the normal as well as the accidental conditions of the plant. For the determination of critical crack depth, SIFs of the corner cracks were compared with the fracture toughness value of the vessel's steel which is *'SA-508 Gr.3 Cl.1'*. Both the linear elastic and elastic plastic material models were used in order to compute linear elastic fracture mechanics (LEFM) based SIFs (K_I) and elasto-plastic fracture mechanics (EPFM) based SIFs (K_J) of the cracks. It has been demonstrated, in this study, that the LEFM based SIFs are not sufficient for fracture evaluation of the vessel, and the EPFM based SIFs are essentially required for such analysis. In this thesis, SIFs for the wide range of corner cracks under various loading conditions have been presented in a suitable graphical format that provides a useful tool for the fracture mechanics analysis of the RPV.

7.1 Fracture Mechanics Analysis under Normal Operating Conditions

The design pressure of the RPV is equal to 17.16 *MPa* (see Section 0) and it is taken as the internal pressure of the vessel under normal operating conditions of the plant. The coolant of the reactor enters into the vessel (after releasing heat in steam generator) at around $288\ ^{\circ}C$ [69] through the set-in nozzle. Hence, the temperature at the inner surface of the set-in nozzle is taken equal to $288\ ^{\circ}C$ under normal operating conditions of the plant. In this section, the temperature gradient along the vessel wall, in the radial direction of the vessel, was neglected and hence only pressure loadings at $288\ ^{\circ}C$ were applied. However, the effects of such temperature gradient on the SIFs of the corner cracks have been investigated separately and will be presented in the Chapter 8.

Table 7.1 The sets of the corner cracks.

Set of corner cracks	Depth of corner crack	Elliptical cracks	Circular cracks
1	a/t = 0.01	a/c = 0.33, a/c = 0.40 a/c = 0.50, a/c = 0.60 a/c = 0.70, a/c = 0.80 a/c = 0.90	a/c = 1.00
2	a/t = 0.05	a/c = 0.33, a/c = 0.40 a/c = 0.50, a/c = 0.60 a/c = 0.70, a/c = 0.80 a/c = 0.90	a/c = 1.00
3	a/t = 0.10	a/c = 0.33, a/c = 0.40 a/c = 0.50, a/c = 0.60 a/c = 0.70, a/c = 0.80 a/c = 0.90	a/c = 1.00
4	a/t = 0.15	a/c = 0.33, a/c = 0.40 a/c = 0.50, a/c = 0.60 a/c = 0.70, a/c = 0.80 a/c = 0.90	a/c = 1.00
5	a/t = 0.20	a/c = 0.33, a/c = 0.40 a/c = 0.50, a/c = 0.60 a/c = 0.70, a/c = 0.80 a/c = 0.90	a/c = 1.00
6	a/t = 0.25	a/c = 0.33, a/c = 0.40 a/c = 0.50, a/c = 0.60 a/c = 0.70, a/c = 0.80 a/c = 0.90	a/c = 1.00

For the fracture mechanics analysis under normal operating conditions, forty-eight corner cracks were postulated at the optimized nozzle-cylinder intersection of the

vessel. For presentation of the SIFs of the cracks in a suitable graphical format, the cracks have been divided into six sets. Each set has a different *'a/t'* ratio. In each set of the cracks, there are eight different cracks of different aspect ratio (*a/c*). Each set has seven elliptical corner cracks ($a/c \neq 1.0$) and one circular corner crack (*a/c* =1.0). The details of the sets of the corner cracks is given in Table 7.1.

7.1.1 Hoop Stresses in the RPV

The hoop stress distributions in the un-cracked RPV with the optimized set-in nozzle under the normal operating conditions have been computed using the FE model presented in Figure 5-1 (b). It is evident from the stress distributions that the optimized nozzle-cylinder intersection is the highest stress concentration point (HSCP) of the nozzle as well as of the RPV. This HSCP was selected for the fracture mechanics analysis of the nozzle.

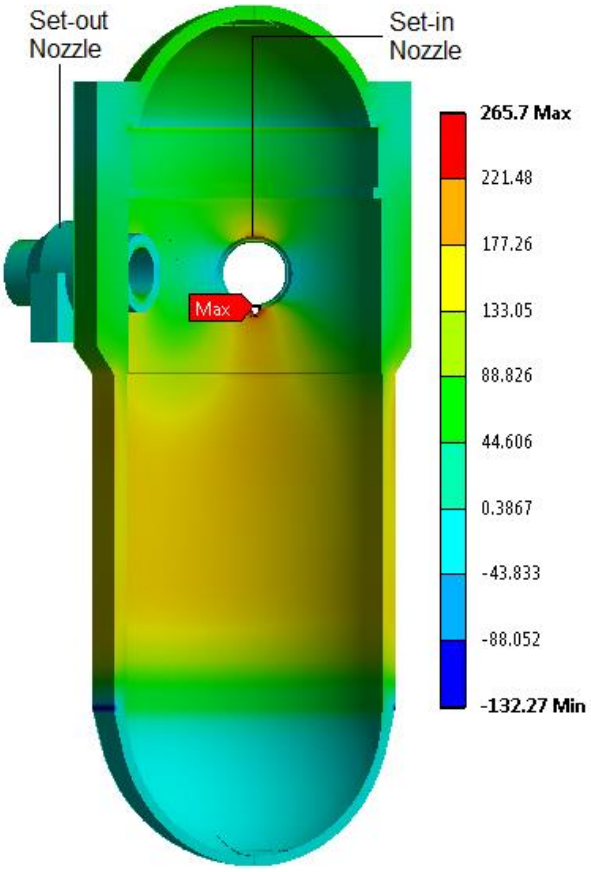

Figure 7-1 The hoop stress distributions *(MPa)* in RPV.

7.1.2 The Pallet Body Fracture Model of the RPV

The orientation of the corner cracks, at the nozzle-cylinder intersection of the vessel, is shown in Figure 7-2 (a). The postulated corner cracks are normal to the maximum

principal stress (hoop stress) of the vessel. The crack tip position parameters which are '*a*, *c*, and ϕ' are shown in Figure 7-2 (b).

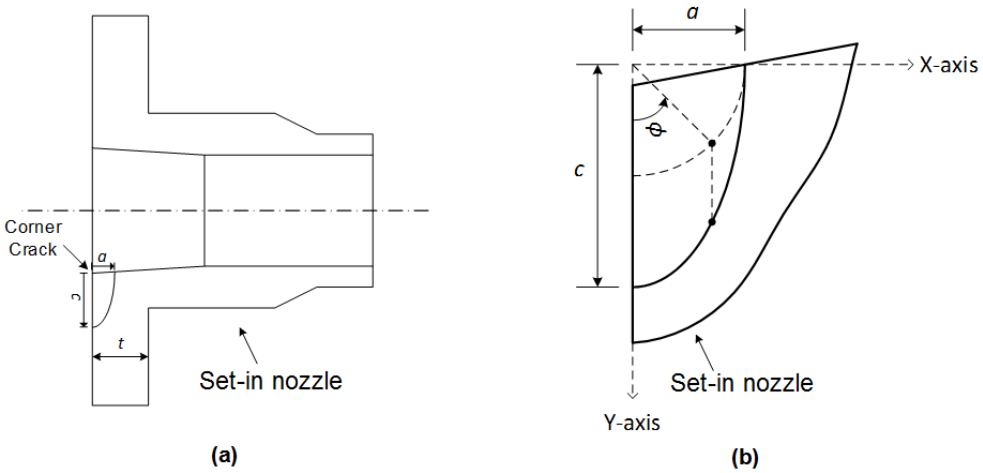

Figure 7-2 (a) Orientation of the corner crack (b) Crack tip position parameters.

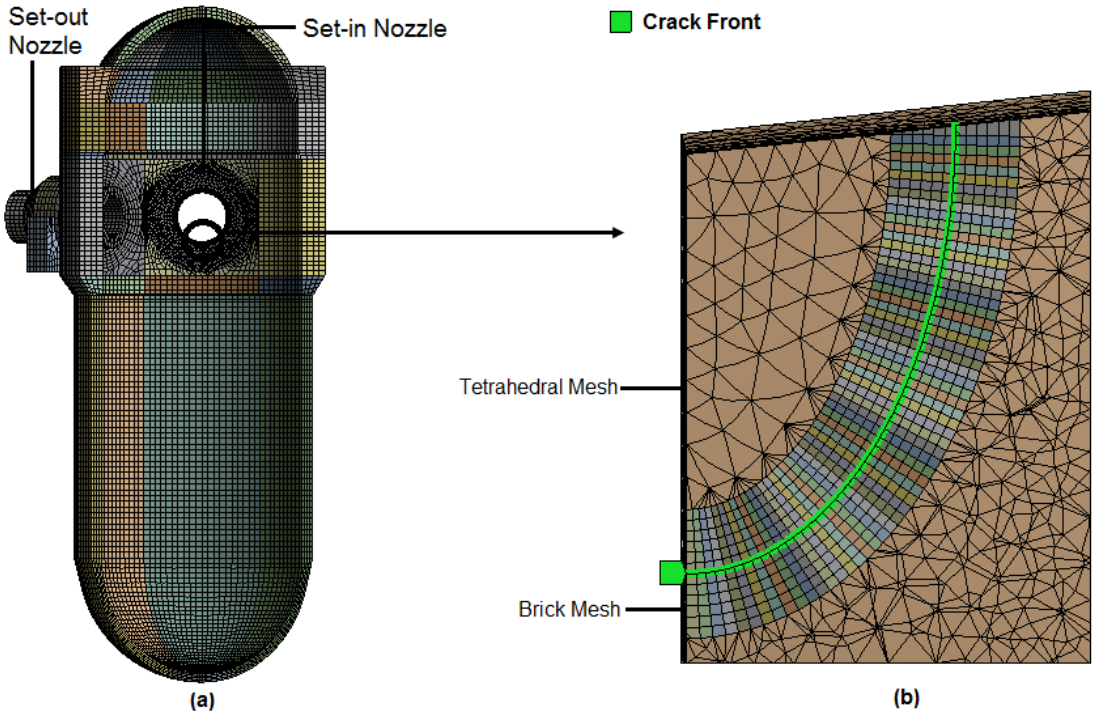

Figure 7-3 (a) The pallet body fracture model of the RPV (b) Close-up view of cracked region.

The 'pallet body fracture model' developed for the RPV having corner crack (a = 0.25t and a = 0.50c) at nozzle-cylinder intersection is shown in Figure 7-3 (a). The close-up view of the cracked region is shown in Figure 7-3 (b). The details of the fracture model are given in Table 7.2.

Table 7.2 Details of the 'pallet body fracture model' of the RPV.

Region	Element Type	No. of elements	No. of nodes	No. of layers	No. of pallets
The Tube around the crack front	Solid-186	4320	18709	06	60
Half of the RPV including the tube	Solid-186 and Solid-187	78459	171308	06	60

7.1.3 The LEFM Based SIFs under Normal Operating Conditions

The LEFM based SIFs under only pressure loading (K_{IN}^{p}) for all the corner cracks listed in Table 7.1 have been computed and are being presented in Figure 7-4 (a-f). The linear elastic material model at $288\ ^{\circ}\mathrm{C}$ (see Table 4.1) were used for these LEFM based SIFs computations. Figure 7-4 (a), (b), (c), (d), (e) and (f) present the LEFM based SIFs of the cracks having minor axis *(a)* equal to 1 percent, 5 percent, 10 percent, 15 percent, 20 percent and 25 percent of the wall thickness (*t*), respectively.

It is evident from Figure 7-4 (a-f) that all the elliptical corner cracks have varying SIF along the crack front (from $\phi = 0^{\circ}$ to 90°). However, the circular corner cracks have almost constant SIFs along the crack fronts. It is also evident that as the '*a/c'* ratio increases (for all values of '*a/t'*), SIF at $\phi = 0^{\circ}$ also increases while SIF at $\phi = 90^{\circ}$ decreases. The maximum SIF of the worst crack (*a* = 0.25*t* and *a* = 0.33*c)* has value $K_{IN,\max}^{p} = 117.35\ MPa\sqrt{m}$ as shown in Figure 7-4 (f).

It is evident from the trends in Figure 7-4 (a-f) that at specific angle (which is different for each crack) the slope of SIF curve changes; and finally it gives an intersection point of the curves which actually shows that the elliptical crack is the intersection of two curvatures: the minor curvature and the major curvature of the ellipse.

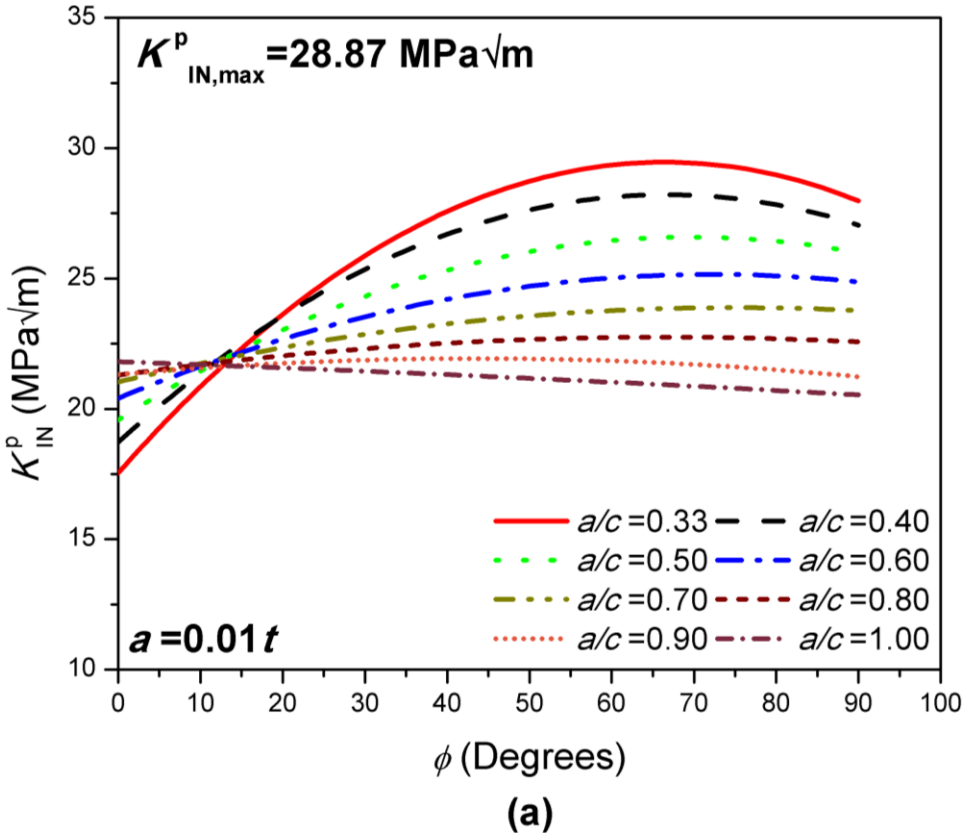

(a)

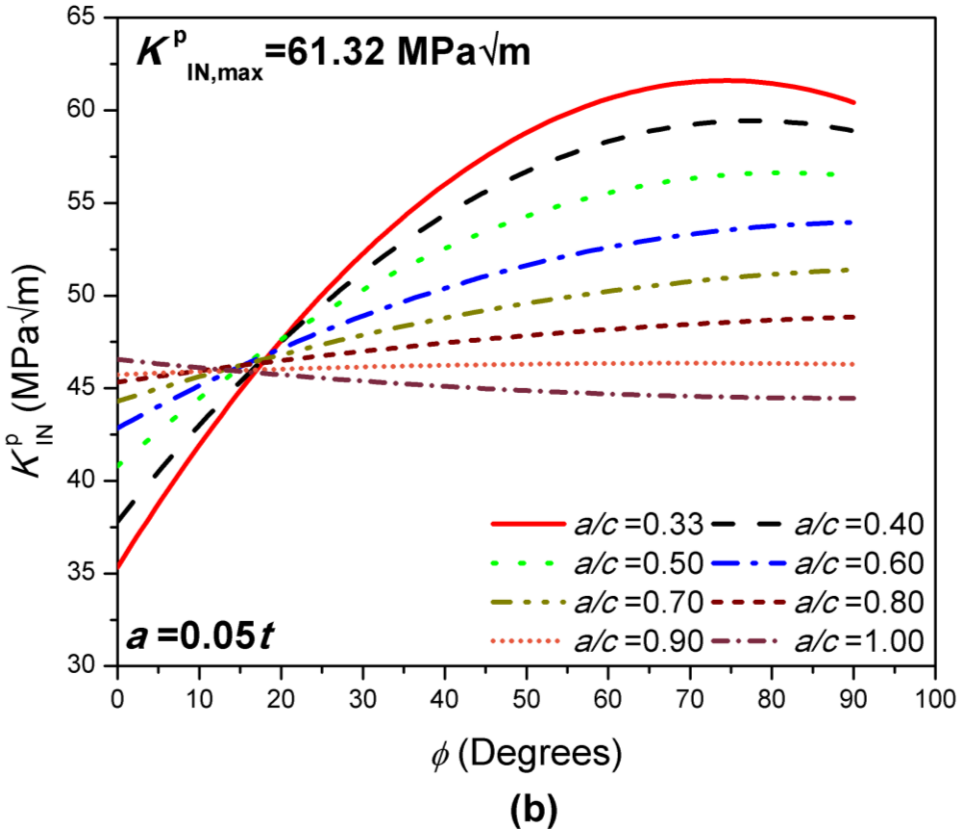

(b)

Figure 7-4 The LEFM based SIFs under normal operating conditions …

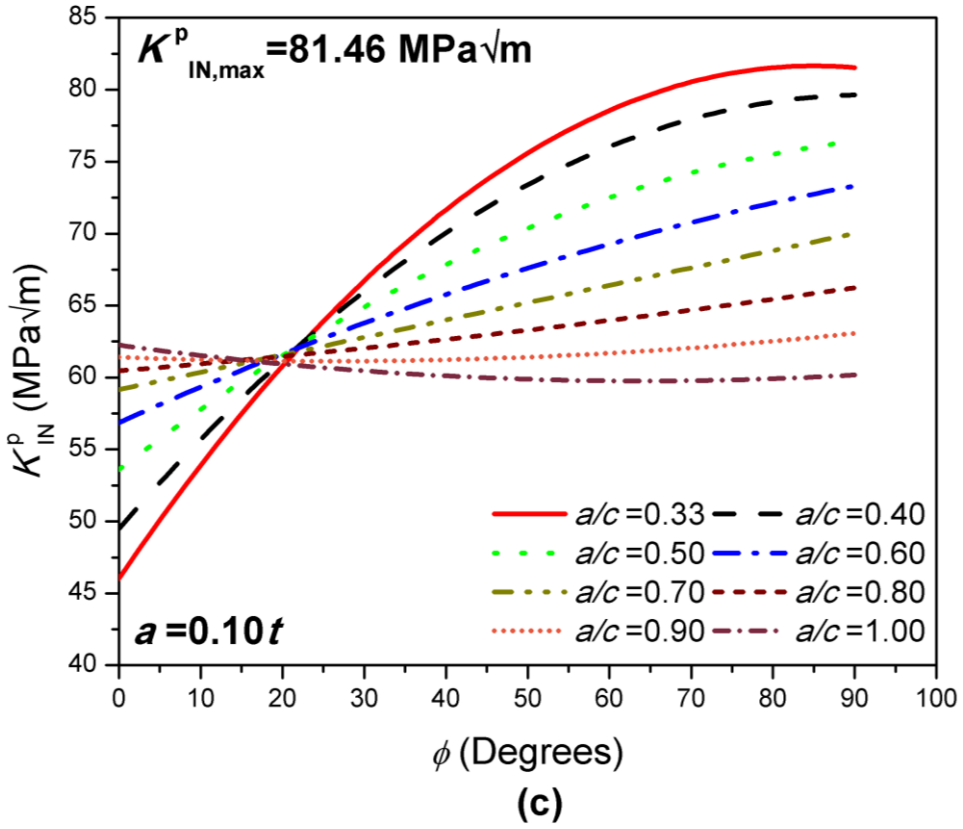

(c)

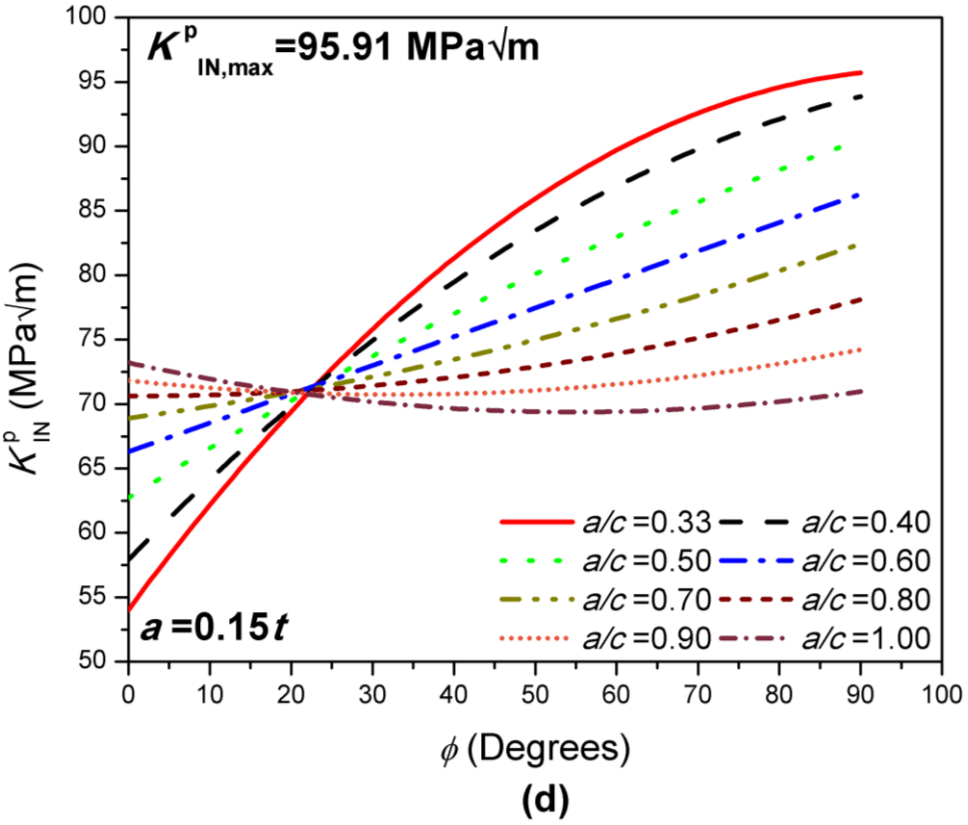

(d)

Figure 7-4 The LEFM based SIFs under normal operating conditions …

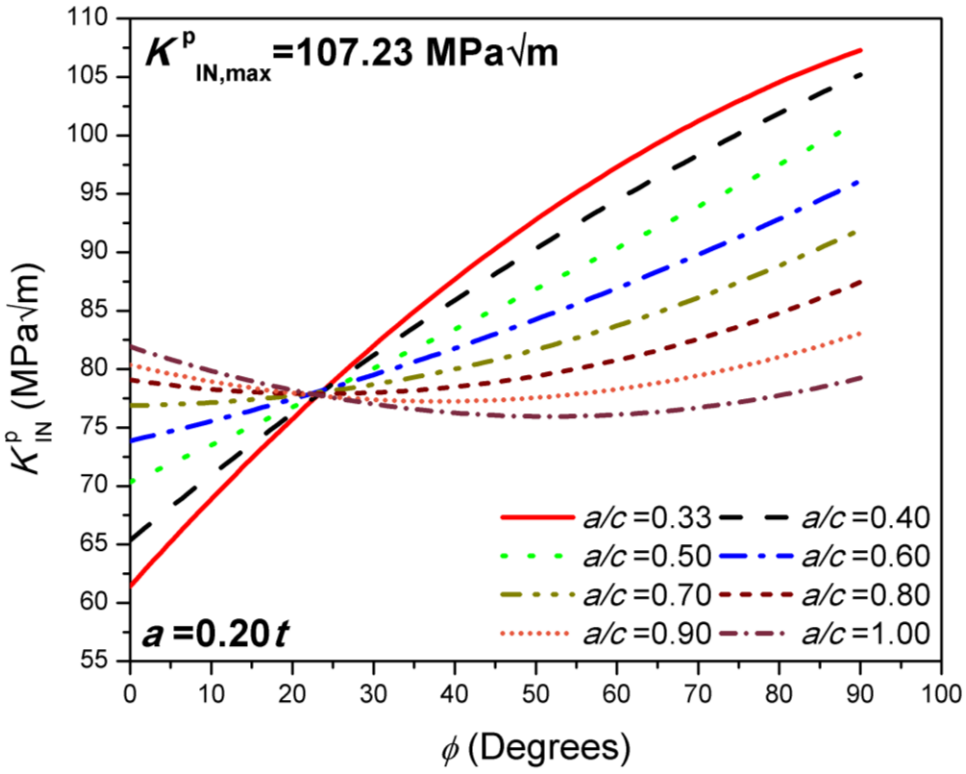

(e)

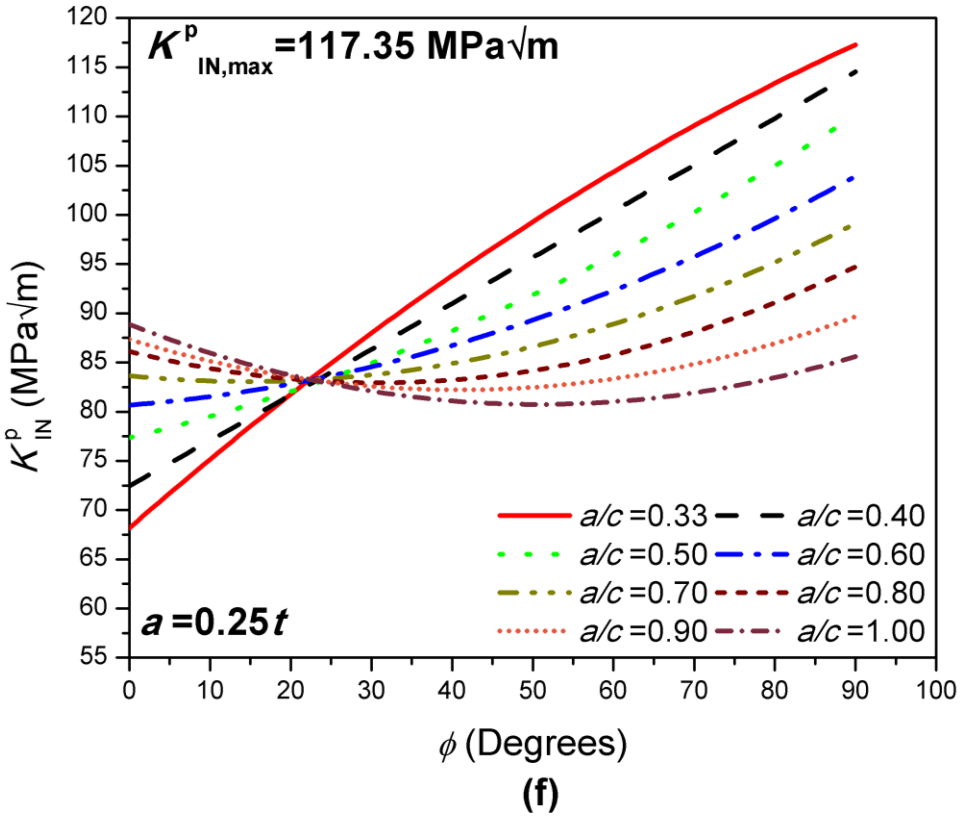

(f)

Figure 7-4 The LEFM based SIFs under normal operating conditions.

7.1.4 The Shape and Size of Plastic Zone

Using the Von-Mises yielding criterion, the size and shape of plastic zone at the minor axis ($\phi = 90^{\circ}$) of the corner crack (a = 0.25t and a = 0.50c) is presented in Figure 7-5. The yield strength (σ_{ys}) of the material *'SA-508 Gr.3 Cl.1'* at 288 $^{\circ}$C is equal to 294 *MPa* (see Table 4.1) and hence the Von-Mises stress more than 294 *MPa* generates yielding of the material.

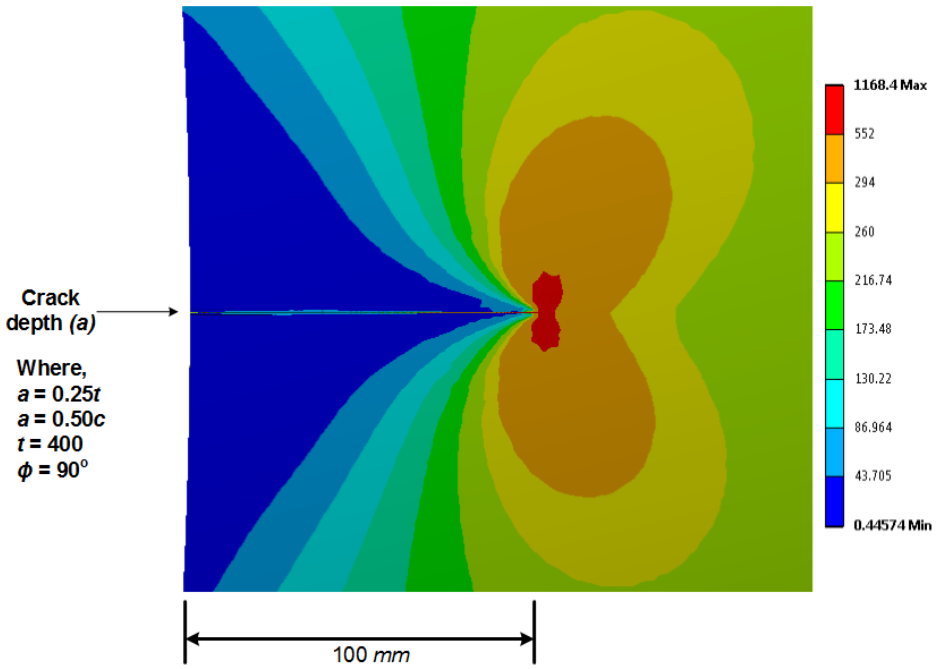

Figure 7-5 The shape and size of plastic zone using Von-Mises failure criteria.

It is evident from Figure 7-5 that the size of the plastic zone is smaller than the depth of the crack (a = 0.25t = 100 *mm*). However, the size of the plastic zone is comparable to the thickness of the vessel wall which is t = 400 *mm*. The size of the plastic zone indicates that the small scale yielding condition [54] is not satisfied in the case of RPV made of '*SA-508 Gr.3 Cl.1'* nuclear grade steel. This observation leads to the fact that the LEFM based SIFs are not sufficient solutions for the fracture evaluation of the RPV. Hence, the EPFM based SIFs are essentially required which have also been computed and are being presented in Section 7.1.6.

7.1.5 Mesh Independent Study of the RPV's Fracture Model

The basic mesh independent study of the 'pallet body fracture model' of the RPV for computing the EPFM based SIFs was also conducted. For the demonstration, corner

crack having dimensions 'a = 0.25t' and 'a = 0.33c' was taken and SIF at $\phi = 90^{\circ}$ of the crack has been presented in Figure 7-6. The exponentially growing trend of the SIF was achieved with increase in number of nodes as shown in Figure 7-6. It can be concluded from the graph that the 'pallet body fracture model' used for evaluation of SIFs yields good converging or mesh independent results. The 'pallet body fracture model' having global nodes 171308 (see Table 7.2) were used for the computations of the SIFs. It is evident from Figure 7-6 that the fracture model of RPV having 171308 nodes yields converged results.

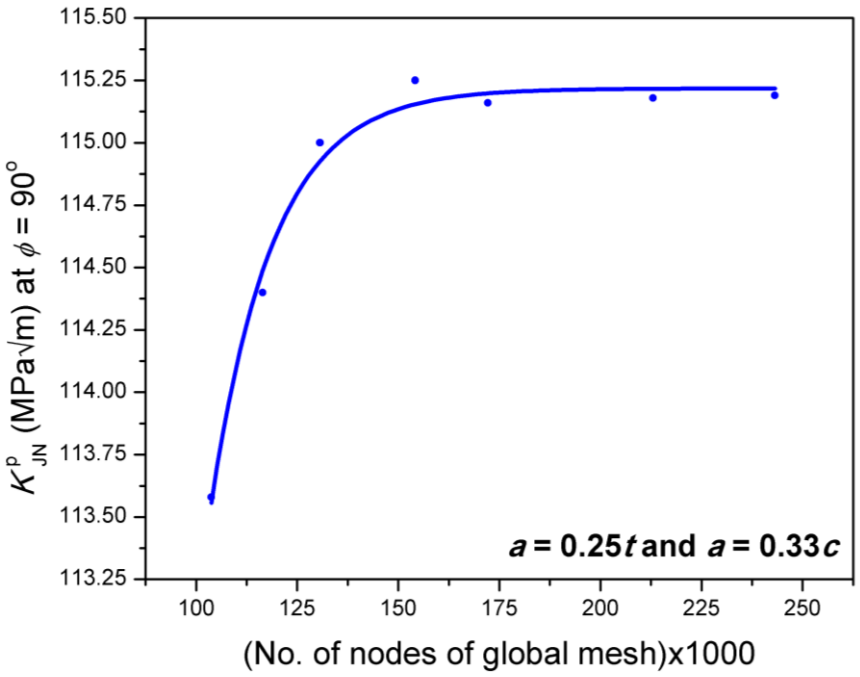

Figure 7-6 Mesh independent study of the pallet body fracture model.

7.1.6 The EPFM Based SIFs under Normal Operating Conditions

The EPFM based SIFs under only pressure loadings (K^{p}_{JN}) for all the corner cracks listed in Table 7.1, have been presented in Figure 7-7. The elastic plastic material characteristics as shown in Figure 4-3 at $288\ ^{\circ}C$ were used for the computations of the EPFM based SIFs. Figure 7-7 (a), (b), (c), (d), (e) and (f) show EPFM based SIFs of the cracks having minor axis *(a)* equal to 1 percent, 5 percent, 10 percent, 15 percent, 20 percent and 25 percent of the wall thickness (*t*), respectively.

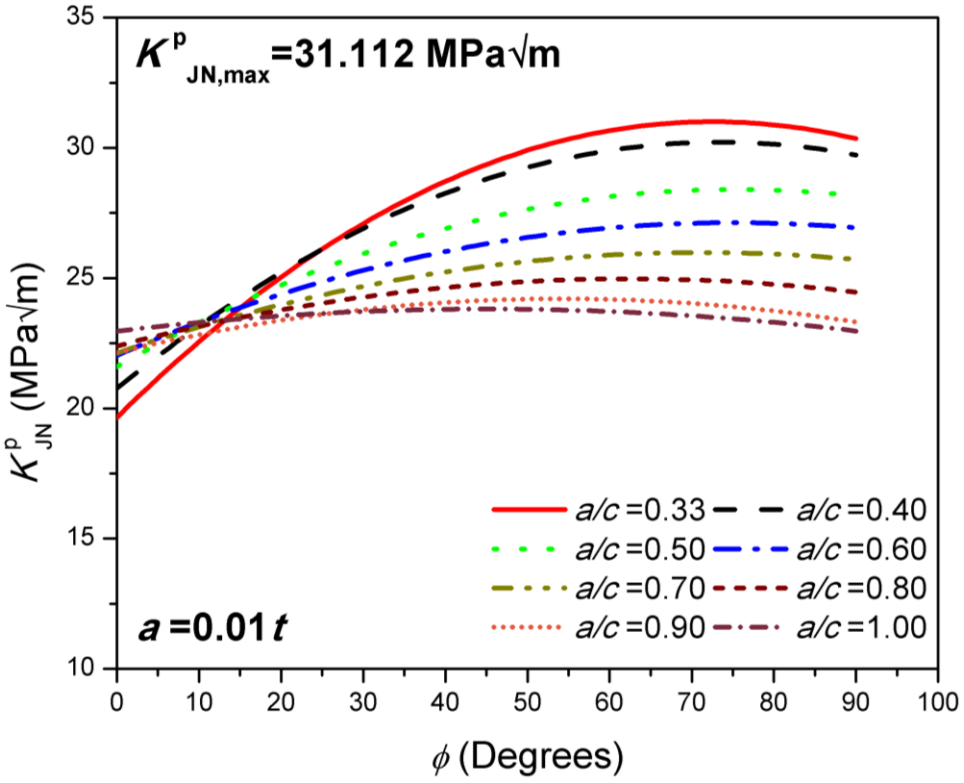

(a)

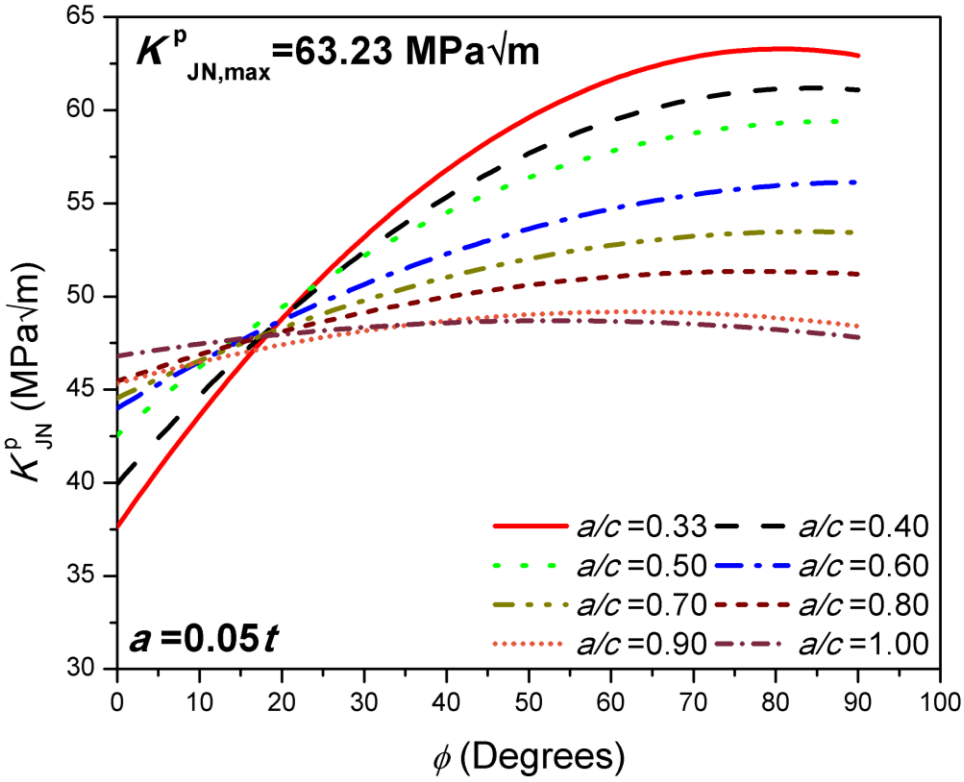

(b)

Figure 7-7 The EPFM based SIFs under normal operating conditions …

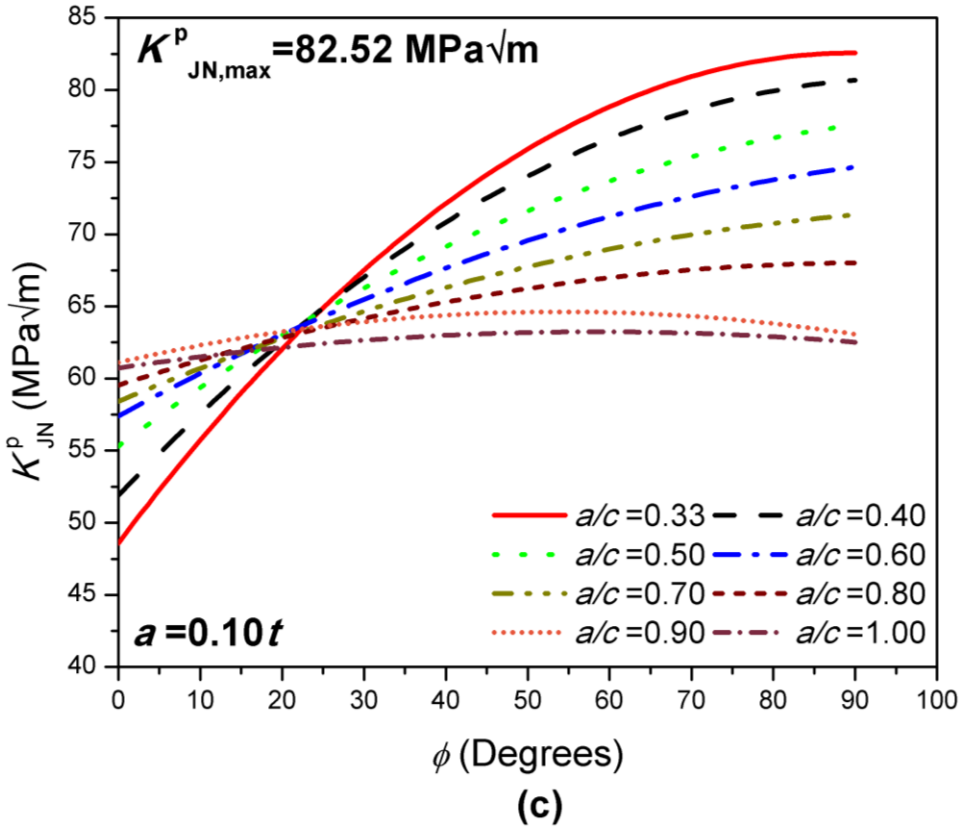

(c)

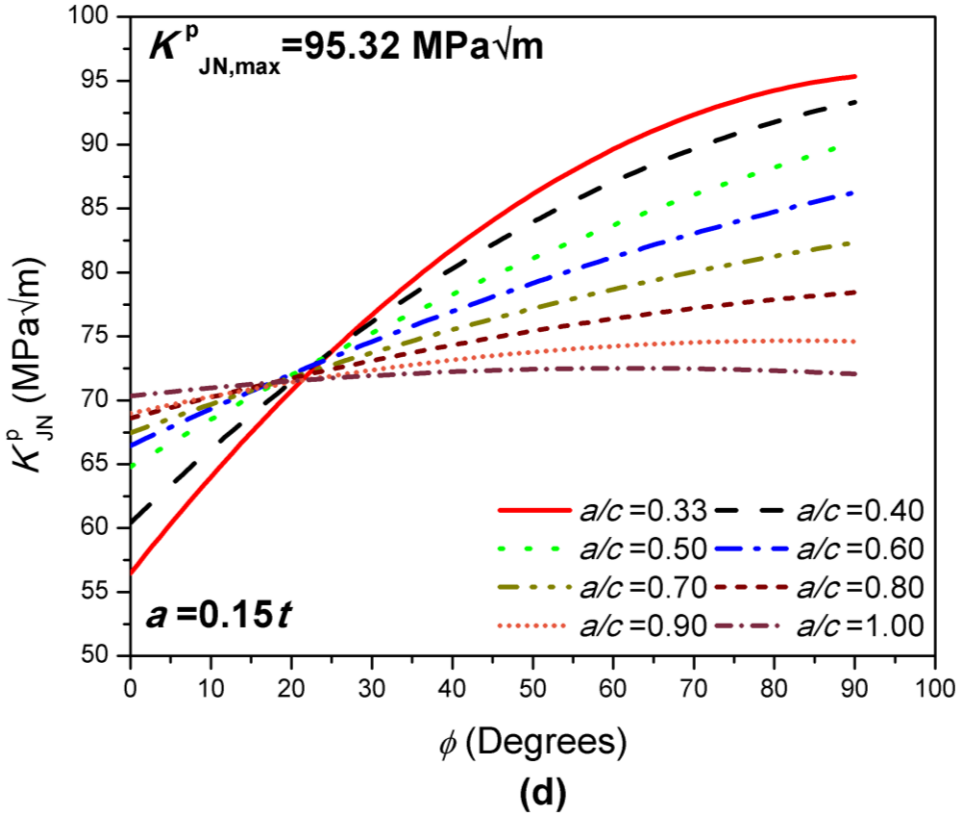

(d)

Figure 7-7 The EPFM based SIFs under normal operating conditions …

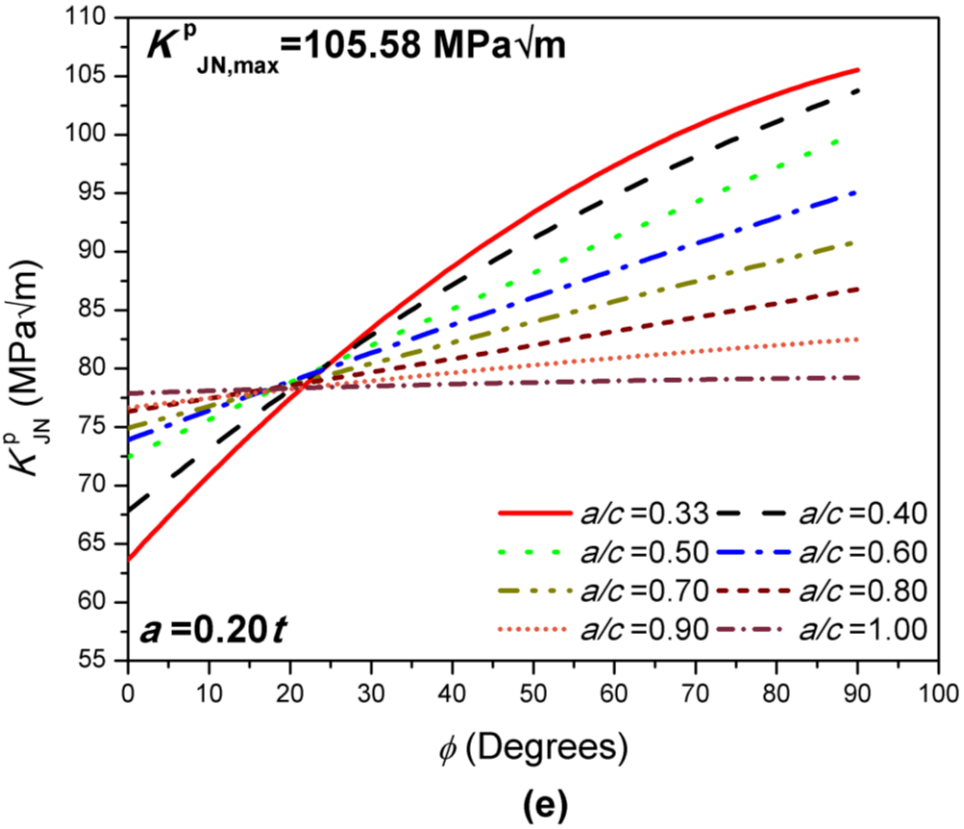

(e)

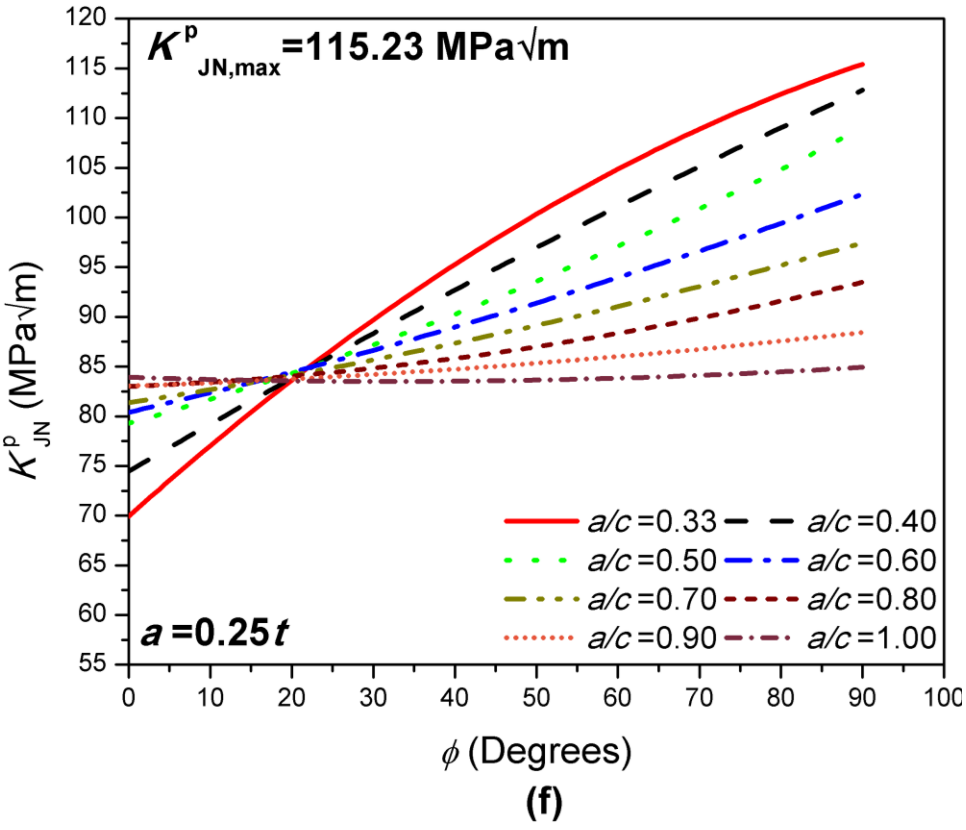

(f)

Figure 7-7 The EPFM based SIFs under normal operating conditions.

The worst crack (a = 0.25t and a = 0.33c) under normal operating conditions has the EPFM based maximum SIF equal to $K^{p}_{JN,\max} = 115.23\ MPa\sqrt{m}$ as shown in Figure 7-7 (f).

For the comparison of the LEFM based SIFs with the EPFM based SIFs under normal operating conditions, SIFs of the cracks having aspect ratio 'a/c = 0.33' are plotted in the Figure 7-8. It is clear from Figure 7-8 that initially up to a = 52.5 mm the EPFM based SIFs are higher than the LEFM based SIFs. However, for the larger cracks when a > 52.5 mm the LEFM based SIFs are higher than the EPFM based SIFs. The bahaviour is probably due to the fact that for bigger cracks the plastic zone at the crack tips becomes bigger. The larger plastic zones at crack tip actually blunts the crack tip, which finally leads to the reduction of the SIF. It can be concluded from the results that larger plastic zones at the crack tips are actually beneficial for the cracks.

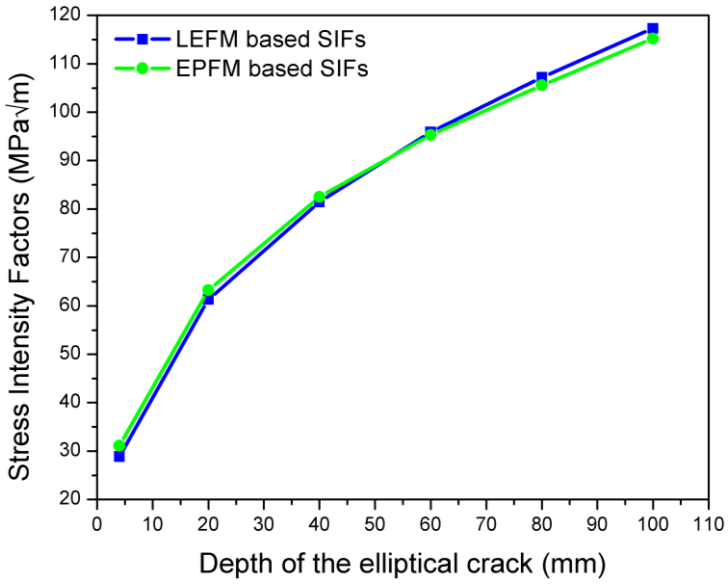

Figure 7-8 The comparison between LEFM based SIFs and EPFM based SIFs.

7.1.7 The Normalized LEFM Based SIFs

The maximum SIF at the deepest point of semi-elliptical surface crack in finite plate under remote tension as shown in Figure 6-1 (a), can be evaluated using a simple analytical relationship [46].

$$K_{I,\max} = \left(T_F \cdot \sqrt{\pi . a / Q}\right) \tag{7-1}$$

Where *'T_F'* is the remote tension, *'a'* is the crack depth, and *'Q'* is the flaw shape parameter. If the remote tension in Eq. (7-1) is replaced by hoop stress in a cylindrical portion then the formula can give a rough estimation of a maximum SIF of the surface crack in a cylindrical portion [46]. In order to investigate the strength of the corner crack at nozzle-cylinder intersection in comparison to surface crack in simple cylindrical potion, the SIFs of the corner crack can be normalized according to Eq. (7-1) if the remote tension is replaced with the hoop stress. If thickness of the cylindrical portion is taken equal to the nozzle belt's thickness of the RPV (t = 400 *mm*), then membrane hoop stress in the cylindrical portion can be calculated as $\sigma_h = P_{\text{int}}.R_m / t = 80.48\ MPa$. Where '*$P_{int}$*' is the internal pressure of the RPV (17.16 *MPa*), and '*R_m*' is the mean radius of the nozzle belt (1876 *mm*). In this way, SIFs of the corner cracks at the nozzle-cylinder intersection of the RPV can be normalized by dividing them with the term $\left(\sigma_h.\sqrt{\pi.a/Q}\right)$. The normalization factor will help to investigate the effects of stress concentrations around the nozzle, on the SIFs of the corner cracks at the nozzle-cylinder intersection.

The normalized LEFM based SIFs under only pressure loadings for all the corner cracks listed in Table 7.1, have been computed and are being presented in Figure 7-9. Figure 7-9 (a), (b), (c), (d), (e) and (f) show normalization factors of the corner cracks having minor axis *(a)* equal to 1 percent, 5 percent, 10 percent, 15 percent, 20 percent and 25 percent of the wall thickness (t), respectively.

It is evident from Figure 7-9 (a-f) that the maximum normalization factor is in the case of circular corner crack (a/c = 1.0). The circular crack of depth $a = 0.01t$ has maximum normalization factor which is around 5.7 as shown in Figure 7-9 (a). In comparison to this, circular crack of depth $a = 0.25t$ has maximum normalization factor which is around 4.7 as shown in Figure 7-9 (f). It means that the larger circular crack has lesser normalization factor. It is due to the fact that larger cracks do have relatively higher cracked area and the effects of stress concentrations are reduced in higher area compared to smaller area. It is also evident from Figure 7-9 (a-f) that the minimum normalization factor is in the case of elliptical corner crack having aspect ratio 'a/c = 0.33'. The elliptical corner crack of depth *'$a = 0.25t$'* has minimum normalization factor which is around 2.

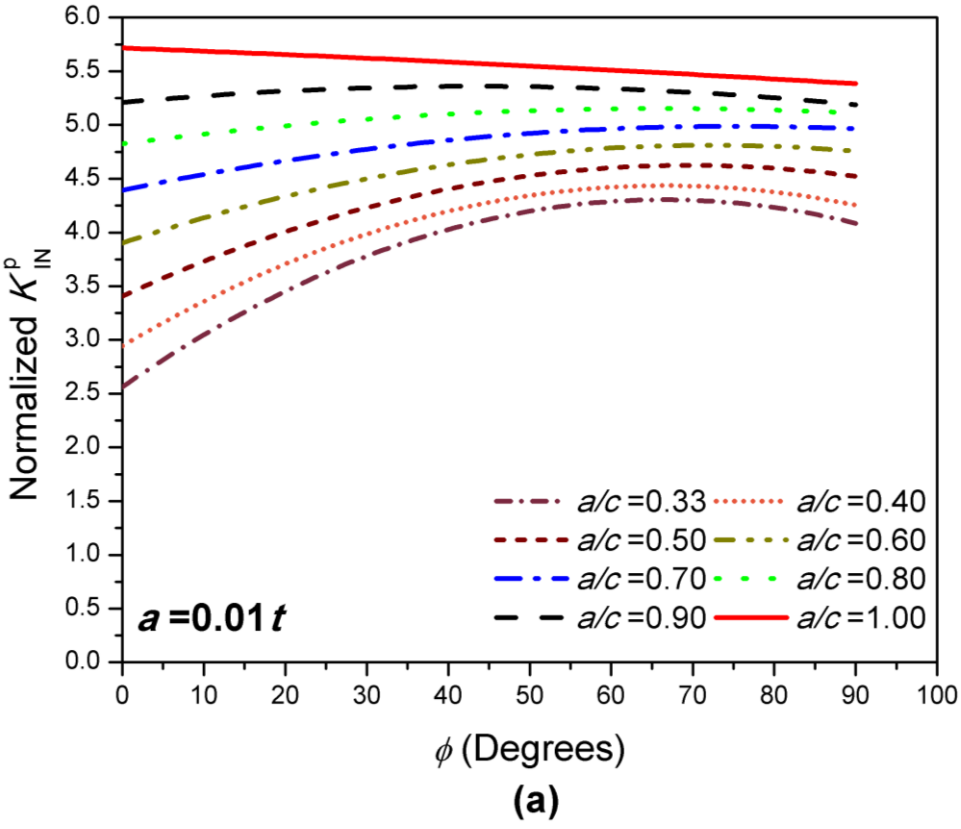

(a)

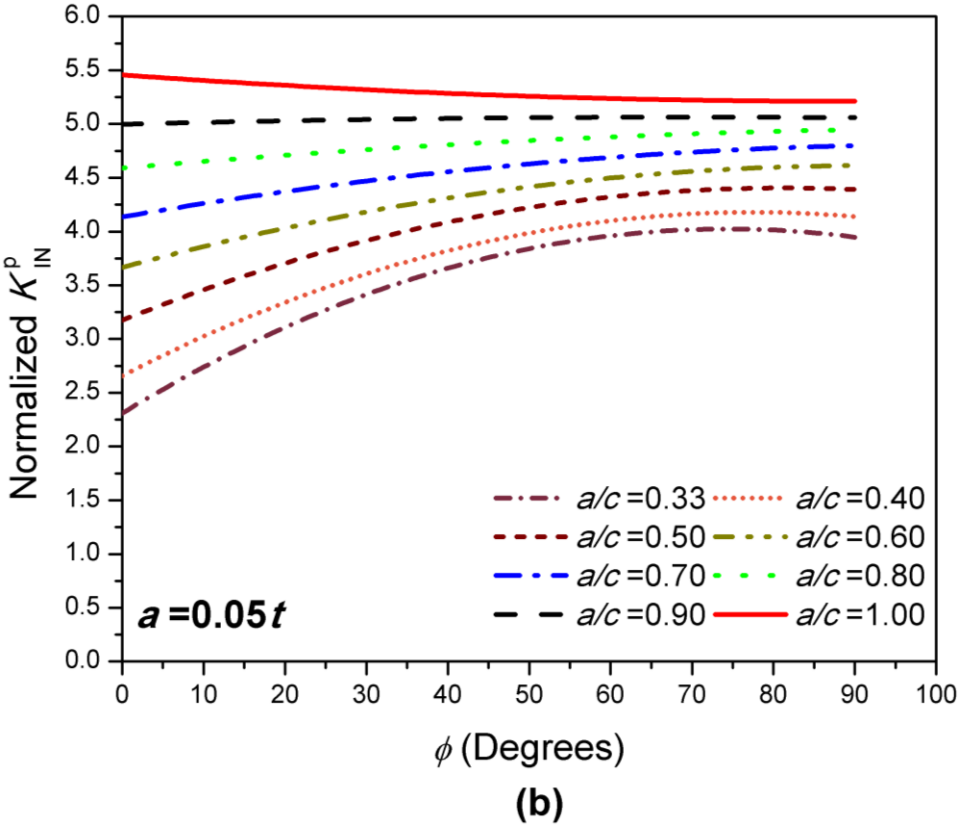

(b)

Figure 7-9 The LEFM based normalized SIFs of the corner cracks…

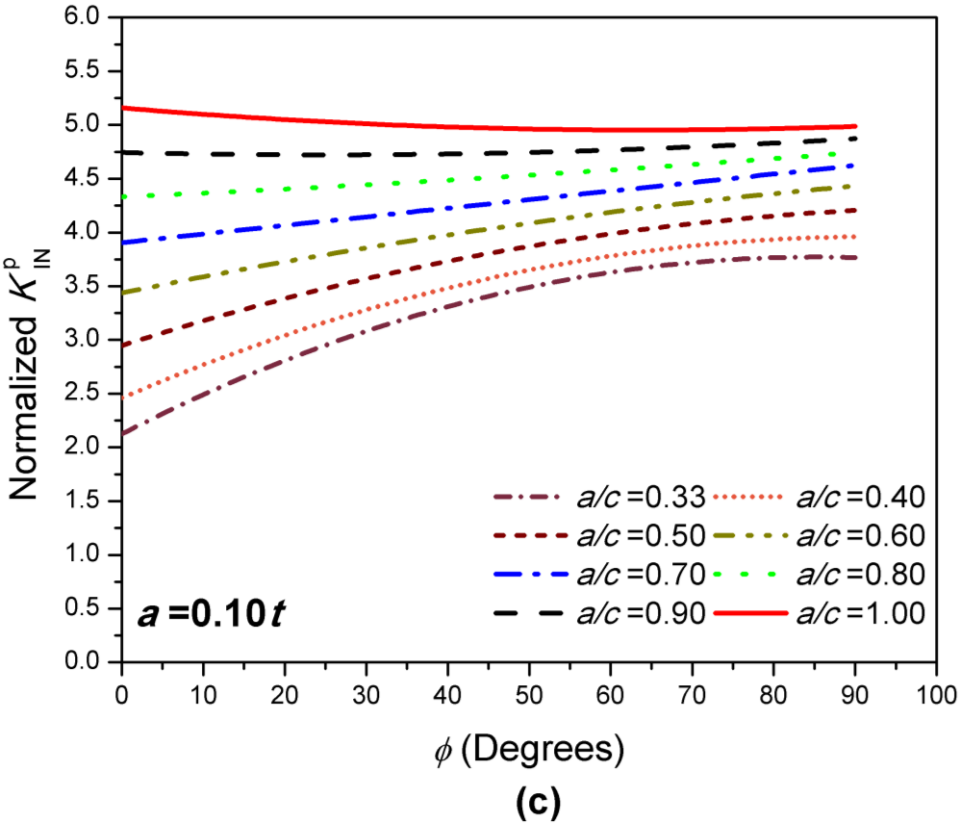

(c)

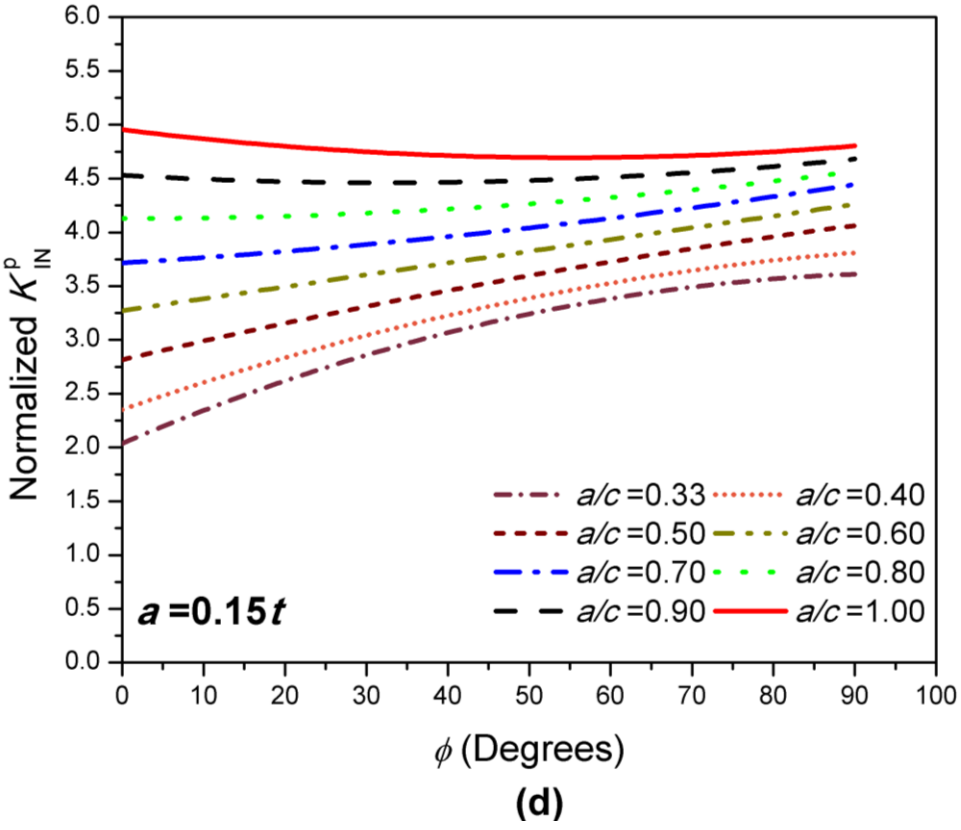

(d)

Figure 7-9 The LEFM based normalized SIFs of the corner cracks…

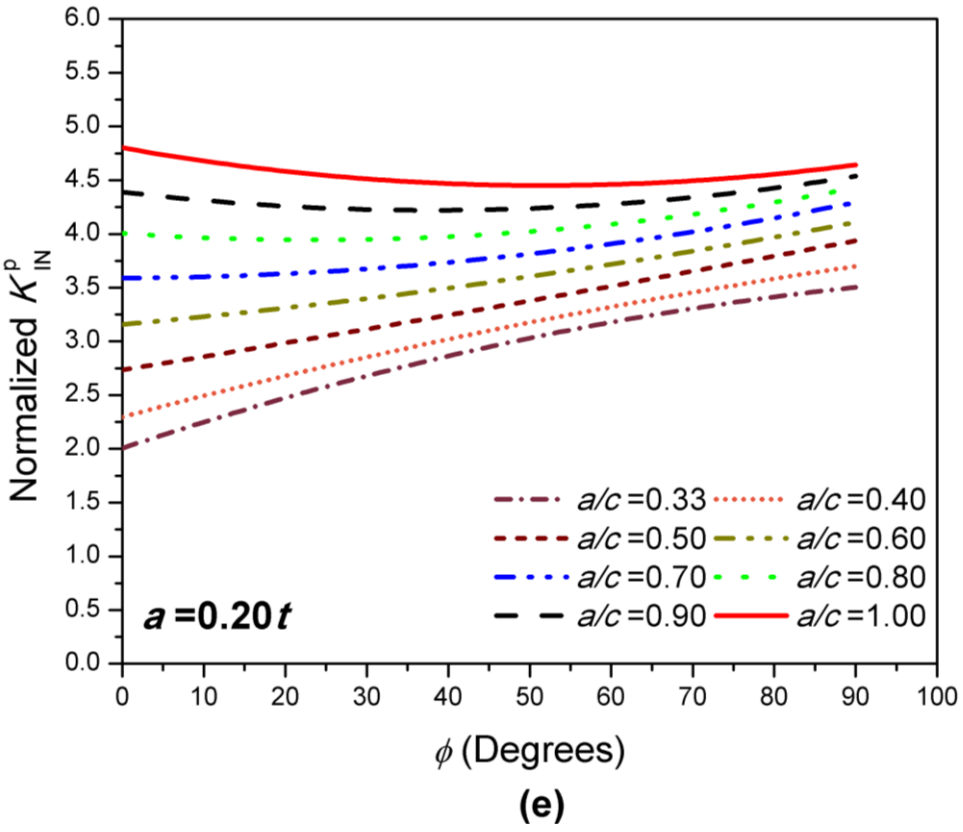

(e)

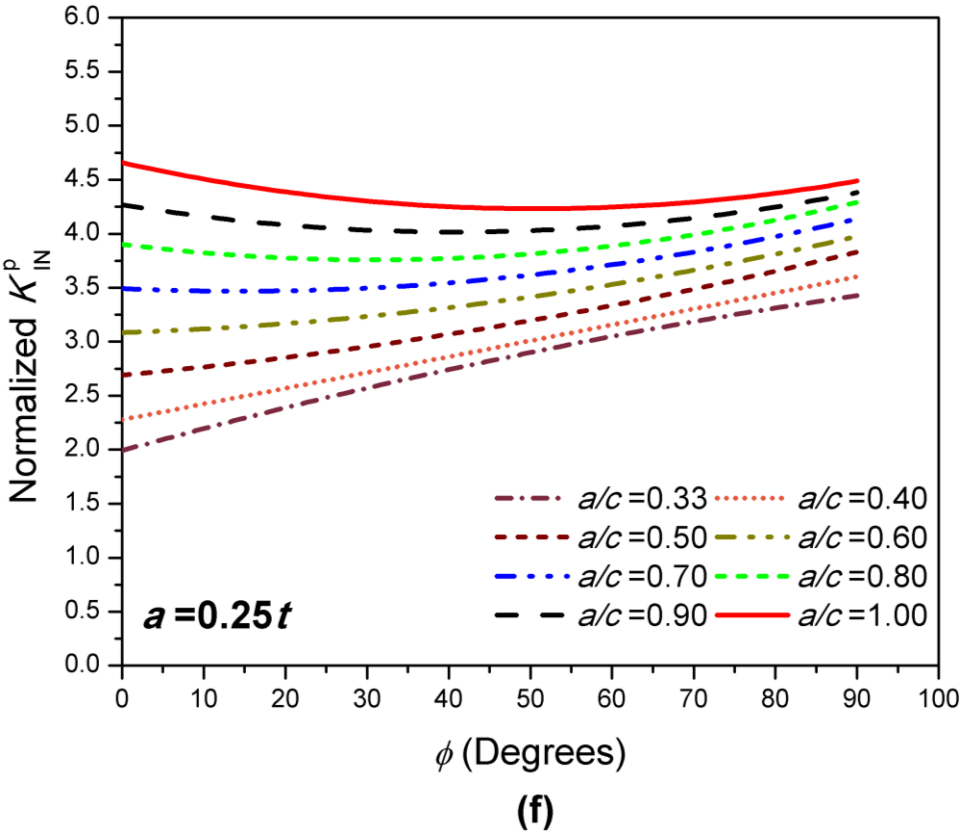

(f)

Figure 7-9 The LEFM based normalized SIFs of the corner cracks.

It can be concluded from the discussion that the corner cracks at a circular hole in a vessel may have up to 5.7 times greater SIF than the SIF of the same crack contained in an infinite plate under tension equivalent to hoop stress in the vessel. The normalization factor in the case of cracks is much more than the stress concentration factor around a circular hole that normally happens to be 3 [10].

7.1.8 Fracture Evaluation under Normal Operating Conditions

For fracture evaluation of the RPV with optimized set-in nozzle, SIFs of the corner cracks were compared with the fracture toughness of the RPV's steel as determined in Section 4.1.2. It is evident from Figure 4-5, that fracture toughness of the material at normal operating temperature ($288\ ^{\circ}C$) including safety factor of $\sqrt{2}$ is $K_{IC} = 155.60\ MPa\sqrt{m}$. The maximum SIFs of the worst corner cracks (a = 0.33c) from each set of cracks (see Table 7.1) were used for comparison and determination of the critical crack depth. The maximum LEFM based SIFs and EPFM based SIFs of the worst cracks (a = 0.33c) of various depths as shown in Figure 7-4 and Figure 7-7 are tabulated below.

Table 7.3 The SIFs of the worst cracks under normal operating conditions.

Crack depth	LEFM based SIF $MPa\sqrt{m}$	EPFM based SIF $MPa\sqrt{m}$
a = 0.01t	28.87	31.11
a = 0.05t	61.32	63.23
a = 0.10t	81.46	82.52
a = 0.15t	95.91	95.32
a = 0.20t	107.23	105.58
a = 0.25t	117.35	115.23

It is evident from Table 7.3, that the SIF of the worst crack (a = 0.25t and a = 0.33c) approaches a maximum of $K^{p}_{IN,\max} = 117.35\ MPa\sqrt{m}$ which is less than the fracture toughness ($K_{IC} = 155.60\ MPa\sqrt{m}$) value of the RPV's steel. Hence, the corner cracks up to 'a = 0.25t' are safe cracks under normal operating conditions of the plant and they don't threaten the integrity of the RPV.

Our next goal is to perform fracture evaluation or critical crack determination under accidental conditions of the plant. Two types of the reactor's accidental conditions called small break loss of coolant accident (SB-LOCA) and Rancho-Seco transient (RST) have been analyzed in this thesis.

7.2 The Fracture Mechanics Analysis under SB-LOCA

As already discussed in Section 4.5.1, that the SB-LOCA conditions generate a pressurized thermal shock (PTS) that remains for 5000 *sec*. For fracture mechanics analysis, duration of the event has been discretized into five steps of 1000 *sec* each. The temperature profiles, along the path through the nozzle-belt wall as shown in Figure 4-2 (b), have been determined under the conditions using the developed FE model presented in Figure 5-1 (b). The temperature profiles at time intervals of 1000 *sec*, 2000 *sec*, 3000 *sec*, 4000 *sec*, and 5000 *sec* have been presented in Figure 7-10.

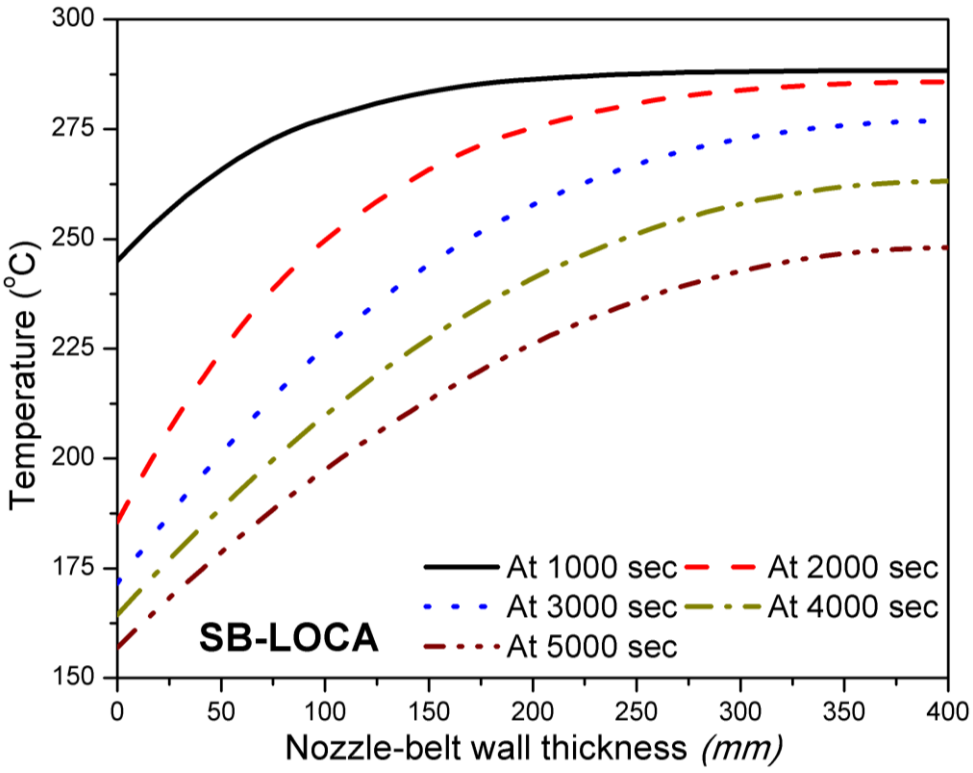

Figure 7-10 Temperatures distributions through-the-thickness of the nozzle belt under SB-LOCA.

The temperature differences between outer and inner surfaces of the nozzle-belt's wall are clear from Figure 7-10. Such temperature gradients will generate thermal stresses in the vessel's wall in addition to the pressure stresses. In order to capture the combined (pressure plus thermal) stresses under the event, a coupled field

structural-transient thermal analysis was performed. The SIFs of the corner cracks under the combined stresses have also been computed and are being presented in the following Section.

7.2.1 The LEFM Based SIFs under SB-LOCA

The corner cracks of constant aspect ratio *'a* = 0.33*c'* and varying depth in the range of '0.01 < *a/t* < 0.25' were used to probe that what kind of flaw, at what time of transient during SB-LOCA is most detrimental for the optimized set-in nozzle. The SIFs of all the corner cracks were computed for fracture evaluation of the nozzle considering the pressurized thermal shock that would occur under SB-LOCA. The SIFs of the corner cracks at 0 *sec*, 1000 *sec*, 2000 *sec*, 3000 *sec*, 4000 *sec*, and 5000 *sec* of the event were computed in order to investigate that at what time the most detrimental PTS exists.

Figure 7-11 (a), (b), (c), (d), (e) and (f) show the LEFM based SIFs under SB-LOCA (K_{IS}^{ps}) of the cracks having minor axis *(a)* equal to 1 percent, 5 percent, 10 percent, 15 percent, 20 percent and 25 percent of the wall thickness (*t*), respectively. It is obvious from Figure 7-11 (a-f) that for all type of cracks the LEFM based 'maximum SIF' occurs at the specific time of 2000 *sec* where the drop rate in temperature (see Figure 7-10) is fastest during the SB-LOCA accidental condition. Hence, the PTS at 2000 *sec* is the most critical event during the SB-LOCA. The maximum SIF of the worst crack (*a* = 0.25*t* and *a* = 0.33*c*) at 2000 sec approaches $K_{IS,\max}^{ps} = 151.99\ MPa\sqrt{m}$ as shown in Figure 7-11 (f).

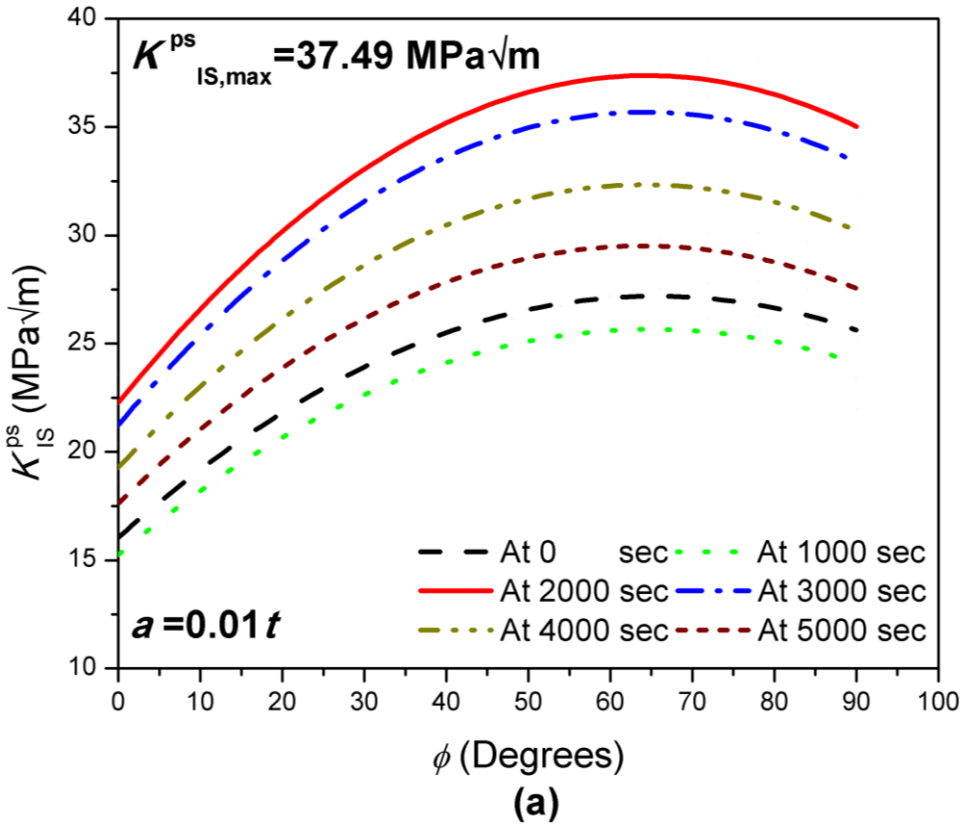

(a)

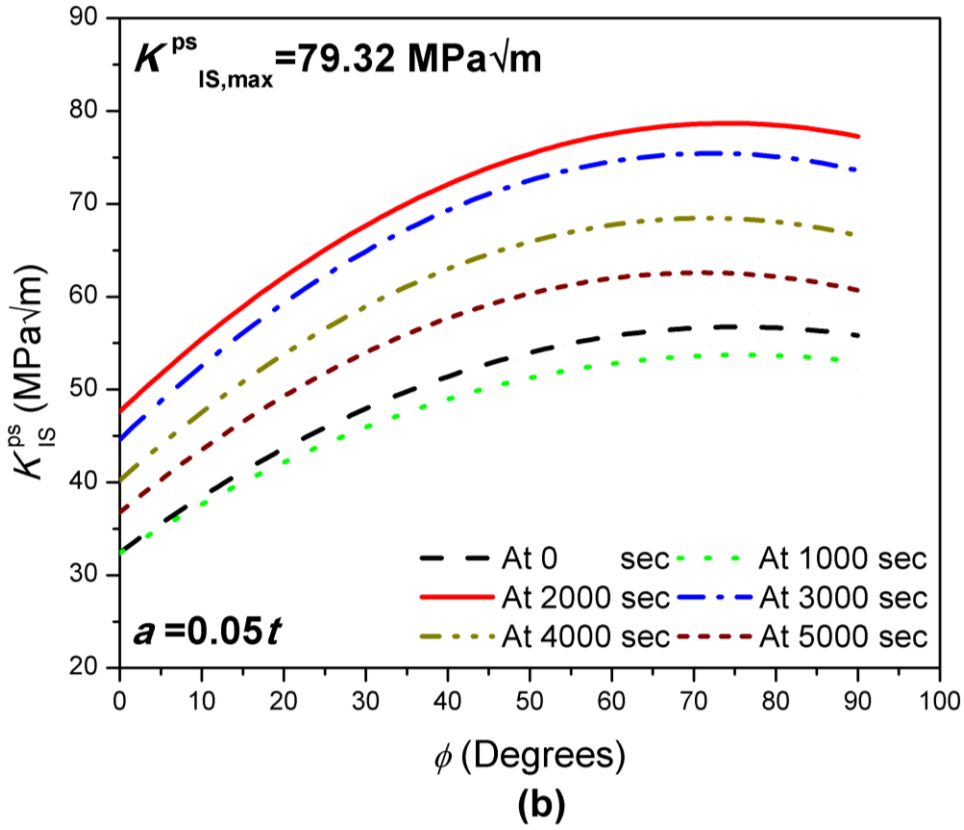

(b)

Figure 7-11 The LEFM based SIFs under SB-LOCA…

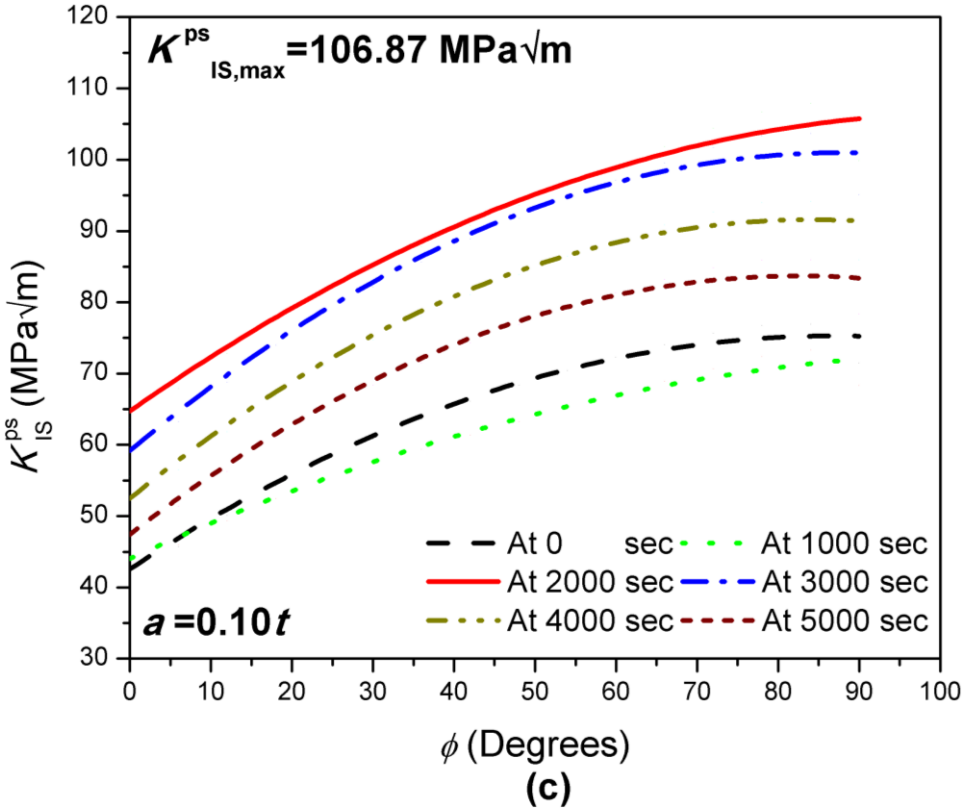

(c)

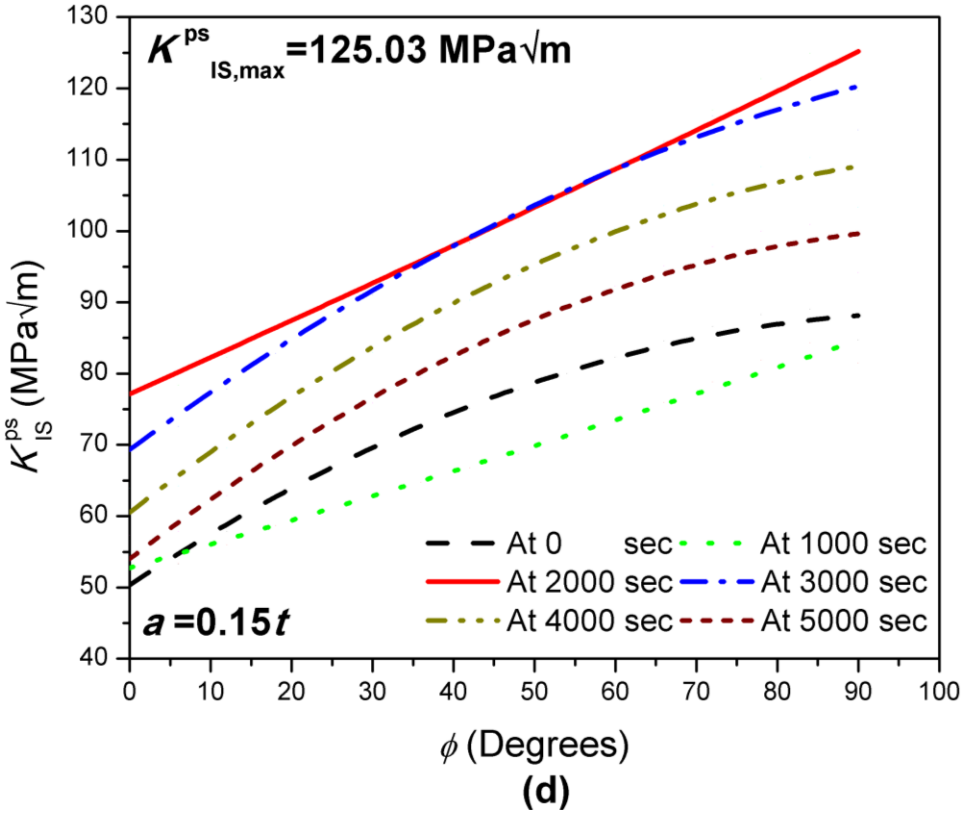

(d)

Figure 7-11 The LEFM based SIFs under SB-LOCA…

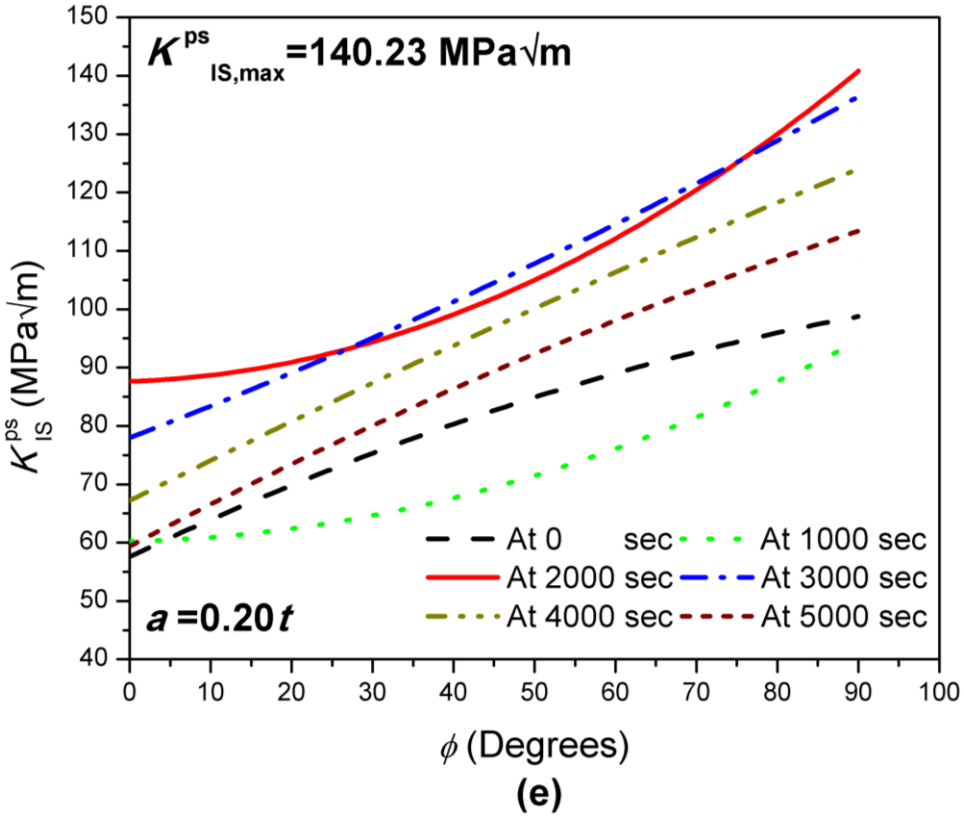

(e)

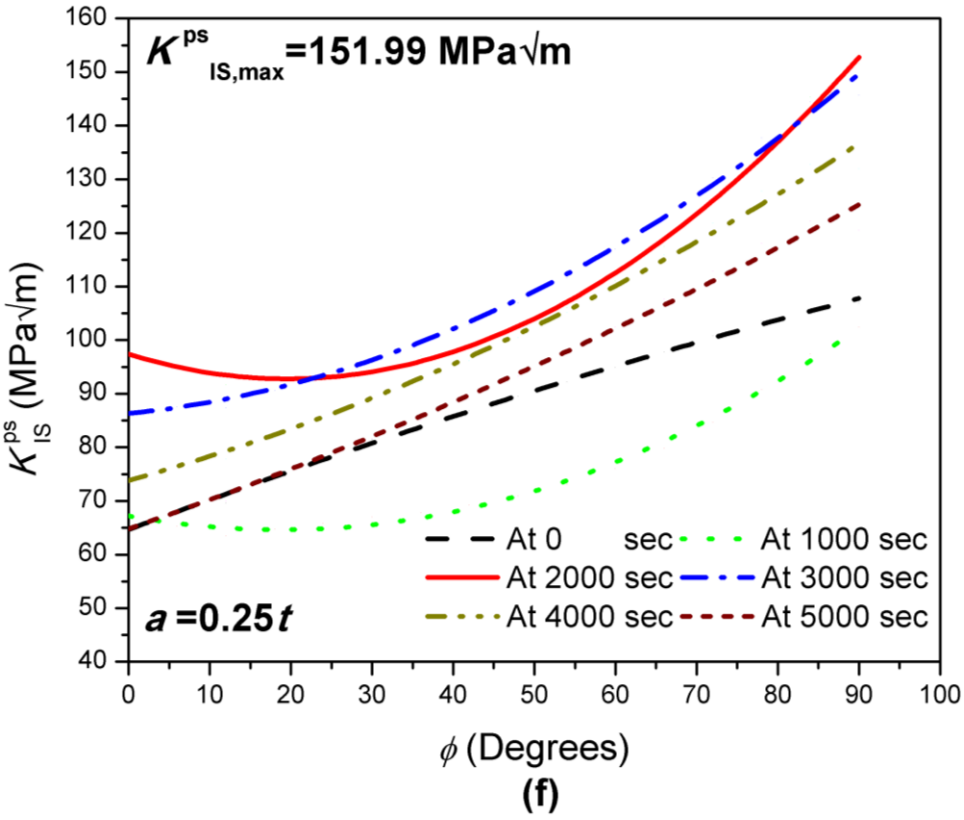

(f)

Figure 7-11 The LEFM based SIFs under SB-LOCA.

7.2.2 The EPFM Based SIFs under SB-LOCA

The EPFM based SIFs under SB-LOCA (K_{JS}^{ps}) at 0 *sec*, 1000 *sec*, 2000 *sec*, 3000 *sec*, 4000 *sec*, and 5000 *sec* have been presented in Figure 7-12 (a-f). Figure 7-12 (a), (b), (c), (d), (e) and (f) show EPFM based SIFs of the cracks having minor axis *(a)* equal to 1 percent, 5 percent, 10 percent, 15 percent, 20 percent and 25 percent of the wall thickness (*t*) respectively. The EPFM based SIFs of the worst crack (a = 0.25t and a = 0.33c) approaches $K_{JS,\max}^{ps} = 142.65\ MPa\sqrt{m}$ as shown in Figure 7-12 (f).

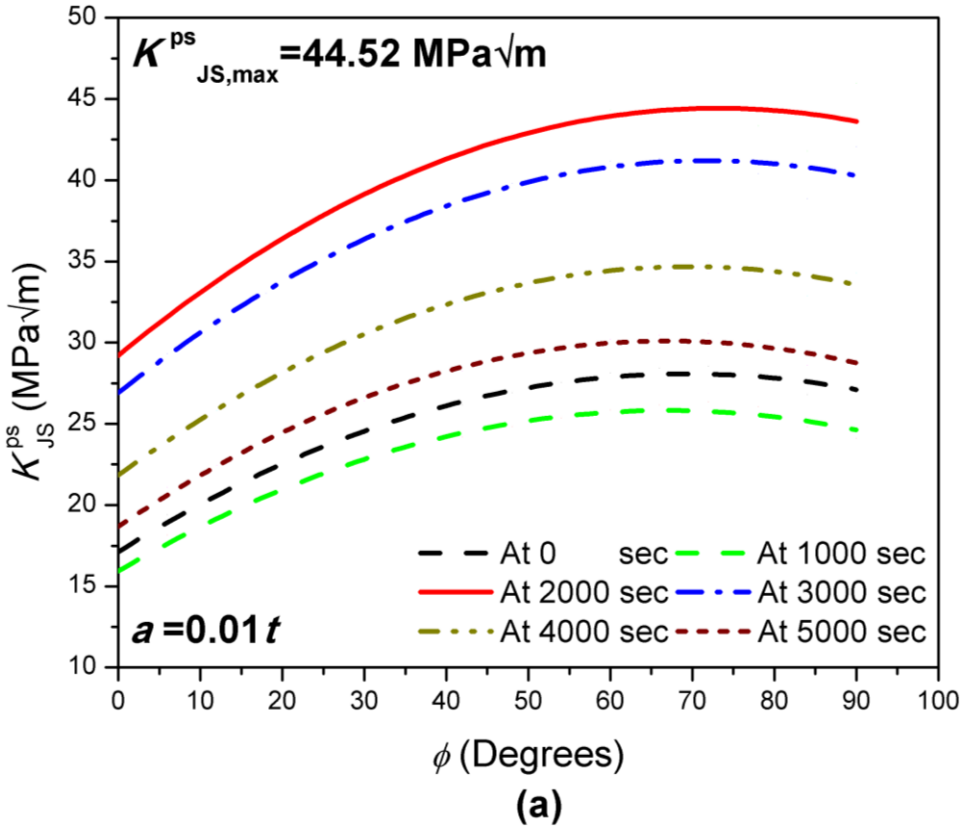

Figure 7-12 The EPFM based SIFs under SB-LOCA…

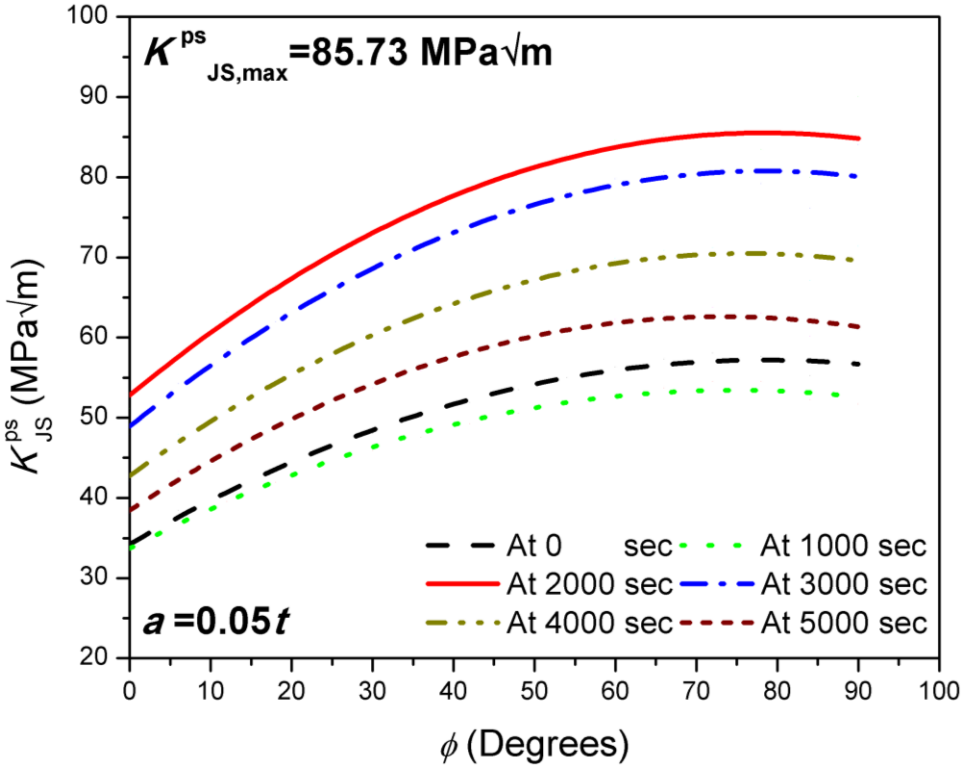

(b)

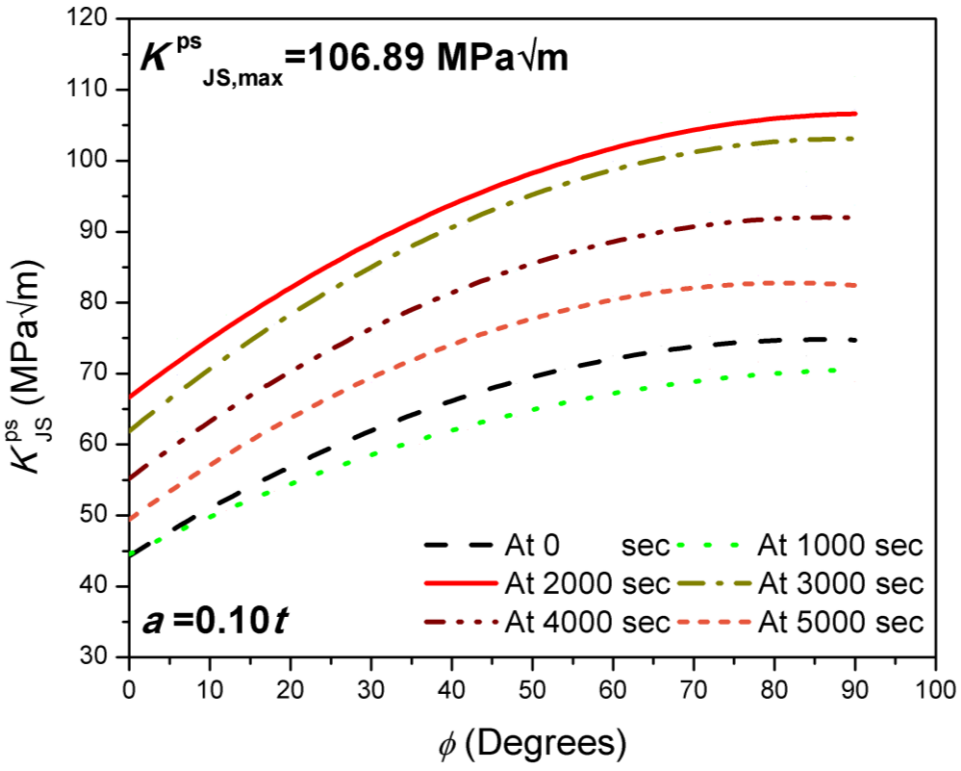

(c)

Figure 7-12 The EPFM based SIFs under SB-LOCA…

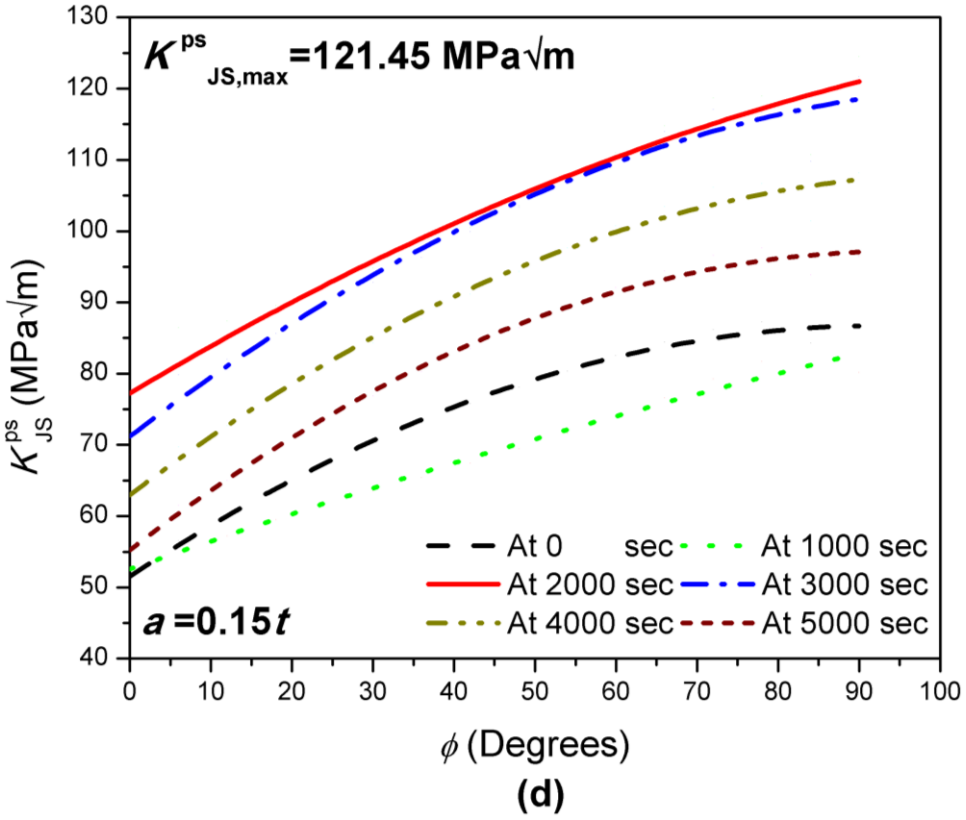

(d)

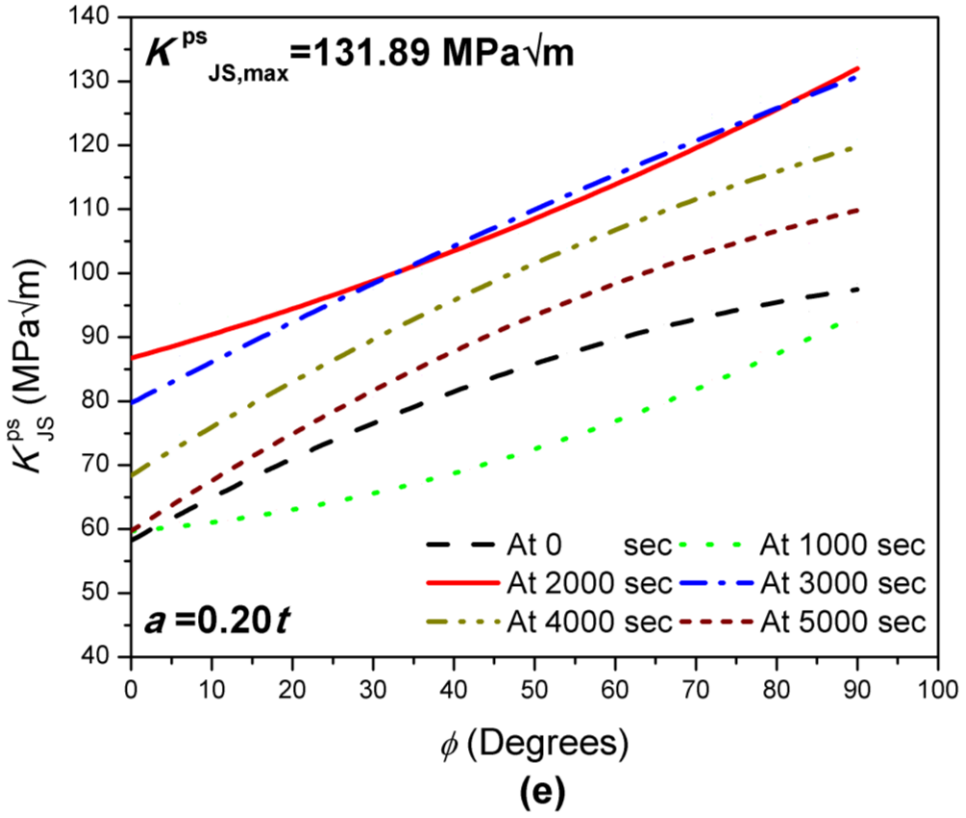

(e)

Figure 7-12 The EPFM based SIFs under SB-LOCA…

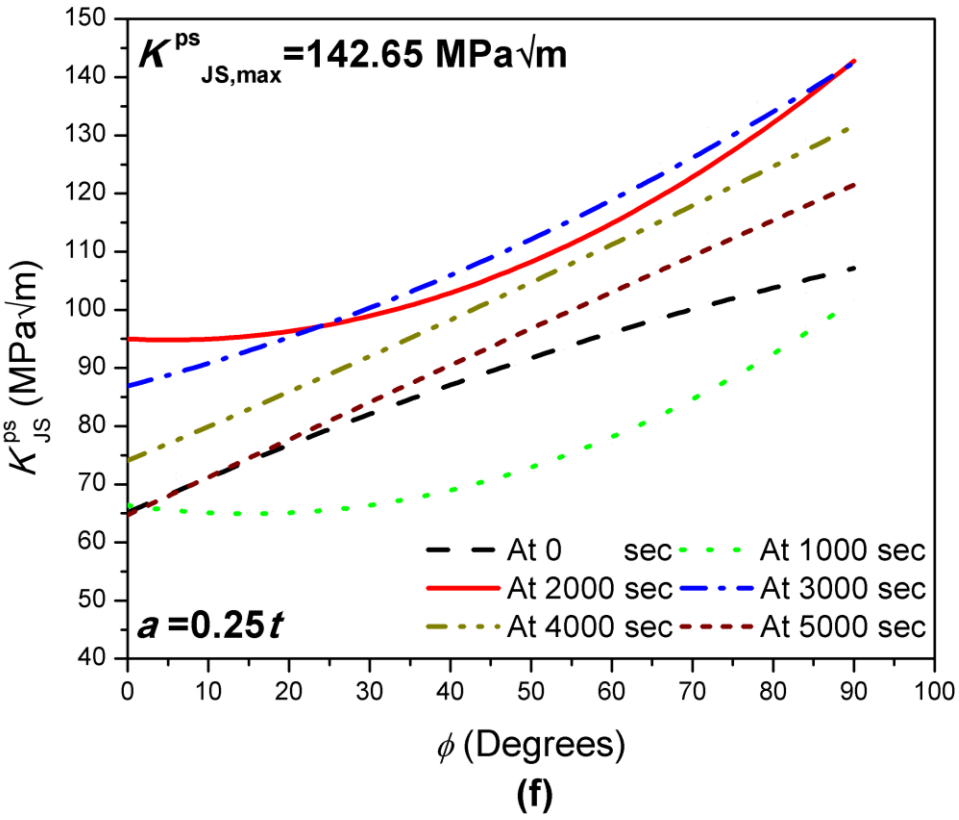

Figure 7-12 The EPFM based SIFs under SB-LOCA.

The comparison of the LEFM based SIFs and the EPFM based SIFs under SB-LOCA conditions have been given in Table 7.4 considering the maximum value of each crack at 2000 *sec*. It is evident from the comparison that the LEFM based SIFs are lesser than the EPFM based SIFs up to 'a = 0.10t', but for a > 0.10t the LEFM based SIFs are always larger.

Table 7.4 The maximum SIFs under SB-LOCA conditions.

Crack depth	LEFM based SIF $MPa\sqrt{m}$	EPFM based SIF $MPa\sqrt{m}$
a = 0.01t	37.49	44.52
a = 0.05t	79.32	85.73
a = 0.10t	106.87	106.89
a = 0.15t	125.03	121.45
a = 0.20t	140.23	131.89
a = 0.25t	151.99	142.65

7.2.3 The Fracture Evaluation under SB-LOCA

For fracture evaluation of the RPV having optimized set-in nozzle under SB-LOCA, the 'maximum SIFs' of the worst corner crack (a = 0.33c) of all the crack depths at

time of 0 *sec*, 1000 *sec*, 2000 *sec*, 3000 *sec*, 4000 *sec* and 5000 *sec*, have been compared to the fracture toughness of the RPV's material (see Figure 4-5).

The comparison is presented in Figure 7-13. Both the LEFM based SIFs and the EPFM based SIFs have been compared with the fracture toughness of the material in Figure 7-13. Figure 7-13 (a), (b), (c), (d), (e) and (f) show the comparison of the cracks having minor axis *(a)* equal to 1 percent, 5 percent, 10 percent, 15 percent, 20 percent and 25 percent of the wall thickness (*t*), respectively. It is evident from Figure 7-13 (a), (b), (c), (d), (e) and (f) that all the postulated cracks up to the depth '$a = 0.25t$' have the SIFs which do not approach the fracture toughness of the material. Even the worst crack ($a = 0.25t$ and $a = 0.33c$) under the most severe event of SB-LOCA (at the time of 2000 *sec*) produces LEFM based 'maximum SIF' equal to $K_{IS,\max}^{ps} = 151.99\ MPa\sqrt{m}$ which is below the fracture toughness value of the material at that temperature (see Figure 7-13 (f)). Hence, it can be concluded from the results that the analyzed cracks up to '$a = 0.25t$' are the safe cracks and they do not predict failure of the RPV by fracture under SB-LOCA conditions.

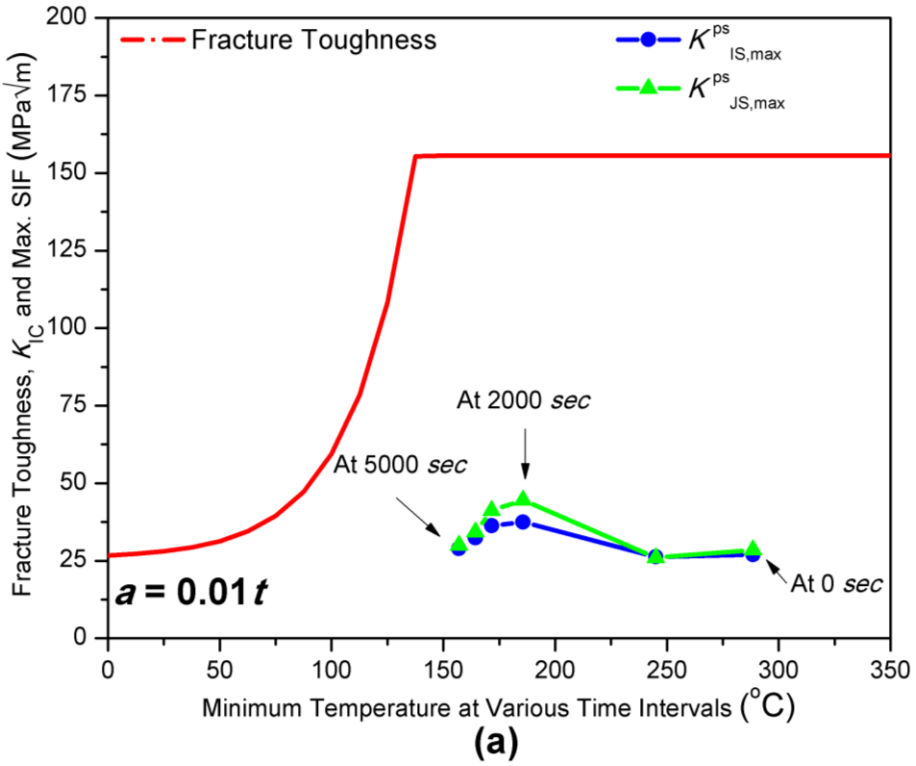

Figure 7-13 The fracture evaluation under SB-LOCA …

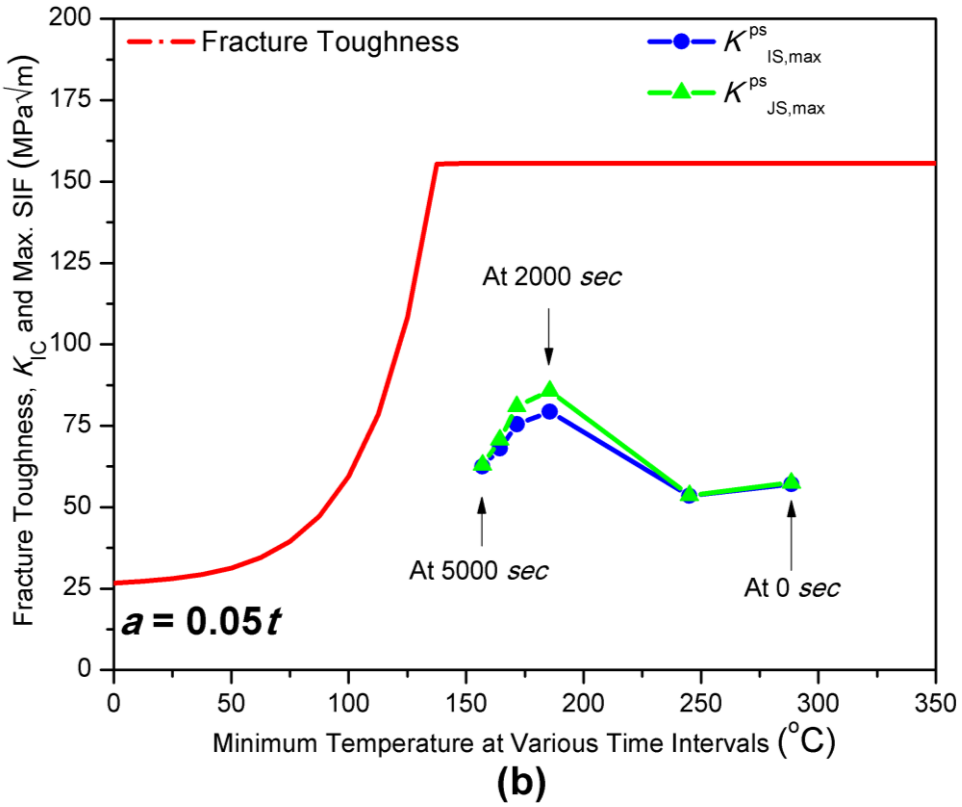

(b)

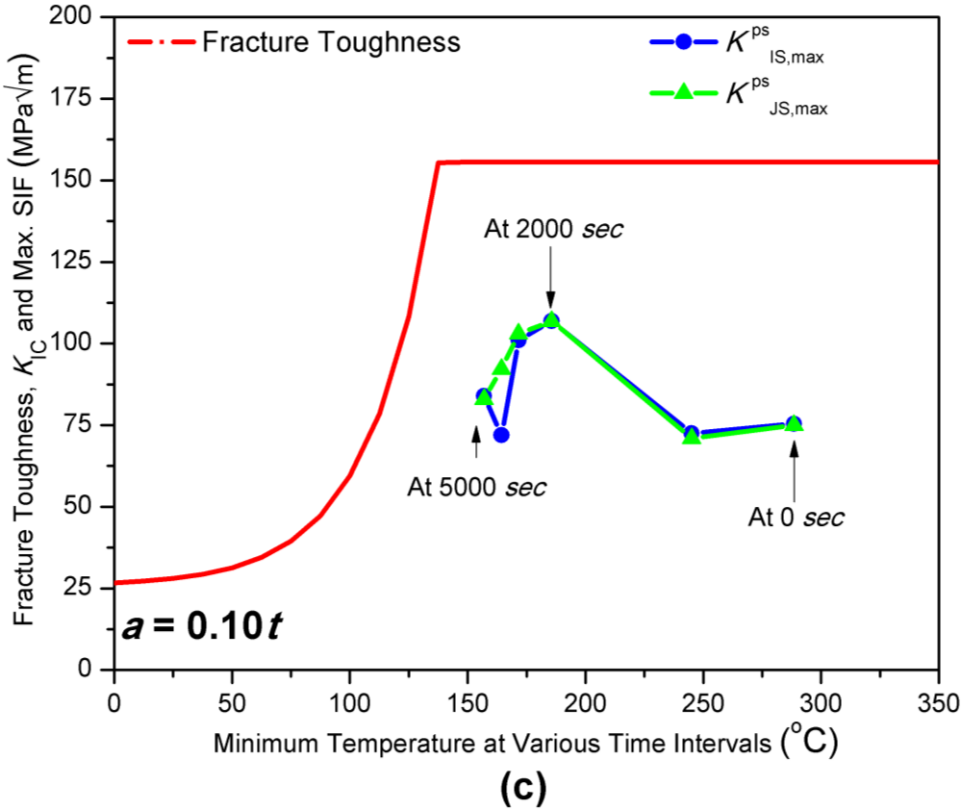

(c)

Figure 7-13 The fracture evaluation under SB-LOCA …

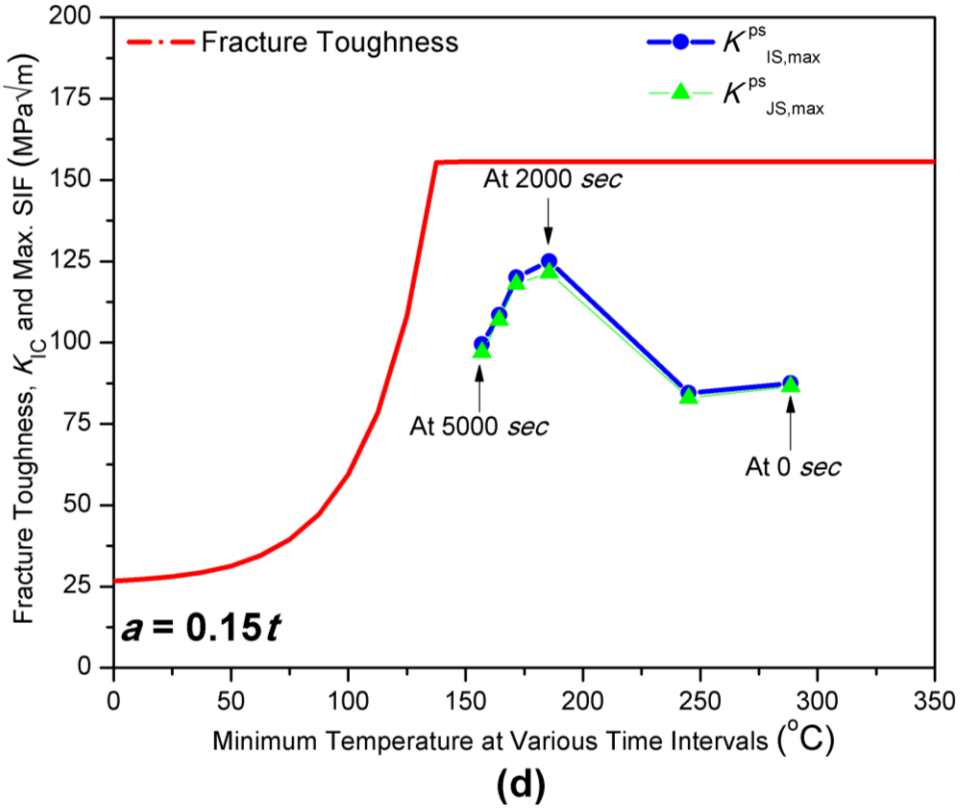

(d)

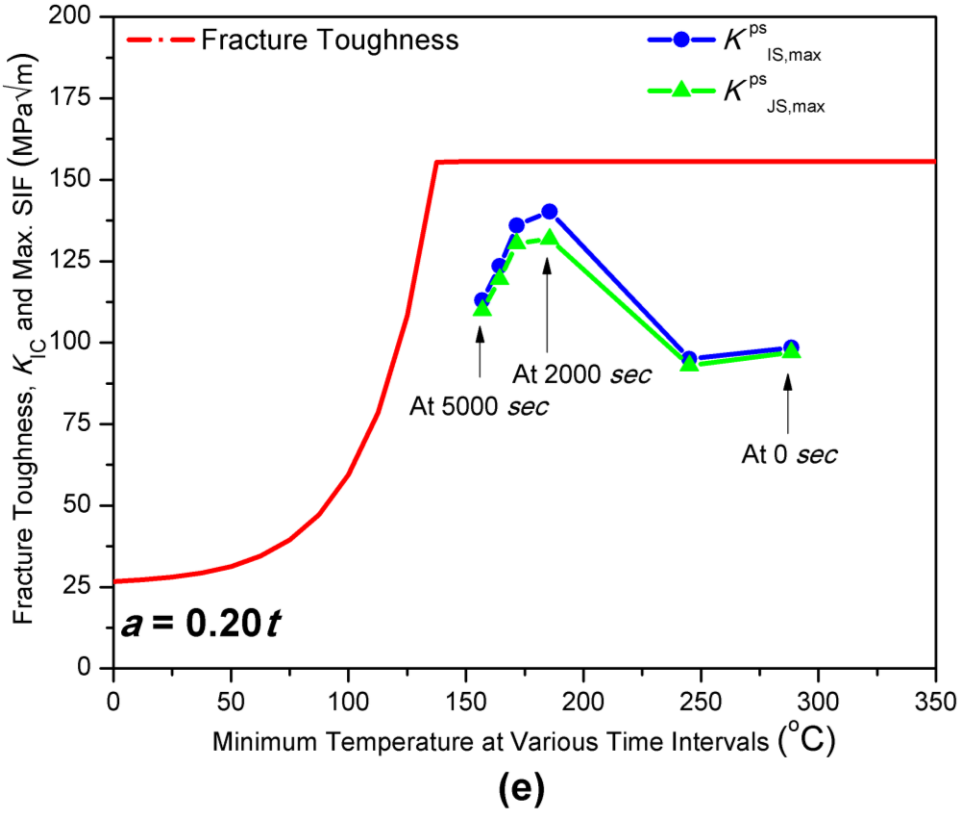

(e)

Figure 7-13 The fracture evaluation under SB-LOCA …

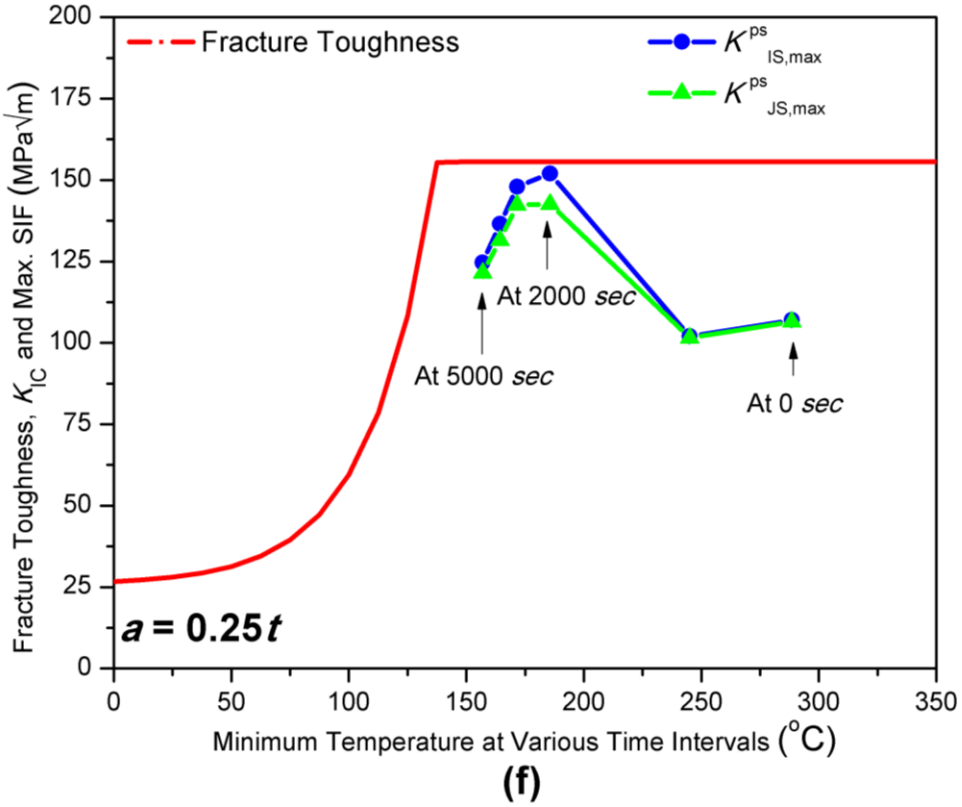

Figure 7-13 The fracture evaluation under SB-LOCA.

7.3 The Fracture Mechanics Analysis under RST

It has been shown in Figure 4-8 that the RST accidental condition generates a pressurized thermal shock (PTS) that remains for 6000 *sec*. For fracture mechanics analysis, under the RST, the duration has been discretized into six steps of 1000 *sec* each. The temperature profiles, along the path as shown in Figure 4-2 (b), have been determined under the RST conditions using the FE model of the RPV as presented in Figure 5-1 (b). The temperature profiles at time intervals of 1000 *sec*, 2000 *sec*, 3000 *sec*, 4000 *sec*, 5000 *sec*, and 6000 *sec* have been presented in Figure 7-14. Here, again the thermal gradients through-the-thickness generates thermal stresses in the vessel's wall. These thermal stresses together with pressure stresses constitute a PTS which would occur during RST accidental conditions.

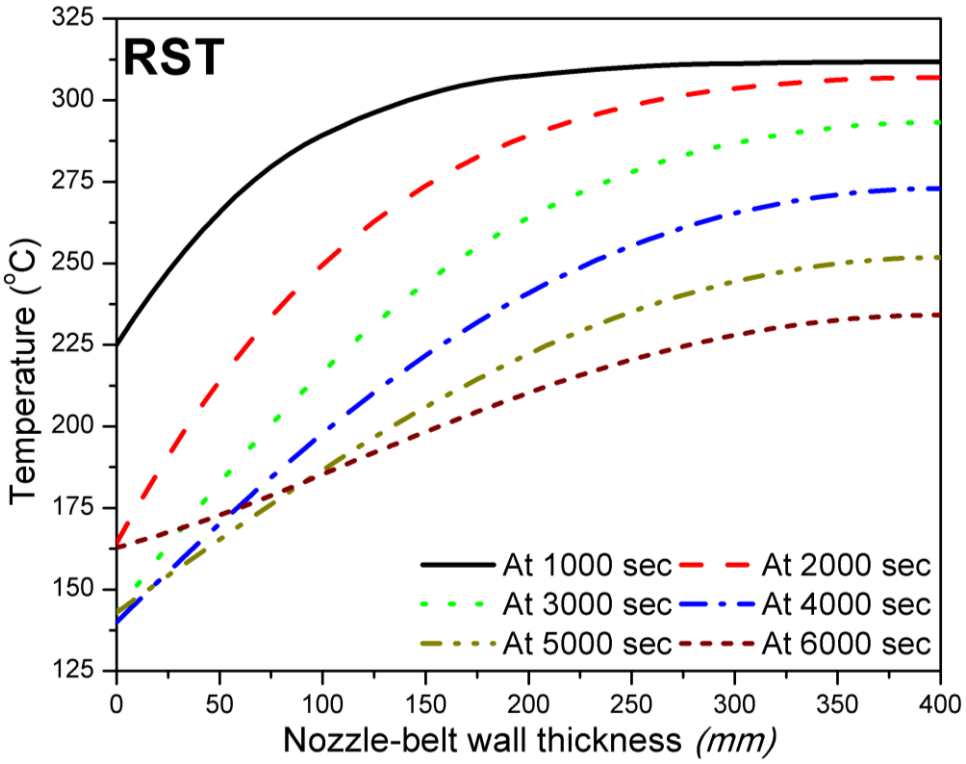

Figure 7-14 Temperatures distributions through-the-thickness of the nozzle belt under RST.

7.3.1 The LEFM Based SIFs under RST

The corner cracks of constant aspect ratio *'a* = 0.33*c'* and varying depth in the range of '0.01 < *a/t* < 0.25' were observed under RST in order to probe that what kind of flaw, at what time of transient is most detrimental for the optimized set-in nozzle. The LEFM based SIFs under RST (K_{IR}^{ps}) of the corner cracks at 0 *sec*, 1000 *sec*, 2000 *sec*, 3000 *sec*, 4000 *sec*, 5000 *sec*, and 6000 *sec* were determined and are presented in Figure 7-15 (a-f). Figure 7-15 (a), (b), (c), (d), (e) and (f) show SIFs of the cracks having minor axis *(a)* equal to 1 percent, 5 percent, 10 percent, 15 percent, 20 percent and 25 percent of the wall thickness (*t*), respectively. It is obvious from Figure 7-15 (a-f) that for all types of cracks the 'maximum LEFM based SIF' occurs at the specific time of '2000 *sec'*. The LEFM based SIF of the worst crack (*a* = 0.25*t* and *a* = 0.33*c*) approaches $K_{IR,\max}^{ps} = 231.46\ MPa\sqrt{m}$ as shown in Figure 7-15 (f).

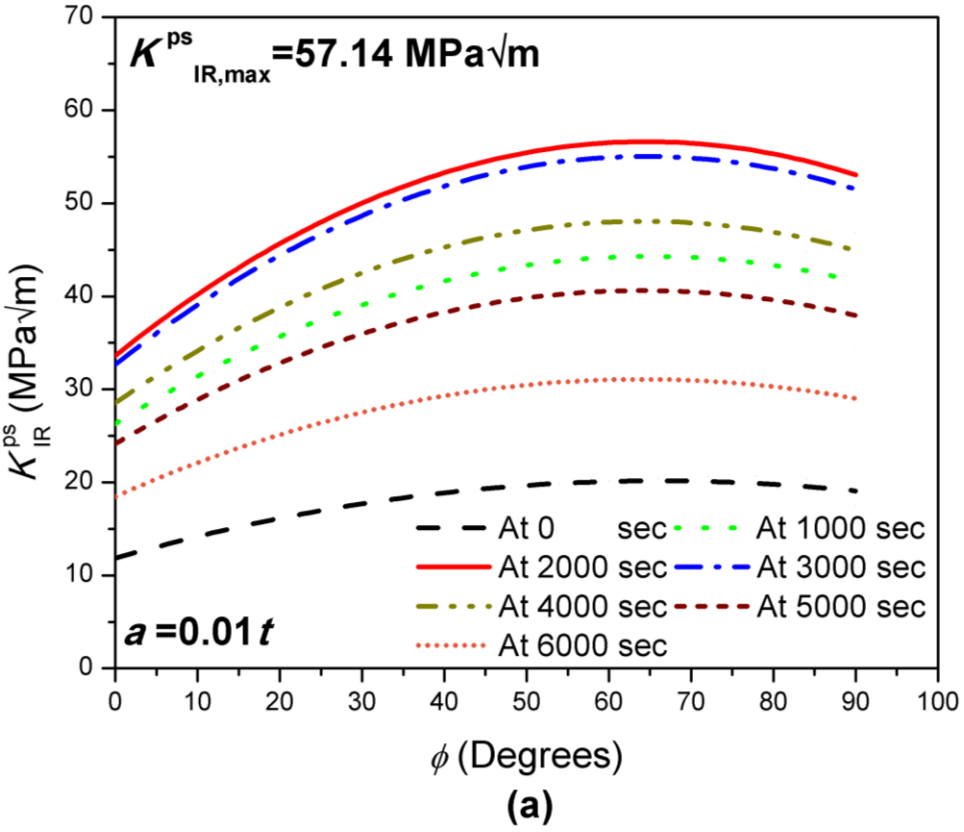

(a)

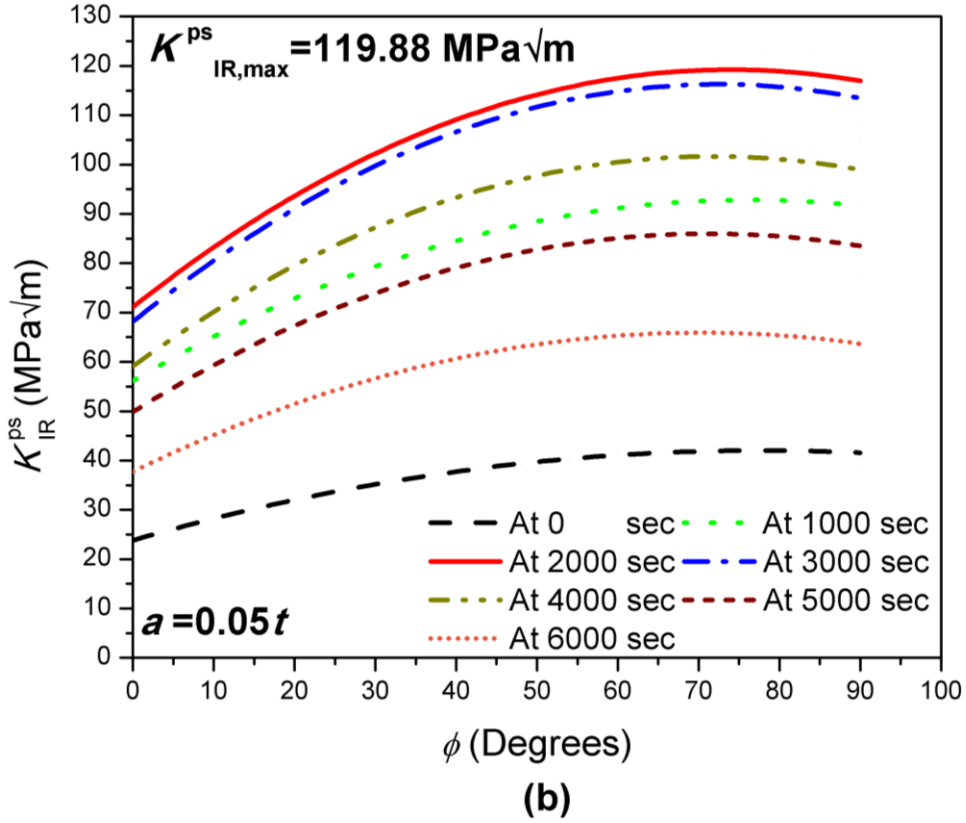

(b)

Figure 7-15 The LEFM based SIFs under RST…

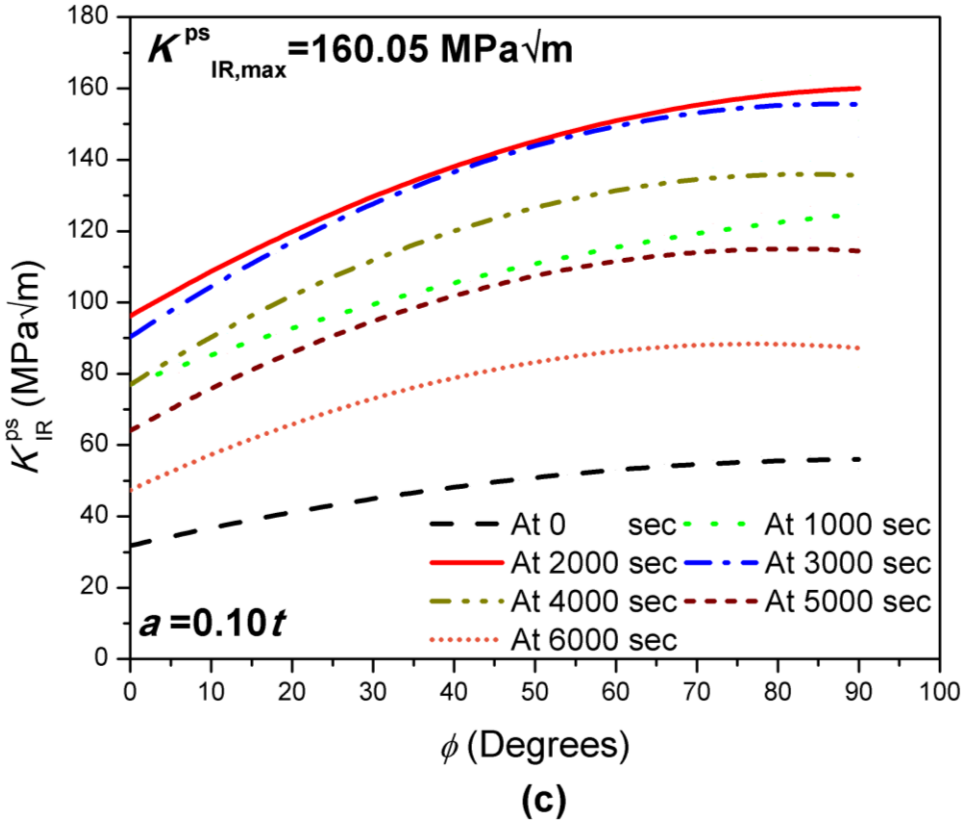

(c)

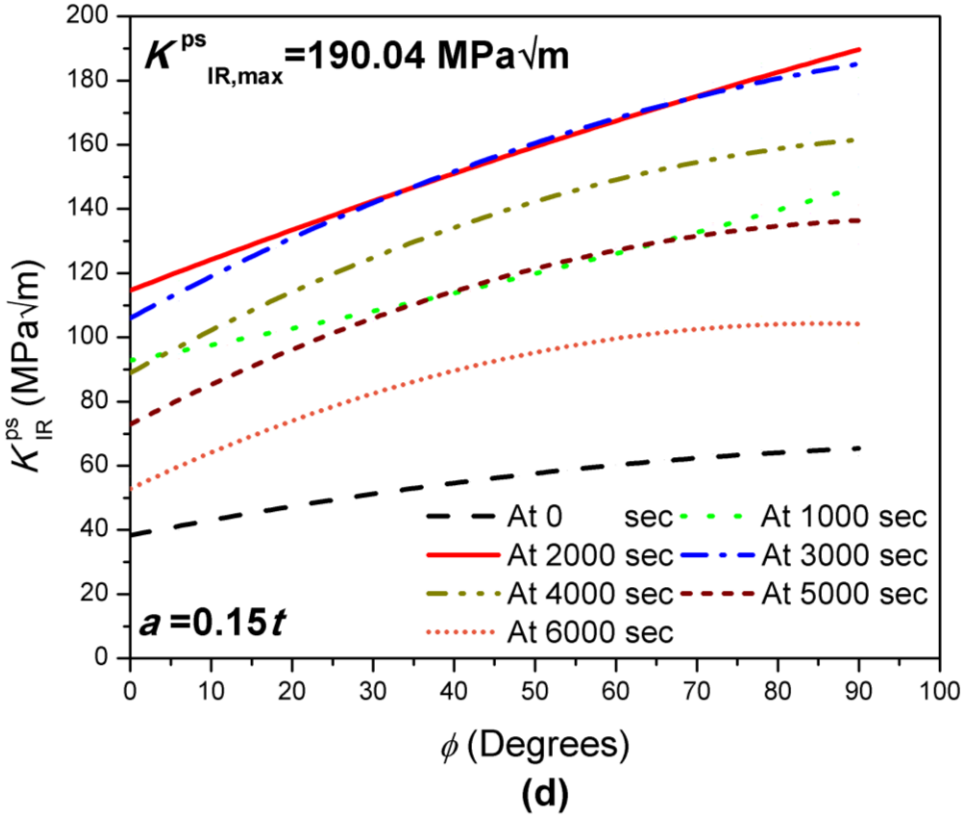

(d)

Figure 7-15 The LEFM based SIFs under RST…

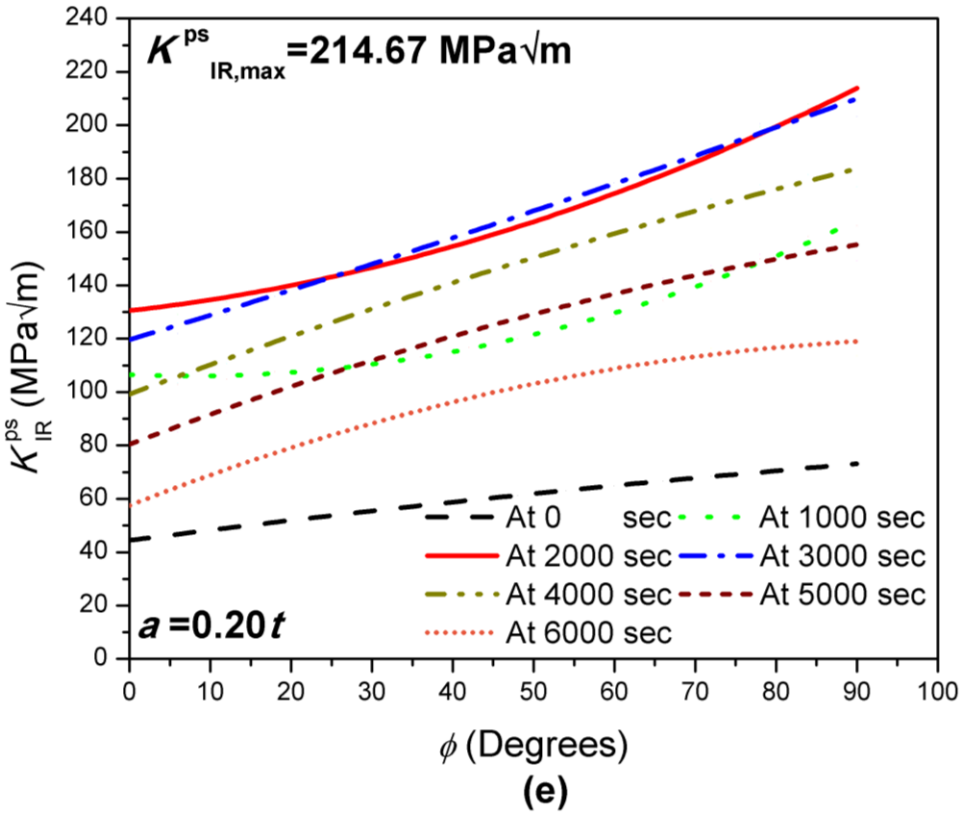

(e)

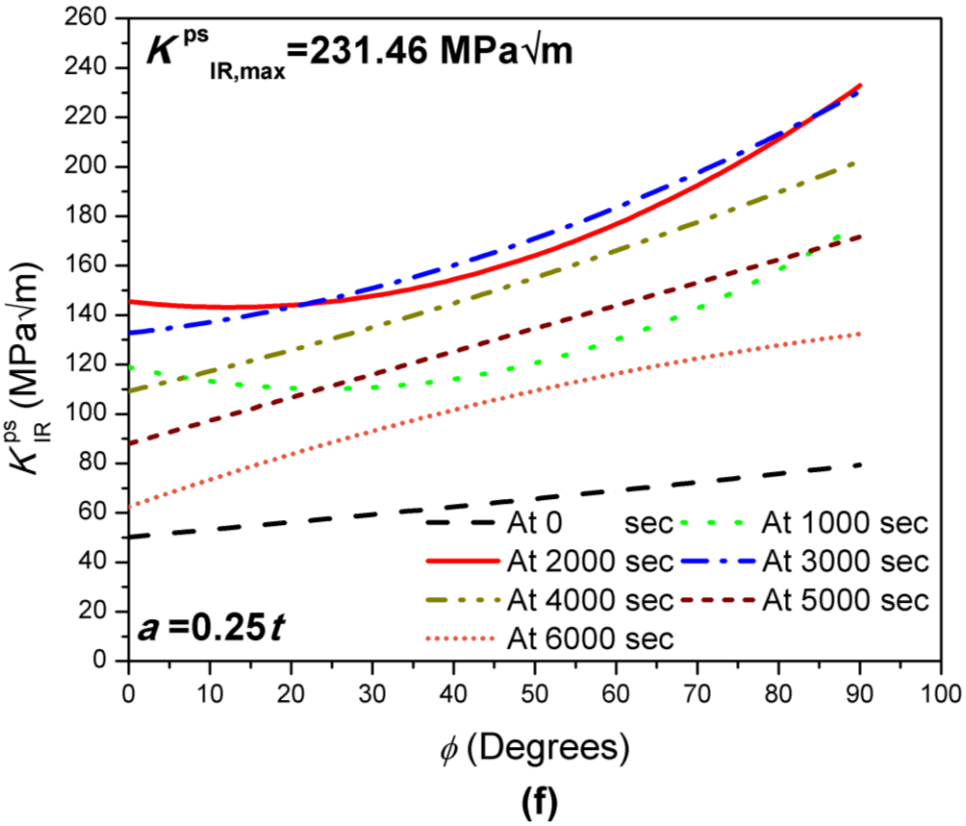

(f)

Figure 7-15 The LEFM based SIFs under RST.

7.3.2 The EPFM Based SIFs under RST

The EPFM based SIFs under RST (K_{JR}^{ps}) at 0 *sec*, 1000 *sec*, 2000 *sec*, 3000 *sec*, 4000 *sec*, 5000 *sec*, and 6000 *sec* have been presented in Figure 7-16 (a-f). Figure 7-16 (a), (b), (c), (d), (e) and (f) show SIFs of the cracks having minor axis *(a)* equal to 1 percent, 5 percent, 10 percent, 15 percent, 20 percent and 25 percent of the wall thickness (*t*), respectively. The maximum EPFM based SIF of the worst crack (a = 0.25t and a = 0.33c) approaches $K_{JR,\max}^{ps} = 240.05\ MPa\sqrt{m}$ as shown in Figure 7-16 (f).

In this case, as it can be seen in Figure 7-16 (a-f), the worst time interval shifts from 2000 *sec* to 3000 *sec*. The cracks up to 'a = 0.10t' produce maximum SIFs at 2000 *sec* while the cracks having depths greater than 'a = 0.10t produce maximum SIFs at 3000 *sec*.

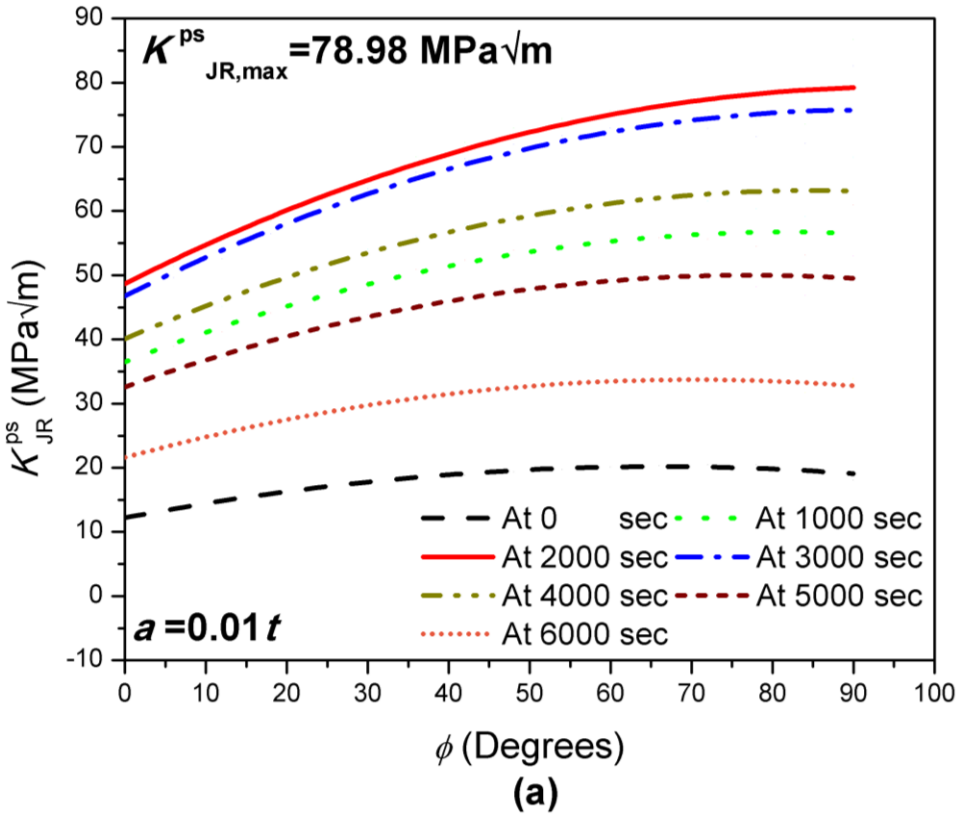

Figure 7-16 The EPFM based SIFs under RST…

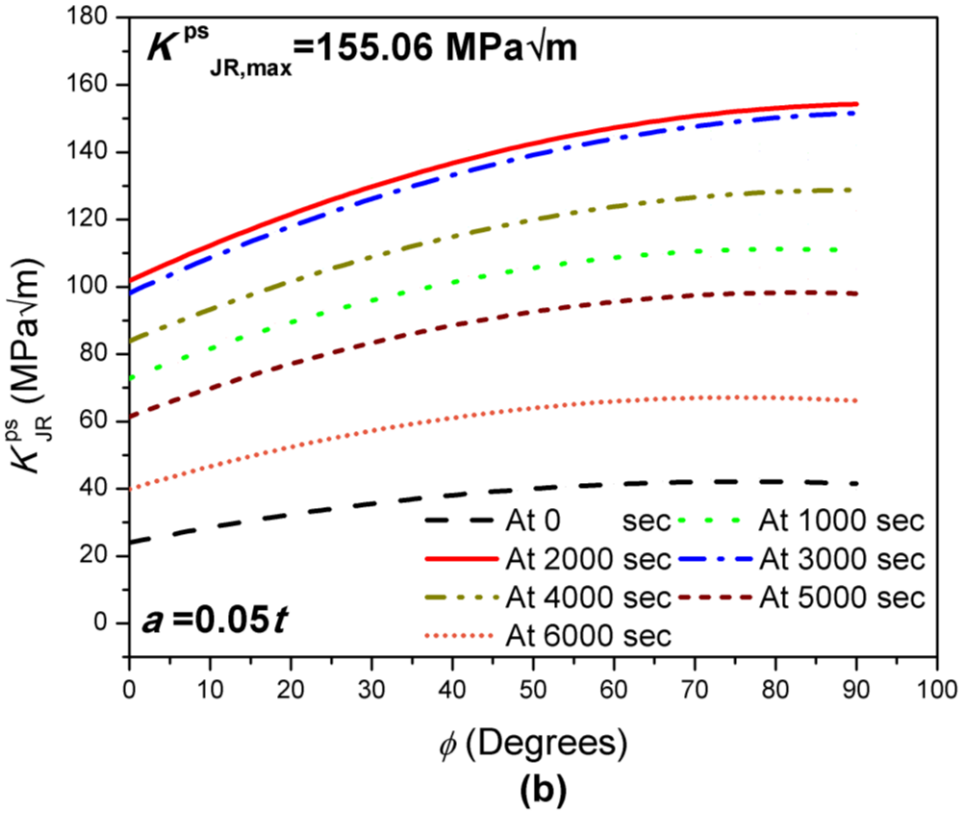

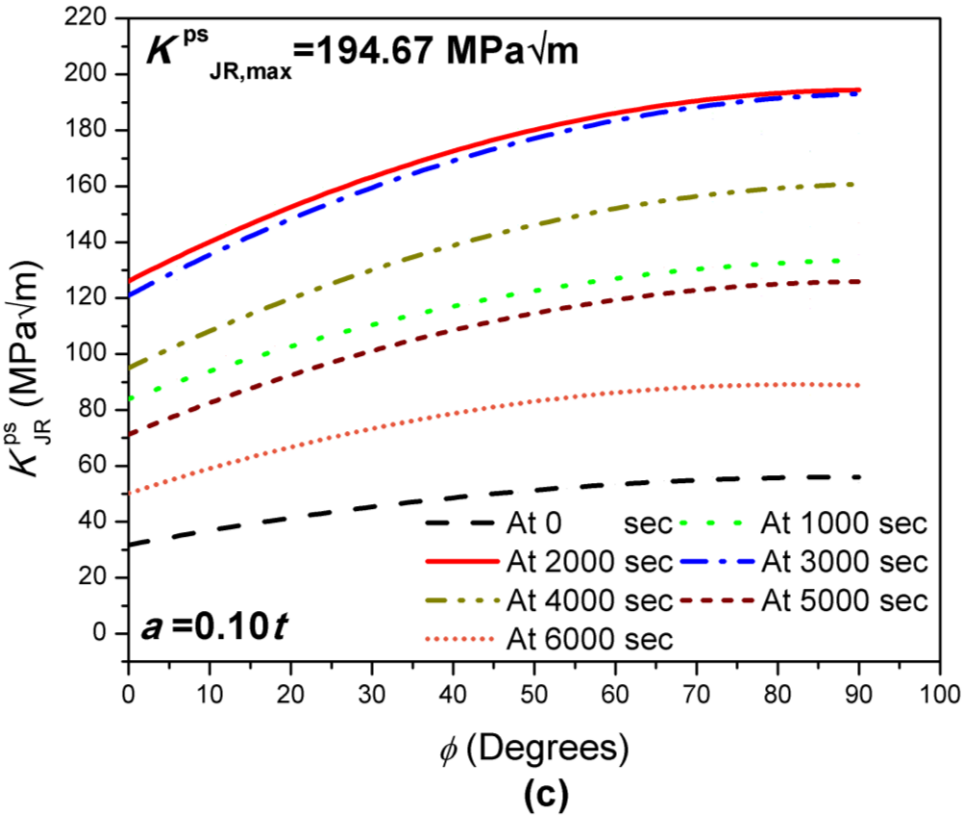

Figure 7-16 The EPFM based SIFs under RST…

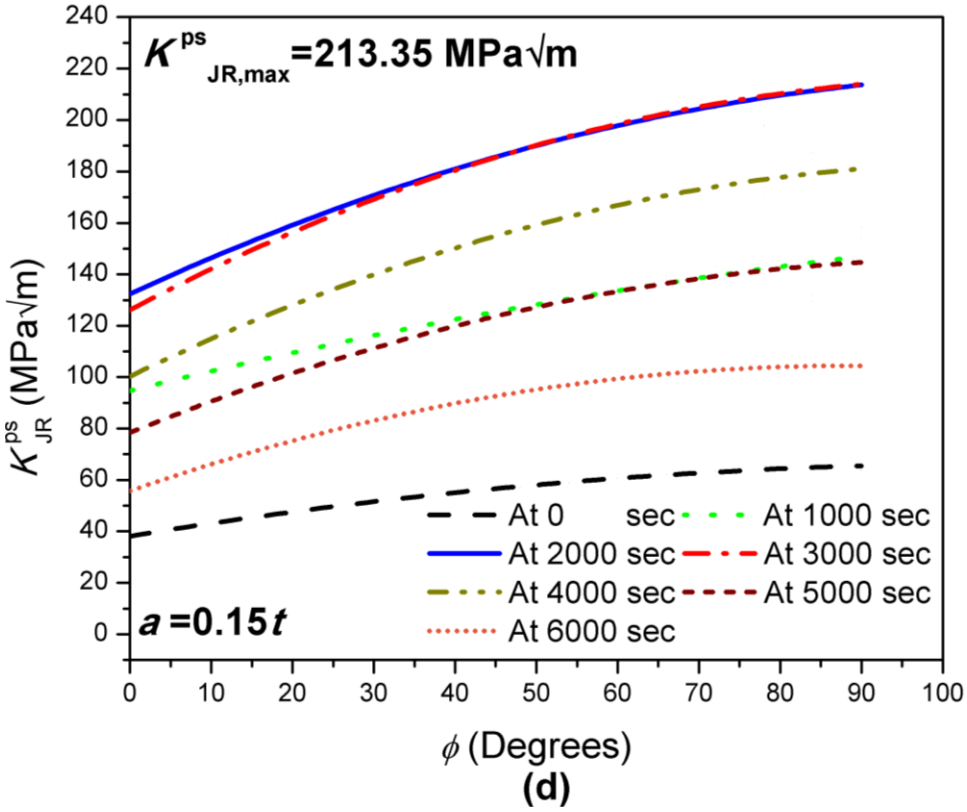

(d)

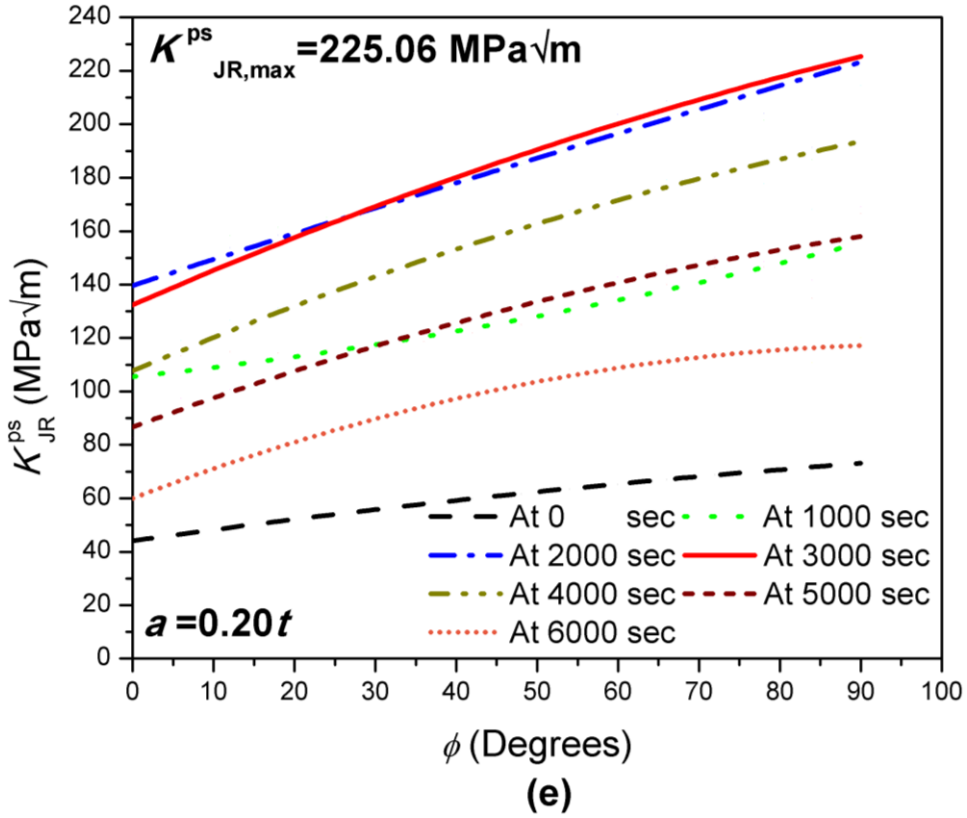

(e)

Figure 7-16 The EPFM based SIFs under RST…

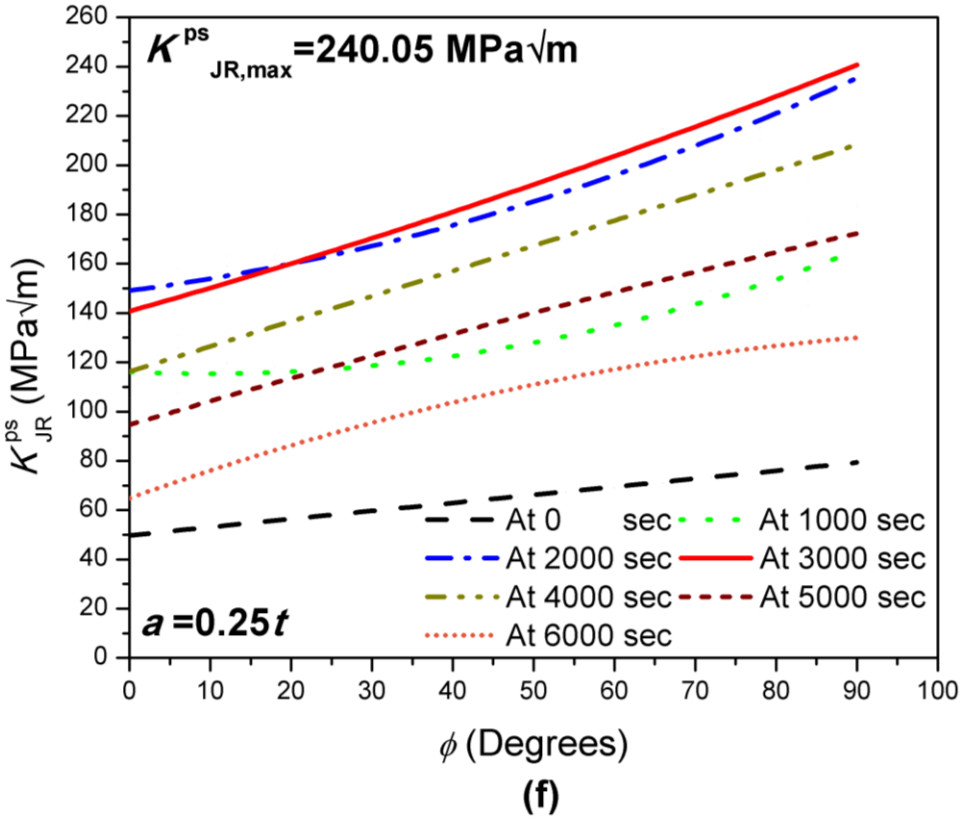

Figure 7-16 The EPFM based SIFs under RST.

The comparison of the maximum LEFM based SIFs and the maximum EPFM based SIFs under RST conditions have also been given in Table 7.5. It is evident from the comparison that the LEFM based SIFs are always lesser than the EPFM based SIFs under RST conditions.

Table 7.5 The maximum SIFs under RST conditions.

Crack depth	LEFM based SIF $MPa\sqrt{m}$	EPFM based SIF $MPa\sqrt{m}$
$a = 0.01t$	57.14	78.98
$a = 0.05t$	119.88	155.06
$a = 0.10t$	160.05	194.67
$a = 0.15t$	190.04	213.35
$a = 0.20t$	214.67	225.06
$a = 0.25t$	231.46	240.05

7.3.3 The Fracture Evaluation under RST

Taking the 'maximum SIFs' of the worst cracks ($a = 0.33c$) for all the crack depths, at the time of 0 *sec*, 1000 *sec*, 2000 *sec*, 3000 *sec*, 4000 *sec*, 5000 *sec*, and 6000 sec,

fracture evaluation under RST in comparison to fracture toughness *'K_{IC}'* is presented in Figure 7-17 (a-f).

It is obvious from Figure 7-17 (a) that crack having depth 'a = 0.01t' is the safe crack as because both 'LEFM based SIFs' and 'EPFM based SIFs' of the crack are much lower than the fracture toughness value of the material. Similarly, the corner crack having depths 'a = 0.05t' is also the safe crack as shown in Figure 7-17 (b). However, in this crack the 'EPFM based SIFs' which is equal to $K^{ps}_{JR,\max} = 155.06\ MPa\sqrt{m}$ is just approaching the fracture toughness value of the material and therefore 'a = 0.05t' may be called as the critical crack depth under RST conditions of the plant. The cracks having depths greater than 'a = 0.05t' (see Figure 7-17 (c-f)) are not the safe cracks and may threatens the safety of the RPV. The crack initiation will start in such cases, which ultimately leads to the failure of the RPV by fracture.

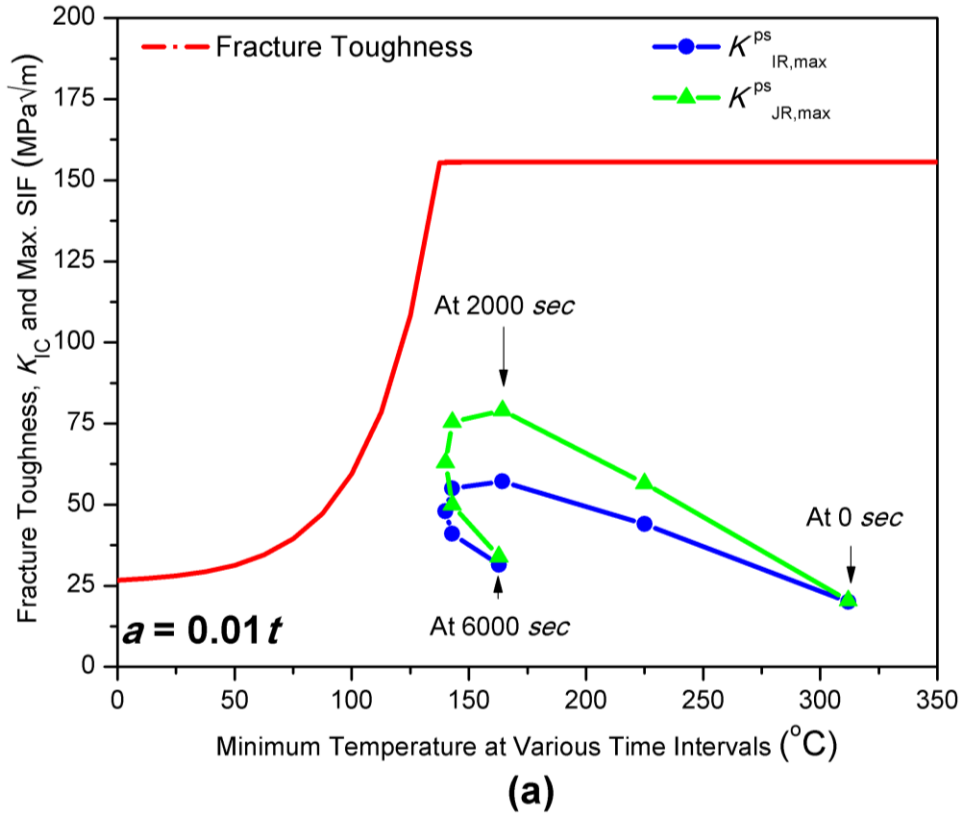

Figure 7-17 The fracture evaluation under RST …

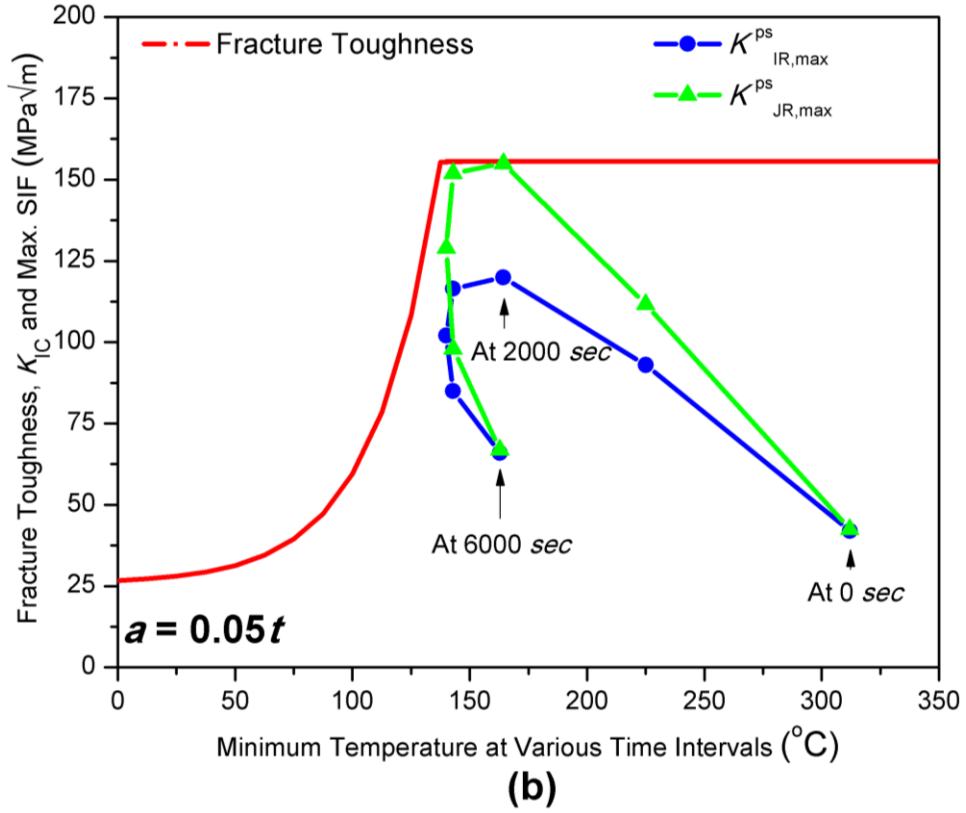

(b)

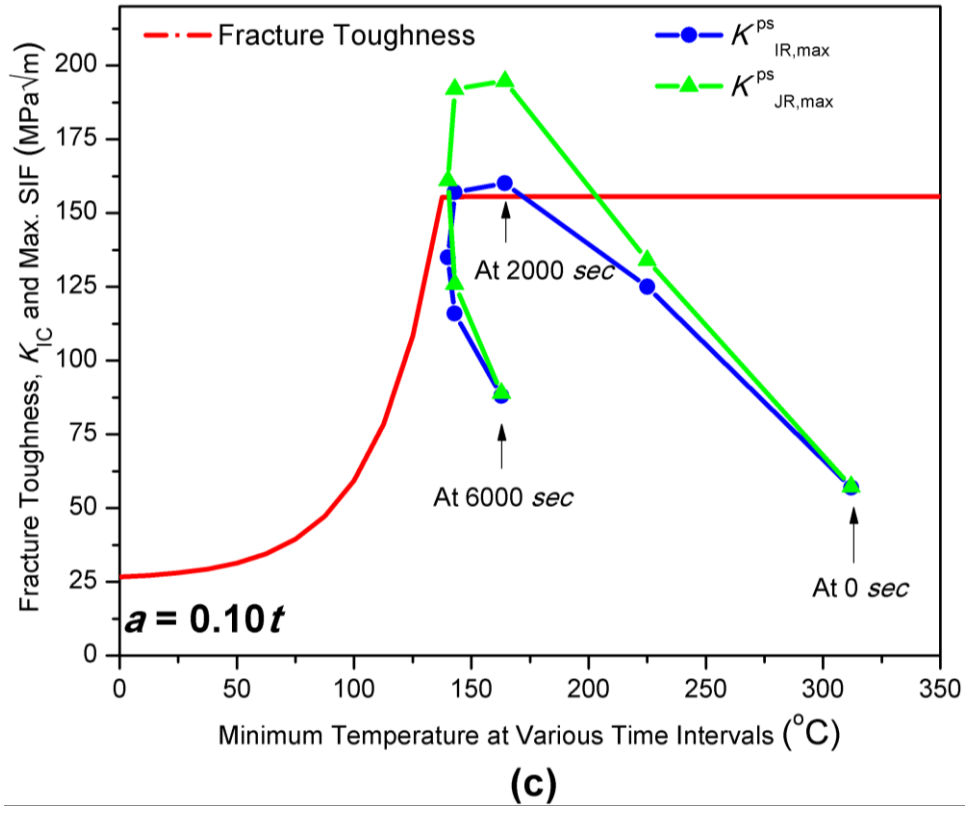

(c)

Figure 7-17 The fracture evaluation under RST …

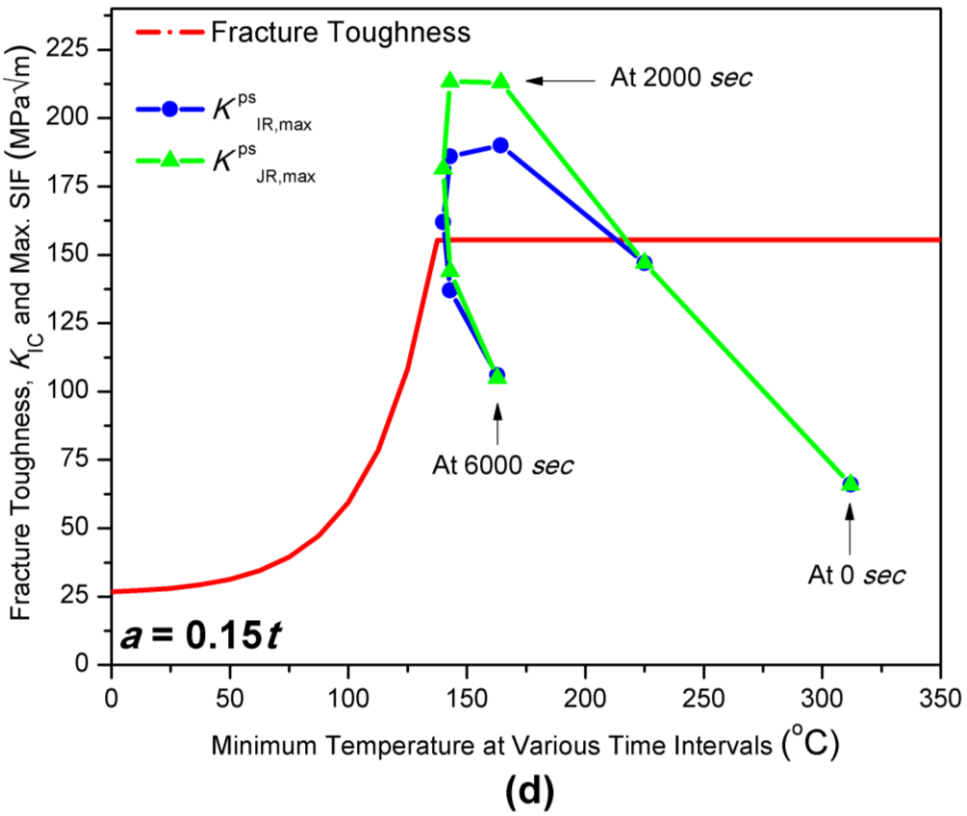

(d)

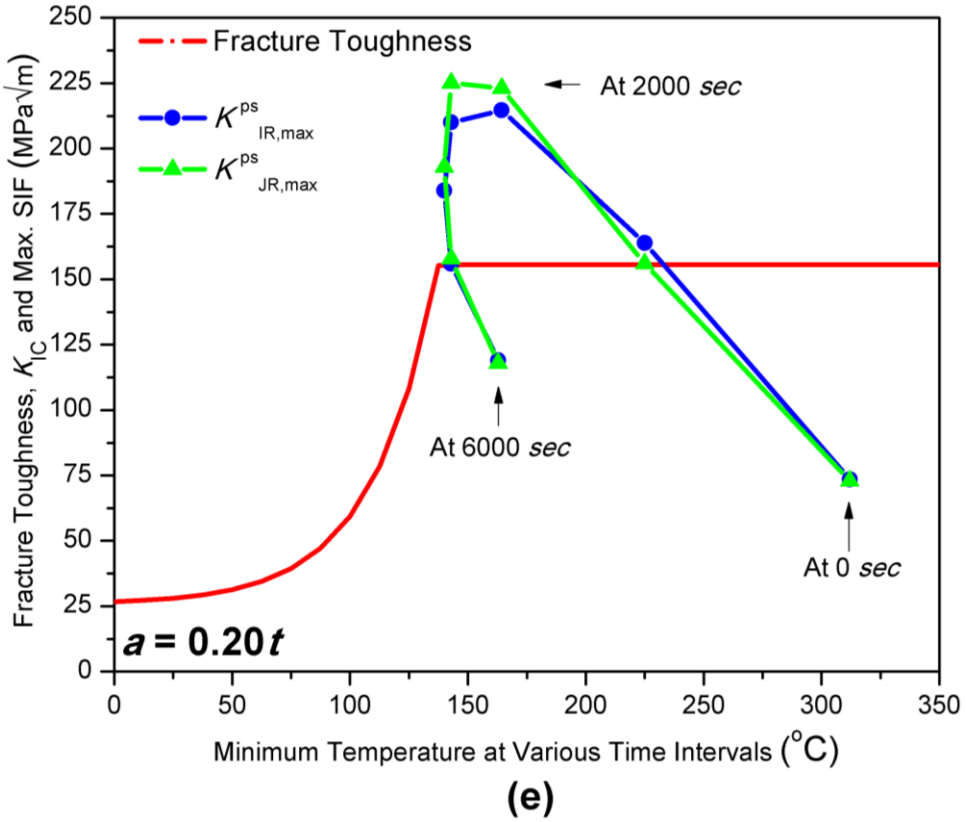

(e)

Figure 7-17 The fracture evaluation under RST …

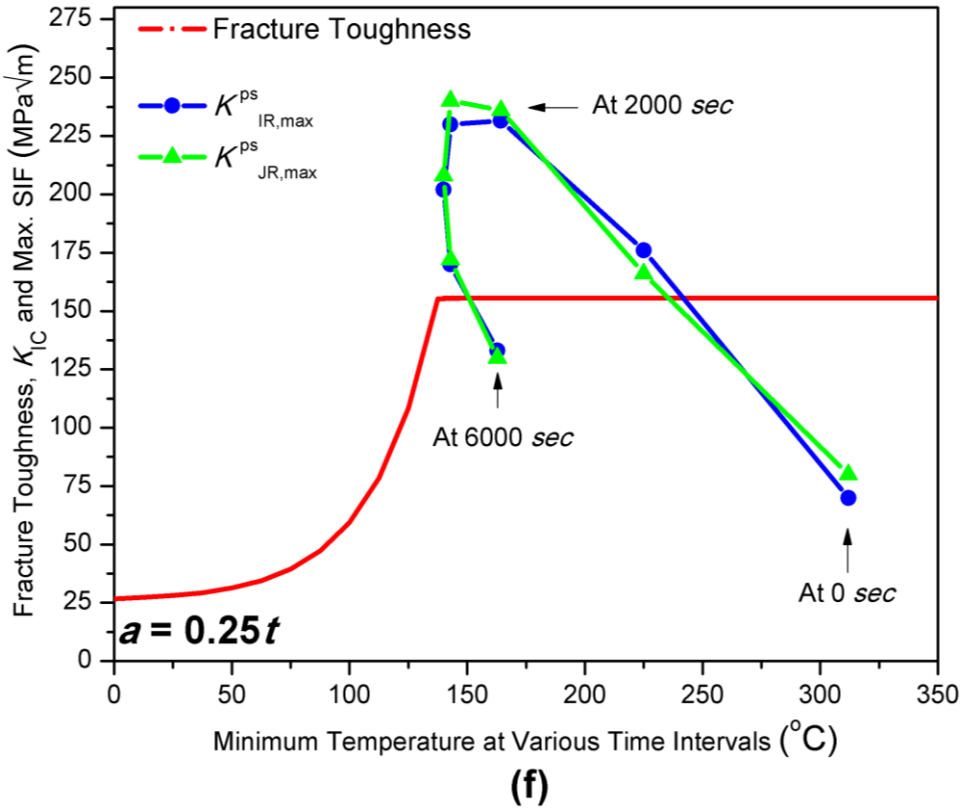

Figure 7-17 The Fracture evaluation under RST.

7.4 Summary of the Chapter

In this chapter, fracture mechanics analysis of the optimized set-in nozzle was performed under normal operating, small loss of coolant accidental and Rancho-Seco transient conditions of the plant. A wide range of corner surface cracks in the limits of '$0.01 < a/t < 0.25$' and '$0.33 < a/c < 1.0$' was analyzed at the optimized nozzle-cylinder intersection of the RPV. Both the 'LEFM based SIFs' and 'EPFM based SIFs' of all the cracks have been presented in a graphical format under all loading conditions. It has been demonstrated, with the size of plastic zone at the crack tip, that the 'LEFM based SIFs' are not sufficient solutions for the fracture evaluation of the RPV made of *'SA-508 Gr.3 Cl.1'* steel.

The normalized 'LEFM based SIFs' have also been provided in this chapter. In normalization, the SIFs of the corner cracks at the nozzle-cylinder intersection were divided with the SIFs of the same crack contained in an infinite plate under tensile loadings. The tensile loadings applied to the infinite plate was taken equivalent to the hoop stress in the reactor pressure vessel. It was found that the corner cracks at the circular hole in the RPV have (in some cases) '5.7 times' greater SIF than the SIF

of the same crack in an infinite plate. The normalization factor in the case of cracks is much more than the stress concentration factor around the circular hole which is about '3'.

It has also been shown in this chapter that the Rancho-Seco transient (RST) conditions are the most detrimental conditions for the reactor pressure vessel. The critical crack depth, found under RST conditions that is '$a = 0.05t$', has been finalized as the critical crack depth for the optimized set-in nozzle. This critical crack depth under RST conditions produces maximum 'EPFM based SIF' at '2000*sec*' which is equal to $K^{p}_{JN,\max} = 155.06\ MPa\sqrt{m}$. This maximum 'EPFM based SIF' of the critical crack is just approaching the fracture toughness value of the vessel's steel which is $K_{IC} = 155.6 MPa\sqrt{m}$.

8 The Effects of Operational Thermal Stresses on SIFs

As discussed in Section 4.6, the provision of the annular chamber for external reactor vessel cooling (ERVC) generates temperature gradients in wall of the RPV under normal operating conditions of the plant. The temperature at the inner surface of the RPV at the set-in nozzle was taken equal to $T_{in} = 288\ ^{\circ}C$ while the temperature at the outer surface of the RPV was found to be $T_{out} = 272.98\ ^{\circ}C$. The temperature difference between the inner and outer surface of the RPV at the nozzle belt region is therefore equal to $\Delta T = 15.02\ ^{\circ}C$. This temperature difference will generate operational thermal stresses in the vessel's wall. In order to investigate the effects of such thermal stresses, a coupled field structural-thermal analysis under combined pressure plus thermal loadings (called hereinafter 'the combined loadings') was performed. The SIFs of all the corner cracks as listed in Table 7.1 have been computed under 'the combined loadings'. The effects of the operational thermal stresses on the SIFs of the corner cracks were investigated and have been presented in this chapter.

8.1 Stress Analysis under Only Thermal Loading

Initially, the stress analysis of the RPV under only thermal loadings was performed using the FE model as shown in Figure 5-1 (b). The temperature distributions in the nozzle belt of the RPV resulted from steady-state finite element thermal analysis have been shown in Figure 8-1.

These temperature distributions were used to compute operational thermal stresses in the nozzle belt of the RPV. The thermal stress distributions in the hoop direction of the nozzle belt are shown in Figure 8-2. It is clear from Figure 8-2, that compressive thermal stresses are produced at the inner surface of the nozzle belt while tangential thermal stresses are produced at the outer surface of the nozzle belt. It is due to the fact that at the inner surface of the cylinder, the material 'wants to grow' but is restricted by the adjacent material at the lower temperature, and therefore

results compressive hoop stresses at this section. Hence, the operational thermal stresses will decrease the mechanical tensile hoop stresses (crack opening stresses) at the nozzle-cylinder intersection which were generated due to the only pressure loading.

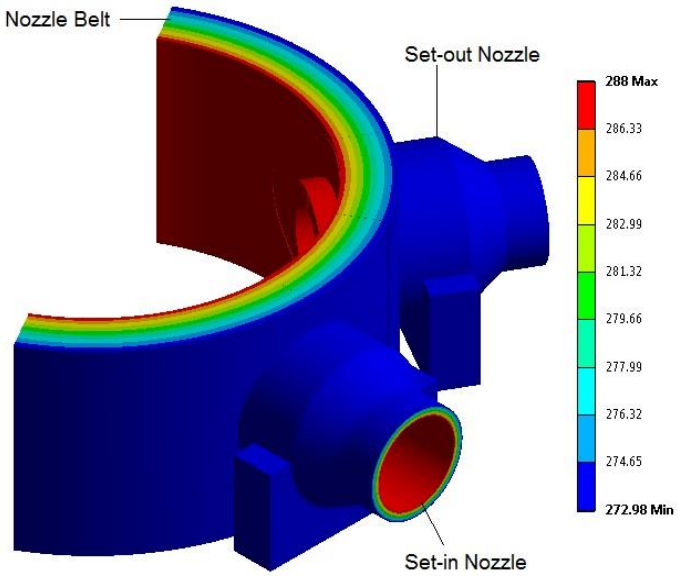

Figure 8-1 Temperature distributions in the nozzle belt, temperature in ^{o}C.

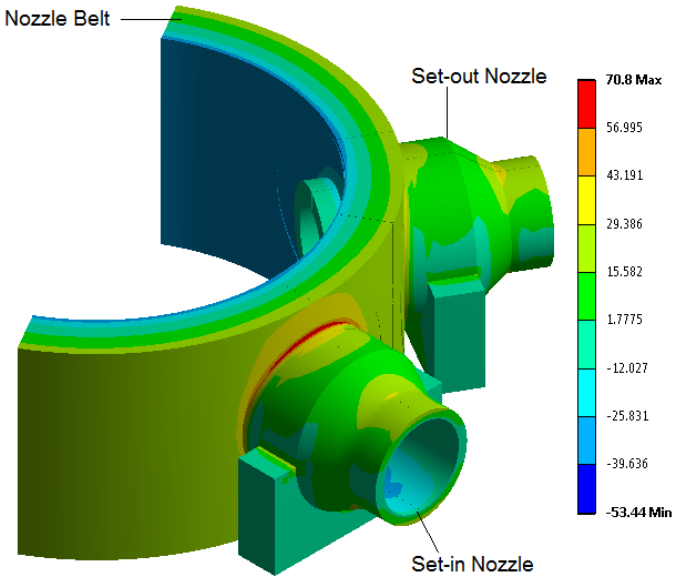

Figure 8-2 Thermal stress distributions in the hoop direction, stresses in MPa.

8.2 Stress Analysis under the Combined Loadings

The structural pressure stresses were coupled with the operational thermal stresses and the resulting hoop stress distributions in RPV under the combined loadings have been shown Figure 8-3. It is clear that the optimized set-in nozzle-cylinder

intersection is the highest stress concentration point of the vessel under the combined loadings. Although, the magnitude of hoop stress at the nozzle-cylinder intersection is slightly lesser in case of the combined loadings when compared to the hoop stress under the only pressure loading (see Figure 7-1).

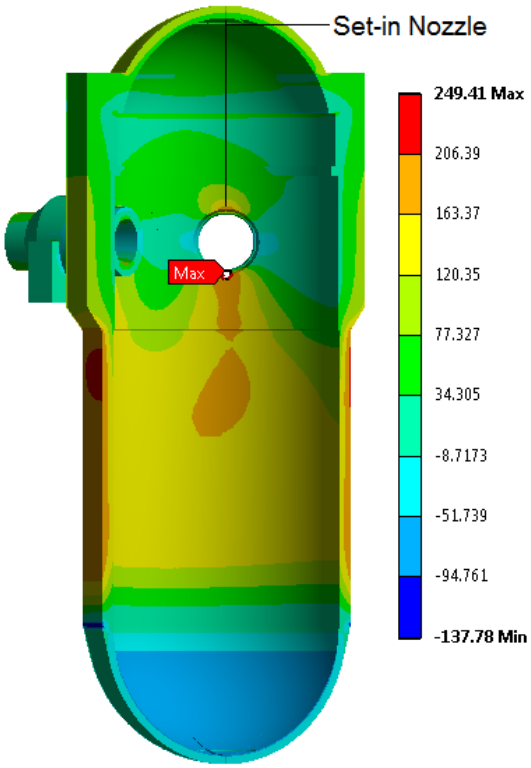

Figure 8-3 Hoop stress distributions under the combined loadings.

8.3 The LEFM Based SIFs under the combined Loadings

For comparison, all the corner cracks listed in Table 7.1, were analyzed under the combined loadings. The LEFM based SIFs under the combined pressure and thermal loadings (K_{IN}^{ps}) for all the corner cracks have been presented in Figure 8-4. The Figure 8-4 (a), (b), (c), (d), (e) and (f) show LEFM based SIFs of the cracks having minor axis *(a)* equal to 1 percent, 5 percent, 10 percent, 15 percent, 20 percent and 25 percent of the wall thickness (*t*), respectively.

It is evident from Figure 8-4 (a-f) that as the '*a/c*' ratio increases (for all values of '*a/t*'), SIF at $\phi = 0^{\circ}$ also increases while SIF at $\phi = 90^{\circ}$ decreases.

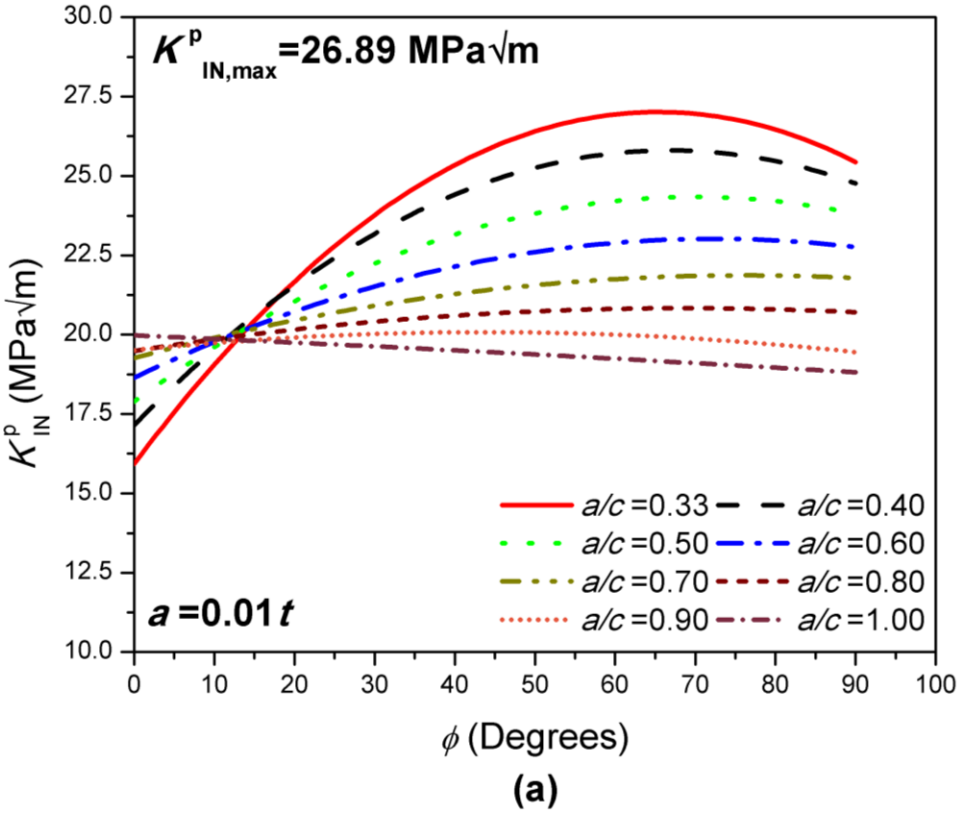

(a)

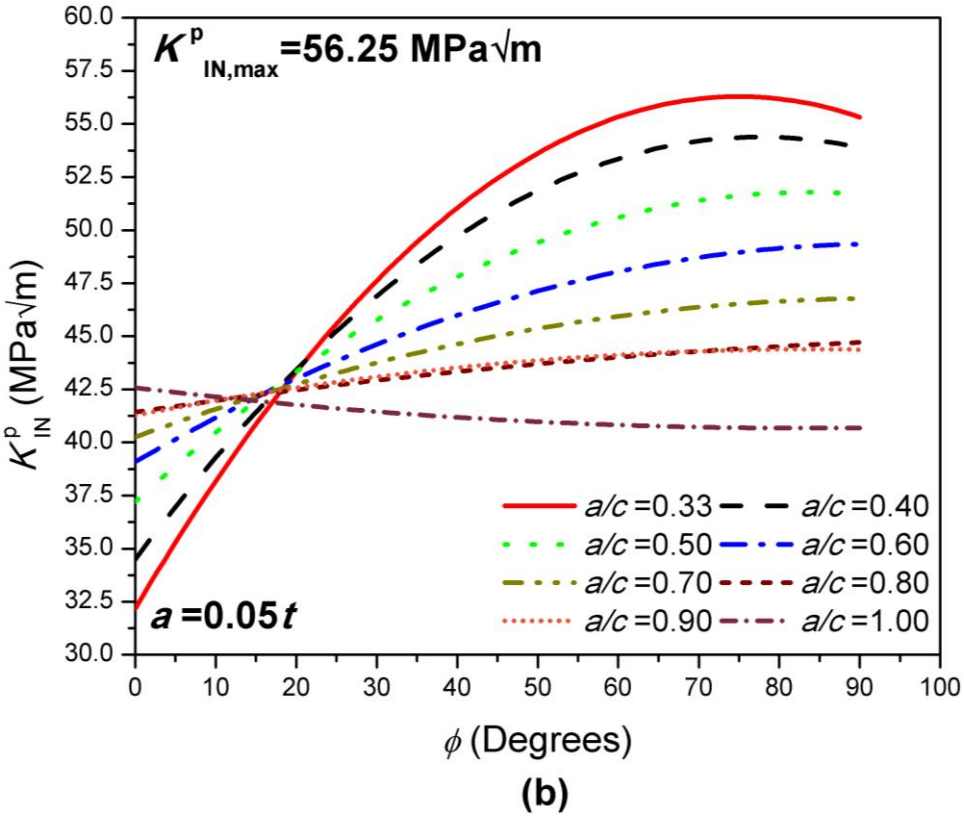

(b)

Figure 8-4 The LEFM based SIFs under the combined loadings…

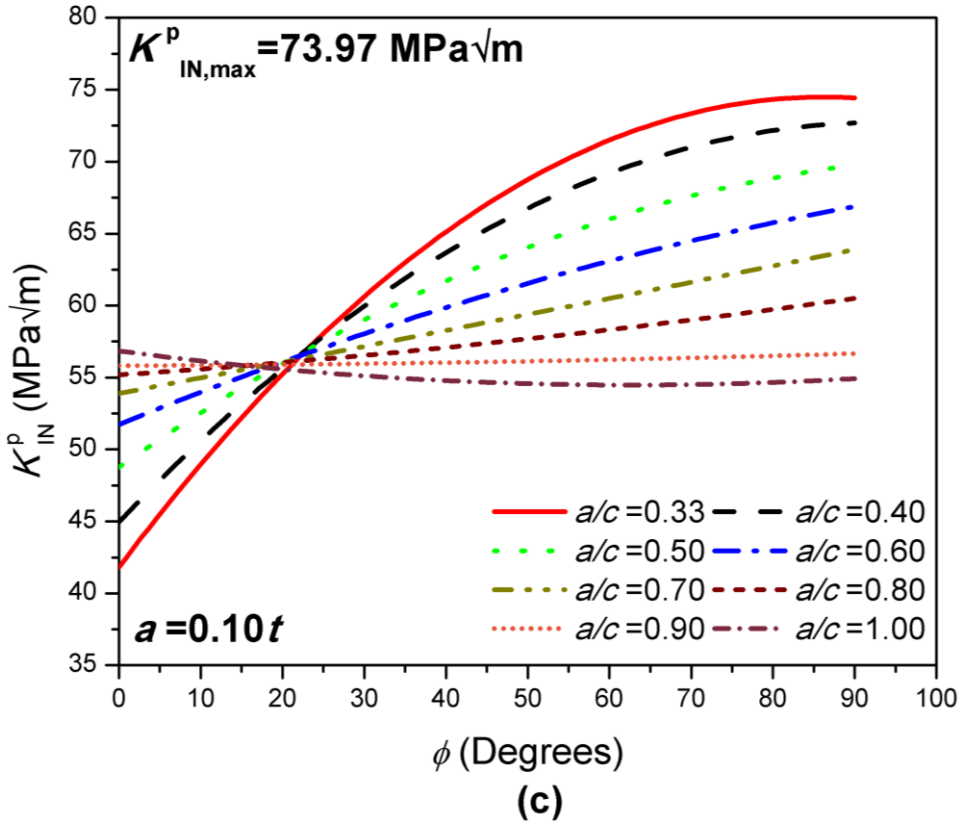

(c)

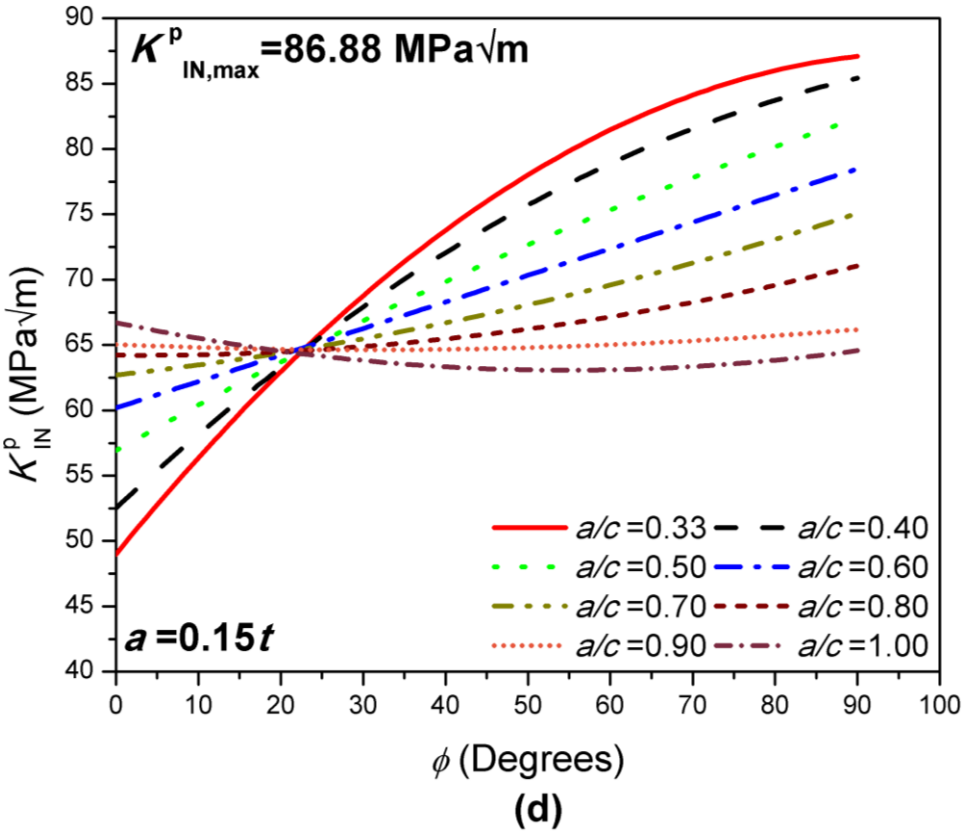

(d)

Figure 8-4 The LEFM based SIFs under the combined loadings…

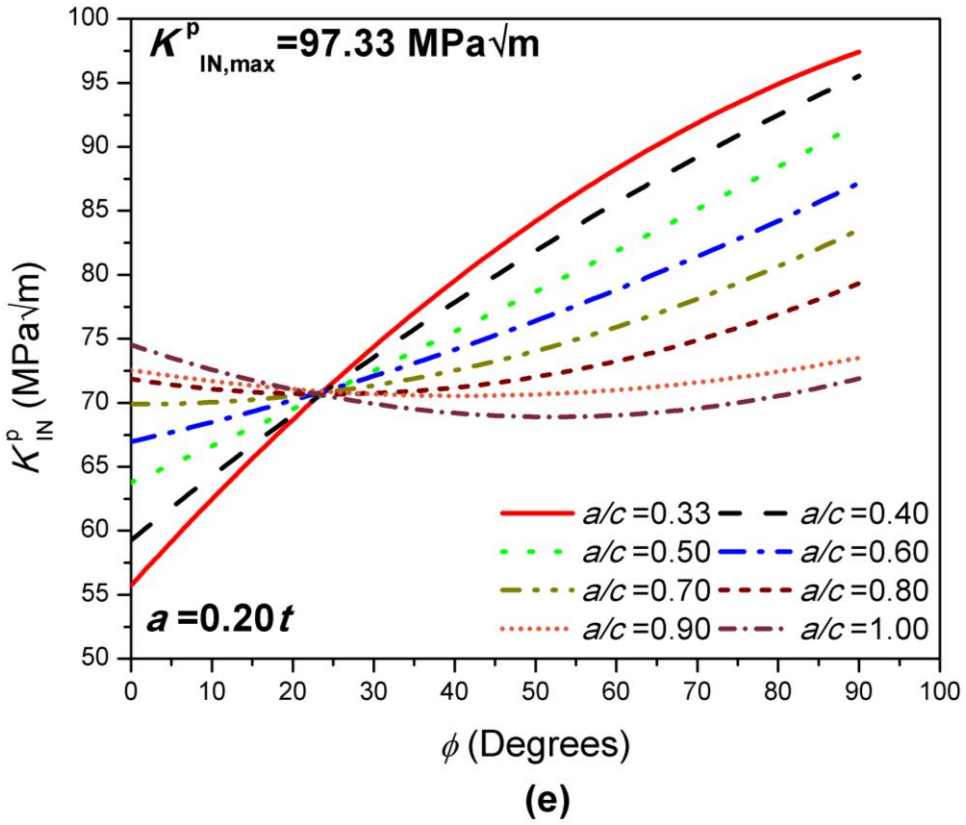

(e)

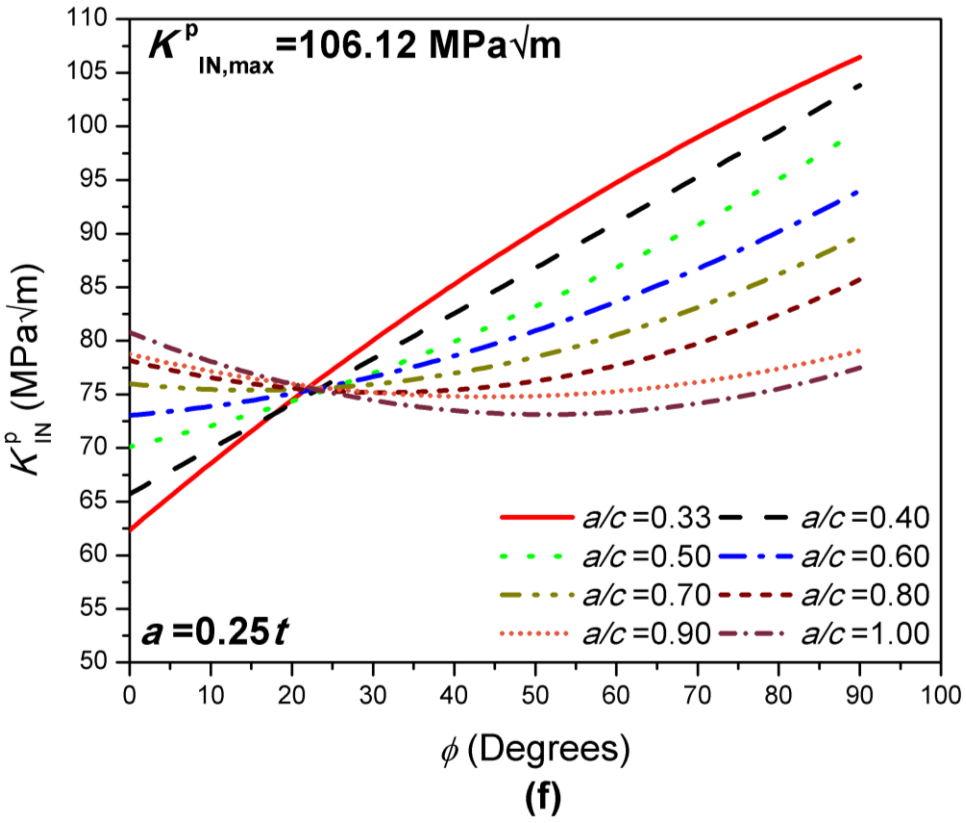

(f)

Figure 8-4 The LEFM based SIFs under the combined loadings.

8.4 The Effects of Operational Thermal Stresses on SIFs of the Cracks

For presenting the effects of the operational thermal stresses on SIFs of the corner cracks, six corner cracks having aspect ratio $a = 0.33c$ for all six 'a/t' ratios ($a = 0.01t$, $a = 0.05t$, $a = 0.10t$, $a = 0.15t$, $a = 0.20t$, *and* $a = 0.25t$) were considered. The SIFs under the only pressure loading were taken from Figure 7-4 while the SIFs under the combined loadings were taken from Figure 8-4. The comparison between the SIFs is given in Figure 8-5. The decreasing slope of all the lines predicts that the operational thermal stresses reduce the SIFs of the corner cracks at the set-in nozzle-cylinder intersection of the RPV.

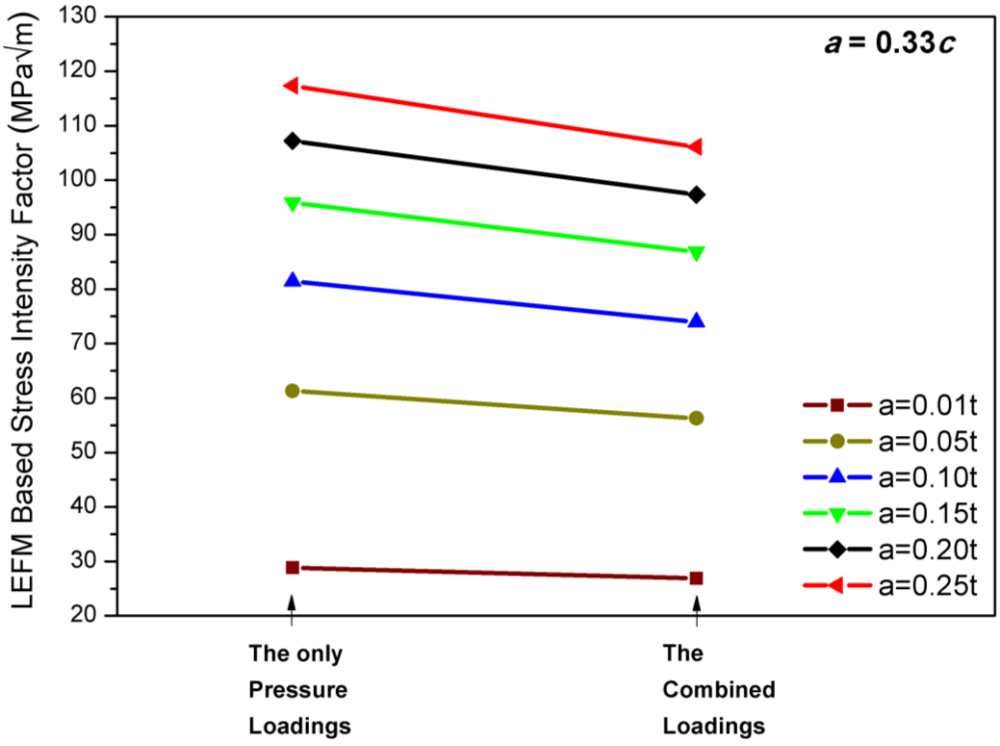

Figure 8-5 Effects of operational thermal stresses on the SIFs of the cracks.

Hence, it can be concluded from the discussion that the operational thermal stresses caused by the provision of annular chamber of air between the RPV and the RVI for ERVC actually reduce the SIFs due to the only pressure loading. Such operational thermal stresses do not endanger the safety of the RPV. Therefore, the application of the annular chamber for the external reactor vessel cooling is fully successful and safe from fracture mechanics point of view.

9 Conclusion and Future Work

In this thesis, the optimization and fracture mechanics analysis of the set-in nozzle of a typical reactor pressure vessel of a 300 MW pressurized water reactor have been performed successfully. A nuclear grade steel *'SA-508 Gr.3 Cl.1'* has been used as the material of the RPV for this study. This chapter briefly states the novelty of the thesis, the conclusion of the thesis, and the future directions drawn from the thesis. The research work may be treated as an academic work or a very preliminary step towards the economical and safe design of reactor pressure vessels.

9.1 Novelty of the Thesis

The following three achievements constitute the overall novelty of the thesis.

1. The thesis proposes a design of a set-in nozzle, for the reactor pressure vessel of a 300 MW pressurized water reactor (see Chapter 5).
2. The thesis presents a novel 'pallet body approach' for assessment of a 3D curved surface cracks (see Chapter 6). The approach presents a methodology for the development of finite element mesh in the cracked region. The approach is capable of efficiently computing stress intensity factors (SIFs) along the crack front. The approach is so versatile that it can be used to analyze edge, embedded and corner cracks having straight, elliptical, and circular crack fronts. The approach is also capable of analyzing inclined and undulated cracks in engineering structures [70].
3. The thesis presents the fracture mechanics analysis of the proposed set-in nozzle (see Chapter 7 & 8). The SIFs of the corner cracks at the nozzle-cylinder intersection of the RPV, under normal operating and accidental conditions of the plant, were missing in the literature as discussed in Section 3.3. This thesis presents the SIFs of a wide range of the corner surface cracks under normal operating, SB-LOCA, and RST conditions of the plant. The SIFs under all the conditions have been presented in a suitable graphical format, which provides a tool for fracture mechanics analysis of the set-in nozzle.

9.2 Conclusion of the Thesis

The following conclusions have been drawn from the thesis.

9.2.1 Optimization of the Set-in Nozzle

In this thesis, starting from a typical set-in nozzle, an optimized design of the nozzle has been proposed for the reactor pressure vessel of a 300 MW pressurized water reactor. The dimensions of the typical nozzle was 'R = 375 *mm*', 'X = 900 *mm*', and 'θ = 3.5º'; where *'R'* is the inner radius of the nozzle, *'θ'* is the taper angle at the nozzle-cylinder intersection and *'X'* is the span of the nozzle. These three variables have been named as the design variables of the set-in nozzle. The set-in nozzle was optimized based on maximum stress intensity at the nozzle-cylinder intersection and the mass of the nozzle. These two conflicting variables have been named as the state variables in the optimization process. The optimal design of the set-in nozzle is the one, which reduces the maximum stress intensity (Tresca yield criterion) along the nozzle below the yield strength of the material provided that the mass of the nozzle is kept constant. The maximum stress intensity at the nozzle-cylinder intersection in the case of typical nozzle was *'maximum S.I* = 296.06 *MPa'* and the mass of the typical nozzle with the material *'SA-508 Gr.3 Cl.1'* was found to be 8767.1 *kg*. The dimensions of the optimized set-in nozzle which have been investigated, in this study, are 'R = 358.13 *mm*', 'X = 776.42 *mm*', and 'θ = 6.0º'. The maximum stress intensity at the optimized nozzle-cylinder intersection was *'maximum S.I* =283.14 *MPa'* and the mass of optimized nozzle was found to be 8763.3 *kg*.

It has also been demonstrated that the maximum allowable pressure of the 'RPV with the optimized nozzle' is 21.9 *MPa* with the safety margin of 1.5 over the criterion given in ASME code [1]. Moreover, the proposed design of the nozzle is a safe design and the margin of safety is '2' as per design-by-analysis approach given in ASME code [1].

9.2.2 The Pallet Body Approach

In order to perform fracture mechanics analysis of the optimized set-in nozzle an approach to insert a 3D surface crack and to generate mesh in the cracked region was developed using 'ANSYS Workbench'. The approach has been named as the 'pallet body approach' of crack modeling. In this approach, small pallet shape bodies are

generated around the whole crack front, which controls the high quality hexahedral finite element mesh around the crack. It has been shown that the 'pallet body fracture model' developed using the 'pallet body approach' is reliable and efficient for the computations of stress intensity factors. The fracture model shows a good agreement with Newman and Raju analysis [6] and difference between the two studies is within 5 % along the whole crack front. Further, the model has also been verified by ASME code [7] where it also shows a good agreement and the difference between the two studies is within 4 %. It has also been demonstrated that the stress intensity factors presented by the 'pallet body approach' can be used with confidence for the computations of loading and unloading beach marks, and corresponding life of the component. These crack growth parameters during the process of crack growth have been validated by comparing the results with the experimental work of Reytier [8].

9.2.3 The Fracture Mechanics Analysis

In order to determine the critical crack depth at the optimized nozzle-cylinder intersection, the fracture mechanics analysis was performed under normal operating conditions and accidental conditions of plant. The accidental conditions include small break loss of coolant accident (SB-LOCA) and Rancho-Seco transient (RST) conditions. A wide range of corner elliptical surface cracks in the limits of '$0.01 < a/t < 0.25$' and '$0.33 < a/c < 1.0$' was analyzed under all the loading conditions of the reactor. Where *'a'*, *'c'* and *'t'* represent minor axis of the crack, major axis of the crack and thickness of the vessel wall at the nozzle-cylinder intersection, respectively. Both the 'LEFM based SIFs' and the 'EPFM based SIFs' of all the cracks were computed and have been presented in a suitable graphical format. It was demonstrated with the size of plastic zone at the crack tip that small scale yielding condition is not satisfied in the case of RPV made of *'SA-508 Gr.3 Cl.1'* steel. Hence, only the 'LEFM based SIFs' of the corner cracks are not sufficient solutions and the 'EPFM based SIFs' are also required for the fracture evaluation of the vessel. It has also been found that the 'EPFM based SIFs' are always greater than the 'LEFM based SIFs' of the cracks.

The limits of the corner crack as described above has the worst crack having dimensions '$a = 0.25t$ and $a = 0.33c$'. This worst corner crack has 'LEFM based SIFs' under normal, SB-LOCA, and RST conditions equal to $K^{p}_{IN,\max} = 117.23\ MPa\sqrt{m}$,

$K^{ps}_{IS,\max} = 151.99\ MPa\sqrt{m}$, and $K^{ps}_{IR,\max} = 231.46\ MPa\sqrt{m}$, respectively. The 'EPFM based SIFs' of the worst crack under normal, SB-LOCA, and RST conditions have much higher values which are equal to $K^{p}_{JN,\max} = 115.23\ MPa\sqrt{m}$, $K^{ps}_{JS,\max} = 142.65\ MPa\sqrt{m}$, and $K^{ps}_{JR,\max} = 240.05\ MPa\sqrt{m}$, respectively. It has also been shown that the RST conditions produce most detrimental pressurized thermal shock when compared with the normal operating and the SB-LOCA conditions of the plant.

The fracture evaluation and the determination of critical crack depths under normal, SB-LOCA and RST conditions were also conducted in this thesis. For the purpose, fracture toughness of the RPV's steel *(SA-508 Gr.3 Cl.1)* was determined considering the end-of-life neutron fluence of the reactor. A factor of safety equivalent to $\sqrt{2}$ was also applied to the fracture toughness curve. The corner crack having depth equal to '$a = 0.05t$' has been finalized as an overall critical crack depth for the proposed set-in nozzle.

Finally, the effects of operational thermal stresses on stress intensity factors of all the corner cracks have been investigated. The operational thermal stresses generated in the RPV due to the provision of annular chamber for external reactor vessel cooling, were considered for the analysis. It has been demonstrated that such operational thermal stress do not endanger the safety of the RPV. It is due to fact that the operational thermal stresses actually reduce SIFs of the corner cracks resulted under the only pressure loadings to the RPV. It is therefore concluded that the application of the annular chamber between reactor pressure vessel and reactor vessel insulation is fully successful and safe from the fracture mechanics point of view.

9.3 Future Direction of the Thesis

The following future works have been identified for extending the work presented in this thesis.

9.3.1 Optimization and Fracture Mechanics Analysis of the Complete RPV

The optimization methodology and approach for fracture mechanics analysis developed in this thesis can be used for performing optimization and fracture

mechanics analysis of all other vulnerable areas of the RPV. These areas may include set-out nozzle of the RPV, beltline region (cylindrical shell) of the RPV, and the junction of the hemispherical heads with the cylindrical shell of the RPV.

9.3.2 Analysis of Inclined Corner Cracks

In this thesis, corner cracks were analyzed at the nozzle-cylinder intersection, perpendicular to the maximum principal stress or hoop stress in the RPV. However, the developed 'pallet body approach' can be used to analyze inclined corner crack at nozzle-cylinder intersection of the RPV. The inclined corner crack at nozzle-cylinder intersection means that the crack comes combinedly under the effects of hoop stress and longitudinal stress in the vessel's wall. The mixed mode stress intensity factors will be computed for the inclined cracks.

9.3.3 Analysis of Undulated Corner Cracks

The cracks analyzed, in this thesis, were quarter elliptical and quarter circular corner cracks. However, the developed 'pallet body approach' can be used for the analysis of undulated corner cracks (see Figure 3-1) at the nozzle-cylinder intersection. The comparison of elliptical corner cracks can be made with the various types of undulated corner cracks at the nozzle-cylinder intersection of the RPV in order to investigate the most detrimental shape of the crack.

9.3.4 Life Estimation of the RPV

Considering a manufacturing crack of known dimensions at the nozzle-cylinder intersection of the RPV, the crack's growth profiles and the safe life of the vessel under fatigue loadings can be investigated as shown in Section 6.2.4. The life of the vessel will be the count of the incremental loading cycles at which the pre-crack will approach the critical crack depth that is '$a = 0.05t$'. It should be kept in mind, that the fatigue crack growth at the corner of the nozzle is mainly caused by the thermal stresses due to the fluid temperature fluctuations. These temperature fluctuations forms a cyclic or fatigue thermal loadings which in addition to pressure loadings can be utilized as the input loadings for the fatigue crack growth.

9.3.5 Use of Ceramic Metal Composite for Set-in Nozzle

The Ceramic metal/matrix composites (CMCs) can be used as a nozzle's material since they may require less or no cooling. The major setback in this approach is that the existing ASTM (or similar) standards may not be compatible with the use of newly developed advanced materials for high pressure and temperature applications. But there are emerging studies on use of these materials especially in aerospace/aviation industries [87].

References

[1] *ASME Boiler and Pressure Vessel Code, Section III, Division 1: Rules for construction of nuclear facility componenets,* New York, 2010.

[2] Y. Bangash, "PWR steel pressure vessel design and practice," *Progress in Nuclear Energy,* vol. 16(1), pp. 1-40, 1985.

[3] D. Broek, *Elementary engineering fracture mechanics*, 4th revised ed.: Kluwer Academic Publishers, Dordrecht, 1986.

[4] G. E. Dieter, *Mechanical metallurgy*, 3rd ed. USA: McGraw-Hill, 1987.

[5] A. T. Diamantoudis and T. Kermanidis, "Design by analysis versus design by formula of high strength steel pressure vessels: a comparative study," *International Journal of Pressure Vessels and Piping,* vol. 82, pp. 43-50, 2005.

[6] J. C. Newman Jr. and I. S. Raju, "An empirical stress intensity factor equation for the surface crack," *Engineering Fracture Mechanics,* vol. 15, pp. 185-192, 1981.

[7] *ASME Boiler and Pressure Vessel Code, Section XI, Rules for in-service inspection of nuclear power plant components, Non Mandatory Appendix A, Article A-3000,* New York, 2010.

[8] M. Reytier, "Fatigue crack growth in large cracked plates of martensitic P91 steel at 550 C," *Power Plant Oper Mainten Mater Issue,* vol. 3(2), pp. 1-10, 2004.

[9] https://en.wikipedia.org/wiki/Pressurized_water_reactor [Online].

[10] J. E. Shigley, *Mechanical engineering design*, First ed. Singapore: McGraw-Hill, 1986.

[11] M. J. Hyder and M. Asif, "Optimization of location and size of opening in a pressure vessel cylinder using ANSYS," *Engineering Failure Analysis,* vol. 15, pp. 1-19, 2008.

[12] U. T. Murtaza and M. J. Hyder, "Optimization of the Size and Shape of the Set-in Nozzle for a PWR Reactor Pressure Vessel," *Nuclear Engineering and Design*, vol. 284, pp. 219-227, 2015.

[13] *ASME Boiler and Pressure Vessel Code, Section XI, Rules for in-service inspection of nuclear power plant components*, New York, 2010.

[14] *Code of Federal Regulations, Fracture toughness requirements for protection against pressurized thermal shock events, Title 10, Part 50, Section 50.61 and Appendix G*, 1996.

[15] *U.S. Nuclear Regulatory Commission, Loss of integrated control system power and overcooling transient at Rancho Seco on December 26, 1985, USNRC Report NUREG 1195*, 1986.

[16] J. W. Park, "Analytical evaluation of two-phase natural circulation flow characteristics under external reactor vessel cooling," *Annals of Nuclear Energy,* vol. 36, pp. 1668-1675, 2009.

[17] J. S. Kim and T. E. Jin, "Structural integrity assessment of the reactor pressure vessel under the external reactor vessel cooling condition," *Nuclear Engineering and Design,* vol. 191, pp. 117-133, 1999.

[18] B. Dureta, J. C. Bonnarda, J. M. Seilera, G.Greffierb, J. Drub, and B. Tourniaireb, "Experimental investigation of the permeability of PWR insulation panels for ex-vessel cooling," *Nuclear Engineering and Design*, vol. 278, pp. 406-413, 2014.
[19] Z. A. Hassan, "Fatigue analysis of pressure vessel using ANSYS," M.S. Thesis, Dept. Mech. Engg., Pak. Inst. of Engg. and Appl. Sciences., 2010.
[20] A. Javaid, "Effect of opening in pressure vessel cylinder," M.S. Thesis, Dept. Mech. Engg., Pak. Inst. of Engg. and Appl. Sciences., 2011.
[21] T. Gul, "To study the effect of opening in pressure vessel head using ANSYS," M.S. Thesis, Dept. Mech. Engg., Pak. Inst. of Engg. and Appl. Sciences., 2011.
[22] A. Khan, "Structural analysis of PWR pressure vessel (effect of opening)," M.S. Thesis, Dept. Mech. Engg., Pak. Inst. of Engg. and Appl. Sciences., Pakistan, 2012.
[23] M. Adil, "Structural analysis of typical PWR pressure vessel (effect of cylindrical thickness)," M.S. thesis, Dept. Mech. Engg., Pak. Inst. of Engg. and Appl. Sciences., 2012.
[24] M. Haseeb, "Pressure vessel inlet nozzle strength analysis using ANSYS," M.S. thesis, Department of Nuclear Engineering, Pak. Inst. of Engg. and Appl. Sciences., Pakistan, 2014.
[25] M. Kuna, *Finite Elements in Fracture Mechanics Theory-Numerics-Applications*: Springer, 2013.
[26] G. R. Irwin, "Crack extension force for a part - through crack in a plate," *Journal of Applied Mechanics Trans ASME, Ser E*, vol. 29, pp. 651–4., 1962.
[27] F. W. Smith, A. F. Emery, and A. S. Kobayashi, "Stress intensity factors for semicircular cracks Part 2 - semi-infinite solid," *Journal of Applied Mechanics*, vol. 34, pp. 947–52., 1967.
[28] R. W. Thresher and F. W. Smith, "Stress intensity factors for a surface crack in a finite solid," *Journal of Applied Mechanics*, vol. 39, pp. 95–200, 1972.
[29] C. Y. Liao and S. N. Atluri, "Stress intensity factor variation along a semicircular surface flaw in a finite-thickness plate," *Engineering Fracture Mechanics*, vol. 34, pp. 957–76, 1989.
[30] T. A. Cruse, "Application of the boundary-integral equation method to three dimensional stress analysis," *Computers and Structures*, vol. 3, pp. 509–27, 1973.
[31] C. Guozhong and Z. Kangda, "Stress intensity factor for semi-elliptical surface cracks in plates and cylindrical pressure vessels using the hybrid boundary element method," *Engineering Fracture Mechanics*, vol. 52, pp. 1035-1054, 1995.
[32] C. Guozhong and Z. Kangda, "Stress intensity factors for internal semi elliptical surface cracks in pressurized thick walled cylinders using the hybrid boundary element methods," *Engineering Fracture Mechanics*, vol. 52, pp. 1055-1064, 1995.
[33] W. S. Blackburn and T. K. Hellen, "Calculation of stress intensity factors in three dimensions by finite element methods," *International Journal for Numerical Methods in Engineering*, vol. 11, pp. 211-29, 1972.
[34] H. G. Delorenzi, "Energy release rate calculations by the finite element method," *Engineering Fracture Mechanics*, vol. 21, pp. 129-43, 1985.
[35] T. Fett, "Estimation of stress intensity factors for semi-elliptical surface cracks," *Engineering Fracture Mechanics*, vol. 66, pp. 349-356, 2000.

[36] J. R. Rice and N. Levy, "The part-through surface crack in an elastic plate," *Journal of Applied Mechanics,* vol. 39, pp. 185–94, 1972.
[37] F. Erdogan and B. Aksel, "Line spring model and its applications to part-through crack problems in plates and shells, NASA Contractor Report 178141," LEHIGH University Bethlehemj Pennsylvania1986.
[38] R. Sethuraman and I. T. Ilango, "Analysis of interacting semi-elliptical surface cracks in finite thickness plates under remote bending load," *International Journal of Pressure Vessels and Piping,* vol. 82, pp. 528-545, 2005.
[39] B. E. K. Hachi, S. Rechak, Y. Belkacemi, and G. Maurice, "Modeling of elliptical cracks in an infinite body and in a pressurized cylinder by a hybrid weight function approach," *International Journal of Pressure Vessels and Piping,* vol. 82, pp. 917-924, 2005.
[40] I. S. Raju and J. C. Newman Jr., "Stress-intensity factors for a wide range of semi-elliptical surface cracks in finite thickness plates," *Engineering Fracture Mechanics,* vol. 11, pp. 817-29, 1979.
[41] J. C. Newman Jr. and I. S. Raju, "Analysis of surface cracks in finite plates under tension and bending loads," *NASA TP-1578,* 1979.
[42] J. C. Newman Jr. and I. S. Raju, "Stress intensity factors for internal surface cracks in cylindrical pressure vessels," *NASA-TM-80073,* 1979.
[43] A. O. Ayhan and H. F. Nied, "Stress intensity factors for three-dimensional surface cracks using enriched elements," *International Journal for Numerical Methods in Engineering,* vol. 54, pp. 899-921, 2002.
[44] A. O. Ayhan, "Mixed mode stress intensity factors for deflected and inclined surface cracks in finite-thickness plates," *Engineering Fracture Mechanics,* vol. 71, pp. 1059-1079, 2004.
[45] A. O. Ayhan, "Mixed mode stress intensity factors for deflected and inclined corner cracks in finite-thickness plates," *International Journal of Fatigue,* vol. 29, pp. 305-317, 2007.
[46] A. T. Diamantoudis and G. N. Labeas, "Stress intensity factors of semi-elliptical surface cracks in pressure vessels by global-local finite element methodology," *Engineering Fracture Mechanics,* vol. 72, pp. 1299-1312, 2005.
[47] A. R. Shahani and S. E. Habibi, "Stress intensity factors in a hollow cylinder containing a circumferential semi-elliptical crack subjected to combined loading," *international Journal of Fatigue,* vol. 29, pp. 128-140, 2007.
[48] D. Bremberg and G. Dhont, "Automatic mixed-mode crack propagation based on a combined hexahedral-tetrahedral approach," *Key Engineering Materials,* vol. 348-349, pp. 581-584, 2007.
[49] D. Bremberg and G. Dhondt, "Automatic crack insertion for arbitrary crack growth," *Engineering Fracture Mechanics,* vol. 75, pp. 404-416, 2008.
[50] *European Committee for Standardization, EN 13445, Unfired Pressure Vessels - Part 3: Design*, 2002.
[51] M. A. Guerrero, C. Betegon, and J.Belzunce, "Fracture analysis of a pressure vessel made of high strength steel (HSS)," *Engineering Failure Analysis,* vol. 15, pp. 208-219, 2008.
[52] E. Nart and A. O. Ayhan, "Crack insertion, meshing and fracture analysis of structures using tetrahedral finite elements," *European Journal of Mechanics A-Solids,* vol. 30, pp. 293-306, 2011.

[53] M. Uslu, O. Demir, and A. O. Ayhan, "Surface cracks in finite thickness plates under thermal and displacement-controlled loads - part 1: Stress intensity factors," *Engineering Fracture Mechanics,* vol. 115, pp. 284-295, 2014.
[54] K. Ramesh. (2007). *E-Book on engineering fracture mechanics*.
[55] G. Dhondt, "Automatic 3-D mode I crack propagation calculations with finite elements," *International Journal for Numerical Methods in Engineering,* vol. 41, pp. 739-757, 1998.
[56] X. B. Lin and R. A. Smith, "Finite element modelling of fatigue crack growth of surface cracked plates Part I: The numerical technique," *Engineering Fracture Mechanics,* vol. 63, pp. 503-522, 1999.
[57] X. B. Lin and R. A. Smith, "Finite element modelling of fatigue crack growth of surface cracked plates Part II: Crack shape change," *Engineering Fracture Mechanics,* vol. 63, pp. 523-540, 1999.
[58] B. J. Carter, P. A. Wawrzynek, and A. R. Ingraffea, "Automated 3-D crack growth simulation," *International Journal for Numerical Methods in Engineering,* vol. 47, pp. 229-253, 2000.
[59] J. Hou, M. Goldstraw, S. Maan, and M. Knop, "An evaluation of 3D crack growth using ZENCRACK, Defense Science and Technology," 2001.
[60] M. Schöllmann, M. Fulland, and H. A. Richard, "Development of a new software for adaptive crack growth simulations in 3D structures," *Engineering Fracture Mechanics,* vol. 70, pp. 249-268, 2003.
[61] A. O. Ayhan, "Simulation of three-dimensional fatigue crack propagation using enriched finite elements," *Computers and Structures,* vol. 89, pp. 801-812, 2011.
[62] M. Uslu, O. Demir, and A. O. Ayhan, "Surface cracks in finite thickness plates under thermal and displacement controlled loads - Part 2: Crack propagation," *Engineering Fracture Mechanics,* vol. 115, pp. 255-269, 2014.
[63] D. Siegele, L. Hodulak, I. Varfolomeyev, and G. Nagel, "Failure assessment of RPV nozzle under loss of coolant accident," *Nuclear Engineering and Design,* vol. 193, pp. 265-272, 1999.
[64] Y. He and T. Isozaki, "Fracture mechanics analysis and evaluation for the RPV of the Chinese Qinshan 300 MW NPP under PTS," *Nuclear Engineering and Design,* vol. 201, pp. 121-137, 2000.
[65] Ü. Çolak and O. Özdere, "Comparative analysis of pressure vessel integrity for various LOCA conditions," *Journal of Nuclear Materials,* vol. 297, pp. 271-278, 2001.
[66] O. Ö. Gülol and Ü. Çolak, "Comparison of pressure vessel integrity analyses and approaches for VVER 1000 and PWR vessels for PTS conditions," *Nuclear Engineering and Design,* vol. 226, pp. 231-241, 2003.
[67] M. Chen, F. Lu, R. Wang, and A. Ren, "Structural integrity assessment of the reactor pressure vessel under the pressurized thermal shock loading," *Nuclear Engineering and Design,* vol. 272, pp. 84-91, 2014.
[68] U. T. Murtaza and M. J. Hyder, "Design by analysis versus design by formula of a PWR reactor pressure vessel," in *International MultiConference of Engineers and Computer Scientists,* Hong Kong, 2015, pp. 942-946.
[69] U. T. Murtaza and M. J. Hyder, "The effects of thermal stresses on the elliptical surface cracks in PWR reactor pressure vessel," *Theoretical and Applied Fracture Mechanics,* vol. 75C, pp. 124-136, 2015.

[70] U. T. Murtaza and M. J. Hyder, "Methodology to analyze 3-D curved surface cracks using hybrid finite elements," in *International Young Engineers Convention*, Lahore, 2014, pp. 158-165.
[71] ESS, "Assessment and management of ageing of major nuclear power plant components important to safety: PWR pressure vessels," International Atomic Energy Agency, IAEA-TECDOC-1120, 1999.
[72] *ASME Boiler and Pressure Vessel Code, Section II, Part D: Properties, Materials*, New York, 2010.
[73] *USNRC Regulatory Guide 1.99, Rev. 2, Radiation embrittlement of reactor vessel materials*, Washington, DC, 1988.
[74] I. Kaplan, *Nuclear Physics*, 2nd ed. USA: Addison-Wesley Publishing Company, 1977.
[75] *ASME Boiler and Pressure Vessel Code, Section III, Division 1, Appendix G: Fracture toughness criteria for protection against failure*, New York, 2010.
[76] *API 579-1/ASME FFS-1 Fitness-For-Service standard, ANNEX F Material properties for A FFS assessment*, 2007.
[77] M. J. Jhung and Y. W. Park, "Deterministic fracture mechanics analysis of pressurized thermal shock," *Journal of the Korean Nuclear Society*, vol. 30, pp. 470-484, 1998.
[78] J. F. Harvey, *Theory and Design of Modern Pressure Vessels*, 2nd ed. New York, USA: Van Nostrand Reinhold Company, 1974.
[79] H. H. Lee, *Finite element simulations with ANSYS Workbench 14*. USA: Stephen Schroff, 2012.
[80] K. Deb, *Multi-objective optimization using evolutionary algorithms*, First ed. Chichester: John Wiley & Sons, 2001.
[81] ANSYS Inc., *Design exploration user's guide*, 2014.
[82] M. Muscat, D. Mackenzie, and R. Hamilton, "A work criterion for plastic collapse," *International Journal of Pressure Vessels and Piping*, vol. 80, pp. 49-58, 2003.
[83] A. G. Miller, "Review of limit loads of structures containing defects," *International Journal of Pressure Vessels and Piping*, vol. 32, pp. 197-327, 1988.
[84] S. T. Lie, B. F. Zhang, T. Li, and Z. M. Yang, "Numerical and experimental plastic collapse loads and CTODs of a cracked square hollow section (SHS) K-joint," in *13th International Symposium on Tubular Structures*, Hong Kong, 15 – 17 December 2010.
[85] C. F. Shih, B. Moran, and T. Nakamura, "Energy release rate along a three-dimensional crack front in a thermally stressed body," *International Journal of Fracture*, vol. 30, pp. 79-102, 1986.
[86] *ASME Boiler and Pressure Vessel Code, Section XI, Division 1, Non Mandatory Appendix A: Article A-4000, Material Properties*, 2010.
[87] S. Schmidt, S. Beyera, H. Knabe, H. Immich, R. Meistring, and A. Gessler, "Advanced ceramic matrix composite materials for current and future propulsion technology applications," *Acta Astronautica*, vol. 55, pp. 409-420, 2004.